ZIRCONIA-MATRIX COMPOSITES REINFORCED WITH METAL

A thesis submitted for the degree of

Doctor of Philosophy

at the University of Strathclyde

By

MUHAMMAD W. WILDAN

Registration No: 975 4559

Materials and Metallurgy Group

Department of Mechanical Engineering

University of Strathclyde

October 2000

PREFACE

This thesis describes an original work which has not been submitted for a degree at any university.

The research was performed in the Department of Mechanical Engineering at the University of Strathclyde, Glasgow, Scotland during the period of November 1997 to October 2000 under the supervision of Professor Alan Hendry and Dr. HJ. Edrees.

This thesis describes the production of zirconia-matrix composites reinforced with metal (chromium, iron and stainless steel) powders. The effects of the reinforcements on the sintering behaviour, characterisation and properties (mechanical, thermal and electrical) are examined.

ACKNOWLEDGEMENT

I would like to thank my supervisors, Professor Alan Hendry and Dr. HJ. Edrees for their remarkable help, advice and continuous encouragement during doing this work.

I also wish to thank:
Dr. CF. Burdett for the XRD training, Dr. H. Ewing for the supervision of thermal diffusivity measurement, and technicians: Mr Jim Doherty, Mr. G Johnston, Mr James Kelly, Mr. D. McColl, Mr Chris Cameron, Mr Neil McCrindle, and Mr. A Crockett for their help during performing experimental work.

My sponsor EEDP (Engineering Education Development Project) - the Government of Indonesia for funding my study.

The University of Gadjah Mada Indonesia where I work, for allowing me to undertake further study at the University of Strathclyde, Glasgow.

My wife for her patience, love and constant support.
My parents in Indonesia for their constant support, love and patience.

All of my friends with whom I spent my time in the 'Materials and Metallurgy Group'.

ABSTRACT

The aim of this study was to investigate a zirconia-matrix reinforced with metal powder (chromium, iron and stainless steel (AISI 316)) including processing, characterisation, and measurements of their properties (mechanical, thermal and electrical).

Zirconia stabilised with 5.4 wt% Y_2O_3 (3 mol%) as the matrix was first studied and followed by an investigation of the effects of metal reinforcement on zirconia-matrix composites. Monolithic zirconia was pressureless sintered in air and argon to observe the effect of sintering atmosphere, while the composites were pressureless sintered in argon to avoid oxidation. Sintering was carried out at various temperatures for 1 hour and 1450°C was chosen to get almost fully dense samples. The density of the fired samples was measured using a mercury balance method and the densification behaviour was analysed using TMA (Thermo-mechanical Analysis). The TMA was also used to measure the coefficient of thermal expansion. In addition, thermal analysis using DTA and TGA was performed to observe reactions and phase transformations. Moreover, optical microscopy and SEM were used to observe the microstructures, XRD was used for phase identification, and mechanical properties including Vickers hardness, fracture toughness and bending strength were measured. The effect of thermal expansion mismatch on thermal stresses was also analysed and discussed. Finally, thermal diffusivity at room temperature and as a function of temperature was measured using a laser flash method, and to complete the study, electrical conductivity at room temperature was also measured.

The investigation of monolithic zirconia showed that there was no significant effect of air and argon atmosphere during sintering on density, densification behaviour, microstructures, and properties (mechanical and thermal). Furthermore, the results were in good agreement with that reported by previous researchers.

However, the presence of metal in the composites influenced the sintering behaviour and the densification process depends on the metal stability, reactivity, impurity, particle size, and volume fraction. Iron reacted with yttria (zirconia stabiliser), melted and reduced the densification temperature of monolithic zirconia, while chromium and AISI 316 did not significantly affect the densification temperature and did not react with either zirconia or yttria. AISI 316 melted during fabrication. Moreover, all of the metal reinforcements reduced the final shrinkage of monolithic zirconia.

In terms of properties, the composites showed an increase in fracture toughness, and a reduction in Vickers hardness and strength with increasing reinforcement content. In addition, the thermal diffusivity of the composites showed an increase with reinforcement content for the zirconia/chromium and zirconia/iron composites, but not for the zirconia/AISI 316 composites due to intrinsic mircocracking. Furthermore, all the composites became electrically conductive with 20 vol% or more of reinforcement

It has been concluded that of those composites the zirconia/chromium system may be considered as having the best combination of properties and although further development is needed for such composites to be used in real applications in structural engineering, the materials may be developed based on these findings. In addition, these findings may be used in development of ceramic/metal joining as composite interlayers are frequently used.

CONTENTS

CHAPTER 1
INTRODUCTION

It is well known that ceramics are materials which generally have excellent properties such as high melting point, good high temperature strength, high Young's Modulus, high hardness, good wear and corrosion resistance, relatively low thermal expansion and thermal conductivity, and relatively low density. Ceramics however have limitations in engineering applications because of their brittleness and low fracture toughness [Barsoum, 1997].

Zirconia and zirconia-containing ceramics are ceramic materials, which are used widely in traditional and engineering areas [Lee, 1994; Ruhle, 1997]. For instance, in traditional applications, they are used as abrasives, refractories, foundry sand and flours. In engineering applications, they are being developed to be used as extrusion dies, tribological materials (wear resistance parts), and piston caps [Wood and Oda, 1982] because of their toughness, wear resistance and refractory nature. Moreover because of its low thermal conductivity, zirconia can be used as a thermal barrier coating [Bratton and Lau, 1981]. Also zirconia can be applied as an oxygen sensor and in ceramic fuel cell based on oxygen-ion conduction [Minh, 1993; Wiemhover, 1994].

In his review, Subbarao (1981) noted that research in zirconia ceramics has been increasing rapidly since the 1930s. That research may be classified into two main areas, in which the first area consists of research in atomic structures, microstructures, defects, phase transformations and processing and the second research area considers properties such as mechanical, thermal, electrical, and optical properties. Reviews on zirconia have also been given by several authors such as Garvie (1970), and Lee (1994). More specifically reviews on zirconia have been reported such as Nettleship and Stevens (1987) on Tetragonal Zirconia Polycrystal (TZP); Ruhle (1997) on microstructures of zirconia; Evans and Heuer (1980), Butler

(1985) and Hannink *et al* (2000) on transformation toughening of zirconia-containing ceramics, and Stevens (1994) on engineering properties of zirconia.

The main objectives of work in ceramics such as zirconia in order to enhance applications in engineering is to overcome their brittleness and improve their fracture toughness. Incorporating ductile metal as a second phase into the ceramic matrix has become a way to overcome such brittleness and increase fracture toughness since the ductile metal inclusion may reduce crack propagation [Guichard *et al*, 1998]. Zirconia-based materials are attractive ceramic materials in engineering applications with a thermal expansion coefficient (around 10 x 10^{-6} /°C for tetragonal zirconia polycrystal) close to that of many of metals, which enables development of zirconia composites with metal. However, to the best of the author's knowledge, zirconia matrices reinforced with metals have not been widely observed and are therefore still wide open for development.

Several researchers have reported work in zirconia metal composites. Works on nickel-zirconia ceramic metal composites used in SOFC (solid oxide fuel cell) have been reported by several authors such as Ishizuka *et al* (1995), Jung *et al* (1997), Hu *et al* (1998), and Tamburini *et al* (1998). Work on the investigation of sintering processes for composites of stainless steel and zirconia has been carried out by Wenquan *et al* (1999). Also other researchers have observed zirconia stainless steel composites such as Mihara (1992), Yamada *et al* (1994), and Jung *et al* (1997). Furthermore work on a laminated composite of magnetic metal (Fe-Co-V alloy) and zirconia has been reported by Moorhead (1999).

The aim of this present research is to investigate zirconia ceramic-matrix composites reinforced with metal powder i.e:

a. Zirconia reinforced with chromium (Cr) powder
b. Zirconia reinforced with iron (Fe) powder
c. Zirconia reinforced with stainless steel AISI 316 powder

In this work, zirconia (ZrO_2) stabilised with 5.4 wt% (or 3 mol%) Y_2O_3 (3Y-TZP) is chosen as the matrix, because it has attractive properties in term of mechanical and thermal behaviour, and is widely used in engineering. The incorporation of metal in each composite is intended to improve the fracture toughness of 3Y-TZP since the metals have much better toughness than monolithic 3Y-TZP. In addition because those metals have higher thermal diffusivity and electrical conductivity than that of 3Y-TZP, it is important to know the effect of the reinforcements on such properties in the composites. In more detail this present research observes the sintering process, shrinkage behaviour (densification), the effects of sintering temperature, density, phase analysis and microstructures; mechanical properties such as Vickers hardness, fracture toughness and bending strength; thermal properties such as thermal expansion coefficient and thermal diffusivity; and electrical conductivity.

The research undertaken is presented in this thesis with the structure indicated in Figure 1.1. Chapter 1 introduces the background of the research, the aims and the outline of the thesis.

Chapter 2 describes a literature review of zirconia particularly zirconia stabilised with yttria. It also discusses ceramic-matrix composites and zirconia-matrix composites reinforced with metal.

Chapter 3 describes the materials used in the present research and the procedures of the experimental work.

The experimental results and discussion of 3Y-TZP are presented in Chapter 4 including the processing, characterisation, microstructures, and properties.

Then in Chapter 5, the processing, and characterisation of 3Y-TZP composites reinforced with metals are described and discussed.

The mechanical, thermal, and electrical properties of the composites are provided and discussed in Chapters 6, 7, and 8 respectively. The mechanical

properties include Vickers hardness, fracture toughness, and bending strength. The thermal properties consist of thermal expansion coefficient and thermal diffusivity. The electrical property reported here is electrical conductivity.

All the results in the previous chapters are generally discussed in Chapter 9. Finally in Chapter 10, conclusions and the future work that may be developed are presented.

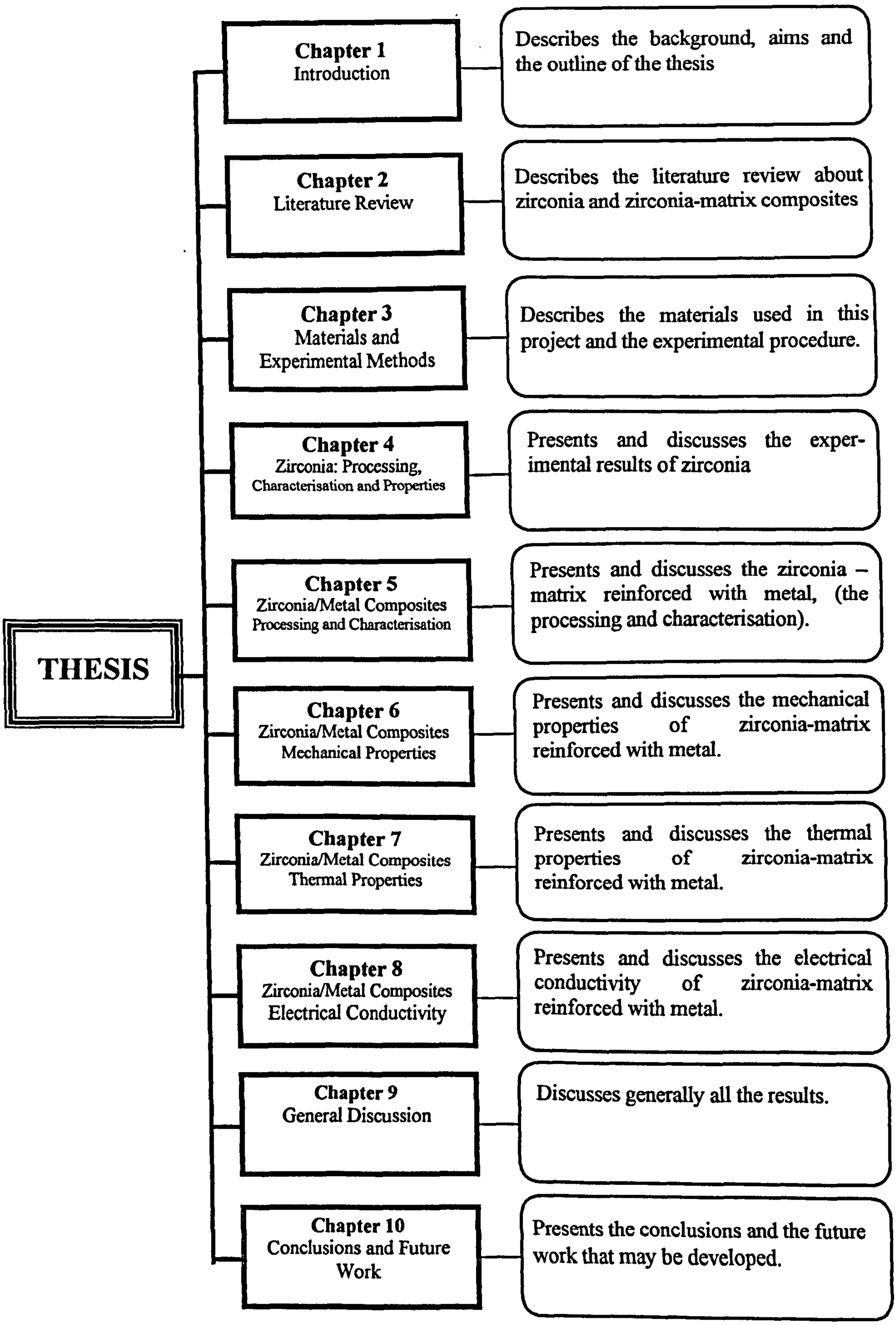

Figure 1.1. Outline of the Thesis

CHAPTER 2

LITERATURE REVIEW

2.1. ZIRCONIA

2.1.1. PURE ZIRCONIA

There are three well-established polymorphs of zirconia, viz monoclinic (m), tetragonal (t) and cubic (c). In pure zirconia, the monoclinic phase exists at room temperature and is stable up to 1170°C. Above 1170°C the monoclinic phase transforms to tetragonal phase and is stable up to 2370°C where the tetragonal phase transforms to cubic phase and is stable up to the melting point at 2680°C. The reverse transformations take place on cooling [Garvie, 1970; Subbarao, 1981; Stevens, 1994].

$$\text{Monoclinic Phase} \underset{}{\overset{1170\,^{\circ}C}{\rightleftharpoons}} \text{Tetragonal Phase} \overset{2370\,^{\circ}C}{\rightleftharpoons} \text{Cubic Phase} \overset{2680\,^{\circ}C}{\rightleftharpoons} \text{Liquid}$$

The phase transformation in pure zirconia from tetragonal to monoclinic during cooling causes a volume increase on the order of 3 - 4% which is big enough to exceed the elastic limit of the zirconia grains and cause cracking. The fabrication of large size pieces of pure zirconia is therefore impossible and this prevents pure zirconia being used in structural ceramics. Wolten (1963) was the first who suggested that this phase transformation is martensitic. He also found that the transformation exhibits a large thermal hysteresis as shown in Figure 2.1. On heating the transition occurs at 1170°C and during cooling it occurs between 850°C and 1000°C, depending on the surface and strain energies. Bansal and Heuer (1972)

established metallographic evidence that the transformation is athermal and shear type in nature, which is consistent with a diffusionless reaction.

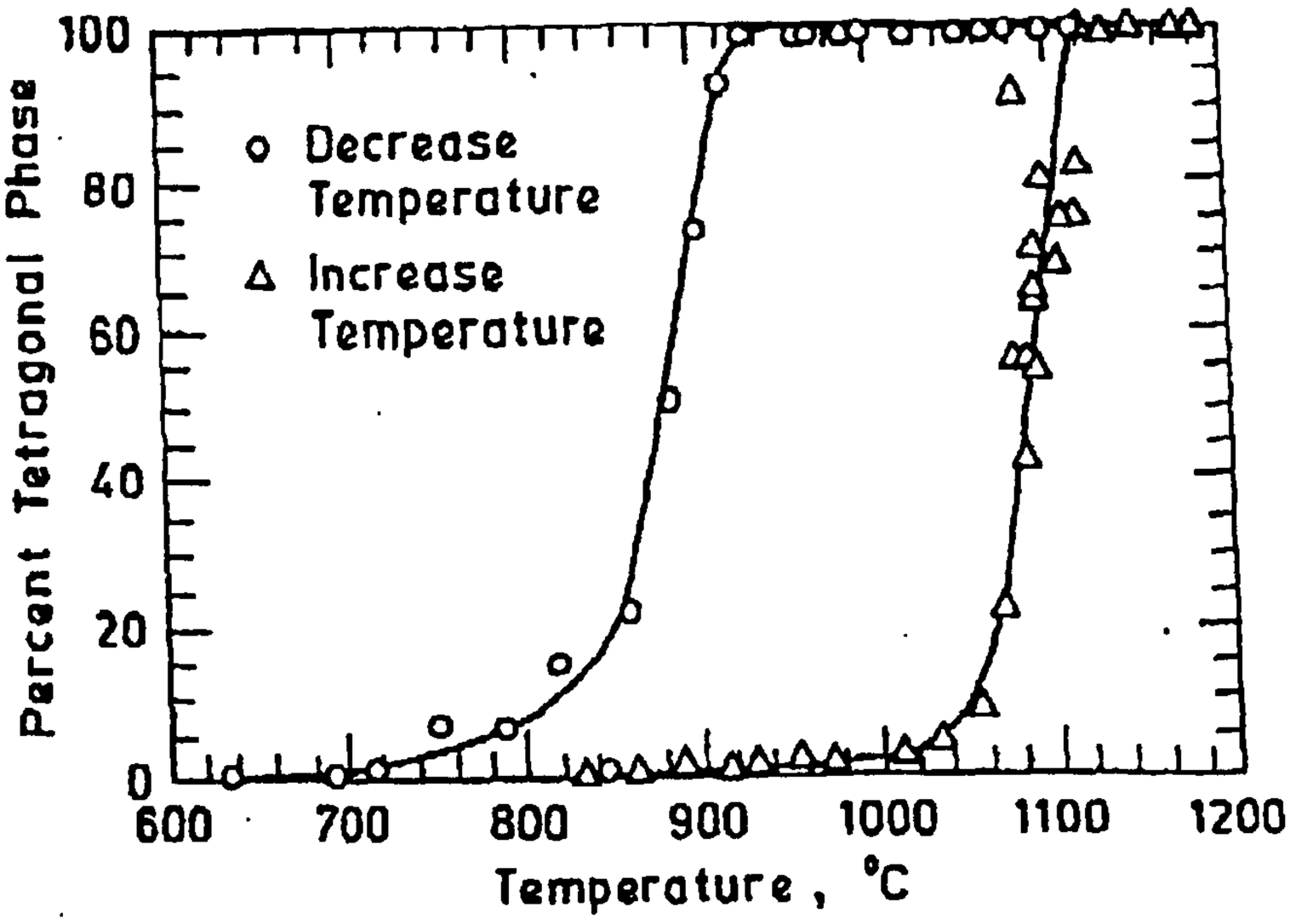

Figure 2.1. Thermal hysteresis on zirconia during heating and cooling through the monoclinic-tetragonal phase transformation [Wolten, 1963].

2.1.2. ADDITIVES FOR STABILISING ZIRCONIA

The addition of a certain amount of oxide as a stabiliser to zirconia such as MgO (magnesia), CaO (calcia), CeO (ceria) or Y_2O_3 (yttria) results in a stable cubic phase which does not transform during cooling. The volume change caused by phase transformation can therefore be avoided [Lee, 1994].

However if the amount of the stabiliser is less than that required to stabilise the cubic phase, it will result in a partially stabilised zirconia or tetragonal zirconia polycrystal. So, there are three different types of stabilised zirconia according to the amount of the stabiliser. First, Tetragonal Zirconia Polycrystals (TZP) which contains almost 100% tetragonal phase. Second, Partially Stabilised Zirconia (PSZ)

which contains of a mixture of cubic and tetragonal and/or monoclinic phases. Third, Fully Stabilised Zirconia (FSZ) which consists of cubic structure at all temperature [Stevens, 1994].

2.1.3. YTTRIA STABILISED ZIRCONIA

2.1.3.1. The ZrO_2 - Y_2O_3 Phase Diagram

Among the ZrO_2 binary systems, the ZrO_2-Y_2O_3 is the most interesting one because it has a relatively large cubic solution field [Stubican and Helmann, 1981]. Duwez *et al* (1951) were the first who reported this system. They pointed out that ZrO_2 cubic solid solution can be found at 7 to 50% mol Y_2O_3 at all temperatures.

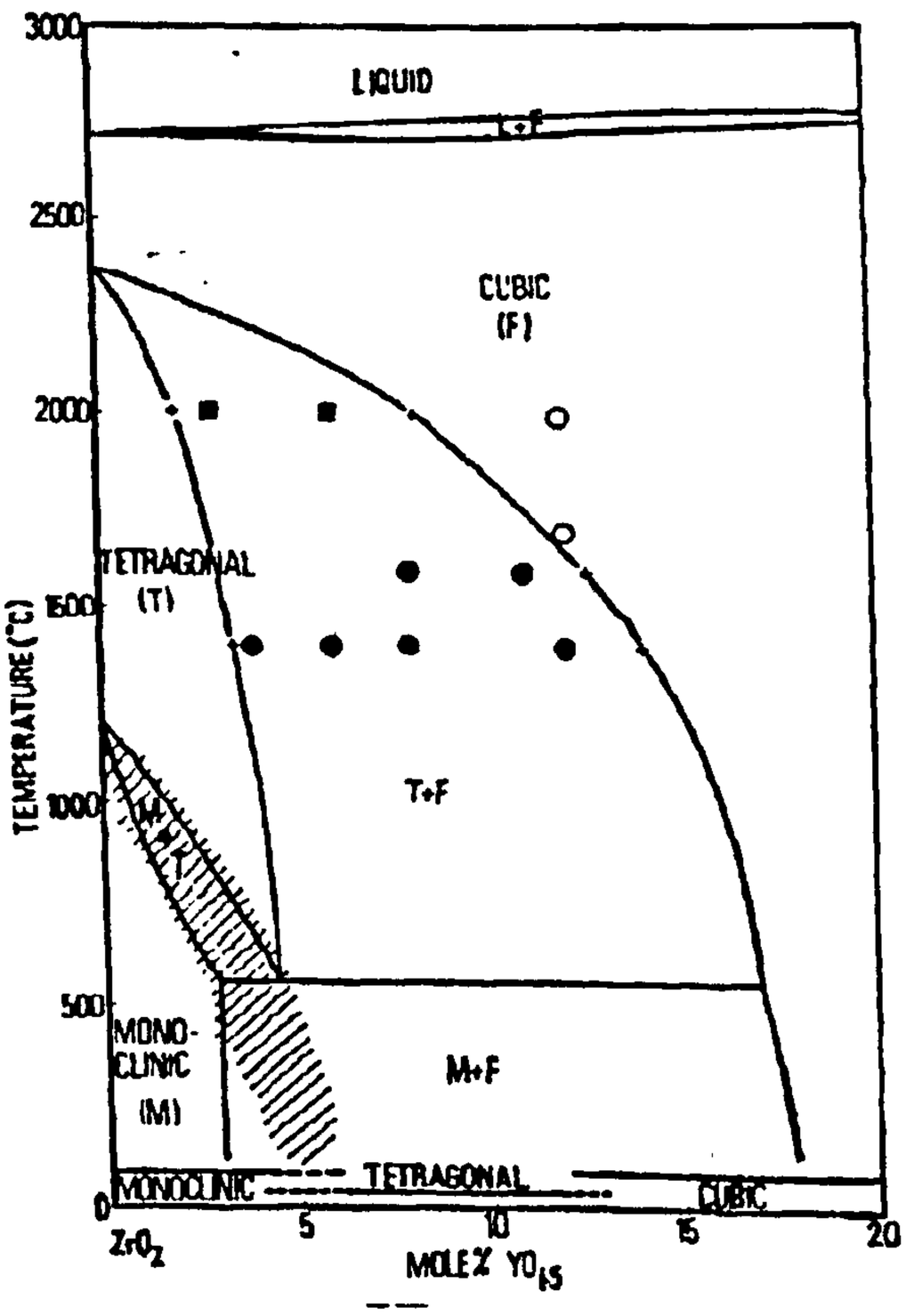

Figure 2.2. Phase diagram for the ZrO_2-Y_2O_3 at the ZrO_2-rich portion [Scott, 1975].

Since then the phase diagram of $ZrO_2 - Y_2O_3$ system has been extensively studied by many researchers such as Srivastava *et al* (1974), Scott (1975), Stubican *et al* (1984), Pascual and Duran (1983), and Ruh *et al* (1984). Among those phase diagrams, the phase diagram at low yttria contents proposed by Scott (1975) as shown in Figure 2.2 seems to be universally used.

However a number of contradictions in the literature are found regarding the position of the tetragonal (t) and cubic (c) phase boundary in the range 1300°C to 1600°C. Figure 2.3 shows some different studies of the position of the phase boundaries [Scott, 1975; Ruh *et al*, 1984; Ruhle *et al*, 1984; Nettleship and Stevens, 1987]. They differ only on a quantitative basis, but qualitatively they have similar features. The exact position of the phase boundary is important in making different type of yttria stabilised zirconia i.e. Y-PSZ (Yttria - Partially Stabilised Zirconia), Y-TZP (Yttria - Tetragonal Zirconia Polycrystal) and Y-FSZ (Yttria - Fully Stabilised Zirconia).

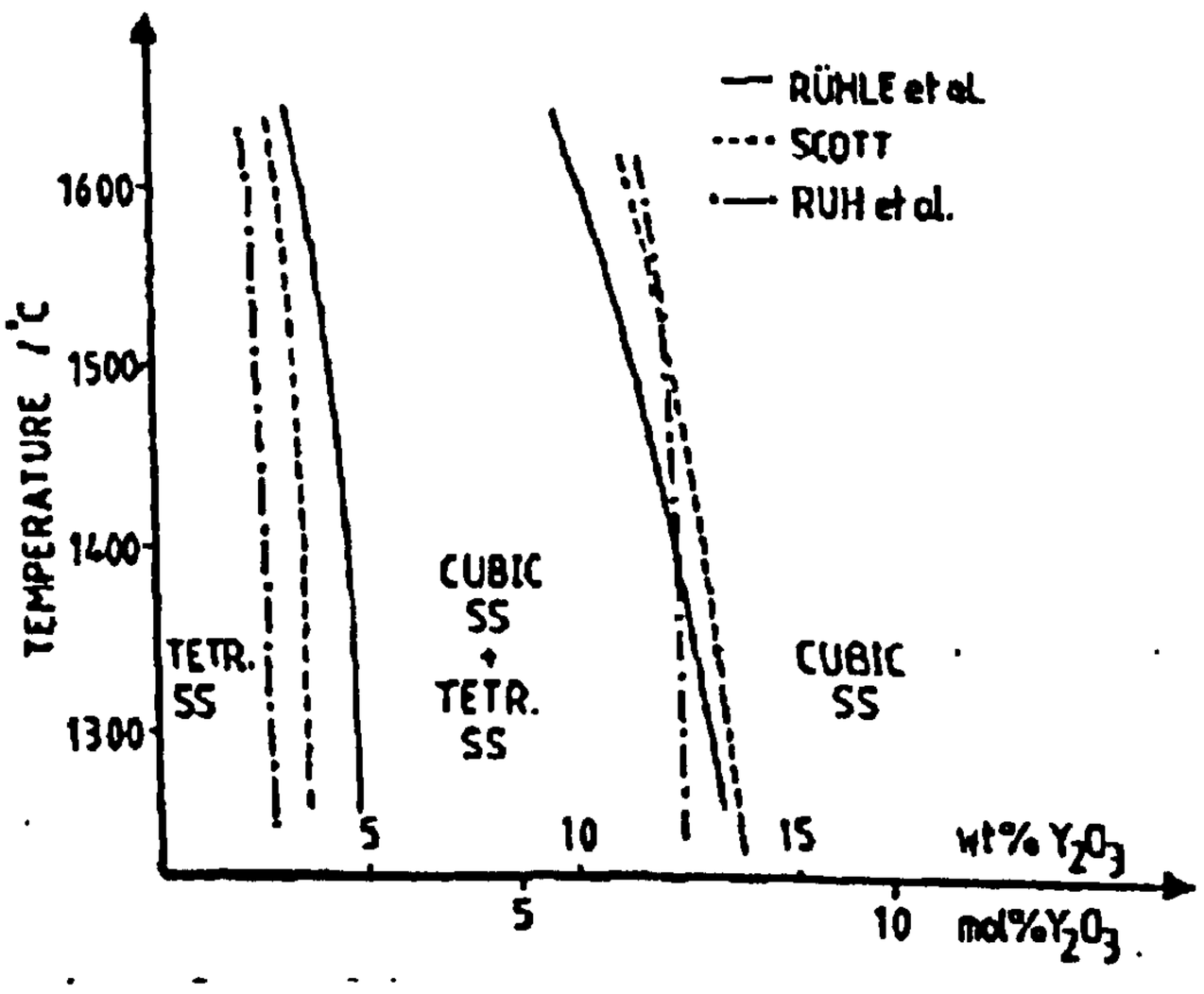

Figure 2.3. Comparison of different studies of part of the ZrO_2-Y_2O_3 system [Nettleship and Stevens, 1987]

2.1.3.2. Types of Y_2O_3-Stabilised Zirconia

Yttria - Tetragonal Zirconia Polycrystal (Y-TZP) can be produced by addition of (2 - 3 mol%) Y_2O_3. It has a fine-grained microstructure (0.2 - 2 μm). The tetragonal structure is retained down to room temperature because of the high activation energy of the transformation. However this tetragonal is available for strain-induced transformation and can transform to monoclinic. It has good mechanical properties such as fracture toughness of (5 - 15 MPa $m^{1/2}$) and transverse bend strength of (700 - 2400 MPa). The microstructure of Y-TZP is predominantly tetragonal or almost 100 % tetragonal [Lee, 1994; Schafer and Schubert, 1998]. However in their research, Ruhle *et al* (1984) found cubic phase ranging from 0 to 42 % in a (3 - 6 wt%) or (2 - 3 mol%) Y-TZP. Also Besson (1996) reported in her study of 3Y-TZP that 18 % cubic has been found. It is difficult to predict accurately the amount of cubic in TZP as several researchers reported the different position of the t/t+c phase boundary in the ZrO_2-Y_2O_3 phase diagram as shown in Figure 2.3. Therefore the distinction between Y-TZP and Y-PSZ is diffuse, particularly in zirconia which contains (3 - 4 mol %) Yttria, because it may contain appreciable quantities of cubic. With superior mechanical properties and a uniform tetragonal grain structure, Y-TZP can be used for precision engineering applications [Luo and Stevens, 1999].

Yttria-Partially Stabilised Zirconia (Y-PSZ) has a coarse-grained microstructure and can be produced with addition of (5 - 7 mol%) Y_2O_3. The microstructure consists of around 40 vol% tetragonal. By ageing in the two-phase region of the phase diagram, small lenticular particles of tetragonal are precipitated [Schafer and Schubert, 1998].

Yttria-Fully Stabilised Zirconia (Y-FSZ) or Cubic Stabilised Zirconia (CSZ) is produced with addition of more than 8 mol% Y_2O_3. It is essentially a single-phase cubic material with large grain size, (10 to 50 μm) [Schafer and Schubert, 1998].

The cubic structure in Y-FSZ results in a high-ionic conductivity ceramic that can be applied as an electrolyte in high temperature solid-oxide fuel cells [Minh, 1993].

2.1.4. DEVELOPMENT OF Y-TZP

Development of tetragonal zirconia polycrystal was initiated by Gupta *et al*, (1977) and Gupta (1978). They reported the fabrication of dense and fine-grained Y-TZP containing nearly 100% metastable tetragonal phase. However they did not mention the exact amount of the yttria additives. They only mentioned that the zirconia used contained a small amount of yttria and other rare earth oxides. Sintering time and temperature were found as parameters that can influence the density, percentage of tetragonal phase, and mechanical properties. The maximum density appears on sintering at temperature between 1400°C and 1500°C as shown in Figure 2.4(a). For longer sintering time the maximum density can be achieved at lower temperature.

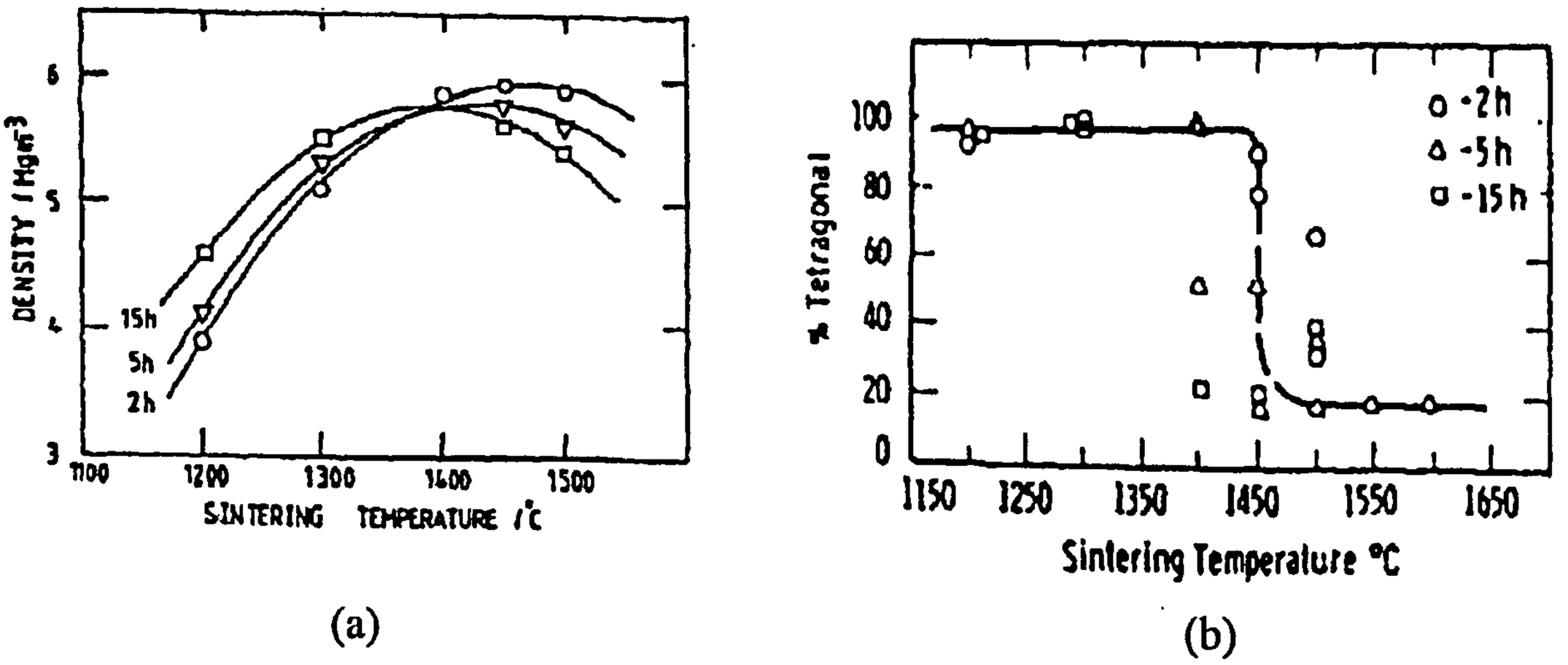

(a) (b)

Figure 2. 4. Effect of time and temperature of sintering of yttria-stabilised zirconia on (a) the density, (b) the formation of tetragonal phase [Gupta, 1978].

The density increase from 1100°C to the temperature of the maximum density is due to the densification process, while the decrease in density above the temperature of maximum density is due to the increase of tetragonal to monoclinic transformation during cooling [Gupta 1978]. Lange[a] (1982) and Matsui *et al* (1984) have also observed such relationships in ZrO_2-Y_2O_3 systems. Lange[a] (1982) concentrated on fabrication in ZrO_2-Y_2O_3 systems with less than 7.5 mol% Y_2O_3. Matsui *et al* (1984) investigated ZrO_2 with Y_2O_3 content between 2 and 6 mol%.

Gupta (1978) found that almost 100% tetragonal can be achieved at sintering temperature <1500°C for 2 h, 5 h or 15h with the critical temperature between 1400°C and 1500°C. Above the critical temperature the amount of tetragonal phase decreases as shown in Figure 2.4(b). He also observed that the tetragonal phase can transform to monoclinic phase irreversibly (and to be martensitic) by subjecting it to mechanical stress such as grinding or breaking the specimens. This phase transformation was clearly shown using X-ray analysis.

Y-TZP exhibited good mechanical properties such as a high strength (≅ 700 MPa) and high fracture toughness (>6 $MN.m^{-3/2}$), which were due to the small grain size, whereas specimens with a high amount of monoclinic phase showed poor strength due to the formation of microcracks from the volume change during phase transformation. Gupta (1978) also reported that tetragonal grain sizes were 0.1 - 0.3 μm, and the monoclinic grain sizes were > 1μm. The tetragonal to monoclinic phase transformation was triggered by grain growth during prolonged sintering time.

2.1.5. TOUGHENING MECHANISM IN CERAMIC SYSTEMS

The use of ceramic materials in engineering applications is limited by their brittleness and low toughness (little resistance to crack propagation). Ceramic materials are therefore very sensitive to flaws, because if the flaws are located in the region of maximum stress such as on the surface under tension, then the materials

will fracture. The fracture strength (σ_f) of ceramics materials can be expressed by the Griffith equation as follows [Butler, 1985; Chiang *et al*, 1997; Harris, 1999]:

$$\sigma_f = \left(\frac{2\gamma E}{\pi c}\right)^{1/2} \qquad \ldots\ldots (2.1)$$

The critical stress-intensity factor or fracture toughness K_{IC} is

$$K_{IC} = \sqrt{2\gamma E} \qquad \ldots\ldots (2.2)$$

So, equation (2.1) becomes:

$$\sigma_f = \frac{K_{IC}}{\sqrt{\pi c}} \qquad \ldots\ldots (2.3)$$

where E is the modulus of elasticity, γ is the fracture-surface energy, and c is the size of the crack that will propagate when the local stress at that point reaches the value of σ_f. The fracture toughness of monolithic ceramic materials (~0.3 to 13 MPa.$m^{1/2}$) is very low compared to that of metals (~30 to 170 MPa.$m^{1/2}$) because the fracture-surface energy of ceramics is very low (~10 J m^{-2}) compared to that of metals (~10^3 to 10^4 Jm^{-2}) [Butler, 1985; Higgins, 1994; Chiang *et al*, 1997].

Therefore the main research objective in structural ceramics for engineering applications is focused on improvement of fracture toughness. Becher and Rose

(1994) classified toughening mechanisms in ceramic systems into two broad categories:

a. Toughening mechanism due to producing an inelastic zone around the crack tip. The example of this is phase transformation toughening, which is discussed in section 2.1.6.
b. Toughening mechanism due to obstructing a crack by reinforcement such as fibres, whiskers, sheets or particulate. This mechanism occurs in ceramic matrix composites materials which will be discussed in section 2.2.3

Those two mechanisms may work simultaneously in composite materials.

2.1.6. TRANSFORMATION TOUGHENING OF ZIRCONIA

Garvie *et al* (1975) were the first who reported transformation toughening of ZrO_2 in a paper entitled 'Ceramic Steel?'. They found that tetragonal-monoclinic phase transformation of metastable tetragonal particles induced by the presence of the stress field ahead of a crack could increase both the strength and toughness of zirconia. The martensitic reaction will generate a volume change and shear strain that are recognised as impeding the opening crack and therefore lead to an increase in the resistance to crack propagation of the ceramics. This discovery has then prompted a tremendous research effort to understand the mechanism of this behaviour. It has also opened developments of a wide range of zirconia-based ceramics known as zirconia toughened ceramics (ZTC). Further comprehensive reviews in transformation toughening of zirconia-containing ceramics have been written by Evans and Heuer (1980), Butler (1985), and Hannink *et al* (2000).

2.1.6.1. Stress Induced Transformation Toughening

This type of toughening can occur in the metastable tetragonal form of ZrO_2 as particles, precipitates, or small grains when they transform due to the stress field of an extending crack [Garvie *et al*, 1975; Porter and Heuer, 1977; Evans and Heuer,

1980; Becher, 1986]. As shown in Figure 2.5, when there is a crack extending under stress, it will generate tensile stresses along the crack and the crack tip. The metastable tetragonal zirconia particles around the crack will transform to monoclinic if the stresses are large enough to release the matrix constraint on the tetragonal particles [Evans and Heuer, 1980; McMeeking and Evans, 1982]. This transformation causes a volume expansion (~3%) and shear strain (~1 to 7%) which generates compressive stress near the crack tip and therefore more energy is required for crack propagation. As a result the fracture toughness is improved.

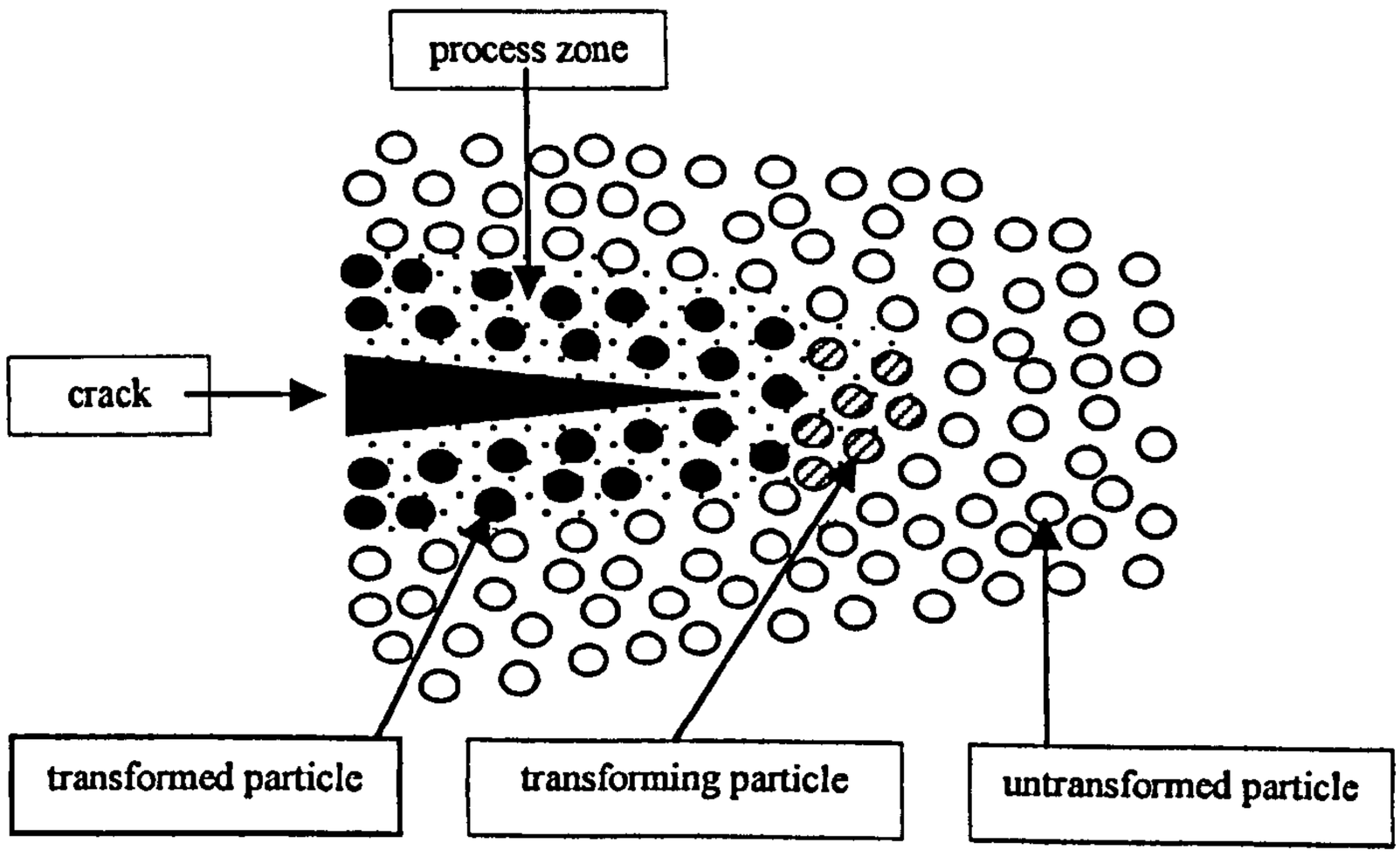

Figure 2.5. Stress-induced transformation of metastable ZrO_2 in the elastic field of a crack [Butler 1985].

2.1.6.2. Microcrack Toughening

Microcrack toughening can be induced when metastable tetragonal zirconia particles precipitate in cubic zirconia or are dispersed in ZTC (zirconia toughened ceramic). When the martensitic transformation occurs from tetragonal to monoclinic phase, the volume expansion (3 - 5 %) generates stresses around the particles and causes microcracks in the matrix as shown in Figure 2.6. The fracture toughness of

the materials is improved because the microcracks around the particles will absorb energy, and deflect or branch the propagation of main cracks [Stevens, 1994].

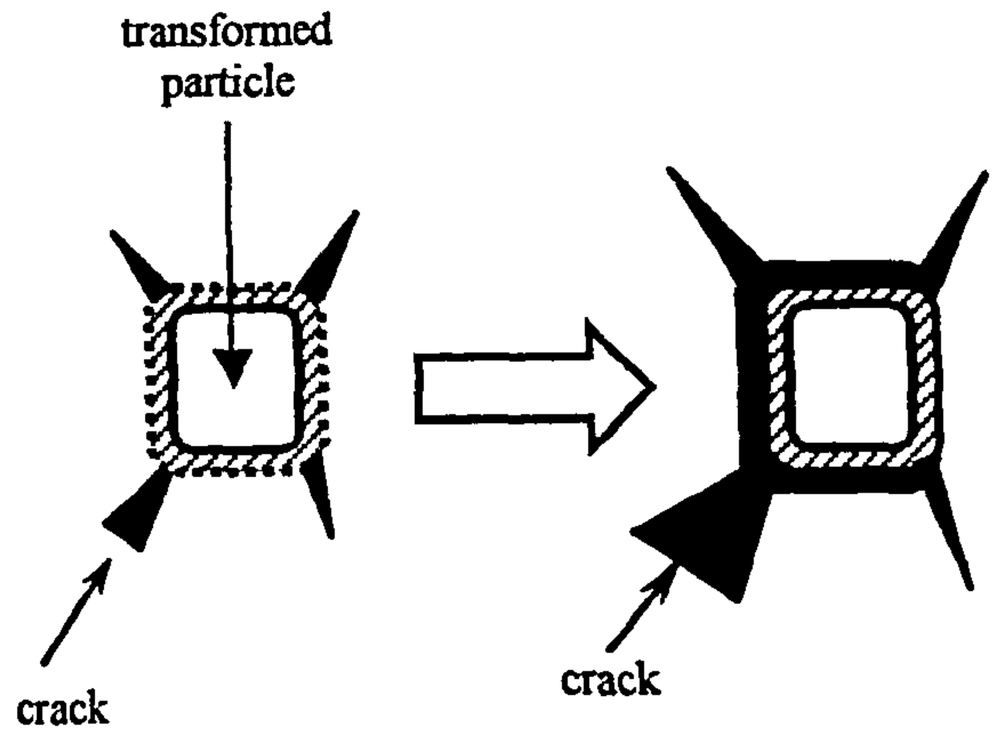

Figure 2.6. Microcrack toughening

However, this toughening mechanism is influenced by the amount of ZrO_2 inclusions. As Claussen (1976) observed on zirconia toughened alumina, there is an optimum amount of zirconia to get maximum toughness. At a certain amount of inclusions both toughness and strength decrease because of interaction of microcracks around the zirconia particles.

2.1.6.3. Compressive Surface Layer

A compressive surface layer on material containing transformable tetragonal zirconia can be produced on cooling and by surface grinding where the tetragonal transforms to monoclinic as shown in Figure 2.7 [Stevens, 1994]. Gupta *et al* (1977) pointed out that strength improvement on TZP during surface grinding could be achieved by controlling optimum surface grinding. The maximum strength can be observed via controlling grinding size to give an optimum compressive layer on the surface. However, when the amount of monoclinic on the surface is large enough to cause surface microcracks, the strength decreases.

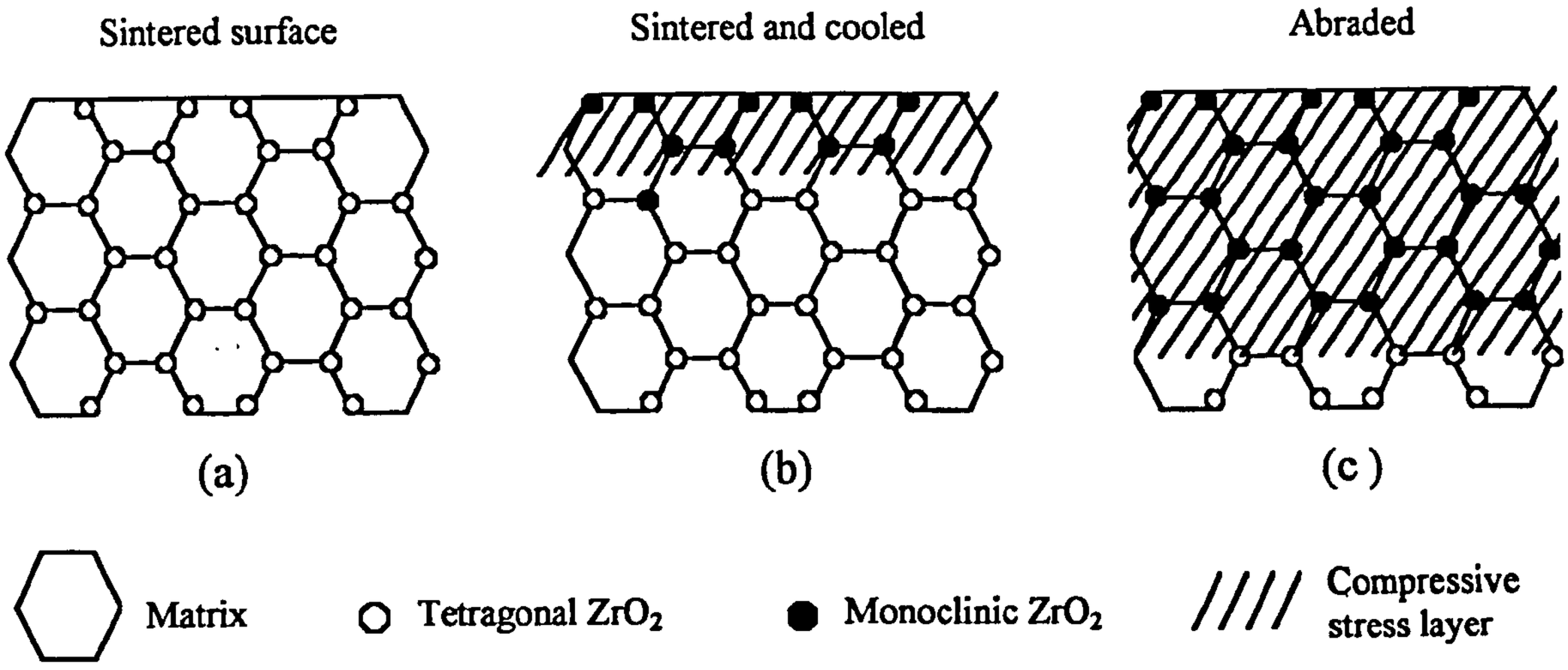

Figure 2.7. A free surface area at (a) sintering temperature, (b) on cooling, t-ZrO_2 particles transform to m-ZrO_2 resulting compressive stress on the matrix, (c) the compressive stress increases due to abrasion or machining [Stevens, 1994].

Moreover Claussen (1978) reported that transformation toughening of metastable tetragonal zirconia could be applied to increase fracture toughness of alumina containing tetragonal zirconia. He found that the tetragonal transforms to monoclinic on the ground surface. The transformed monoclinic can be partly transformed back to tetragonal by ageing above the transformation temperature.

2.1.7. MECHANICAL PROPERTIES OF ZIRCONIA

2.1.7.1. Effect of Y_2O_3 Contents

Mechanical properties of zirconia are influenced by the amount of the stabiliser as reported by Lange[a] (1982), Matsui *et al* (1984), Tsukuma *et al* (1984), and Masaki (1986). The effect of yttria stabiliser on fracture toughness can be seen in Figure 2.8, where the maximum fracture toughness of each study is achieved at about

2 mol% Y_2O_3 i.e. 6.5 MPa $m^{1/2}$ (Lange[a], 1982), 10 MPa $m^{1/2}$ (Tsukuma *et al*, 1984), and 14 MPa $m^{1/2}$ (Masaki, 1986).

Lange[a] (1982) observed that the large amount of monoclinic (>10%) in zirconia containing less than 2 mol% Y_2O_3 caused relatively low fracture toughness. Masaki (1986) also found that the zirconia sample with 1.5 mol% Y_2O_3 had the highest monoclinic proportion (~65%) among his samples. This monoclinic phase is believed to be due to transformation from tetragonal during cooling. Furthermore, Lange[a] (1982) and Tsukuma *et al* (1984) agreed that the decrease of fracture toughness with increasing Y_2O_3 content above 2 mol% is due to a decreasing volume fraction of transformable tetragonal and increasing cubic phase.

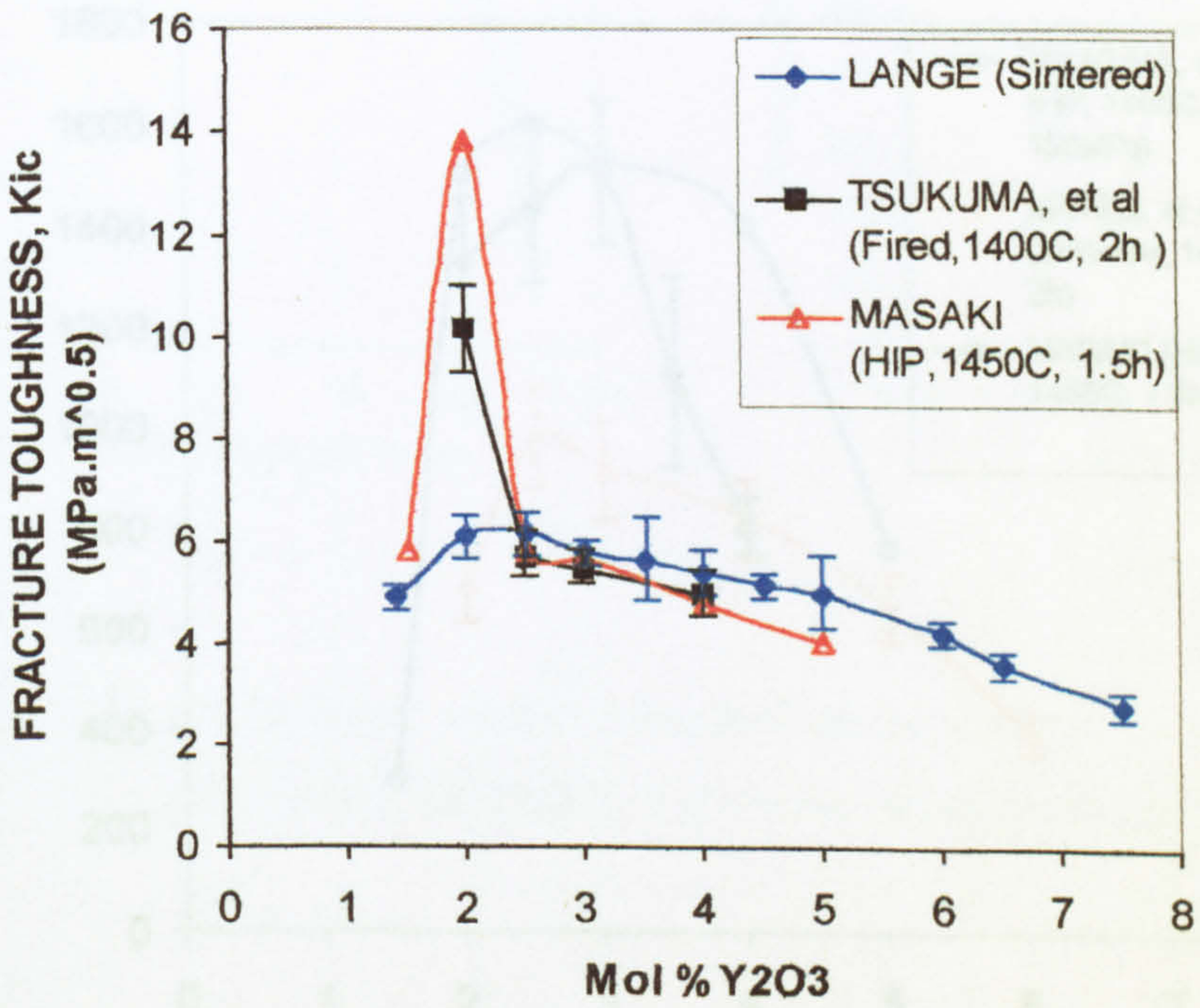

Figure 2.8. The effect of yttria content on fracture toughness of zirconia [Lange[a], 1982; Tsukuma *et al*, 1984; and Masaki, 1986]

In comparison with the effect of Y_2O_3 on fracture toughness, the effect of Y_2O_3 on strength shows a similar trend, but the maximum strength occurs between 2.5 and 3 mol% Y_2O_3 as indicated in Figure 2.9 [Tsukuma *et al*, 1984; Matsui *et al*,

1984; and Masaki, 1986]. Lange[a] (1982) found that the inter-granular microcracks as a result of tetragonal monoclinic phase transformation on cooling caused low strength for the materials with Y_2O_3 less than 2 mol%. Also Matsui (1984) attributed this similar phenomenon (degradation of the strength of materials with Y_2O_3 below 2.5 mol%) to (t - m) transformation. Furthermore Masaki (1986) found 65% monoclinic in the materials with 1.5 mol% Y_2O_3. The strength decreases with the amount of Y_2O_3 above 3 mol% because of the development of cubic phase. Tsukuma *et al* (1984) noticed that the strength of Y-TZP might be enhanced by hot isostatic pressing.

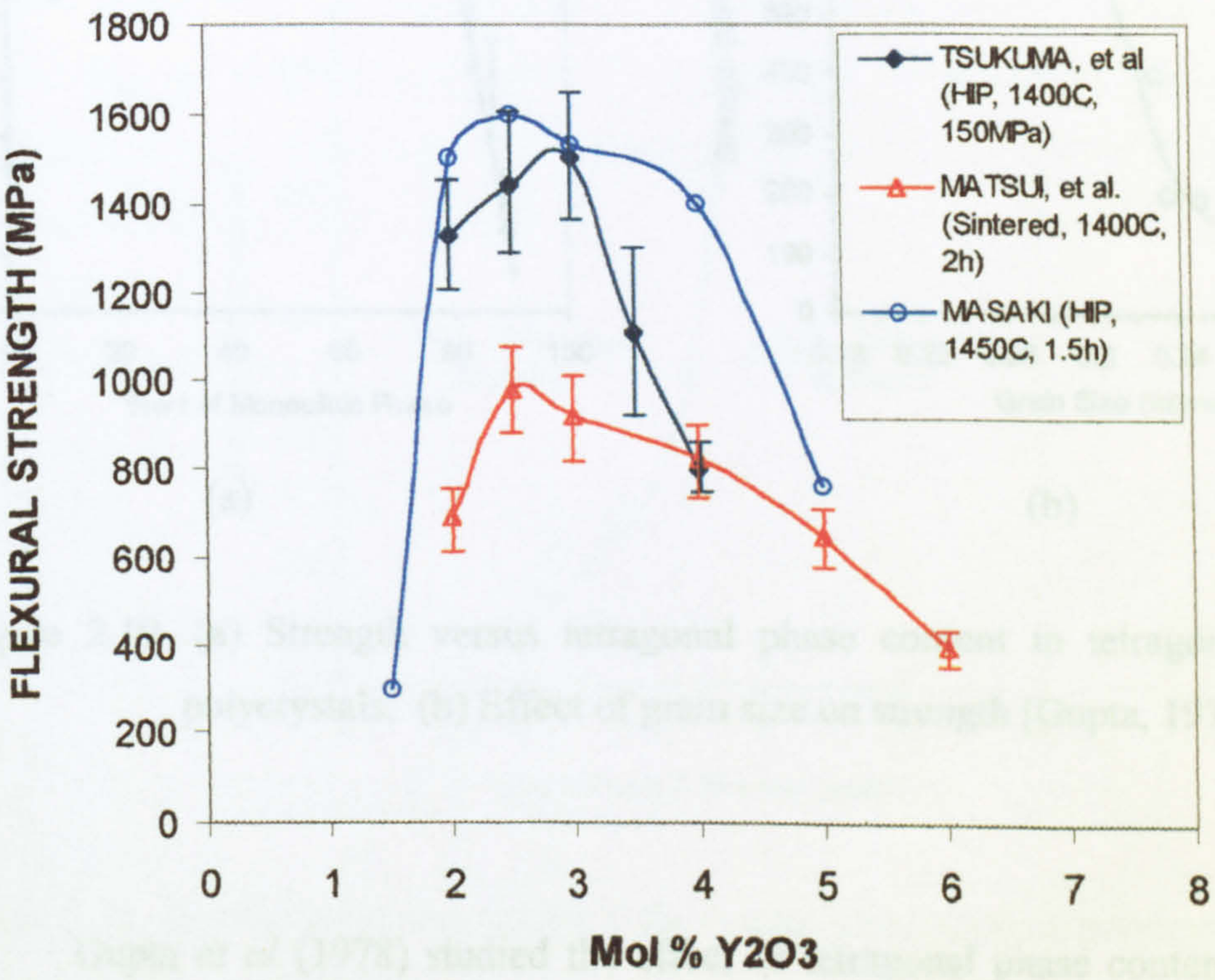

Figure 2.9. The effect of Y_2O_3 on strength of zirconia [Tsukuma *et al*, 1984; Matsui *et al*, 1984; and Masaki, 1986]

2.1.7.2. Effect of Grain Size

There is a relationship between grain size and transformability of tetragonal zirconia. The transformation toughening depends on the presence of metastable tetragonal phase where the grain size is below some critical value. If the grain size is larger than the critical size, transformation will occur spontaneously on cooling from the sintering temperature. In contrast if the grain size is very much smaller than the critical size, the particles are resistant to transformation [Lee, 1994; Stevens, 1994].

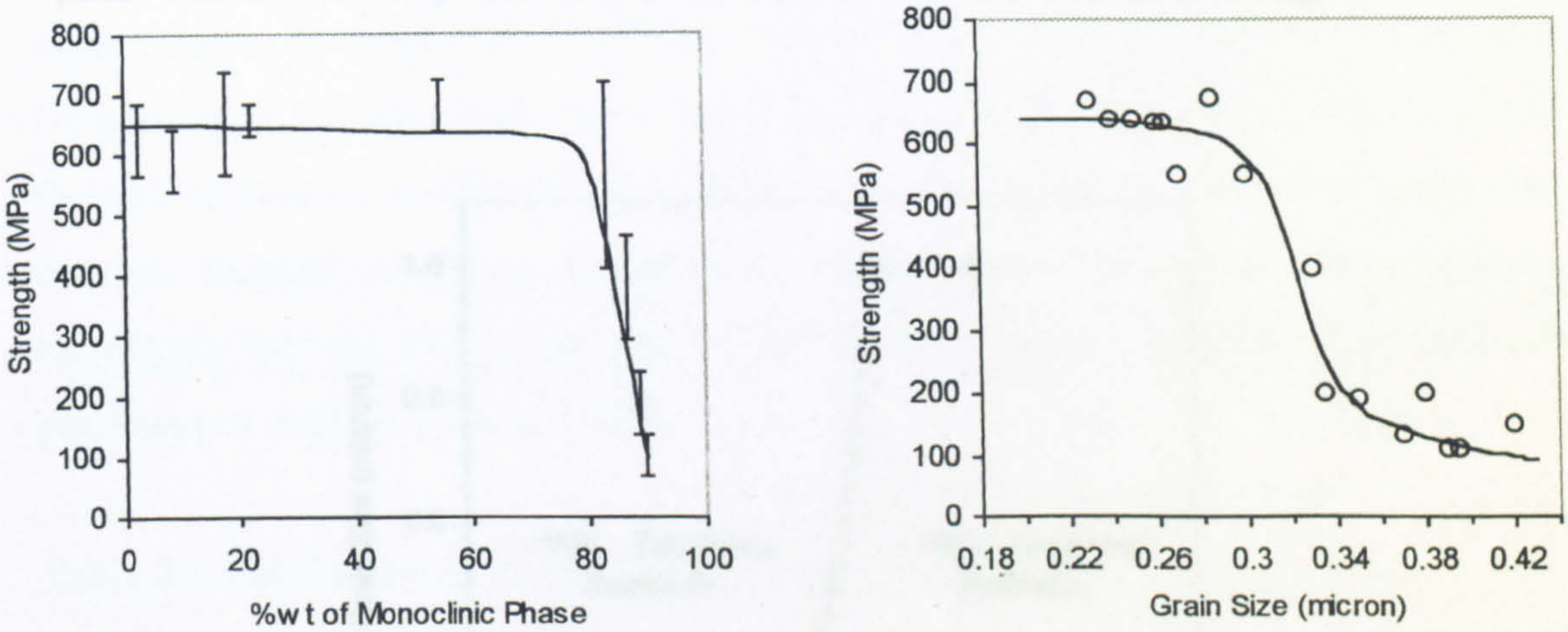

Figure 2.10. (a) Strength versus tetragonal phase content in tetragonal zirconia polycrystals, (b) Effect of grain size on strength [Gupta, 1978].

Gupta *et al* (1978) studied the effect of tetragonal phase content and grain size on the strength of yttria-tetragonal zirconia polycrystals. The strength decreases drastically when the monoclinic content is more than 70% as shown in Figure 2.10(a) and they attributed the strength decrease to material with grain size above 0.3 μm where it contained significant amount of monoclinic phase. This large monoclinic phase yielded large surface cracks and low strength. Figure 2.10(b) shows the critical

grain size is around 0.3 μm. The authors also explained that the rapid increase of strength with the decrease of grain size from 0.34 to 0.3 was not only due to the smaller grain size giving higher strength but also the contribution of stress-induced phase transformation to strength in that grain size range.

Subsequently, Lange[a] (1982) found that there was a relationship between the amount of stabiliser and critical grain size as shown in Figure 2.11. Below 2 mol% Y_2O_3 the tetragonal transforms spontaneously to monoclinic on cooling, followed by microcracking and decrease in fracture toughness. Above 3 mol% Y_2O_3 the cubic phase starts to develop and results in a decrease of transformable tetragonal.

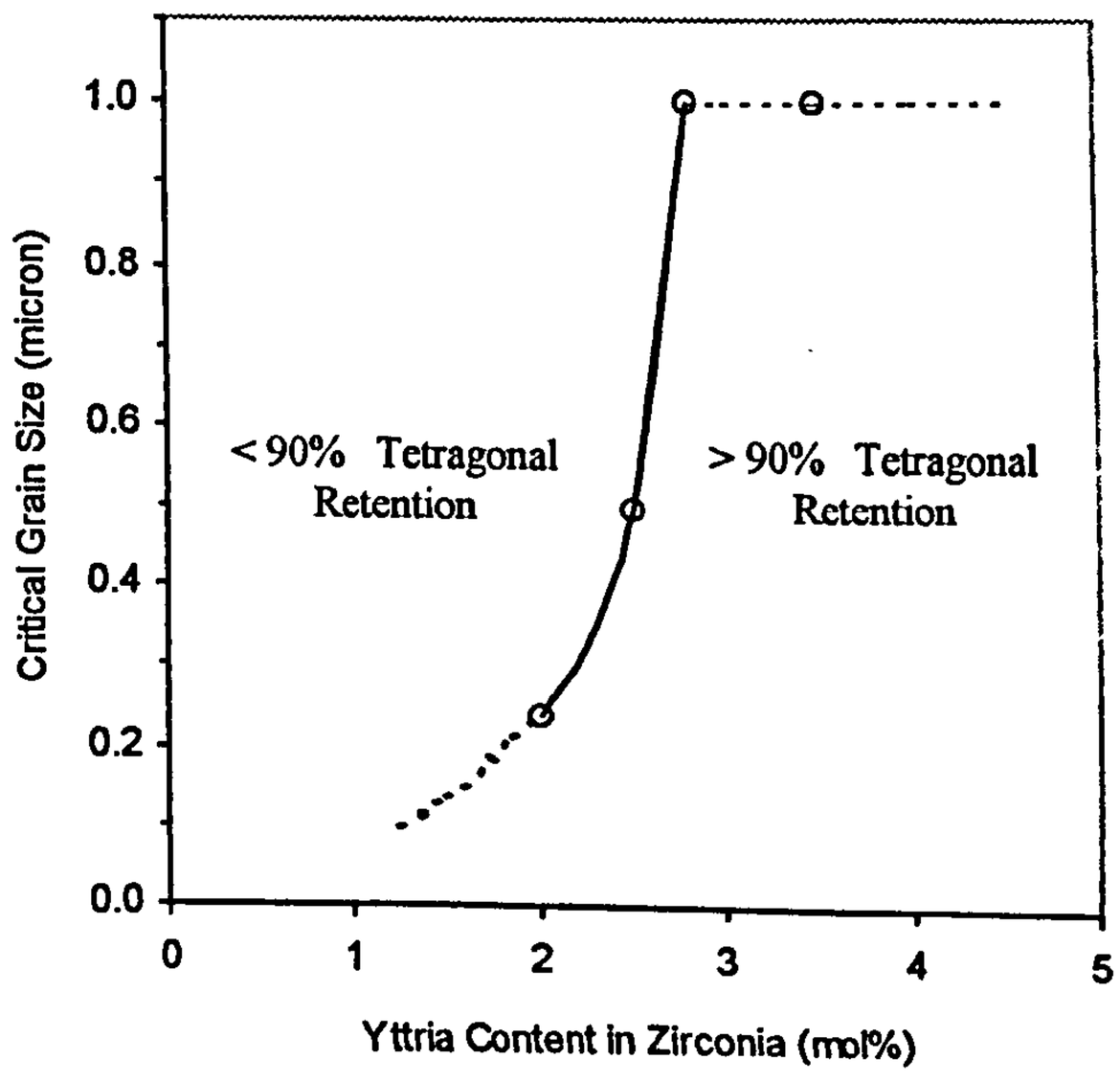

Figure 2.11. Critical grain size versus Y_2O_3 in tetragonal zirconia polycrystal [Lange[a], 1982].

2.1.8. THERMAL PROPERTIES

Two thermal properties that are important in structural ceramic materials are thermal expansion coefficient and thermal diffusivity/conductivity.

2.1.8.1. Thermal Expansion Coefficient

The thermal expansion coefficient of zirconia has been studied by many researchers such as Whittemore and Ault (1957), Patil and Subbarao (1969), Matsui *et al* (1984), Watanabe *et al* (1984), Adams *et al* (1985), Schubert (1986), and Dworak *et al* (1988). Because zirconia has three different atomic structures, the thermal expansion coefficient is dependent on its structure. The cubic phase has isotropic thermal expansion, whereas the monoclinic and tetragonal phases possess anisotropic thermal expansion. Several data of the thermal expansion of zirconia are presented as follows [Green, 1998]:

Table 2.1. Coefficient of thermal expansion of zirconia

Material	Phase	$\alpha 11$ x 10^{-6} /°C	$\alpha 22$ x 10^{-6} /°C	$\alpha 33$ x 10^{-6} /°C	α (average) x 10^{-6} /°C	Temperature range (°C)
ZrO_2	Monoclinic	7.5	1.1	12.5	7	20 - 800
ZrO_2 (2mol%Y_2O_3)	Tetragonal	9.0	9.0	13.0	10.3	20 - 800
ZrO_2 (3mol%Y_2O_3)	Tetragonal	10.1	10.1	11.6	10.6	20 - 800
ZrO_2 (12mol%Y_2O_3)	Cubic	11.1	11.1	11.1	11.1	25 - 1500

Thermal expansion hysteresis can occur in zirconia when there is phase transformation. The effect of grain size in 3Y-TZP on thermal expansion has been

studied by Matsui *et al* (1984) as shown in Figure 2.12. They sintered 3Y-TZP at different temperatures (1300°C, 1400°C, and 1500°C) in air and these sintering conditions resulted in different tetragonal grain size approximately 0.2 μm, 0.5 μm and 1.5 μm, respectively. The samples with grain sizes 0.2 μm and 0.5 μm did not experience thermal expansion hysteresis because these grain sizes were fine so that the tetragonal phase did not transform and it can be retained after thermal cycling. In contrast, the material with grain size 1.5 μm experienced thermal expansion hysteresis indicating tetragonal to monoclinic phase transformation as shown in Figure 2.12. A similar case has been studied by Watanabe *et al* (1984) on zirconia with different contents of yttria sintered at 1500°C for 1 h. Thermal expansion hysteresis due to phase transformation occurred on materials with 2 mol% and 2.5 mol% yttria.

Compared to other ceramic materials, stabilised zirconia has a relatively high thermal expansion coefficient as shown in Figure 2.13.

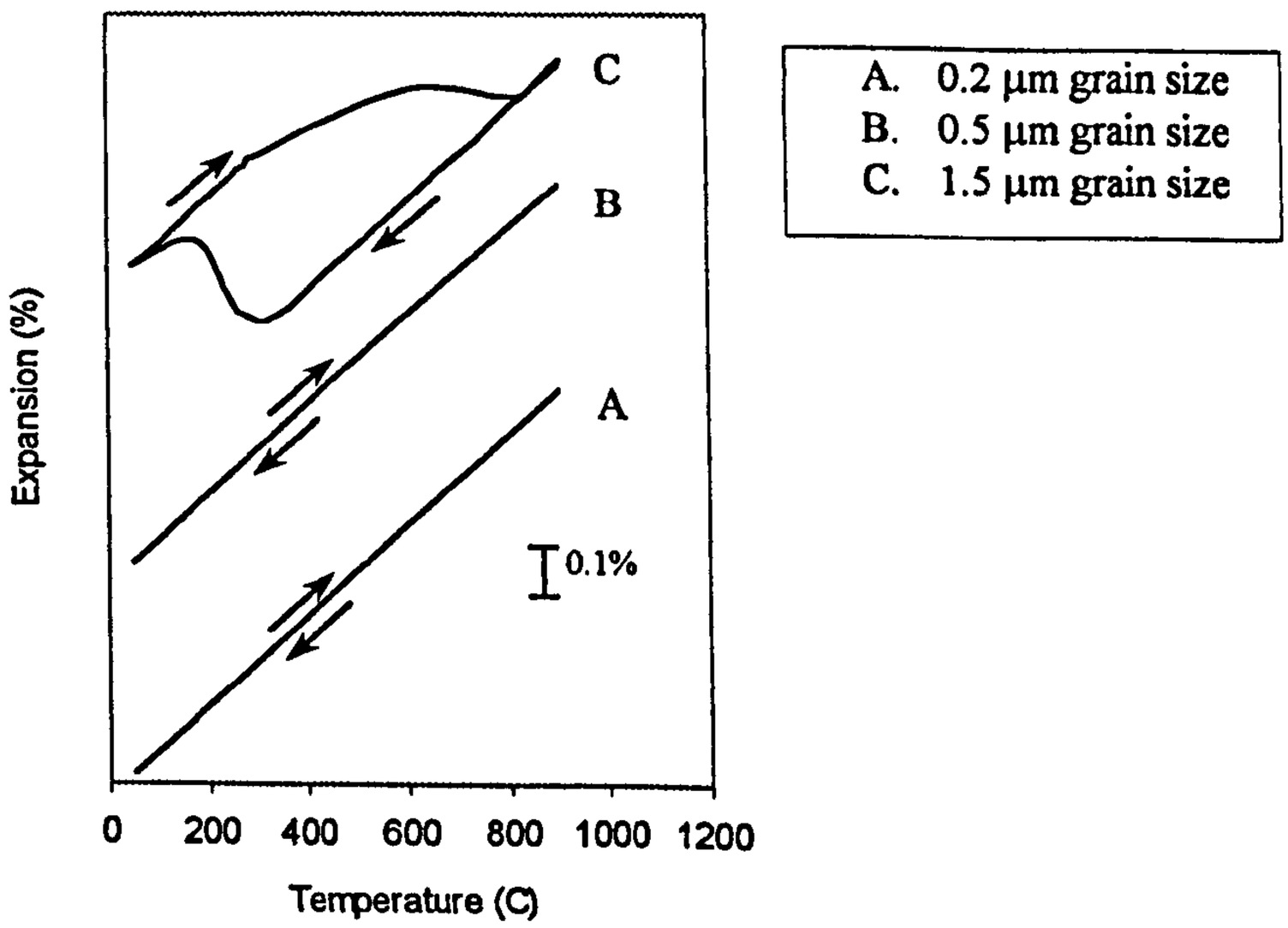

Figure 2.12. Effect of grain size of 3Y-TZP on thermal expansion [Matsui *et al*, 1984].

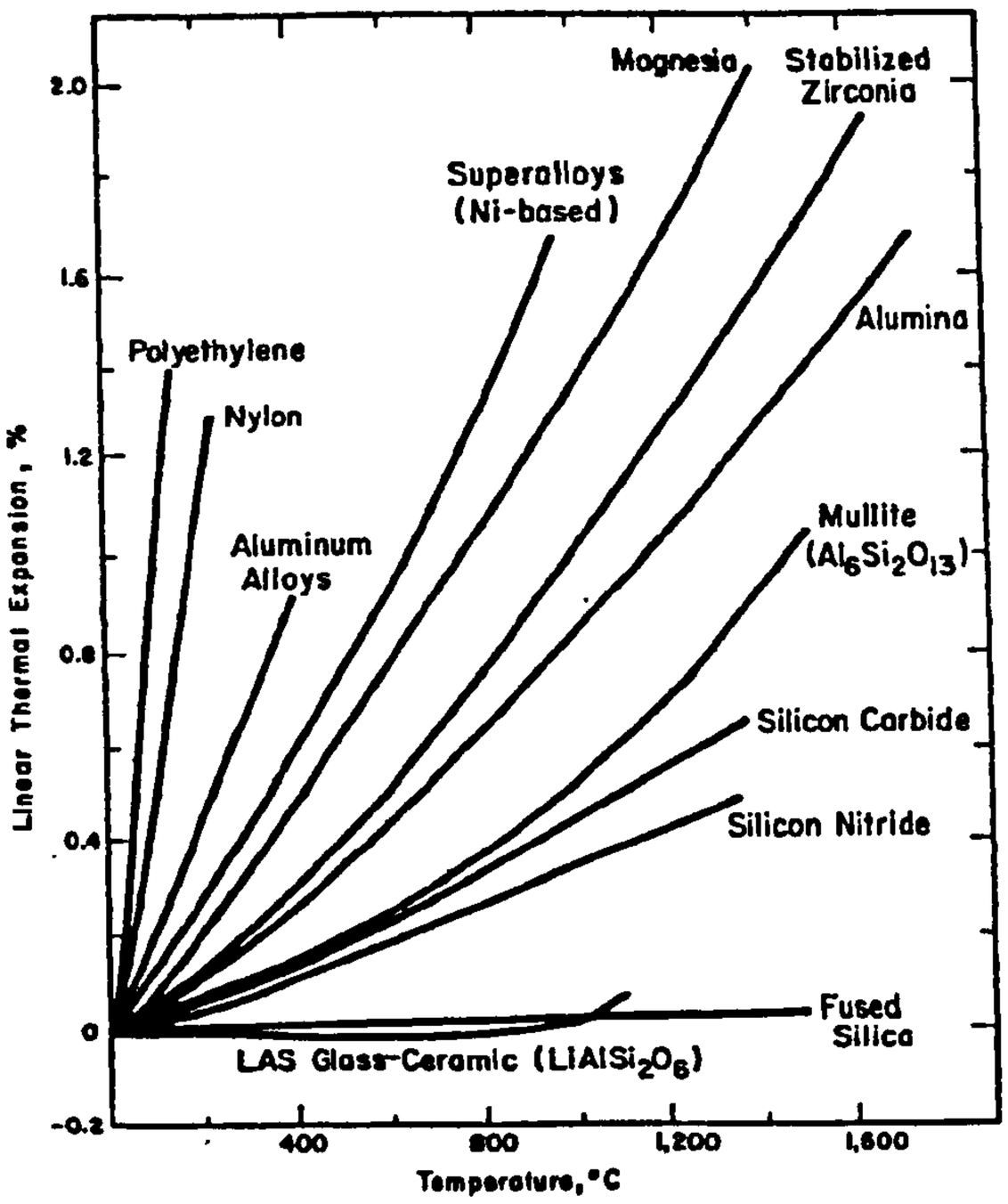

Figure 2.13. Comparison of linear thermal expansion as a function of temperature for some materials [Chawla, 1993].

2.1.8.2. Thermal Diffusivity and Conductivity

A comprehensive survey of thermal diffusivity and conductivity of dense polycrystalline ZrO_2 ceramics has been reported by Hasselman *et al* (1987) using a laser flash method. The study included the effect of stabiliser (MgO or Y_2O_3), temperature, atomic structure, and phase composition on the thermal diffusivity. With data of density and heat capacity they also reported the calculated thermal conductivity from room temperature to 600°C at different amount of stabilisers. The thermal diffusivity at room temperature decreases significantly with increasing amount of Y_2O_3 stabiliser as shown in Figure 2.14(a) because of increasing cubic phase with high concentration of atomic defects. Moreover the thermal diffusivity and conductivity of zirconia with a given amount of stabiliser decreases with increasing temperature. Figure 2.14(b) shows the effect of temperature on thermal conductivity on zirconia with different amounts of yttria.

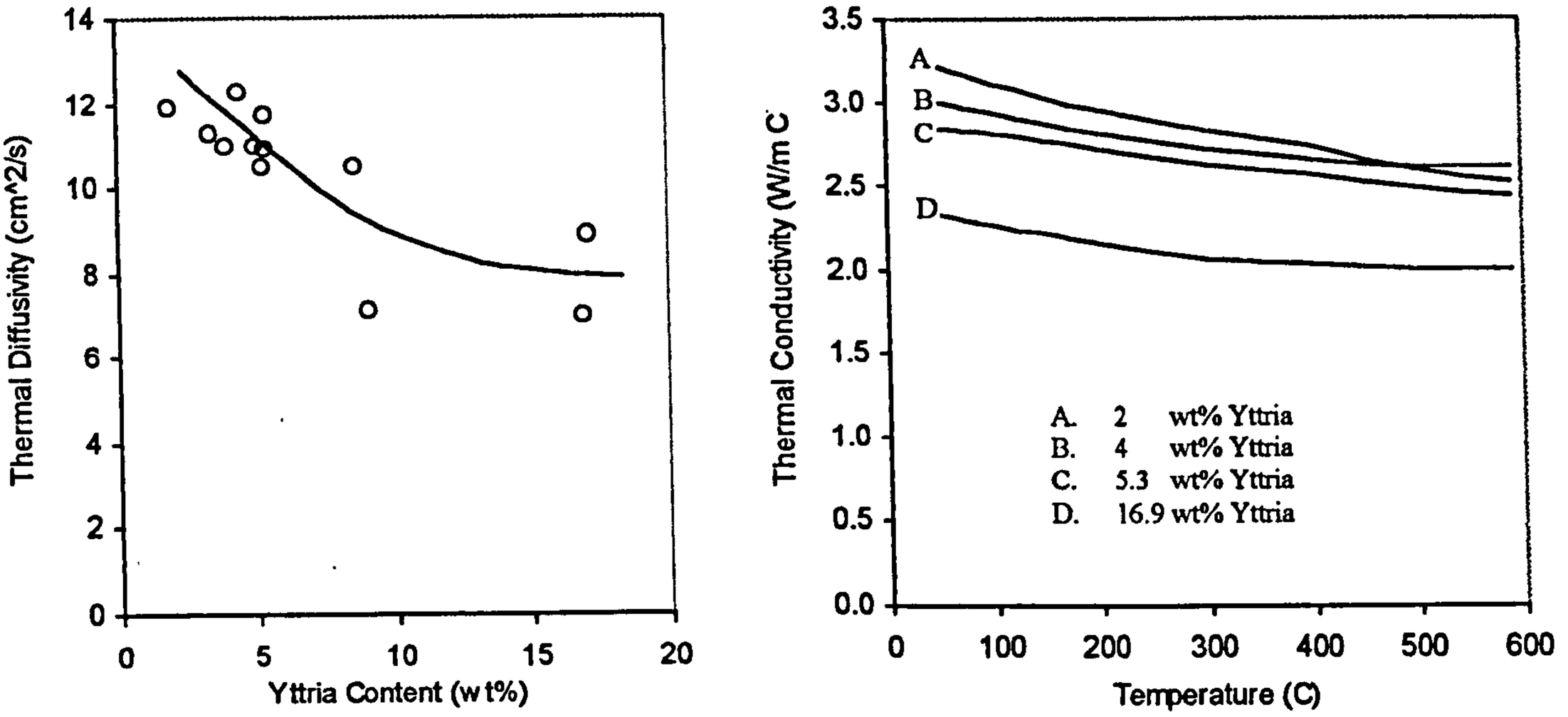

(a) (b)

Figure 2.14. (a). The effect of Y_2O_3 content on thermal diffusivity of zirconia, and (b). temperature dependence of the thermal conductivity of ZrO_2 for a range of Y_2O_3 content [Hasselman *et al*, 1987]

In comparison with other ceramic materials such as Al_2O_3, Si_3N_4 and SiC, the thermal conductivity of ZrO_2 is very low as seen in Figure 2.15 [Butler, 1985]. This value gives a wide range of applications of zirconia as thermal barrier insulation in turbines and heat engines.

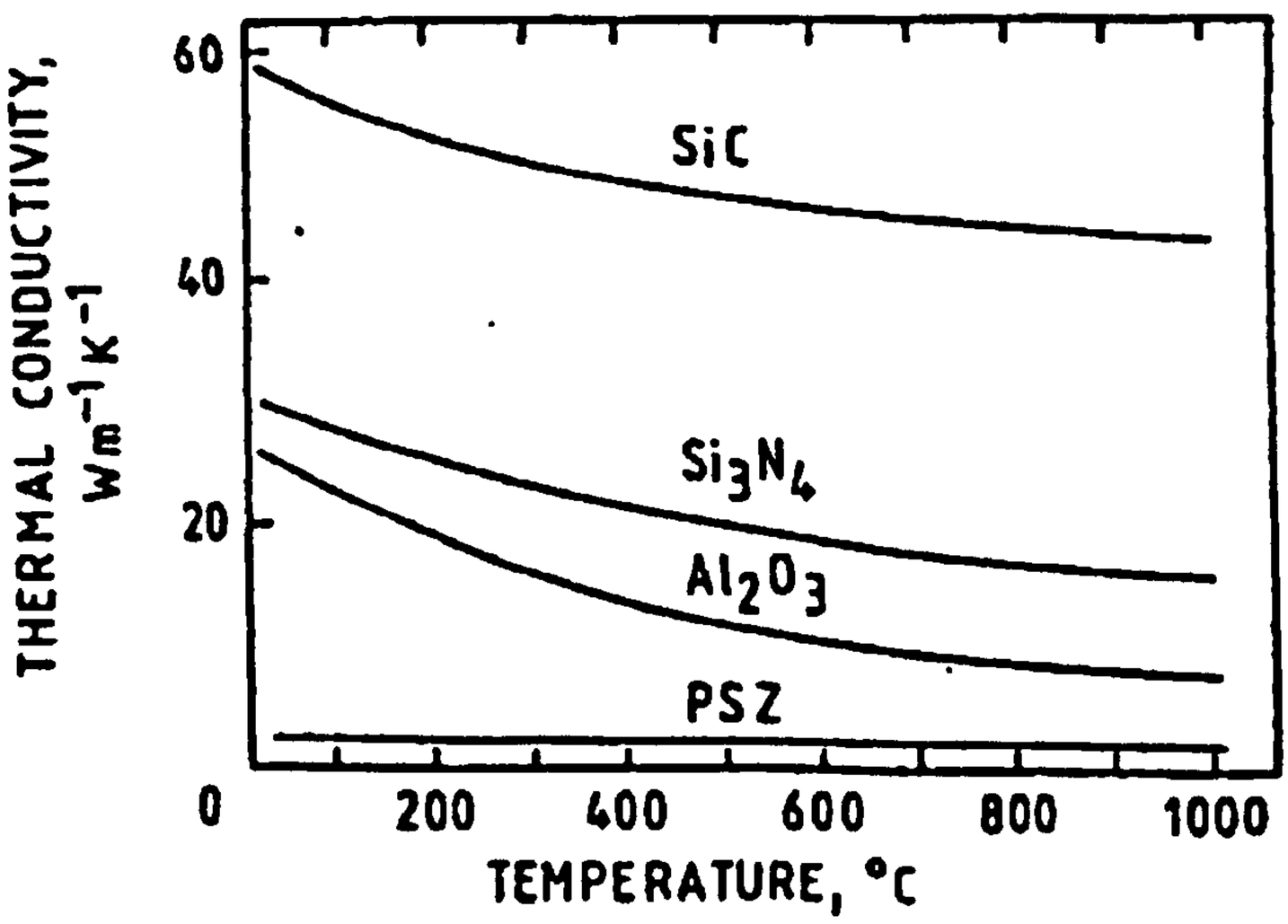

Figure 2.15 Comparison of thermal conductivity of some structural ceramic materials as a function of temperature [Butler, 1985].

2.1.9. ELECTRICAL CONDUCTIVITY

The electrical conductivity of zirconia-based material at room temperature is very low and it can be considered as an insulator, but at high temperature its electrical conductivity becomes quite high mainly due to ionic conduction of mobile oxygen ions [Kingery *et al*, 1959; Badwal, 1994]. With this property, zirconia can be applied as an oxygen sensor or solid electrolyte in solid oxide fuel cell (SOFC). Yttria-stabilised zirconia (YSZ) is interesting in SOFC application because it possesses sufficient level of oxygen ion conductivity and good stability in oxidising or reducing atmospheres. As well as stabilising zirconia, yttria can increase the oxygen vacancy concentration that enhances the ionic conductivity and extends the range of oxygen partial pressure for ionic conduction [Minh, 1993].

However, the ionic conductivity of YSZ depends on the amount of yttria as a dopant, and the operation temperature. At 1000°C the maximum conductivity is achieved with 8 mol% yttria where the minimum amount of yttria is required to make fully cubic zirconia. Above this level of yttria content then the conductivity decreases gradually as defect interactions between oxygen vacancies and dopant cations become inevitable [Badwal and Swain, 1985; Minh, 1993; Yanagida *et al*, 1996]. For lower yttria content between 2 and 7 mol% Y_2O_3, the lattice conductivity is higher than that of fully cubic zirconia at below 600°C [Badwal and Swain, 1985; Badwal, 1994] and has been proposed to be used in SOFC because it also has high toughness and strength. There is however a problem with reducing the mechanical properties from the ageing effect at that temperature or below. Also there is a problem with tetragonal monoclinic transformation under stress, where the monoclinic has been found to degrade the conductivity [Minh, 1993].

2.2. CERAMIC MATRIX COMPOSITES

A composite material can be defined as a material consisting of two or more distinct phases which are processed separately and then bonded to provide properties not yielded by either of them singly [Flinn and Trojan, 1995]. In ceramic matrix composites, ceramic as a matrix is the continuous phase, and other distributed ceramics or metallic phases are present as reinforcement. The form of reinforcement phase can be particulate, whiskers/short fibres, continuous fibre or laminate/sheet.

One of the original aims of research in ceramic matrix composites is to increase fracture toughness of ceramic materials. By incorporating a second phase into a ceramic matrix, it is expected that barriers to crack propagation can be enhanced in the ceramic matrix leading to fracture toughness improvement. However, the results found in the literature are varied and only limited success has been achieved [Donald and McMillan, 1976]. Moreover they suggested that significant fracture toughness improvement in ceramic matrix composites reinforced with dispersed particles should be achieved only if the fracture toughness of the dispersed phase is greater than that of the matrix, and there is strong bonding between the matrix and the reinforcement. Any crack deflection developed in the composite may also improve fracture toughness. Gupta (1974) also suggested that strong bonding between the matrix and reinforcement is required to get strength and fracture toughness improvement concurrently.

One of the problems in ceramic matrix composites is thermal expansion mismatch between the matrix and the reinforcement that can cause thermal stresses. Thermal expansion mismatch induces a hydrostatic stress in the particle and at the interface proportional to the cooling range temperature and thermal expansion coefficient difference [Selsing, 1961]. More details about these thermal stresses are discussed in section 2.2.4.

Considerations which should be taken into account in choosing matrix and reinforcement to produce a ceramic matrix composite [Chawla, 1993] are as follows:

a. melting point
b. volatility
c. density
d. elastic modulus
e. coefficient of thermal expansion
f. creep characteristic
g. strength
h. fracture toughness
i. compatibility between matrix and reinforcement (chemical, thermal, and environmental)

2.2.1. CERAMIC MATRIX REINFORCED WITH METAL

Introducing a ductile metal into ceramics has become an attractive way to increase fracture toughness since metals possess much higher fracture toughness than that of ceramic materials [Hing and Groves, 1972; Guichard *et al*, 1997]. Hing and Groves (1972) showed that incorporating metallic second phase (iron, nickel or cobalt) could increase the fracture toughness of magnesium oxide. However, metals are very sensitive to oxidation [Warren, 1992].

2.2.1.1. Types of Metal Reinforcement

Studies on different forms of metal reinforcement in ceramic matrix composites have been reported by many authors.

a. Metal Wires/Fibres

Some metals such as molybdenum, nickel, tungsten and stainless steel in the form of fibres or wires have been reported to reinforce ceramic materials.

Baskin *et al* (1960) observed that a hot-pressed composite of thoria (ThO_2) reinforced with molybdenum metal fibres had an increase in thermal conductivity compared to thoria. However, the strength of the composite is lower than that of thoria alone because of the presence of fine cracks in the composite.

However, in 1966 Miller *et al* succeeded in using molybdenum (Mo) metal fibres to improve the strength and thermal shock resistance of mullite. They also used tungsten (W) as reinforcement in their research. The composites were fabricated using a vacuum hot-pressing method. Two different treatments have been done to the fibres before being introduced to the matrix. First, the metal fibres were coated with 2 μm thickness of silicide and second, without coating. The MOR of composite reinforced with 20vol% metal fibres (either Mo or W) was increased by about 70% for composites with coated metal fibres and about 90% for the uncoated one. However, the composites had very poor oxidation resistance.

Another application of molybdenum metal fibres to reinforce ceramic has been reported by Simpson and Wasylyshin (1971). They investigated the effect of such fibres on fracture toughness of alumina (Al_2O_3) using a hot pressing process. They found that the fracture toughness was improved. They did not find a chemical bonding between the matrix and the reinforcement. Moreover they suggested that the higher thermal expansion of the matrix ($6.7 \times 10^{-6}/°C$) than that of the Mo fibres ($5.5 \times 10^{-6}/°C$) resulted in contraction of the matrix on cooling resulting in strong gripping action of the matrix on the Mo that prevented fibre pullout.

Other metals such as nickel and stainless steel in the form of wires or fibres have been used to reinforce ceramic materials. Hot pressing sintering has been chosen by Hing and Groves (1972) to overcome the difficulty in preparing composite of magnesium oxide reinforced with nickel metal fibres. They found that the strength of the composite is not influenced by the volume fraction of nickel, however the fracture toughness increased significantly with amount of fibres.

Stainless steel (AISI 304) metal wires with diameter of 6, 12 and 25 μm have been incorporated in a wustite matrix to make composites using hot pressing sintering. The metal fibres improved all the fracture properties of the wustite matrix [Zwissler *et al*, 1977]

b. Metal Particulate

Hing and Groves (1972) also studied a hot-pressed and annealed composite of magnesium oxide matrix reinforced with dispersed metallic phases of nickel, iron and cobalt. The transverse strength increases as volume fraction of metal and annealing temperature increase. The dispersed metal inhibited the grain growth which then strengthens the composites.

Other examples of metal reinforcement in the form of particles can be seen in section 2.2.1.2.

c. Metal Laminate

Another form of metal reinforcement for ceramic matrix composites is laminate or sheet. In their study Moorhead and Kim (1999) developed a laminated composite between magnetic metal foil (Fe-Co-V) alloy and 3Y-TZP using a hot-pressing process. These materials were proposed to be used as a magnetic core in electric motors, generators and transformers. They found that the composite had a maximum interfacial strength of 420 MPa in a sample hot-pressed at 1250°C. Above that temperature the interfacial strength decreased due to excessive reaction at the interface.

2.2.1.2. Zirconia Matrix Reinforced with Metal

Zirconia is an interesting ceramic material for developing ceramic-metal composites because it has good mechanical properties (strength and fracture

toughness) compared to other ceramic materials and also its thermal expansion coefficient (10 x 10^{-6}/°C for Y-TZP) is close to that of some metals, which may minimise the effect of thermal expansion mismatch.

Several works on zirconia reinforced with metals such as nickel, stainless steel, and molybdenum have been reported in the literature [Kawashima and Hishinuma, 1996; Tamburini *et al*, 1998; Kondo *et al*, 1999; Ishizuka *et al*, 1995, Jung *et al*, 1997; Hu *et al*, 1998; Yamada *et al*, 1994; Wenquan *et al*, 1999; Nawa *et al*, 1996]. The increasing application of zirconia as solid electrolyte and zirconia ceramic-metal composites as anodes in solid oxide fuel cells (SOFC) has opened up research in zirconia reinforced with metal. [Minh, 1993; Kawashima and Hishinuma, 1996, and Tamburini *et al*, 1998]. The metal used in this composite should have good oxidation resistance at high temperature in the working condition of the fuel cells. Nickel is usually chosen for this application because of its low cost compared to other suitable metals (such as cobalt, platinum and palladium) [Minh, 1993]. This choice is also to fulfil the requirements of anode material in SOFC, such as good electronic conductivity combined with low metal content and high porosity (50%), good mechanical properties and thermal properties, chemically stable at high temperature [Kawashima and Hishinuma, 1996; Tamburini *et al*, 1998; Kondo *et al*, 1999].

Kawashima and Hishinuma (1996) studied the thermal properties (specific heat, thermal diffusivity and conductivity) of nickel/(8Y-stabilised zirconia) particulate composites with nickel content from 0 - 100 vol% and porosity ranging from 0 - 52%. They found that the specific heat decreased with increasing nickel content. However, the thermal diffusivity as well as conductivity increased with increasing nickel volume fraction because the thermal diffusivity of nickel is 20 times greater than that of zirconia.

Tamburini *et al* (1998) fabricated zirconia/nickel composites without using direct mixing of zirconia and nickel particles, but they investigated a new process to produce such composites using high temperature synthesis as follows:

$$2MeO + Zr + nY_2O_3 \longrightarrow YSZ + 2Me \quad \ldots\ldots\ldots\ldots\ldots\ldots (2.4)$$

where Me = metal, YSZ = yttria stabilised zirconia. This method is actually expensive because of the high cost of Zr compared to ZrO_2.

Zirconia/nickel composites can also be produced from 3Y-TZP and NiO using reductive hot pressing sintering as reported by Kondo *et al* (1999). The reduction was carried out in hydrogen gas atmosphere at 700°C before hot-pressing at 1500°C and 1600°C. By this method NiO transforms to Ni metal and it therefore results in a composite between t-ZrO_2 and Ni metal. The results showed that the fracture toughness increased with increasing volume fraction of nickel. However, the fracture strength (3 point bending) on samples hot-pressed at 1600°C decreased as nickel content increased. This is due to the increasing defect size and formation of microcracks by large agglomerated nickel grains in higher nickel content materials.

Other works on zirconia-nickel composites can be found in the literature as reported by Ishizuka *et al* (1995), Jung *et al* (1997) and Hu *et al* (1998). Ishizuka *et al* (1995) studied the fracture strength of such composites containing nickel metal particle from 0 - 100 vol% using disc-bending tests. Jung *et al* (1997) and Hu *et al* (1998) studied residual stress and thermal properties, and electrical and thermal conductivity of zirconia/nickel composites in the form of functionally graded materials (FGM), respectively. Jung *et al* (1997) also studied a composite of zirconia matrix with stainless steel (SUS 304) metal. They found that the thermal conductivity of the composites increased with increasing nickel or stainless steel content from 0 - 100 vol%. They also indicated that thermal expansion mismatch affected residual stress, in which the stress developed in zirconia/nickel is smaller than that of in zirconia/stainless steel, because thermal expansion difference of zirconia/nickel composite is smaller than that of the zirconia/stainless steel one.

Furthermore, in their study Hu *et al* (1998) showed that the electrical and thermal diffusivity of the FGM composites (zirconia/nickel) increased with

increasing nickel fraction but those properties did not follow the rule of mixing. Then they proposed models to predict such properties as follows:

$$\sigma = [\sigma_{Ni} V_{Ni} - k\sigma_{Ni} V_{Ni}(1 - V_{Ni})](1 - P)^{1.5} \qquad \ldots\ldots\ldots\ldots\ldots\ldots\ldots\ldots (2.5)$$

$$a = [a_{Ni} V_{Ni} + a_{ZrO_2} V_{ZrO_2} - a^{e}_{Ni} k V_{Ni}(1 - V_{Ni})](1 - P)^{1.5} \qquad \ldots\ldots\ldots\ldots\ldots (2.6)$$

Where, σ = electrical conductivity

a = thermal diffusivity

V = volume fraction

k = a proportionality coefficient (0 - 1)

Ni = nickel component

ZrO_2 = zirconia component

e (supercript) = electron contribution of thermal diffusivity

P = porosity (%)

Stainless steel has also been reported as a reinforcement of zirconia ceramic composites [Yamada *et al*, 1994; Wenquan *et al*, 1999]. Yamada *et al* (1994) studied PSZ/stainless steel composites with 20, 40, 60 80 vol% of PSZ and showed that the thermal expansion mismatch between the matrix and the reinforcement has generated interfacial residual stress. At the metal-rich side the residual stress is compressive which opposes debonding and improves the Young's modulus. In contrast, in the ceramic-rich side the residual stress is tensile which enhances debonding.

Wenquan *et al* (1999) developed a metal ceramic multilayer tube between stainless steel (17Cr, 14Ni, 2Mo) and PSZ using multi-billet extrusion forming. They observed the influence of some sintering parameters such as time and sintering temperature, and protective gas pressure on volume shrinkage, density and microstructures. They discovered that sintering in protective gas resulted in a relative density and shrinkage decrease with increasing stainless steel content. However, high

vacuum sintering or gas pressure sintering increases elimination of pores, which increases the shrinkage and relative density. This benefits sintering densification. Samples produced by protective gas sintering resulted in little effect on compressive strength, but fabrication of samples at high sintering vacuum and gas pressure sintering yielded a significant improvement of such strength.

Considerable achievements have been reported by Nawa *et al* (1996) regarding the simultaneous improvements of strength and fracture toughness of 3Y-TZP/Mo (0 - 100 vol%) nanocomposites. They fabricated the materials by hot pressing at 1400°C to 1600°C using applied pressure of 30 MPa for 1 h in vacuum. These simultaneous increases are believed to be due to a decrease in flaw size where the Mo (submicron-size) disperses around the grain boundaries of ZrO_2 and some trapped within the ZrO_2 grains. Also some elongated Mo particles are formed at the ZrO_2 grain boundaries for composites with more than 40 vol% Mo.

It can be seen that research and development of zirconia-matrix composites reinforced with metals is still wide open for development, in term of the reinforcing metals, processing, characterisation and properties. Therefore this present research is focussed on observation of 3Y-TZP reinforced with metal powder (chromium, iron or stainless steel AISI 316). The works include processing and fabrication, characterisation, mechanical properties (Vickers hardness, fracture toughness and bending strength), thermal properties (thermal expansion coefficient and thermal diffusivity), and electrical conductivity. All these are carried out on 3Y-TZP as the matrix with each of those metals as the reinforcement.

2.2.2. EFFECT OF PARTICULATE REINFORCEMENT ON DENSIFICATION

The presence of particles as second phase in ceramic matrix composites may influence the behaviour of sintering. A mathematical model that is derived from the rule of mixing has been proposed by Edrees and Hendry (1999) to describe such effect as follows:

$$\left(\frac{\delta L}{L_o}\right)_c = 1-\left[\left(1-\left(\frac{\delta L}{L_o}\right)_m\right)^3 + f\left(1-\left(1-\left(\frac{\delta L}{L_o}\right)_m\right)^3\right)\right]^{1/3} \quad \ldots\ldots\ldots\ldots (2.7)$$

where, $(\delta L/L_o)$ is the linear dimension change, f is volume fraction of reinforcing phase, the subscripts c and m refer to composite and matrix. This model is only applicable to composites where the volume fraction of reinforcement does not change during sintering, there is no interfacial reaction on the second phase and the densification only occurs in the matrix.

In the above equation, the linear shrinkage of composites only depends on the volume fraction of the reinforcement and the linear shrinkage of the matrix. There should be a limit of the volume fraction of reinforcement such that the densification only occurs in the matrix. At a certain amount of reinforcement, the particles will start to cluster leading to local sintering. Another parameter that should be taken into account is the applied pressure to form green samples. Magnitude of the applied pressure is important in prediction and comparison of linear shrinkage of monolithic ceramics and the composites. Smith (1993) showed that lower final shrinkage would occur if higher pressure were applied in fabrication of green samples.

2.2.3. TOUGHENING MECHANISMS IN PARTICULATE COMPOSITES

Toughening mechanisms in particulate composites can be classified into three types: crack tip interactions, crack tip shielding and matrix compression. The first type is achieved by placing obstacles in the crack path to hinder crack motion. Crack tip interactions consist of three mechanisms: crack deflections, crack bridging by ductile particles and crack bowing. A crack shielding mechanism occurs in a material when the microstructure adjacent to a propagating crack changes due to the stress field close to the crack tip. Transformation toughening and microcracking can be classified into this type. Those mechanisms are briefly explained below.

a. Crack Deflection

Cracks can be deflected when they approach stress fields present around particles or weak grain boundaries or at weak particle/matrix interfaces as shown in Figure 2.16. Faber and Evans[a,b] (1983) have studied crack deflection processes based on a fracture mechanics approach. Two types of crack deflections have been analysed, tilted and twisted deflections. They analysed the tilted cracks using a mixture of fracture mechanics of Mode I (opening) and Mode II (sliding) contributions to stress intensity. While Mode I and Mode III (tearing) were used to analyse the twisted cracks. Crack deflection causes a change in orientation of the crack plane leading to a reduction of force of crack extension (increase in fracture energy). They also demonstrated that the increase of toughness depended on the volume fraction of second phase and particle shape.

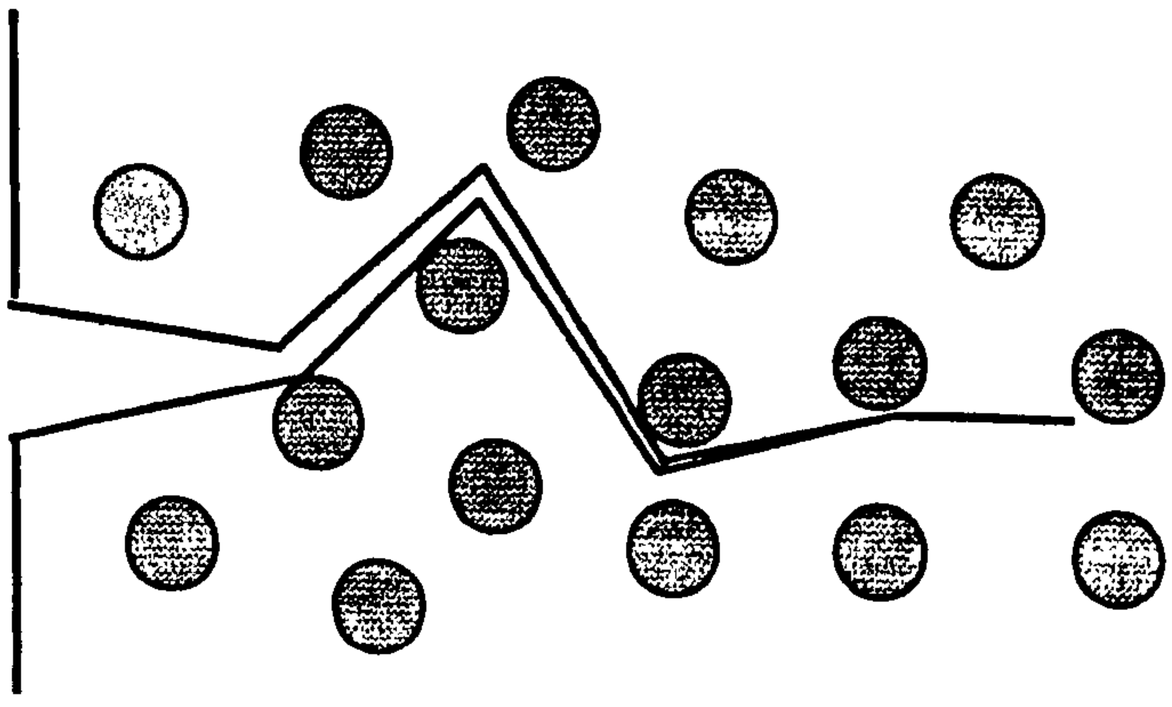

Figure 2.16 A schematic of crack deflection by particles.

b. Crack bridging by ductile particles

Figure 2.17 shows the mechanism of crack bridging by ductile particles. This mechanism of toughening has been studied by Krstic *et al* (1981), Sigl *et al* (1988) and Budiansky *et al* (1988). In this mechanism, the ductile particles that impede a crack will undergo plastic deformation, necking, and fracture if the particles are well bonded in the matrix. Strong interfaces and high particle strength is desirable to provide large plastic deformation of bridging particles before fracture, which leads to a substantial toughening effect. However this is difficult due to particle shape asymmetries and interface sliding, which tend to reduce constraint on the particle.

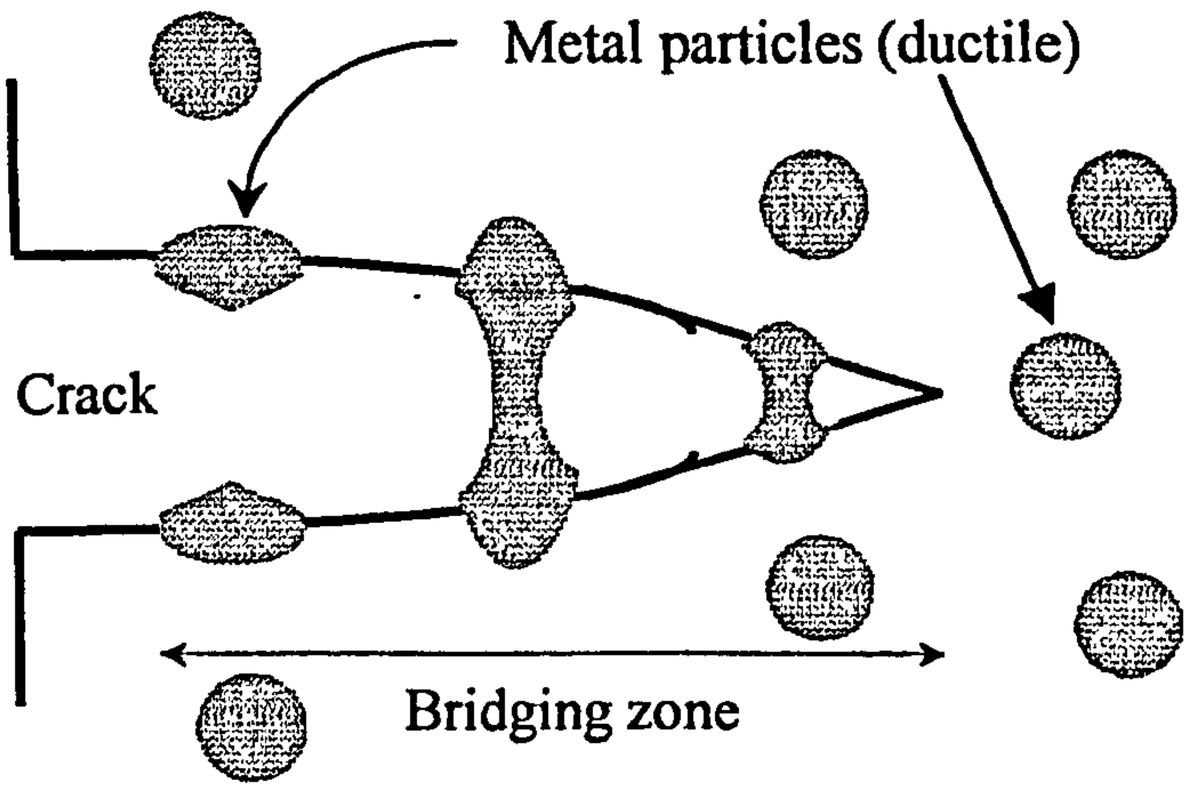

Figure 2.17 A schematic of crack bridging in composites reinforced with ductile particles.

c. Crack bowing

In crack bowing mechanisms a crack can by-pass obstacles although the crack is pinned by them as shown schematically in Figure 2.18. When the crack interacts with two or more obstacles, it tends to bow out between obstacles and form semi-elliptical flaws. Crack bowing mechanisms should lead to an increase in fracture toughness [Lange, 1970] and strength [Evans, 1972].

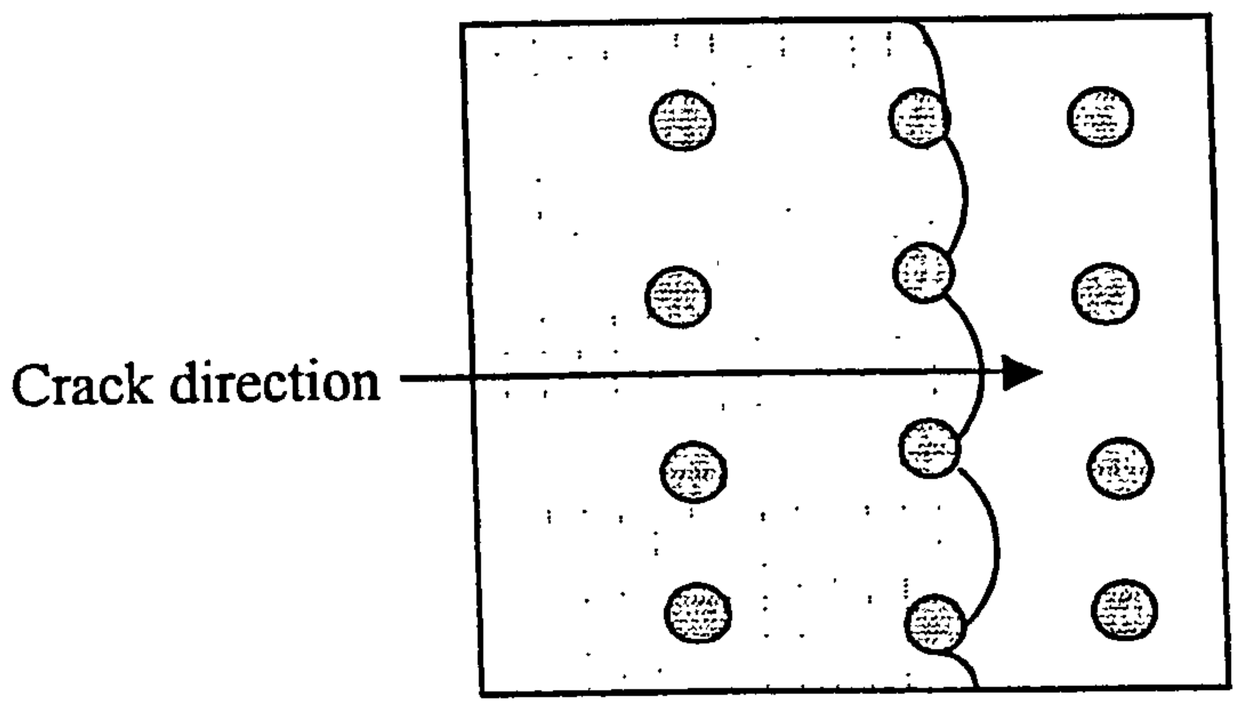

Figure 2.18 A Schematic of cracks front bowing. The shaded area is the cracked region.

d. Transformation toughening

Increase of fracture toughness and strength can be obtained in ceramic materials that undergo stress-induced transformation. Garvie *et al* (1975) have shown this case in zirconia ceramics when the metastable tetragonal phase transforms to monoclinic followed by a volume increase. The volume increase and the shear strain developed during transformation impede the crack opening leading to increase of the crack propagation resistance of the ceramics. Details about this mechanism have been discussed in Section 2.1.6.

e. Microcracking

The fundamental point of this mechanism is that microcracking can be induced in response to the stress field around the crack tip in association with residual stress. This will give two contributions to toughening: formation of a zone with lower elastic modulus and absorption of strain release energy [Warren, 1992]. During fabrication, microcracks can form spontaneously if the grain or particle size is above a critical size. Microcracks will be stress-induced if the grains or particles size is just below the critical size. The critical size can be calculated using the following equation [Davidge and Green, 1968]:

$$r_c = \frac{8\gamma_s}{P^2\left(\frac{1+\upsilon_m}{E_m} + 2\frac{1-2\upsilon_p}{E_p}\right)} \qquad \ldots\ldots\ldots\ldots\ldots\ldots\ldots\ldots\ldots\ldots\ldots\ldots (2.8)$$

where r_c is critical size above which matrix cracking will take place, γ_s is the surface energy of the matrix, P is pressure around the particle due to thermal expansion mismatch, ν is poisson's ratio, subscript m and p are matrix and particle respectively.

f. Matrix Compression

Toughening mechanisms can also arise from appropriate thermal mismatch between particles and the matrix. In ceramic particulate composites with $\alpha_p > \alpha_m$ residual matrix compression will be developed during cooling from the processing temperature to room temperature. The compression state in the matrix will increase crack growth resistance in the composites. Taya *et al* (1990) observed this toughening mechanism on SiC composite reinforced with TiB_2.

2.2.4. THERMAL STRESSES IN COMPOSITES

Thermal stresses are internal stresses that occur in materials when there is a constraint on free dimensional change. If there is no such constraint then the materials can be free of thermal stresses. This constraint can be caused by [Chawla, 1993]:

a. temperature gradient
b. anisotropy of atomic structure
c. volume change due to phase transformation
d. difference in thermal expansion coefficient in the constituent materials

Thermal stress due to a temperature gradient is related to the thermal diffusivity of a material (which indicates how quick the material responds to temperature change). In anisotropic materials thermal stresses are developed when they have different thermal expansion coefficients in different directions of the atomic structure. Volume change due to phase transformation can also generate thermal stresses. A good example of the latter is in fabrication of pure zirconia, where the initial phase at room temperature is monoclinic, but changes to tetragonal at 1170°C. During cooling this tetragonal will revert to monoclinic accompanied by ~4% volume increase.

Thermal stresses in composite materials generated by thermal expansion coefficient mismatch between the matrix and the reinforcement often occurs during cooling from high processing temperature. For example, if $\alpha_m > \alpha_p$ on cooling from T to T_o ($T > T_o$), the matrix will tend to contract more than the reinforcement resulting in a compression stress on the reinforcement. More details about thermal stresses in particulate composites are discussed in section 2.2.4.2.

2.2.4.1. Thermal Expansion Coefficient of Composites

Thermal expansion coefficient of composites can not be predicted simply using the rule of mixing because different expansion coefficient values of the components in a composite will generate a mechanical constraint that should be taken into account. An equation proposed by Turner (1946) may be used to predict the total thermal expansion coefficient of a composite, as follows:

$$\alpha_c = \frac{\alpha_m V_m K_m + \alpha_p V_p K_p}{V_p K_p + V_m K_m} \qquad \ldots\ldots\ldots\ldots\ldots\ldots\ldots\ldots\ldots\ldots (2.9)$$

Where α is thermal expansion coefficient, K is bulk modulus [K=E/(3(1-2ν))], E is Young's modulus, and subscripts (m) and (p) denote matrix and particle, respectively.

Kerner (1956) also proposed a model to predict CTE of a particulate composite that included the effect of shear and isostatic stresses. The model is in the form of volumetric thermal expansion (β), with the assumption that the materials are isotropic, so the linear thermal expansion (α) can be easily estimated ($\beta = 3\ \alpha$). Kerner's model is as follows [Kerner, 1956; Chawla, 1993]:

$$\beta_c = \beta_m V_m + \beta_p V_p - (\beta_m - \beta_p) V_p \left[\frac{1/K_m - 1/K_p}{V_m/K_p + V_p/K_m + 3G_m/4} \right] \qquad ..(7.10)$$

where α and β are linear and volumetric coefficient of thermal expansion respectively; V is volume fraction; K and G denote bulk and shear modulus respectively; and subscripts c, m and p denote the composite, matrix, and particle reinforcement respectively.

The model given by Kerner (1956) does not significantly differ from the rule of mixtures. In their study of metal-matrix composites Vaidya and Chawla (1994) showed that the rule of mixtures and Kerner model gave good agreement to the experimental results. They also found that thermal stress due to thermal expansion mismatch might cause a residual strain after cooling.

2.2.4.2. Thermal Stresses in Particulate Composites due to Thermal Expansion Mismatch

The difference of thermal expansion coefficient of the components in composite materials can cause thermal stresses. In ceramic matrix composites, thermal stress analysis is very important because the ceramic matrix usually has a very low strain to fracture.

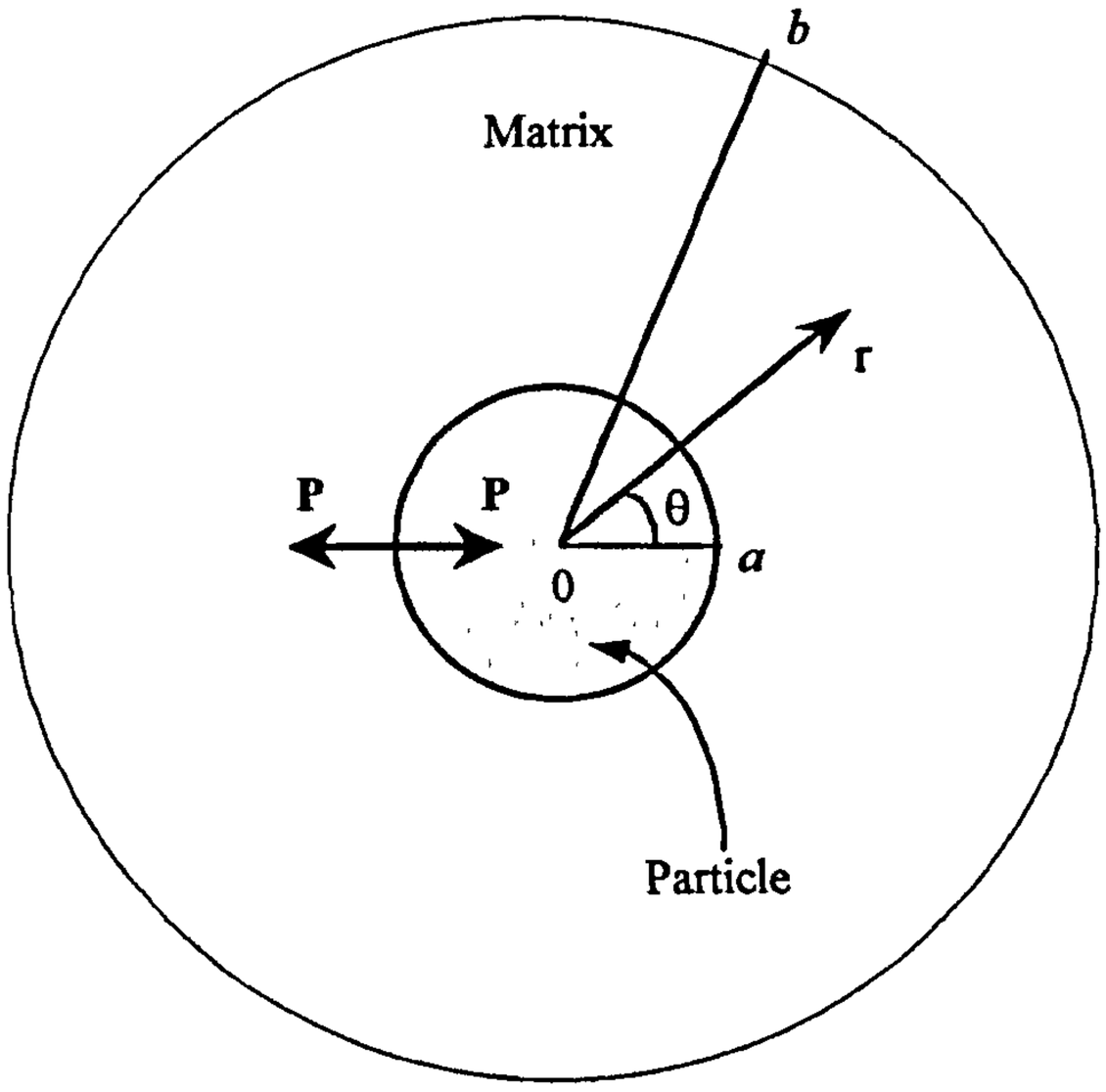

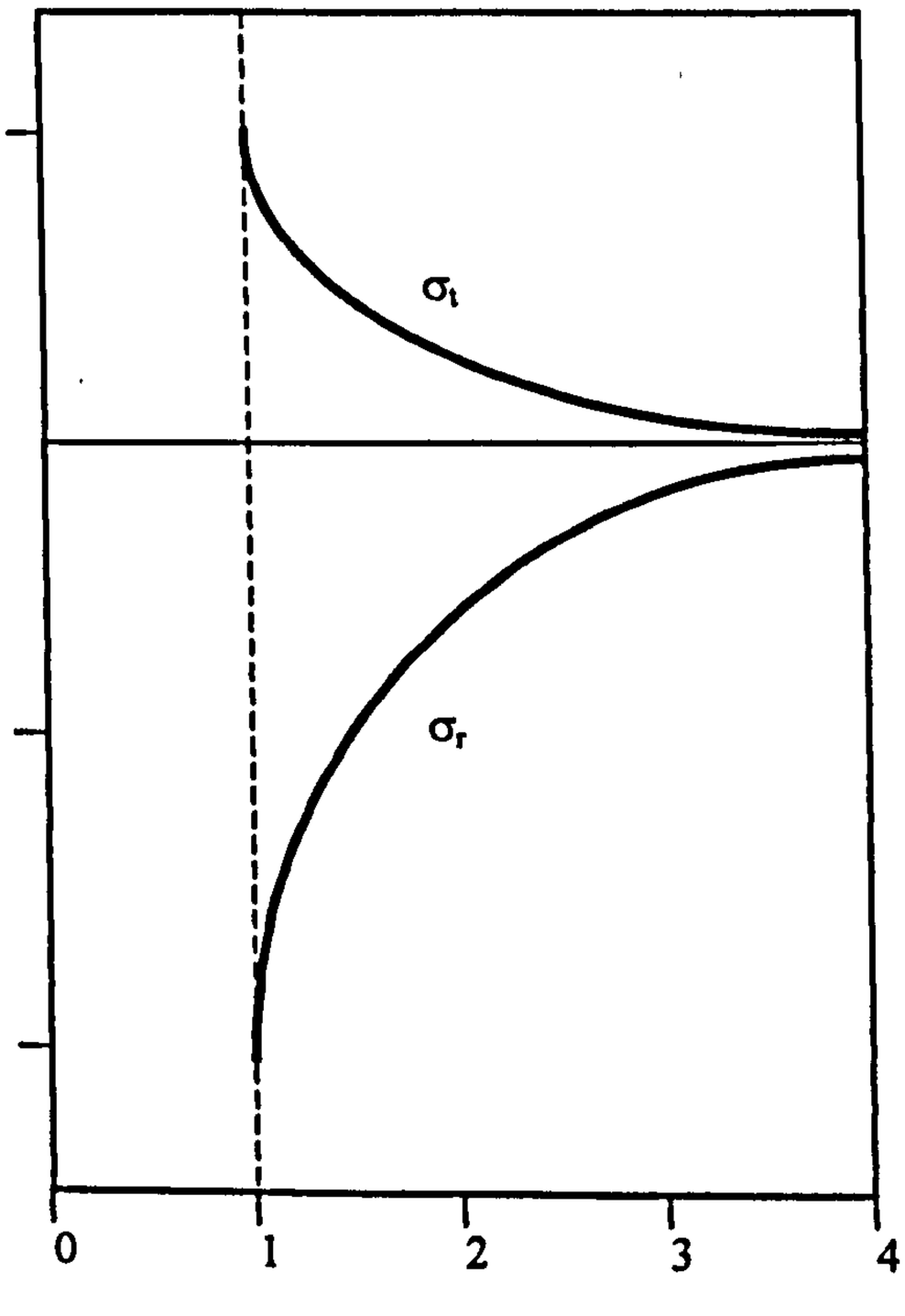

a b

Figure 2.19 (a) A composite with a particle of radius *a* embedded in a matrix of radius *b*, (b) Distribution of thermal stresses around a single spherical particle of composite of (a).

Analysis of thermal stresses in particulate composites can be explained as follows [Selsing, 1961; Chawla, 1993]. For a single spherical particle embedded in an infinite matrix (see Figure 2.19), a hydrostatic stress is created in the particle [Selsing, 1961]. This stress is equal to the hydrostatic pressure (P) in the particle.

$$\sigma_{rp} = \sigma_{tp} = P = \frac{\Delta\alpha.\Delta T}{\left[\frac{(1+\upsilon_m)}{2E_m}\right]+\left[\frac{(1-2\upsilon_p)}{E_p}\right]} \quad \ldots\ldots\ldots\ldots\ldots\ldots (2.10)$$

where $\Delta\alpha$ is thermal expansion coefficient difference of matrix and particle ($\Delta\alpha = (\alpha_m - \alpha_p)$); σ_r and σ_t are the radial and tangential stress components in the particle, respectively; and subscript m and p indicate matrix and particle, respectively.

If *a* is the particle radius, and r is radial distance from the centre of the particle, then the stresses created in the matrix are given by:

$$\sigma_{rm} = -2.\sigma_{tm} = P\left(\frac{a}{r}\right)^3 \quad \ldots\ldots\ldots\ldots\ldots\ldots\ldots\ldots\ldots\ldots (2.11)$$

The stress distribution in the particle and the matrix is illustrated in Figure 2.19.

For particles distributed in a ceramic matrix composite with particle volume fraction (V_p), particle radius (*a*) and matrix radius (*b*), the above equations become [Chawla, 1993]:

The hydrostatic pressure:

$$P = \frac{\Delta\alpha\Delta T}{\left[\frac{0.5(1+\upsilon_m)+(1-2\upsilon_m)V_p}{E_m(1-V_p)} + \frac{(1-2\upsilon_p)}{E_p}\right]} \quad \ldots\ldots\ldots\ldots\ldots (2.12)$$

$$V_p = \left(\frac{a}{b}\right)^3 \quad \ldots\ldots\ldots\ldots\ldots\ldots\ldots\ldots\ldots\ldots\ldots\ldots (2.13)$$

The stresses in the particle:

$$\sigma_{rp} = \sigma_{tp} = P = \text{constant} \qquad \ldots\ldots\ldots\ldots\ldots\ldots\ldots\ldots\ldots\ldots \quad (2.14)$$

The stresses in the matrix at the distance r from the centre of the particle are:

- the radial stress:

$$\sigma_{rm} = \frac{P}{(1 - V_p)}\left[\left(\frac{a}{r}\right)^3 - V_p\right] \qquad \ldots\ldots\ldots\ldots\ldots\ldots\ldots\ldots\ldots\ldots (2.15)$$

- the tangential stress:

$$\sigma_{tm} = -\frac{P}{(1 - V_p)}\left[\frac{1}{2}\left(\frac{a}{r}\right)^3 + V_p\right] \qquad \ldots\ldots\ldots\ldots\ldots\ldots\ldots\ldots\ldots\ldots (2.16)$$

From the above equations and also Figure 2.19b, it can be seen that the maximum stresses in the matrix (radial or tangential) occur at the interface between matrix and particle. The stresses in the matrix then decrease with the distance from the particle centre.

2.2.5. THERMAL DIFFUSIVITY/CONDUCTIVITY OF COMPOSITES

2.2.5.1. Particulate Composites

In particulate composites in which spherical particles are isolated in a continuous matrix with a good thermal contact, the thermal conductivity of the composite can be approximately calculated using the Eucken model as follows [Kingery, 1976]:

$$k_c = k_{mc}\frac{\left[1+\frac{2V_{rd}(1-Q)}{(2Q+1)}\right]}{\left[1-\frac{V_{rd}(1-Q)}{(Q+1)}\right]} \quad \ldots\ldots\ldots\ldots\ldots\ldots\ldots\ldots \quad (2.17)$$

where Q is the ratio of k_{mc} and k_{rd} or ($Q= k_{mc}/k_{rd}$), k is thermal conductivity, V is volume fraction, and subscript **mc** and **rd** represent the continuous phase (matrix) and dispersed spherical particle respectively.

Another model of thermal conductivity for composites with an interfacial thermal barrier has been suggested by Hasselman and Johnson (1987) as follows:

$$k_c = k_m \frac{\left[2\left(\frac{k_d}{k_m}-\frac{k_d}{ah_c}-1\right)V_d+\frac{k_d}{k_m}+\frac{2\,k_d}{ah_c}+2\right]}{\left[\left(1-\frac{k_d}{k_m}+\frac{k_d}{ah_c}\right)V_d+\frac{k_d}{k_m}+\frac{2\,k_d}{ah_c}+2\right]} \quad \ldots\ldots\ldots\ldots \quad (2.17a)$$

Where k is thermal conductivity, m and d represent the continuous phase (matrix) and the dispersed spherical particles, a is radius of spherical particles, h_c is a boundary conductance and V_d is volume fraction.

2.2.5.2. Effect of Microcracks and porosity

Microcracks can influence significantly on the thermal diffusivity or conductivity. In polycrystalline monolithic ceramics, microcracks can often be generated from the thermal expansion anisotropy of the individual grains, while in ceramic matrix composites, microcracks arise from the thermal expansion coefficient mismatch of the individual components [Siebeneck *et al*, 1976; Siebeneck *et al*, 1977; Hasselman, 1986]. In their study, it has been found clearly that microcracks can cause a decrease of the thermal diffusivity or conductivity of iron-titanate (Fe_2TiO_5) [Siebeneck *et al*, 1976] and of magnesium-titanate ($MgTi_2O_5$) [Siebeneck *et al*, 1977]. Hasselman (1978) developed models to predict the effect of microcracks on thermal conductivity by assuming that the microcracks have ellipsoid geometry with minor axis approaching zero and no radiation or convection across the cracks. Three different models were proposed based on the crack orientations i.e. (1) crack orientation is perpendicular to the direction of the heat flow which gives maximum reduction of thermal conductivity, (2) crack orientation is parallel to the heat flow which have no effect on thermal conductivity, and (3) randomly oriented crack which gives reduction value between that of (1) and (2).

If there are microcracks and or porosity in composites then there will be void or gas trapped that has much lower thermal conductivity than that of solid. As a result the total thermal conductivity of the material becomes lower. Another aspect that can influence thermal conductivity in composites is interfacial contact between phases that may generate thermal contact resistance [Incropera and DeWitt, 1996].

2.2.5.3. Percolation

Thermal conductivity is a transport property in a material. In a composite material the total value of thermal conductivity not only depends on the amount of each component but also depends on the degree to which the components are connected [Chiang *et al*, 1997]. It means that the phase that is continuous will

dominate the value. If there is a great difference of the value between the matrix and the reinforcement, then the separation between upper and lower bound given by the rule of mixing becomes wider. The condition where there is a transition from discontinuous phase to continuous chains is termed percolation threshold. The percolation causes a variation in value in a composite usually indicated by an S-shaped curve. Figure 2.20 shows an example of the two-phase system MgO-$MgSiO_4$ indicating the percolation limit occurs at 40 vol% of $MgSiO_4$.

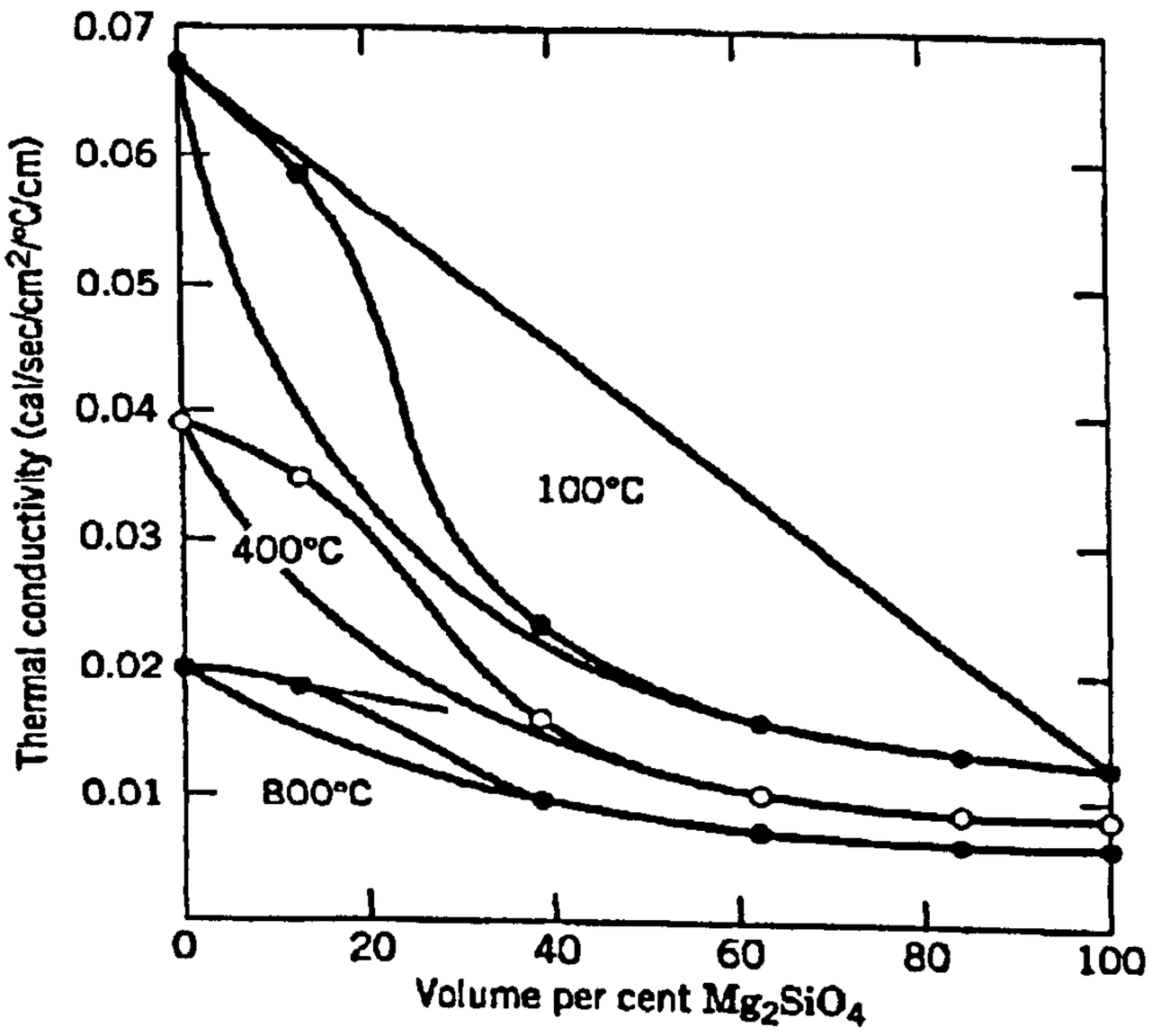

Figure 2.20 Thermal conductivity in two-phase system MgO-$MgSiO_4$ [Chiang *et al*, 1997].

2.2.6. ELECTRICAL RESISTIVITY/CONDUCTIVITY IN COMPOSITES

2.2.6.1. Electrical Resistivity/Conductivity in Particulate Composites

Similar to thermal conductivity, electrical resistivity or conductivity is also a transport property. Therefore the electrical resistivity or conductivity in particulate composites is also dependent on the amount of each component and the degree of connectivity of its component [Chiang *et al*, 1997]. The particle morphology is also another factor [Warren, 1992]. In a composite where the matrix is insulative and the dispersed particles are conductive, the electrical resistivity of the composite can be predicted simply as follows [Warren 1992]:

$$\omega_c = V_p.\omega_p + V_m.\omega_m \qquad \ldots\ldots\ldots\ldots\ldots\ldots\ldots\ldots\ldots\ldots\ldots\ldots (2.18)$$

However, when the dispersed particles become continuous phase at above a certain volume fraction, then the total resistivity becomes:

$$\frac{1}{\omega_c} = \frac{V_p}{\omega_p} + \frac{V_m}{\omega_m} \qquad \ldots\ldots\ldots\ldots\ldots\ldots\ldots\ldots\ldots\ldots\ldots\ldots (2.19)$$

Where, V is volume fraction, ω is resistivity, and p and m are particle and matrix respectively.

2.2.6.2. Percolation Threshold

Electrical conductivity of a composite also experiences percolation if there is a big difference of conductivity between the matrix and the reinforcement. Dees *et al* (1987) show the percolation threshold of electrical conductivity of ZrO_2/nickel composites at 1000°C occurs at about 30 vol% nickel that is indicated by a typical 'S' shaped curve as shown in Figure 2.21(a). The low conductivity below 30 vol% nickel is similar to that of YSZ indicating ionic conduction through YSZ. At above 30 vol%

nickel the conductivity increases dramatically due to a change in conductivity mechanism to electronic conduction through the nickel phase.

Furthermore, Guichard *et al* (1997) suggest that the most important factors that influence the percolation threshold in ceramic/metal composites are the metal distribution, the metal shape and the metal-ceramic interactions. In their study of alumina reinforced with iron nano-powder, Guichard *et al* (1997) found that the percolation threshold of the electrical conductivity at room temperature occurred at 20 vol% Fe as shown in Figure 2.21(b).

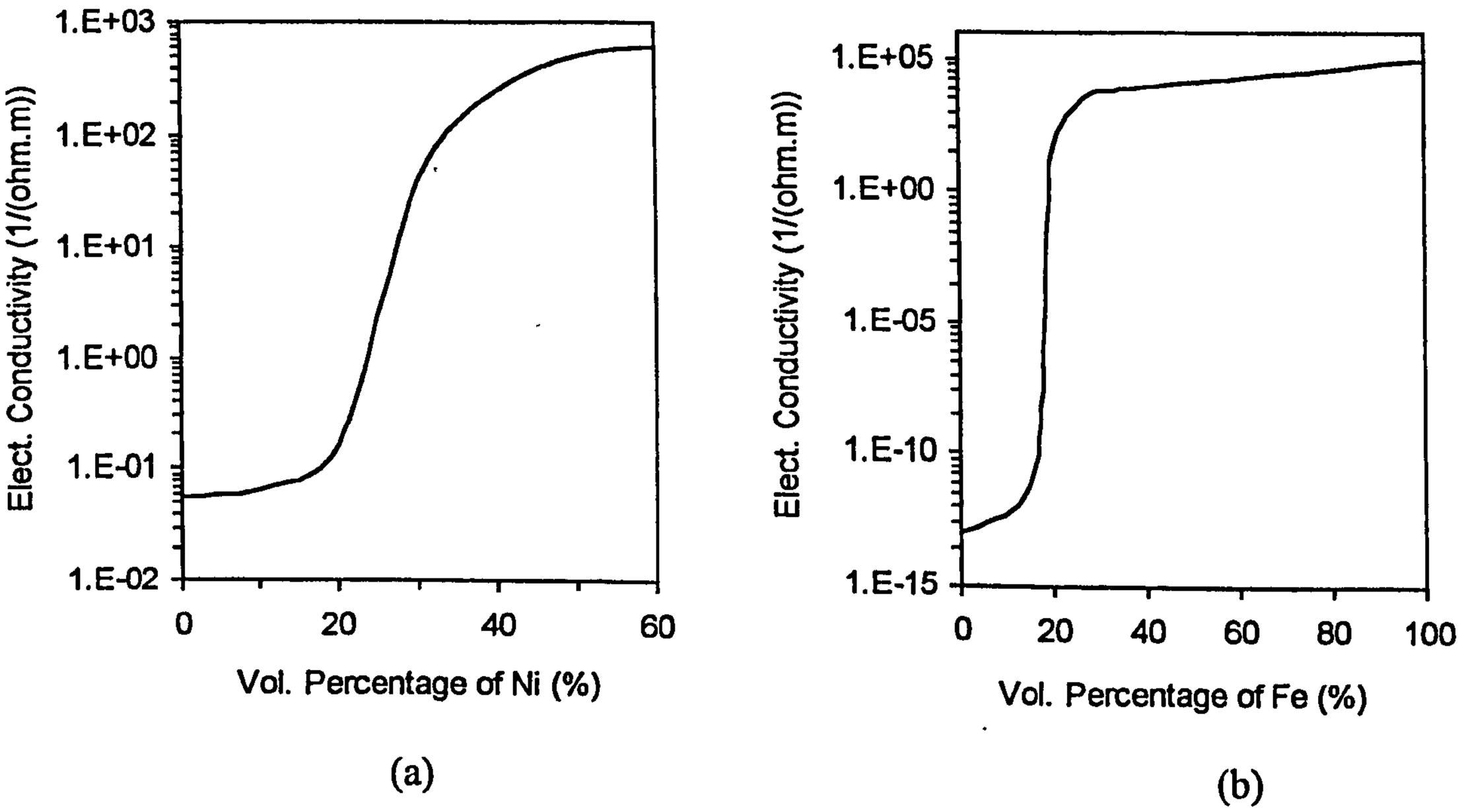

Figure 2.21 Electrical conductivity of (a) ZrO_2/nickel composite at 1000°C [Dees, 1987], and (b) Al_2O_3/Fe composites at room temperature [Guichard *et al*, 1997].

2.3. THERMAL DIFFUSIVITY/CONDUCTIVITY MEASUREMENT

Thermal conductivity (k) indicates the ability of a material to transfer heat. Heat flow through a solid material can be expressed as follows [Callister, 1994; Incropera and DeWitt, 1996].

$$q = -k\frac{dT}{dx} \qquad \ldots\ldots\ldots\ldots\ldots\ldots\ldots\ldots\ldots\ldots\ldots\ldots\ldots\ldots\ldots\ldots (2.20)$$

where q is the heat flux (heat flow) per unit time per unit area, k is thermal conductivity and dT/dx is the temperature gradient. In solid materials, the heat transport is due to two effects, the migration of free electrons and lattice vibration waves (phonons). Accordingly, the total thermal conductivity is the sum of an electronic component (k_e) and a lattice vibration component (k_l).

$$k = k_e + k_l \qquad \ldots\ldots\ldots\ldots\ldots\ldots\ldots\ldots\ldots\ldots\ldots\ldots\ldots\ldots\ldots\ldots (2.21)$$

There is another important property termed the thermal diffusivity *a*, which is the ratio of the thermal conductivity to the heat capacity times the density [Incropera and DeWitt, 1996].

$$a = \frac{k}{\rho.Cp} \qquad \ldots\ldots\ldots\ldots\ldots\ldots\ldots\ldots\ldots\ldots\ldots\ldots\ldots\ldots\ldots\ldots (2.22)$$

where ρ is density and C_p is heat capacity.

The thermal diffusivity characterises the ability of a material to respond to thermal energy relative to its ability to store thermal energy. A material with large *a* will respond quickly to changes in its thermal environment. In contrast, a material with a small *a* will take longer to reach a new equilibrium condition.

Ceramic materials are thermal insulators (low thermal conductivity), which lack a large number of free electrons. Consequently, the phonons are responsible in thermal conduction. In transporting heat energy however the phonons are not as

effective as free electrons [Callister, 1994]. Because of their low thermal conductivity, ceramics materials are at risk of thermal stress [Sheffield and Schorr, 1991]. Hence, accuracy in measurement of thermal diffusivity and or conductivity is important in materials engineering. Sheffield and Schorr (1991) reviewed the methods of thermal diffusivity and conductivity measurement as follows:

Table 2.2. Comparison of thermal diffusivity/conductivity methods.

	METHODS				
	Calorimeter	Guarded Hot Plate	Hot Wire	Radial Heat Flow	Laser Flash
Method Type	Steady state	Steady State	Steady State	Transient	Transient
Property measured	Conductivity	Conductivity	Conductivity	Diffusivity	Diffusivity
Temperature Range (K)	420-1750	100-1700	298-1750	373 - 1923	100-2500
Run Time	24-48h/temp*	24-48h/temp.*	6h/temp*	Complete data scan in 24 h	1h/temp*
a or k range	<29 W/(m.K)	0.009-3.5 W/(m.K)	<14.4 W/(m.K)	10^{-7} - $10^{-5}m^2/s$	10^{-7} - $10^{-5}m^2/s$
Sample size	3 bricks: (23x11.4X6.4) cm^3	Circular Plate:2 20-25 cm dia. 5 cm thick	2 bricks (23x11.4x6.4) cm^3	Cylinder 1.6-5.4 cm dia-meter, 3.5-14 cm long	Disk : 0.6-1.8 cm dia-meter, 0.15-0.4 cm thick

*1h/temp refers to 1 h per test temperature

2.4. MECHANICAL TESTING IN BRITTLE MATERIALS

2.4.1. HARDNESS

Hardness is a measure of the ability of a material to resist permanent surface scratching or indentation. The hardness value varies depending on the hardness test method applied. Therefore a hardness value is defined according to the method and load applied. There are several test methods commonly used in engineering i.e. Brinell test (HB), Vickers test (HV), Knoop test (HK) and Rockwell test (HR). Among those methods, Vickers hardness test (Figure 2.22) is typically used for hard materials like ceramics [Askeland, 1996; Flinn and Trojan, 1995].

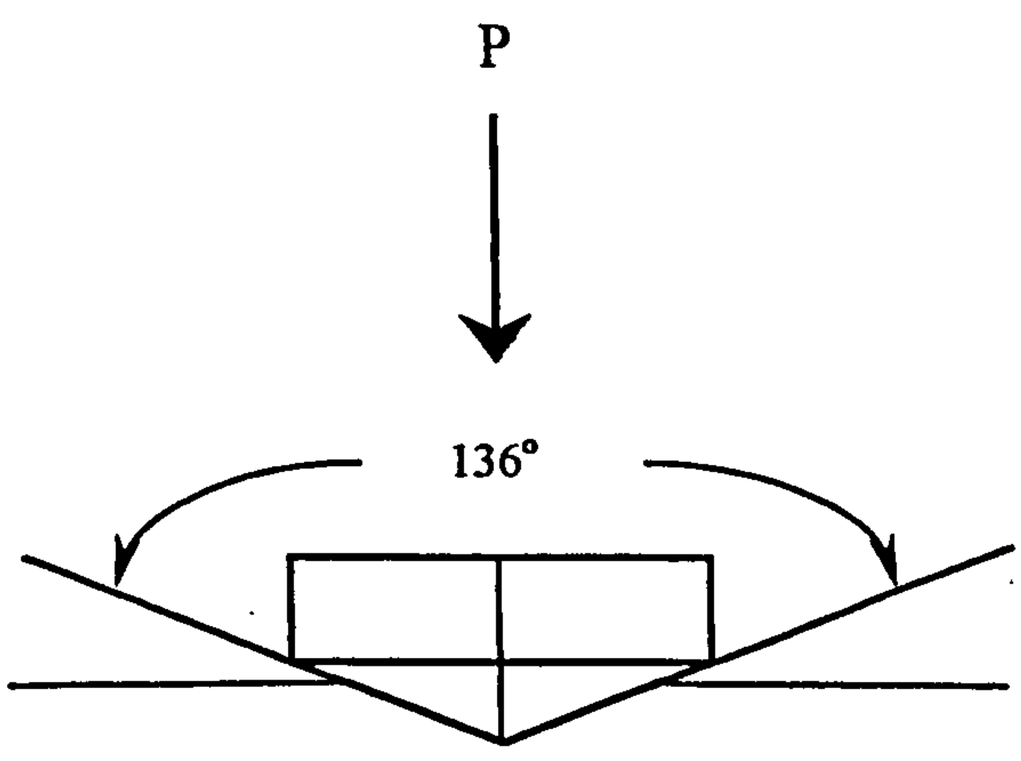

$$Hv = 1.854\frac{P}{d^2} \qquad \text{.....(2.23)}$$

where, Hv = vickers hardness, ($kg/mm^{0.5}$)
P = load applied, (kg)
d = indent diagonal, (mm)

Figure 2.22 A schematic of Vickers hardness indentation.

2.4.2. VICKERS INDENTATION FRACTURE TOUGHNESS TEST

Palmqvist in 1957 was the first who noticed surface radial cracking when sharp indentation such as Vickers or Knoop were applied to a brittle material and that it could indicate its fracture toughness. He intensively studied such phenomena on WC-Co materials. Since then many authors reported studies of using indentation fracture to predict fracture toughness of brittle materials resulting in the many indentation fracture models in the literature. Fracture toughness measurement using the Vickers indentation method has been used widely in glass and ceramics materials. It has advantages compared to conventional methods such as [Ponton and Rawlings[a], 1989]:

a. it can be applied on small samples
b. simple and easy sample preparation and measurement
c. measurement can be carried out using a conventional Vickers machine
d. quick and cost effective
e. non destructive

However it also has a number of drawbacks:

a. accuracy of the crack length measurement
b. many models found in the literature assuming the crack type is median or Palmqvist
c. diversity of equations found in the literature
d. fracture toughness value of a material measured using an indentation method or a conventional method sometimes have different values.

In general indentation fracture toughness models can be classified into two based on the crack type developed during the indentation test, i.e. radial Palmqvist cracks and radial median (halfpenny) cracks as illustrated in Figure 2.23. The first type is composed of four semi-elliptically shaped cracks formed from each indent corner, whereas the latter one consists of two half-penny shaped cracks perpendicular to the indentation plane. In some materials the Palmqvist crack type occurs when a low load Vickers indenter is applied, then at a higher load the crack type will change to median (half-penny) type [Matsumoto, 1987]. Other materials with low fracture

toughness usually exhibit median crack type [Lawn *et al*, 1980; Anstis *et al*, 1981], whereas materials with high fracture toughness such as WC-Co cermet usually exhibit the Palmqvist crack type [Shetty *et al*, 1985]. The simple way to see the crack type whether median or Palmqvist is by gradually polishing the pre-indented surface as shown in Figure 2.24. In addition, Niihara *et al* (1982) gave simple formulas to predict indentation crack type i.e. ((c/a) ≥ 2.5) for median crack type and (0.25 ≤ *l*/a ≤ 2.5) for Palmqvist crack type.

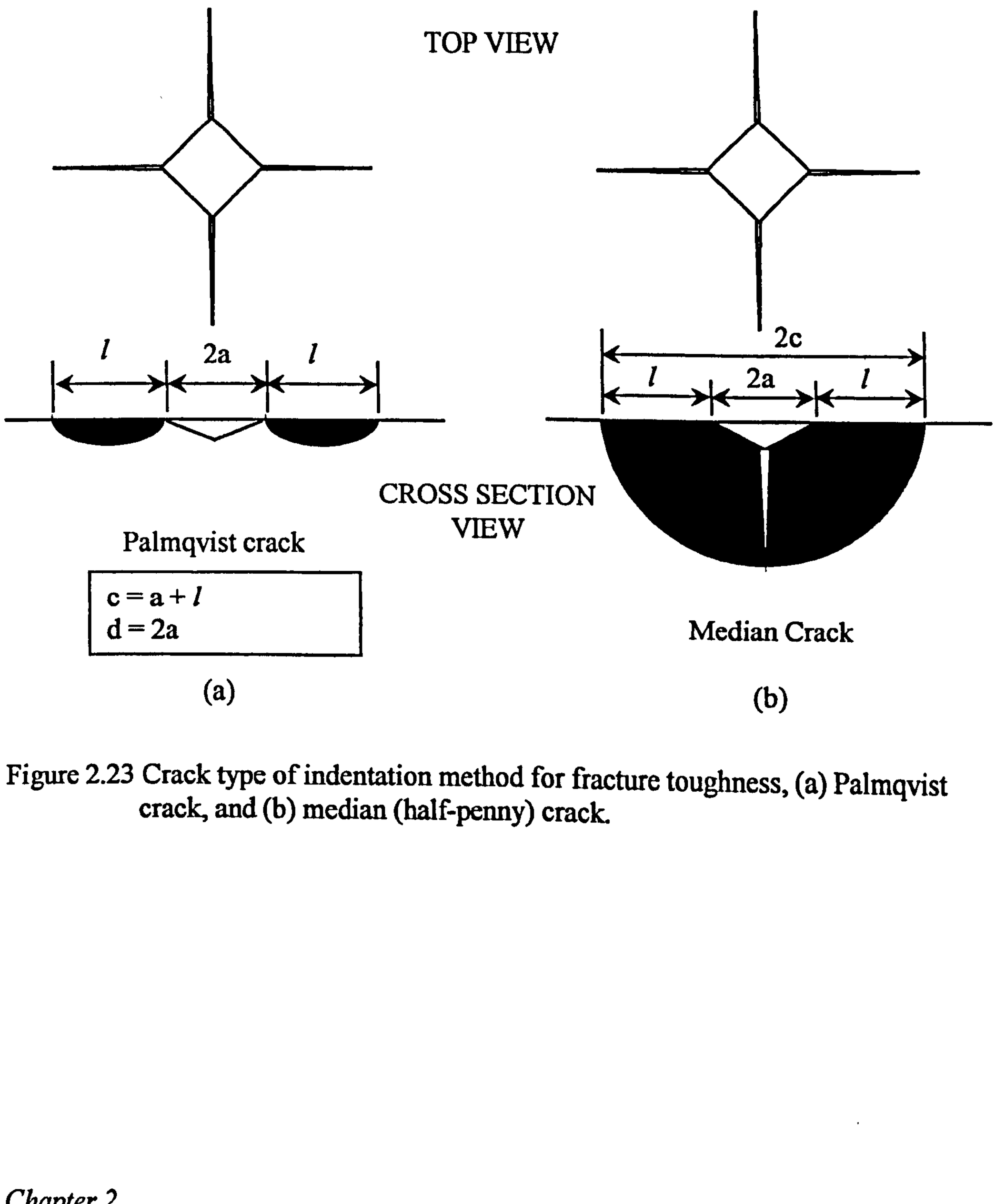

Figure 2.23 Crack type of indentation method for fracture toughness, (a) Palmqvist crack, and (b) median (half-penny) crack.

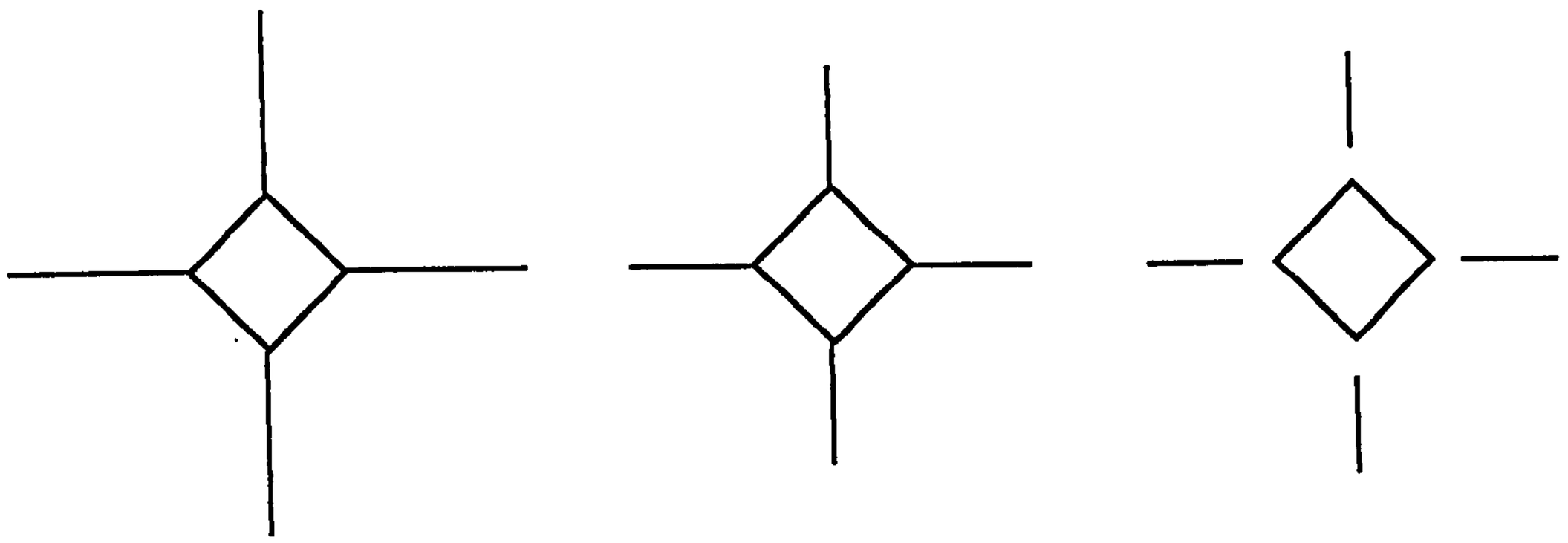

Before Polish | After Polish (Median Crack) | After Polish (Palmqvist crack)

Figure 2.24 Before and after polishing of pre-indented surface.

Many equations for indentation fracture toughness have been developed and reported by many authors. Matsumoto (1987) studied the application of some equations available in the literature to measure fracture toughness of ceria-stabilised tetragonal zirconia polycrystal. He compared the fracture toughness using a conventional method i.e. double cantilever beam (DCB) or single edge notch beam (SENB) and some equations of the indentation fracture method (see Table 2.3). He found that most values of fracture toughness calculated by indentation methods were within the ± 20 % precision of that calculated using a conventional method (DCB or SENB). Moreover, some other authors have used indentation fracture methods to measure fracture toughness of zirconia-based materials, such as Besson (1996) using the Shetty *et al* (1985) equation; Gupta *et al* (1977) and Lange[a] (1982) applied Evans and Charles (1976) equation; Tsukuma *et al* (1984), Masaki (1986) and Takano (2000) applied Niihara *et al* (1982) equation; and Mecartney (1987) used Anstis *et al* (1981) equation.

Table 2.3. Median crack and Palmqvist crack type equations

METHOD	Equation for Fracture Toughness (Kc)
MEDIAN CRACK TYPE	
Evans and Charles, 1976	$Kc = \left(\frac{F_1 H\sqrt{a}}{\phi}\right)\left(\frac{E.\phi}{H}\right)^{0.4}$
Niihara *et al*, 1982	$Kc = 0.129\left(\frac{H\sqrt{a}}{\phi}\right)\left(\frac{E.\phi}{H}\right)^{0.4}\left(\frac{c}{a}\right)^{-1.5}$ For $(c/a) \geq 2.5$
Lankford, 1982	$Kc = 0.142\left(\frac{H\sqrt{a}}{\phi}\right)\left(\frac{E.\phi}{H}\right)^{0.4}\left(\frac{c}{a}\right)^{-1.56}$
Lawn, *et al*, 1980	$Kc = 0.028\left(H\sqrt{a}\right)\left(\frac{E}{H}\right)^{0.5}\left(\frac{c}{a}\right)^{-1.5}$
Anstis, *et al*, 1981	$Kc = 0.016\left(\frac{E}{H}\right)^{0.5}\left(\frac{P}{c^{1.5}}\right)$
PALMQVIST	
Evans and Charles, 1976	$Kc = \left(\frac{F_1 H\sqrt{a}}{\phi}\right)\left(\frac{E.\phi}{H}\right)^{0.4}$
Niihara, *et al*, 1982	$Kc = 0.035\left(\frac{H\sqrt{a}}{\phi}\right)\left(\frac{E.\phi}{H}\right)^{0.4}\left(\frac{l}{a}\right)^{-0.5}$ For $0.25 \leq (l/a) \leq 2.5$
Lankford, 1982	$Kc = 0.142\left(\frac{H\sqrt{a}}{\phi}\right)\left(\frac{E.\phi}{H}\right)^{0.4}\left(\frac{c}{a}\right)^{-1.56}$
Shetty, *et al*, 1985)***	$Kc = 0.0889\left(\frac{H.P}{4l}\right)^{0.5}$

Where, E = Young's Modulus; H = Vickers Hardness ($Hv = 0.4635\ P/a^2$);
P = load on indenter; ϕ = constraint factor (≈ 3)
a = half of vickers indent diagonal; l = crack length; $c = l + a$
ν = poisson's ratio
F_1 is a function determined empirically

Note that in the original paper published by Shetty *et al*, 1985, it has been found that the exponent of π in his equation of Kc is missing. That exponent should be (5/2) [Ponton and Rawling[a], 1989; Ray and Dutta, 1999]. The complete equation then becomes:

$$\mathbf{Kc} = \left[\frac{1}{3\left(1-\upsilon^2\right)\left(2^{1/2}.\pi^{5/2}.\tan\theta\right)^{1/3}}\right]\left[\frac{\mathbf{H.P}}{4l}\right]^{1/2} \qquad \ldots\ldots\ldots\ldots\ldots\ldots\ldots (2.24)$$

Where, θ = half of Vicker indenter angle (68°)

By using ν = 0.22, Shetty *et al* (1985) rewrote the above equation:

$$\mathbf{Kc} = 0.0889\left(\frac{\mathbf{H.P}}{4l}\right)^{0.5} \qquad \ldots\ldots\ldots\ldots\ldots\ldots\ldots\ldots\ldots\ldots\ldots\ldots\ldots (2.25)$$

For ν = 0.3 (for Y-TZP), the above equation becomes:

$$\mathbf{Kc} = 0.0316.\left(\frac{\mathbf{P}}{\mathbf{a}\sqrt{l}}\right) \qquad \ldots\ldots\ldots\ldots\ldots\ldots\ldots\ldots\ldots\ldots\ldots\ldots\ldots (2.26)$$

2.4.3. STRENGTH

Three methods that can be used to measure strength of brittle materials such as ceramics, i.e. tensile test, three point bending test (TPBT), and four point bending test (FPBT) are discussed here [Flinn and Trojan, 1995; Green, 1998]. Tensile testing (Figure 2.25(a)) is the most difficult to apply to ceramics due to the difficulty and high cost of the specimen fabrication (dog-boned shape) either in a circular or rectangular cross-section. Also ceramics are very sensitive to flaws. Any flaws even of small size can propagate quickly due to low fracture toughness as is the nature of most ceramic materials. These flaws can appear during machining the specimen and/or gripping both specimen ends prior to the test. Any misalignment will also cause high stress concentration and lead to premature failure.

Alternatively bending test (flexural test) methods are preferred to measure the strength of ceramic materials. In these methods, the shearing force (SF) and bending moment (BM) that arise during testing can be determined simply using static method (statically indeterminate system) as shown in Figure 2.25(b) and 2.25(c). Specimen preparation for bending tests is much simpler than that of tensile tests.

The bending strength or flexural strength or modulus of rupture can be determined using the following equation, by assuming the specimen fails in tension:

$$\sigma = \frac{Mc}{I} \quad \ldots\ldots\ldots\ldots\ldots\ldots\ldots\ldots\ldots\ldots \quad (2.27)$$

where M is the maximum bending moment, c is the distance from the neutral axis to the lower surface of the specimen (at the maximum tensile stress) and I is the second moment of inertia. For a rectangular cross- section, $c = h/2$ and $I = bh^3/12$, where b is the width and h is the thickness. For a circular sample, $c = r$ and $I = \pi r^4/4$, where r is the radius. The maximum tensile stress (bending strength) of the above test are as follows:

Table 2.4. Equations of the maximum tensile stress on bending tests.

Cross-section type	Three-Point Bending Test	Four-Point Bending Test
Rectangular	$\sigma = \frac{3.P.L}{2b.h^2}$	$\sigma = \frac{3.P.a}{b.h^2}$
Circular	$\sigma = \frac{P.L}{\pi.r^3}$	$\sigma = \frac{2.P.a}{\pi.r^3}$

In comparison to TPBT, FPBT is preferred, because in FPBT the specimen has a larger region of maximum stress and in this region there are no shear stresses as

shown in Figure 2.25c. In TPBT, the maximum stress region is very narrow and the role of flaws is reduced because if the critical flaws are located outside this region, a bigger stress is required to break the specimen resulting in inaccurate value of strength. To get good data of measurement, attention should be given prior to testing to the accuracy of the specimen dimensions, loading geometry, friction effects at the loading points and alignment. More details about flexural tests for engineering ceramics have been reviewed by Quinn and Morrel (1991).

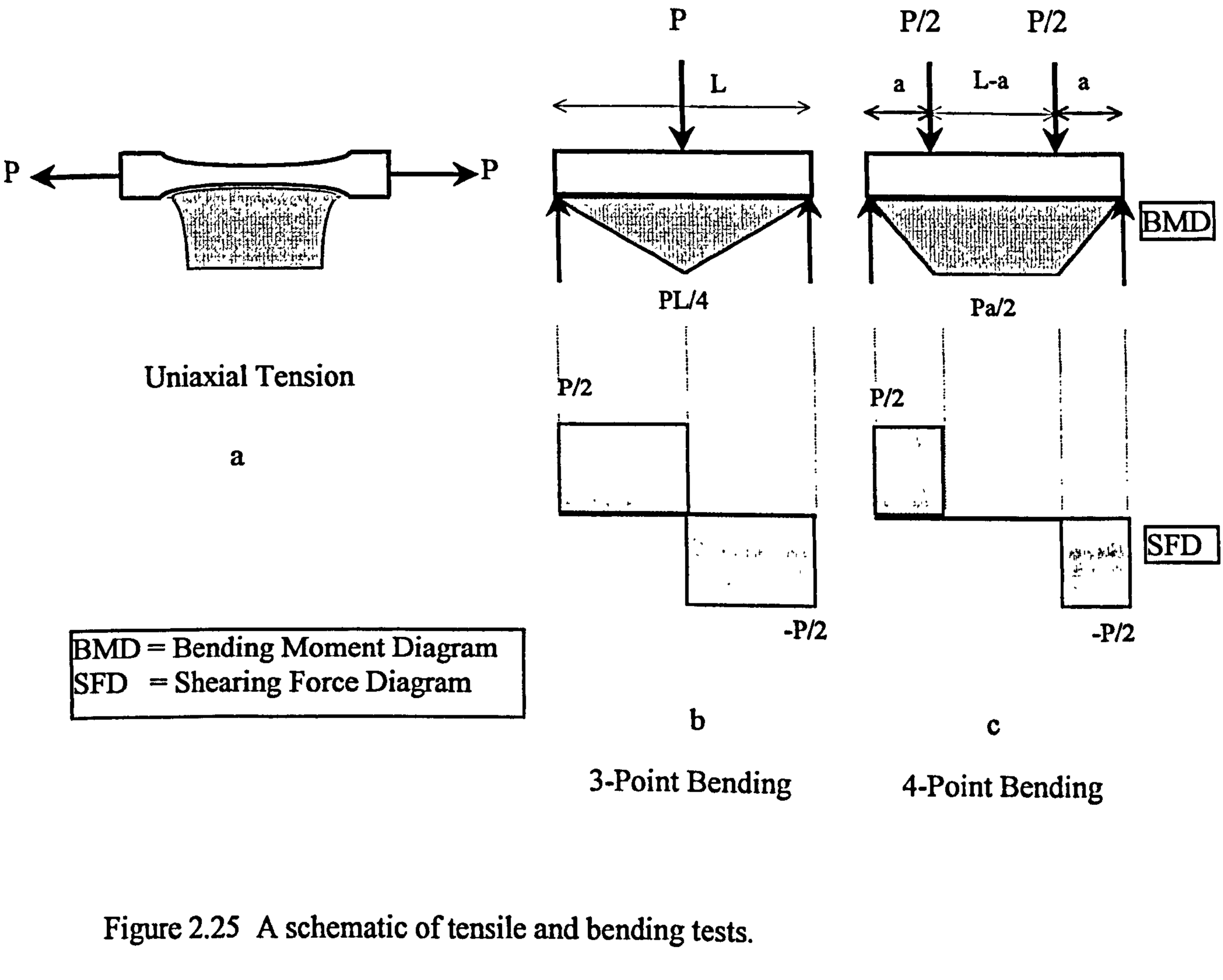

Figure 2.25 A schematic of tensile and bending tests.

CHAPTER 3

MATERIALS AND EXPERIMENTAL METHODS

3.1. MATERIALS

Matrix and reinforcement materials used in this research were supplied by Goodfellow plc UK. Zirconia stabilised with 5.4 wt%Y_2O_3 was used as matrix and chromium (Cr), iron (Fe), and stainless steel (AISI 316) were used as reinforcement. Data of the materials from the supplier are described in the table below.

Table 3.1. Data of the materials used in this study given by the supplier

MATERIAL (Code)	Density (g/cm^3)	Form and Particle size (micron)	Purity (%)	Other Elements
ZrO_2 stabilised with 5.4 wt%Y_2O_3 (ZR616010)	5.9	Powder (0.1 - 2) (mean)	93.8 (ZrO_2+HfO_2)	Y_2O_3, SiO_2, TiO_2, Al_2O_3, Fe_2O_3, CaO, Na_2O
Chromium (Cr) (CR006021)	7.19	Powder (38 max.)	99.0+	Al, C, Fe, Si
Iron (Fe) (FE00641)	7.87	Powder (6 - 8) (mean)	99.0+	C, Si, P, S, H-loss
Stainless steel AISI 316 (FE246020)	7.96	Powder (45 max.)	Fe balance, 17.8%Cr, 13.0%Ni, 2.8%Mo	C

3.2. EXPERIMENTAL METHODS

3.2.1. GREEN STAGE PREPARATION

3.2.1.1. Composition

The samples are categorised into three different composites:

i. Zirconia-matrix composite reinforced with chromium (Cr) powder

ii. Zirconia-matrix composite reinforced with iron (Fe) powder

iii. Zirconia-matrix composite reinforced with stainless steel (AISI 316) powder

Different volume percentages from 5 vol% to 25 vol% of the reinforcement are introduced into the matrix.

3.2.1.2. Mixing Process

Zirconia powder with the appropriate amount of the reinforcement was placed into a plastic container and dry-mixed for 2 hours in a turbula mixing machine.

3.2.1.3. Compacting

Green powder was compacted uni-axially in a 15 mm diameter cylindrical steel die using a pressure of 130 MPa to produce green pellets. A small cylindrical steel die of 5 mm diameter was used to prepare samples for shrinkage analysis in TMA (Thermo-Mechanical Analysis). Samples for four point bending tests were prepared using a square steel die of (30 mm x 30 mm) and pressed uni-axially with 22 MPa to produce tile samples with about 6 mm thickness. After sintering these tile samples shrank into size of about (23 mm x 23 mm x 4.5 mm) depending on the composites compositions. Bar samples of (3 mm x 4.5 mm x 23 mm) for the bending tests were cut from the tile samples.

3.2.3. SINTERING

Pressureless sintering at various temperatures was performed in a horizontal alumina tube furnace with heating and cooling controlled. The sintering of zirconia was carried out under either air or argon gas and the composites were sintered under argon gas to avoid oxidation.

3.2.4. DENSITY MEASUREMENT

The bulk density of fired samples was measured using a mercury balance displacement method and calculated with Archimedes principle as follows:

$$\rho_b = \frac{13.6 m_s}{m_s + m_R} \qquad \ldots\ldots\ldots\ldots\ldots\ldots\ldots\ldots\ldots\ldots \quad (3.1)$$

where, m_s = mass of sample in air, (g)

m_R = mass required to immerse the sample into mercury, (g)

Figure 3.1 shows the schematic of the density measurement using a mercury balance method. First, the two needles positions are adjusted in order to just touch the surface of the mercury. Second, the sample is introduced under the plastic plate and immersed by adding weights until the needles are in the same position as before i.e. touching the surface of the mercury. The density is then calculated by using Equation 3.1.

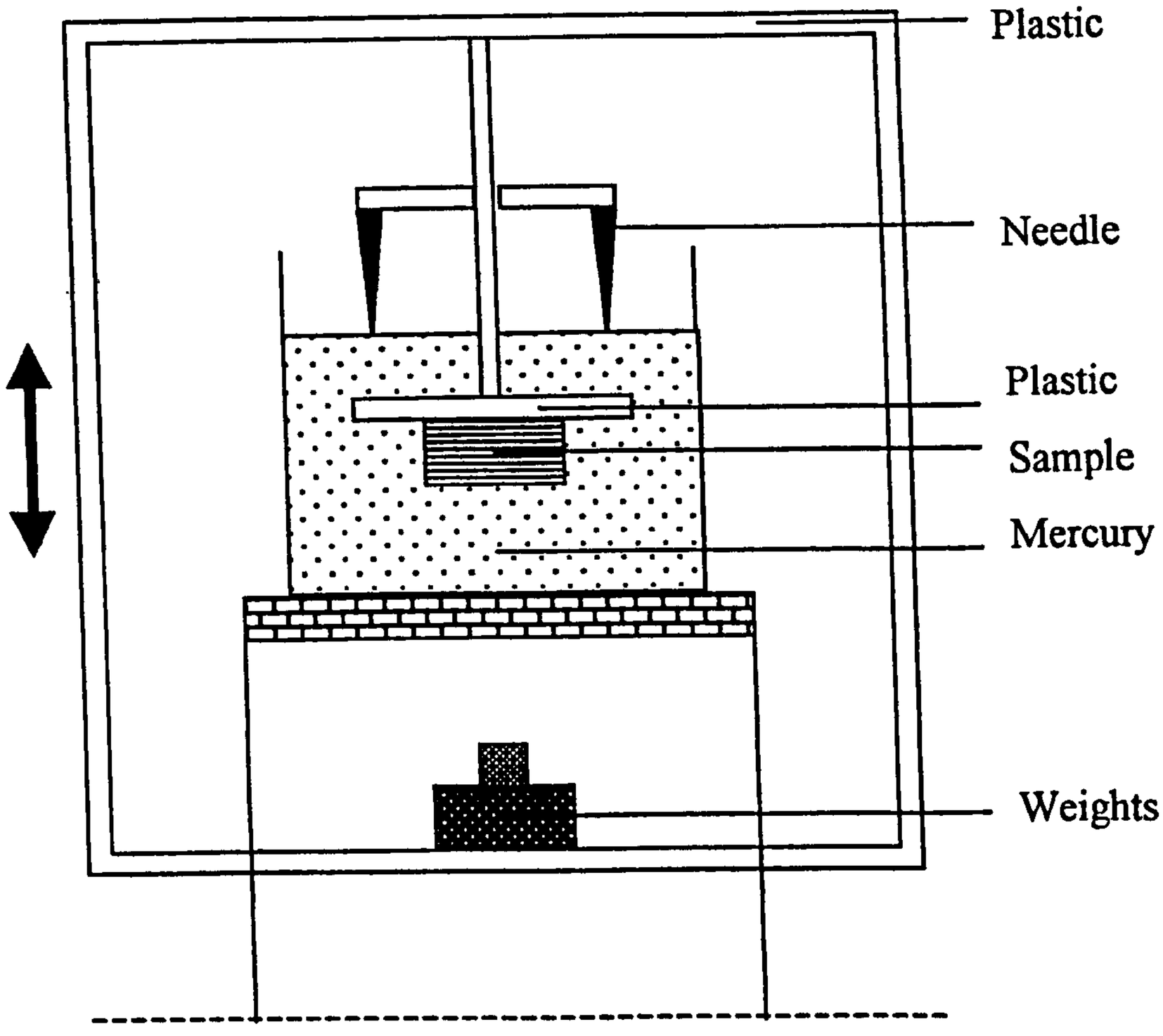

Figure 3.1. A schematic of density measurement using the mercury balance method

3.2.5. OPTICAL MICROSCOPY

Fired samples were cut into two pieces and one of them was mounted in slow setting epoxy resin. Grinding was carried out on the mounted sample using 120 μm, 75 μm and 20 μm grinding wheels. The ground sample was then polished with 9 μm and 3 μm polishing wheels with diamond suspension. An optical microscope was used to observe the polished sample using various magnifications. Pictures were taken using a camera fitted on the microscope.

3.2.6. SEM (SCANNING ELECTRON MICROSCOPY)

A SEM model JEOL 360 was used to examine the polished samples and the fracture surface of samples from four point bending tests. Some polished zirconia samples were also thermal etched in a furnace at 1450°C for 1 hour in air. Before examining under SEM the samples were coated with a thin layer of gold to improve their electrical conductivity and avoid charging effects.

3.2.7. XRD (X-RAY DIFFRACTION)

X-ray Diffraction was used to observe the phases present in samples. The X-ray source was Copper ($K_{\alpha 1}$ = 1.54057 Å, $K_{\alpha 2}$ = 1.54437 Å, and K_{α}(average) = 1.54186 Å). Scanning was carried out from 15° – 85°, with 0.05° increment and 5 seconds counting time. Lower increment and longer time were required for more precise examination at selected ranges of angle.

Each d-spacing was calculated using Bragg's law as follows:

$$2\,d\sin(\theta) = n\lambda \qquad \text{..... (3.2)}$$

where d is d-spacing (interplanar spacing), θ is half angle between the diffracted beam and the original beam direction, and λ is the wavelength of the X-rays.

3.2.8. STA (SIMULTANEOUS THERMAL ANALYSIS)

STA Thermal Sciences model STA-1640 consists of DTA (Differential Thermal Analysis) and TGA (Thermal Gravimetric Analysis), in which both thermal and mass change effects are measured concurrently on the same sample. Around 10

mg of powder was put in a small alumina crucible and placed into the STA, then heated up to a selected temperature. The sample weight during sintering can be seen on the TGA curve and the DTA curve shows whether reactions occur during sintering. The exothermic reaction is shown by peak downward at a certain temperature, whereas peak upward indicates an endothermic reaction.

3.2.9. TMA (THERMO MECHANICAL ANALYSIS)

TMA (Thermo-Mechanical Analysis) Thermal Sciences model TMA-1500 was used to observe the linear dimensional changes of sample during sintering and to measure linear thermal expansion coefficients. The instrument consists of three modules as follows:

a. Main module with furnace, sample holder and probe
b. Temperature programming facility
c. Data acquisition facility

Experiments can be carried out in a temperature range between 20°C and 1500°C under controlled atmospheres using a suitable gas flow system. The furnace temperature is accurately controlled by a temperature programming facility. Any linear dimensional changes of samples during experiment are sensed by a probe in contact with the sample. The analog signals are then received by the data acquisition module and converted into a form which can be readily interpreted and manipulated.

For shrinkage observations during sintering, samples were prepared from green powder and then uniaxially compacted in a 5-mm diameter steel die using 130 MPa pressure. The sample thickness is around 2 mm.

For linear thermal expansion coefficient measurement, a piece of sample with around 5 mm thickness was cut from a larger sintered sample.

3.2.10. THERMAL DIFFUSIVITY

A Laser Flash Apparatus (Netsch model LFA 427) was used to measure thermal diffusivity (a) of samples. With the other properties of specific heat (Cp), and density (ρ), the thermal conductivity (k) can be calculated using the following equation:

$$k(T) = a(T) \,.\, \rho(T) \,.\, Cp(T) \qquad \ldots\ldots\ldots\ldots\ldots\ldots\ldots\ldots\ldots\ldots\ldots\ldots \quad (3.3)$$

Each component in Equation (3.2) is a function of temperature (T).

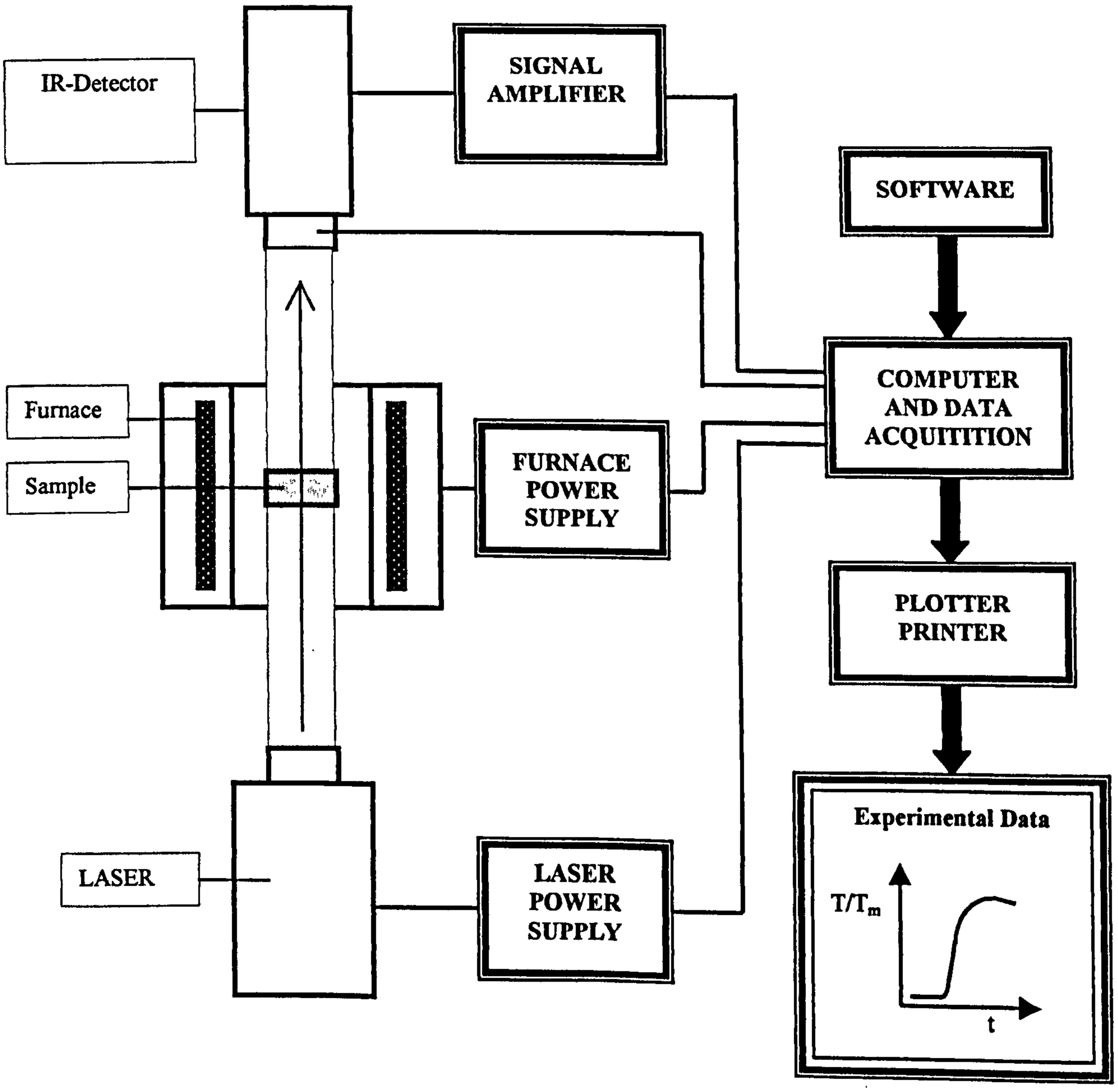

Figure 3.2. A schematic of LFA-427 system

Compared to the direct measurements of thermal conductivity such as calorimeter, guarded hot plate, and hot wire, the laser flash method has advantages such as simple sample geometry, easy sample preparation and small sample size. Further, the other advantages are applicability for a wide range of diffusivity values, excellent accuracy and reproducibility, short time measurement and a wide range of temperature.

Figure 3.2 shows the schematic of the LFA 427 system, which consists of four main components:

a. Measuring unit with furnace, laser and infra red detector
b. Controller for measuring unit
c. Power supply for laser system
d. Data acquisition system and computer

The sample is mounted on a sample holder in a carrier system, which is located in the furnace. The measurement was carried out from room temperature up to 1000°C at every 100°C in an alumina sample holder. After the sample temperature reaches a certain temperature which is determined, the laser system produces a burst of energy from a pulsed laser to the front face of the sample, resulting in homogeneous heating. The increase of relative temperature on the rear face of the sample is measured by an infra red detector. The data as a function of time is sent to a computer and then the thermal diffusivity is computed by the software using time/relative temperature increase data.

The thermal diffusivity (a) for adiabatic conditions is determined with the following equation:

$$a = 0.1388\frac{l^2}{t_{0.5}} \qquad \ldots\ldots\ldots\ldots\ldots\ldots\ldots\ldots\ldots\ldots \quad (3.4)$$

where, l : sample thickness

$t_{0.5}$: time (s) at 50% of the temperature increase

Sample size required for this measurement was around 12 mm diameter with 3 mm thickness. Translucent samples such as zirconia must be coated with a thin layer of graphite spray to avoid the laser beam transmitting trough the samples.

3.2.11. VICKERS HARDNESS (Hv) and FRACTURE TOUGHNESS (K_{IC})

Samples were cut and embedded in resin for ease in handling, grinding and polishing. Vickers hardness was carried out on a polished surface of the samples using a load of 5 kg for 15 seconds. The diagonals of indents were measured using a micrometer attached on a microscope available on the Vickers machine. The Vickers hardness was then calculated with the following equation [Green, 1998]:

$$\mathbf{Hv} = 1.854\,\mathbf{x}\,\frac{\mathbf{P}}{\mathbf{d}^2} \qquad \text{..} \quad (3.5)$$

where, Hv = Vickers hardness, kg/mm^2

P = load applied on the indenter, kg

d = mean diagonal of the indent, mm

The fracture toughness was measured using the crack-indentation method, which is produced from a Vickers indent. This method is simple and non-destructive. The equation given by Shetty *et al* (1985) was used to evaluate the fracture toughness of palmqvist-type crack (with the poisson's ratio, $\nu = 0.3$):

$$\mathbf{Kc} = 0.0316\,\mathbf{x}\,\frac{\mathbf{P}}{\mathbf{a}\sqrt{l}} \qquad \text{..........................} \quad (3.6)$$

Where a is half of the indent diagonal, and l is the length of the radial crack.

3.2.12. MICROHARDNESS

A Vickers microhardness machine was used to measure microhardness on specific parts of the samples such as the matrix, the reinforcement, and the boundary of the matrix and the reinforcement. The testing was performed using 50 g load for 5 seconds.

3.2.13. FOUR POINT BENDING TEST

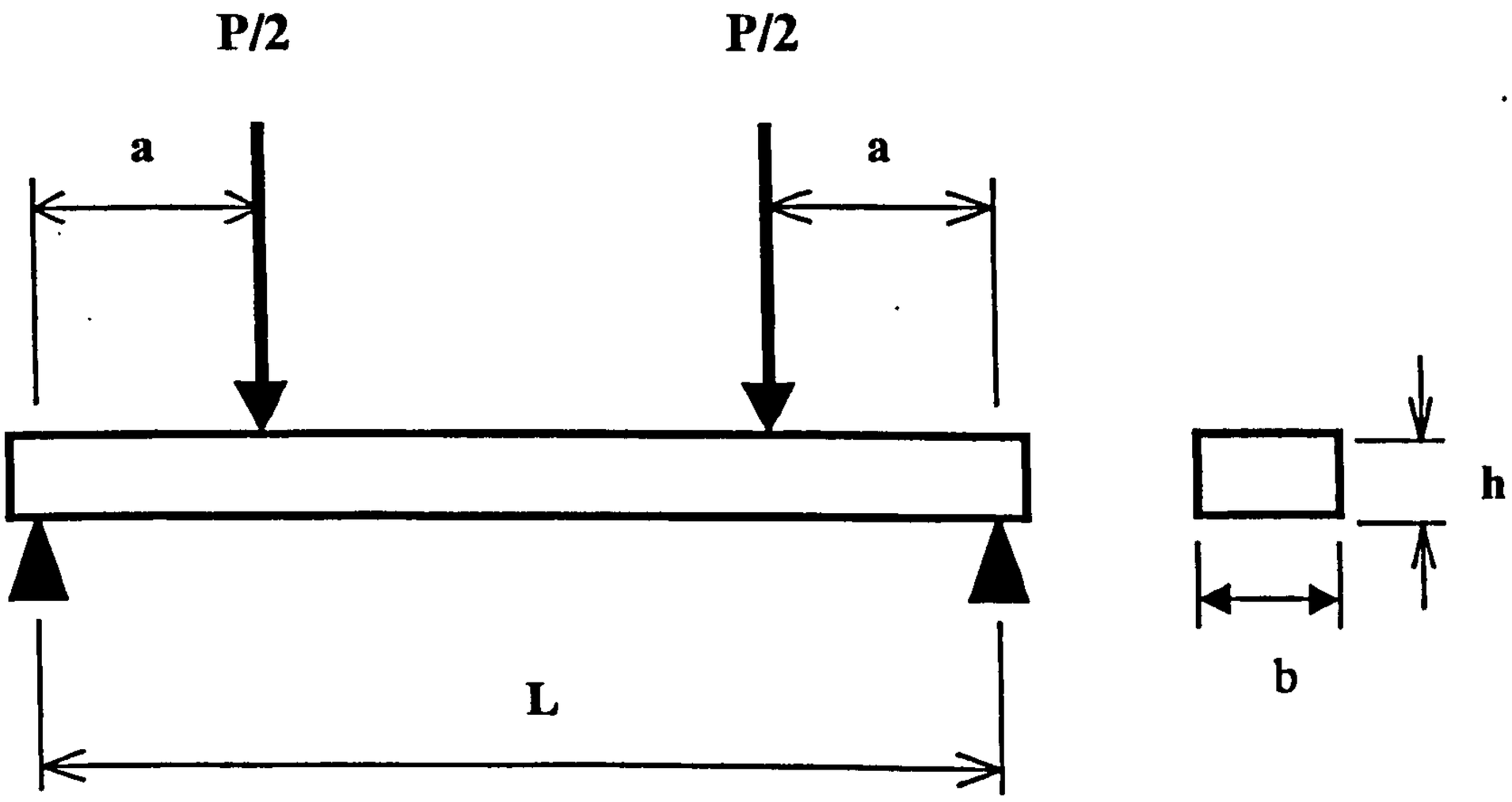

Figure 3.2. A schematic of four point bending test.

Bending strength of samples was measured using a Four Point Bending Test as shown in Figure 3.2. This test was chosen because the samples do not need to be clamped as in tensile tests where the stress caused by the clamp might generate flaws on ceramic samples making the tests invalid. Furthermore, sample preparation for a bending test is much easier and cheaper than that of for tensile tests. Four point bending tests also have the advantage over three point bending tests in that the maximum bending moment in four point bending test is distributed over a volume of

the sample remote from the support anvils. The bending strength in four point bending is calculated with the following equation:

$$\sigma = \frac{M \cdot c}{I} = \frac{3 \cdot P \cdot a}{b \cdot h^2} \qquad \text{.....(3.7)}$$

where, P = applied load, (N)

M = bending moment, (N.m), $M = P.a/2$

I = second moment of area of the cross-section, (m^4), $I = b.h^3/12$

c = distance from neutral axis to the surface, (m), $c = h/2$

a = distance from the support to the load, (m)

L = span of outer support, (m), L = 0.0020 m.

b = width of sample cross-section, (m)

h = thickness of sample cross-section, (m)

The specimens were cut from large sintered samples into pieces of about 23 mm x 3 mm x 4.5 mm dimension. Each specimen was tested in a testing machine at room temperature with a load (crosshead) speed of 0.5 mm/minute. This test was made on 6 specimens of each type of material, which is enough to give a measure of the strength of each type of material, but is not sufficient for statistical or Weibull analysis of the strength data.

3.2.14. ELECTRICAL CONDUCTIVITY

Samples with even parallel surfaces and known surface area and thickness were used for electrical resistivity/conductivity measurement. A digital multimeter was used to measure electrical resistance of the samples. The sample surface where the measurement was directed was coated using silver paint. Each terminal of the multimeter was then placed on each coated parallel surface of the sample and the

resistance was read. Six measurements were performed on each sample on different location of the sample surfaces. The electrical resistivity was then calculated using the following equation [Callister, 1994]:

$$\rho = \frac{\mathbf{R.A}}{\mathbf{L}} \qquad \text{.....(3.8)}$$

$$\sigma = \frac{1}{\rho} \qquad \text{.....(3.9)}$$

where, ρ = electrical resistivity, (ohm.m)

σ = electrical conductivity, $((\text{ohm.m})^{-1})$

R = resistance, ohm

A = cross section area, m

L = thickness, m.

CHAPTER 4

ZIRCONIA:

PROCESSING, CHARACTERISATION AND PROPERTIES

In the study of zirconia ceramic matrix reinforced with metals, understanding zirconia as the matrix is important before observing the effect of reinforcements. This chapter describes and discusses the experimental results of zirconia stabilised with 5.4 wt% or 3 mol% yttria including processing, characterising and properties (mechanical and thermal). Pressureless sintering of this material in air is very common as reported by many authors. In this present work, zirconia was pressureless sintered in air and argon. In the processing of the composites of zirconia reinforced with metals that will be discussed in the next chapters, argon gas was chosen as sintering atmosphere to avoid oxidation. Therefore pressureless sintering of zirconia in argon was performed first to study the matrix of the composites.

4.1. GREEN POWDER AS-RECEIVED

Zirconia powder used in this experiment has compositions as described in Table 4.1. Zirconia stabilised with 5.4 wt% or 3 mol% yttria is known as 3Y-TZP (Tetragonal Zirconia Polycrystal with 3 mol% yttria stabiliser). X-ray examination of the zirconia green powder (as-received) shows tetragonal (t) phase and monoclinic (m) phase as indicated in Figure 4.1. The d-spacing of the peaks were calculated using Bragg's law (Equation 3.2), which were carried out using software within the XRD equipment. The results are tabulated in Table 4.2.

Table 4.1. Composition of as-received zirconia given by the supplier.

Component	ZrO_2 + HfO_2	Y_2O_3	SiO_2	TiO_2	Al_2O_3	Fe_2O_3	Na_2O	CaO
Weight (%)	93.8	5.4	0.11	0.12	0.25	0.003	0.03	0.06
Mol (%)	95.8013	3.0326	0.2322	0.1903	0.3172	0.0025	0.0609	0.1358

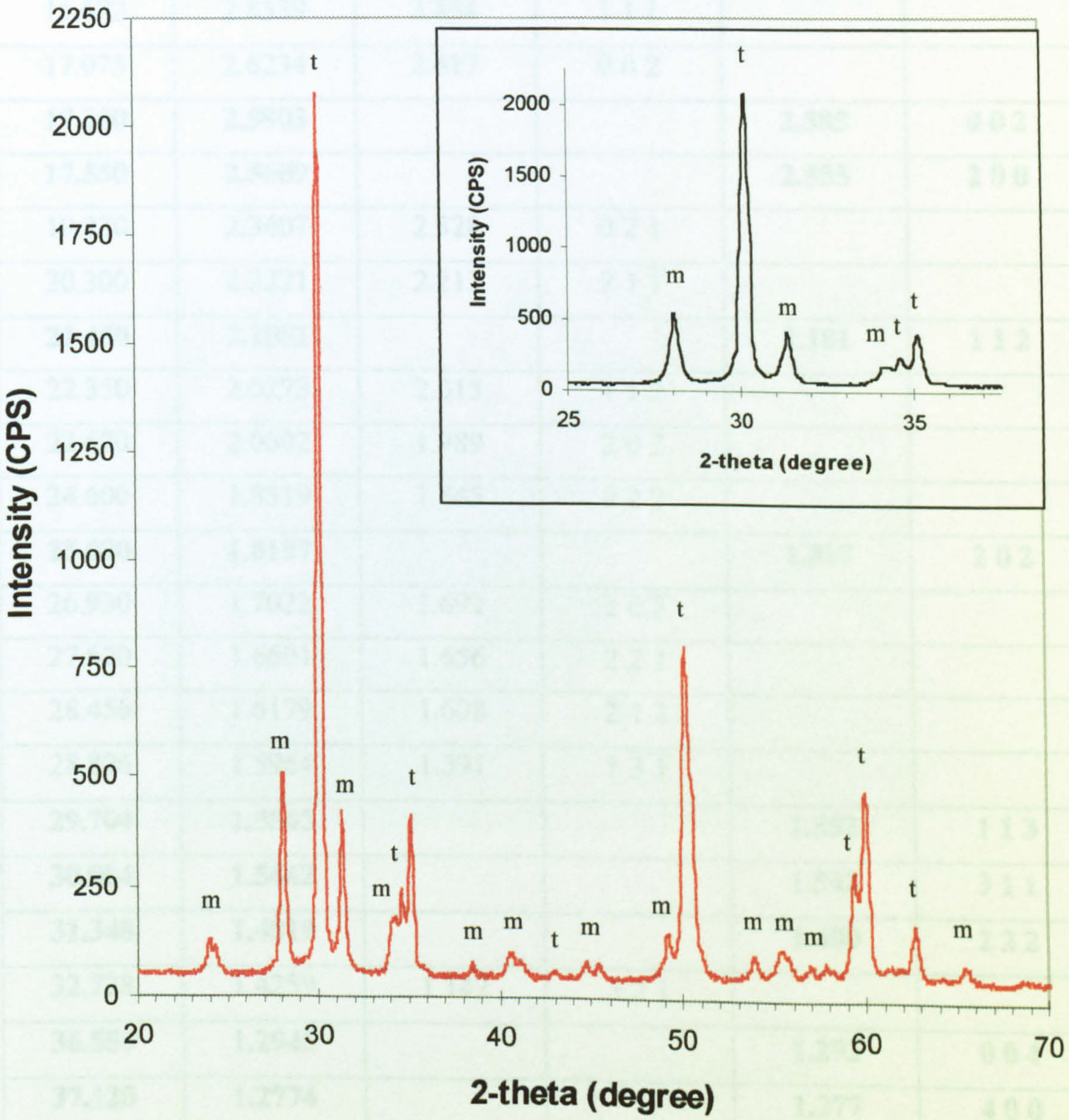

Figure 4.1 X-ray diffraction analysis of 5.4 wt% Y_2O_3 - ZrO_2 green powder (as-received).

Table 4.2. X-Ray diffraction results of as received zirconia.

Angle (theta) deg.	Measured d-spacing (A)	Monoclinic ZrO_2		Tetragonal ZrO_2	
		d-spacing (A)	h k l	d-spacing (A)	h k l
12.000	3.7048	3.690	0 1 1		
12.144	3.6707	3.630	1 1 0		
14.052	3.1751	3.160	1 1 $\bar{1}$		
15.072	**2.9647**			**2.964**	**1 1 1**
15.672	2.8539	2.834	1 1 1		
17.075	2.6234	2.617	0 0 2		
17.300	**2.5903**			**2.585**	**0 0 2**
17.550	**2.5609**			**2.555**	**2 0 0**
19.230	2.3407	2.328	0 2 1		
20.300	2.2221	2.213	2 1 $\bar{1}$		
21.450	**2.1081**			**2.101**	**1 1 2**
22.350	2.0273	2.015	1 1 2		
22.670	2.0002	1.989	2 0 2		
24.600	1.8519	1.845	0 2 2		
25.080	**1.8187**			**1.817**	**2 0 2**
26.930	1.7022	1.691	2 0 $\bar{2}$		
27.670	1.6601	1.656	2 2 1		
28.456	1.6179	1.608	2 1 2		
28.876	1.5964	1.591	1 3 $\bar{1}$		
29.704	**1.5545**			**1.552**	**1 1 3**
30.004	**1.5442**			**1.542**	**3 1 1**
31.348	**1.4819**			**1.480**	**2 2 2**
32.728	1.4259	1.142	3 2 1		
36.550	**1.2945**			**1.292**	**0 0 4**
37.120	**1.2774**			**1.277**	**4 0 0**

The proportion of the monoclinic phase of a mixture of monoclinic and tetragonal in zirconia system can be estimated using the intensities of the diffraction patterns from the t(111), m(111), and m($11\bar{1}$) reflection as follows (Garvie and Nicholson, 1972; Masaki, 1986):

$$\mathbf{m}(\%) = \frac{\mathbf{m}(111) + \mathbf{m}(11\bar{1})}{\mathbf{t}(111) + \mathbf{m}(111) + \mathbf{m}(11\bar{1})} \mathbf{x}100\% \qquad \ldots\ldots\ldots\ldots\ldots\ldots\ldots\ldots \quad (4.1)$$

Using equation 4.1 the proportion of monoclinic at green stage powder is 30%.

The particle size of the powder was small, ranging from 0.1 - 2 micron as reported by the supplier and can be seen in Figure 4.2.

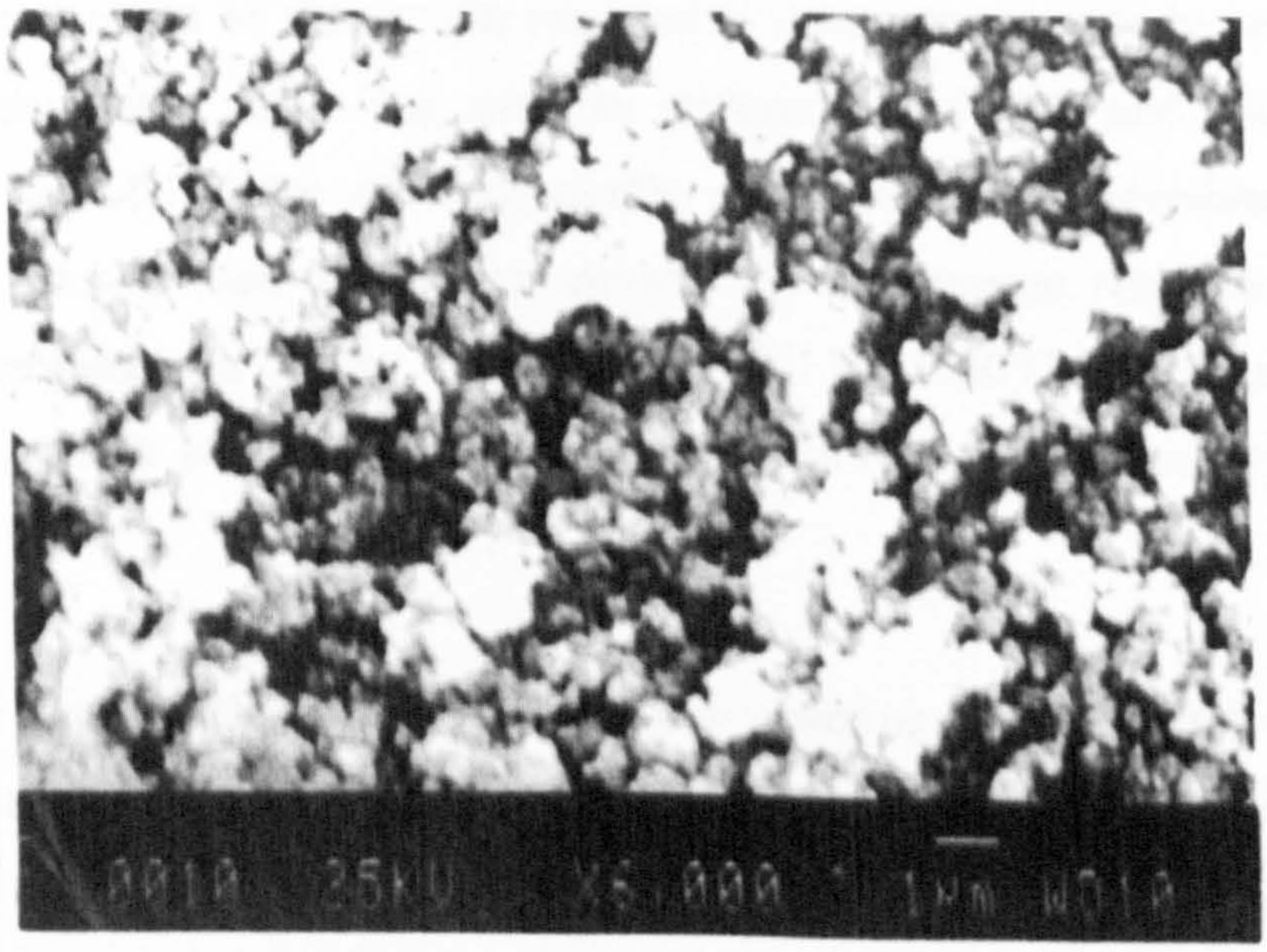

Figure 4.2. SEM of as-received zirconia

4.2. PRESSURELESS SINTERING

4.2.1. DENSITY AND DENSIFICATION

Zirconia samples were pressureless sintered under air and argon gas atmosphere at various temperatures for 1 hour with a heating rate 10 °C/minute and a cooling rate around 10 °C/minute. The theoretical density of the samples after sintering is shown in Figure 4.3. It can be seen in that Figure that samples sintered at 1400°C, 1450°C and 1500°C resulted in more than 99% theoretical density. The increase of density with temperature up to 1450°C is due to densification process.

The technique used to measure the density of the samples was the mercury balance method (see Figure 3.1). This method is not very accurate, but with care during measurement such as avoiding air trapped around the sample during immersion to mercury, positioning accurately of the two needles of the balance, and precise measurement of the weight required to immerse the sample into mercury it can give reasonable data. The samples sintered at 1450°C and 1500°C can be considered as fully dense or theoretically dense samples. Therefore sintering at 1450°C for 1h was used to produce samples for this present research. In addition, sintering temperatures in the range of 1400°C to 1500°C are usually used for fabricating Y-TZP [Gupta, 1978; Ruhle *et al*, 1984; Matsui *et al*, 1984; Masaki, 1986].

The densification process of samples sintering at 1450°C for 1h in air and argon was examined using TMA equipment and the results can be seen in Figure 4.4(a) and 4.4(b) respectively. There is no significant effect of air and argon gas atmosphere on the density and densification process. It can be seen in Figure 4.4(a) that the sample shrinks slightly up to 300°C due to removal of moisture and is followed by expansion of 1.5% up to 1100°C. From 1100°C the sample shrinks quickly on further heating up to 1450°C (21.5%) where the maximum densification rate occurs at temperature of 1425°C. A further shrinkage of (3.7%) occurs during isothermal holding at 1450°C. So the final shrinkage of the sample at sintering

temperature of 1450°C for 1 hour in air is 23.7%. A similar behaviour occurs on a sample sintered in argon for the same sintering temperature and time (the final shrinkage is 22.7%). It can be seen in Figures 4.4(a) and 4.4(b) that the desification process is mainly influenced by the heating process (~85% of the total densification) and a little further densification during isothermal holding at 1450°C (~15% of the total densification).

It was beyond the scope of this study to investigate whether it is solid state or liquid phase sintering, but the high rate of densification as seen in Figures 4.4(a) and 4.4(b) suggest it could be a liquid phase sintering mechanism. In addition, the presence of impurities such as Al_2O_3 and SiO_2 may contribute to the liquid phase sintering as also reported by Mecartney (1987) on pressureless sintering of Y-TZP at 1400°C and Besson (1996) on pressureless and hot-pressed sintering of 3Y-TZP at 1450°C.

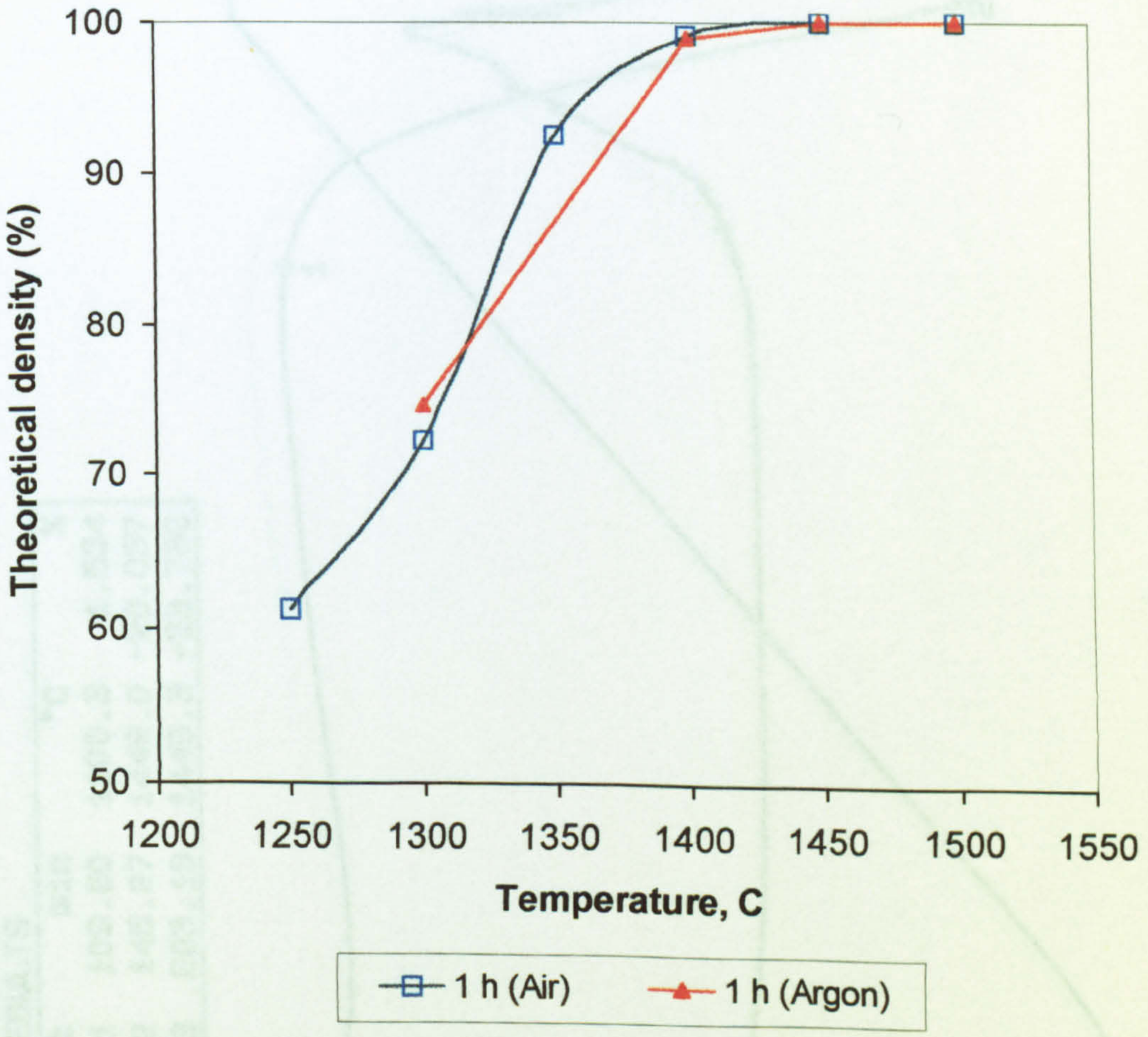

Figure 4.3. Theoretical density of zirconia samples sintered in air and argon gas for 1 hour.

TMA 1500 *(VERSION V5.12)*

SMP ID: ZrO_2 RUN ID: MWW-23 SIZE: 2.123 mm OPERATOR: MUH GAS: AIR

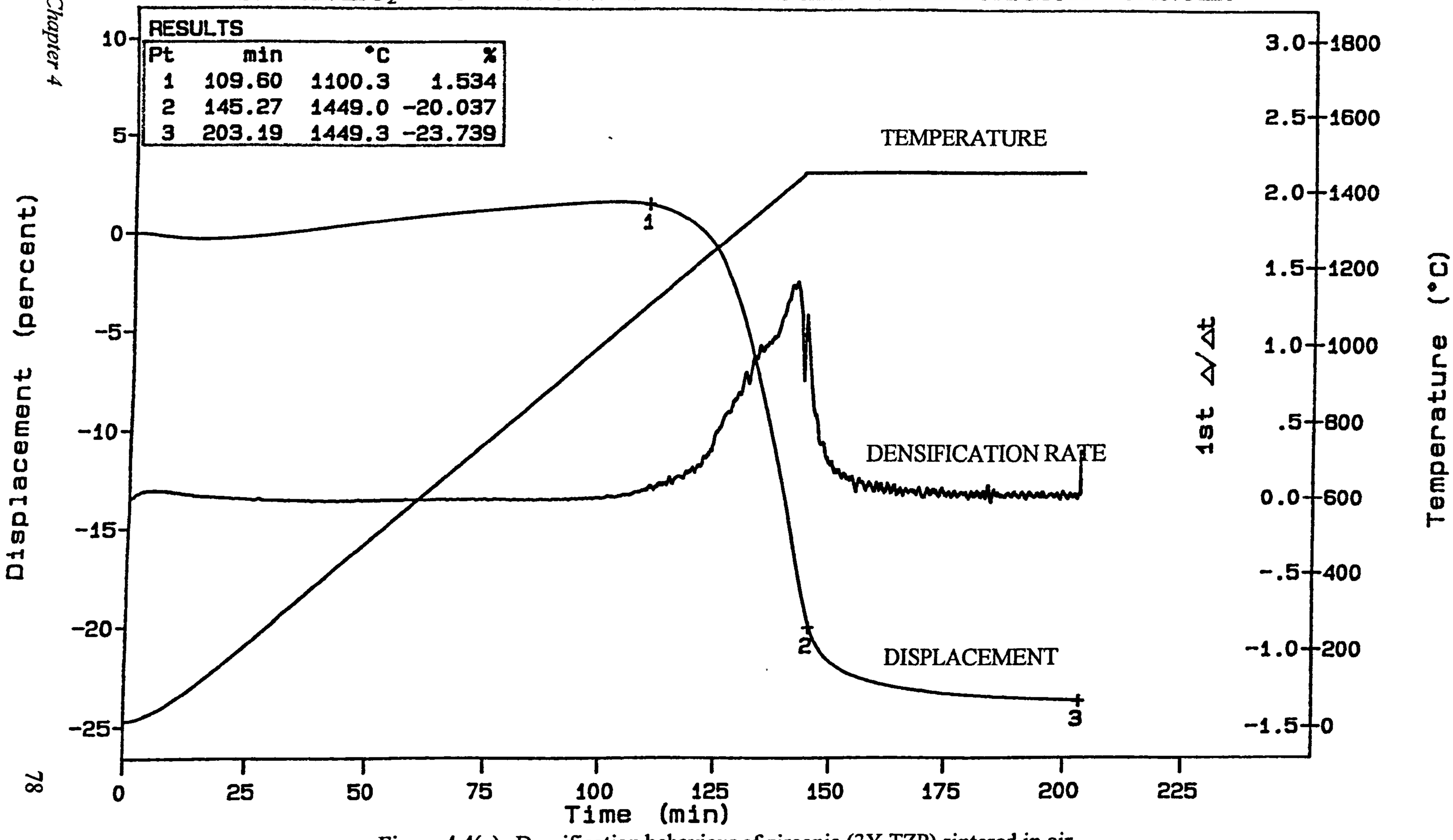

Figure 4.4(a) Densification behaviour of zirconia (3Y-TZP) sintered in air

TMA 1500 *(VERSION V5.12)*

SMP ID: ZrO_2 RUN ID: MWW-15 SIZE: 2.050 mm OPERATOR: MUH GAS: ARGON

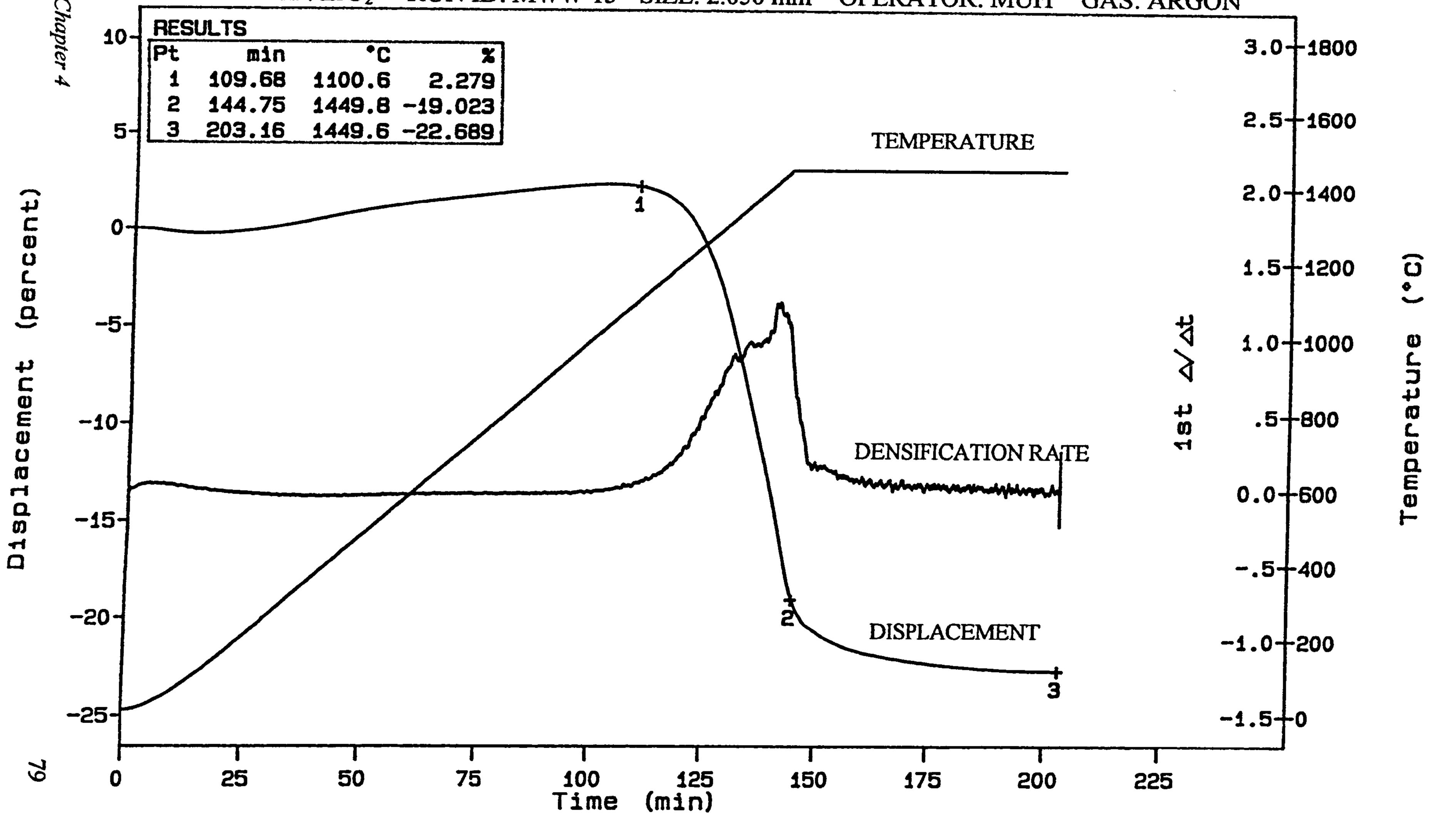

Figure 4.4(b) Densification behaviour of zirconia (3Y-TZP) sintered in argon

4.2.2. PHASE IDENTIFICATION/X-RAY ANALYSIS

X-ray diffraction analysis was performed on as-fired zirconia samples pressureless sintered at 1450°C for 1 h in argon and air as shown in Figures 4.5(A) and 4.5(B), respectively. The samples were scanned at angles between 15° and 85° with an angle increment 0.05° and 5 seconds of counting time. Each d-spacing was calculated using Bragg's law (Equation 3.2 in Chapter 3) using the software within the equipment. The references of d-spacing data used in this analysis are presented in Figure 4.6. It has been found in the literature that there are several data of d-spacing of tetragonal zirconia, two standard data of tetragonal zirconia that match well with this present study are shown in Figure 4.6. The matching between the results and the standard data are presented in Table 4.3.

Table 4.3 XRD results of 3Y-ZrO2 sintered at 1450° for 1h in Argon

Angle (theta) (degree)	Measured d-spacing (Å) (experiment)	Tetragonal ZrO_2 (see Figure 4.6)	
		d-spacing (Å)	h k l
15.075	2.9641	2.964	1 1 1
17.290	2.5917	2.585	0 0 2
17.550	2.5609	2.555	2 0 0
21.480	2.1081	2.101	1 1 2
25.080	1.8187	1.817	2 0 2
25.280	1.8082	1.806	2 2 0
29.630	1.5580	1.552	1 1 3
30.000	1.5444	1.542	3 1 1
31.360	1.4814	1.480	2 2 2

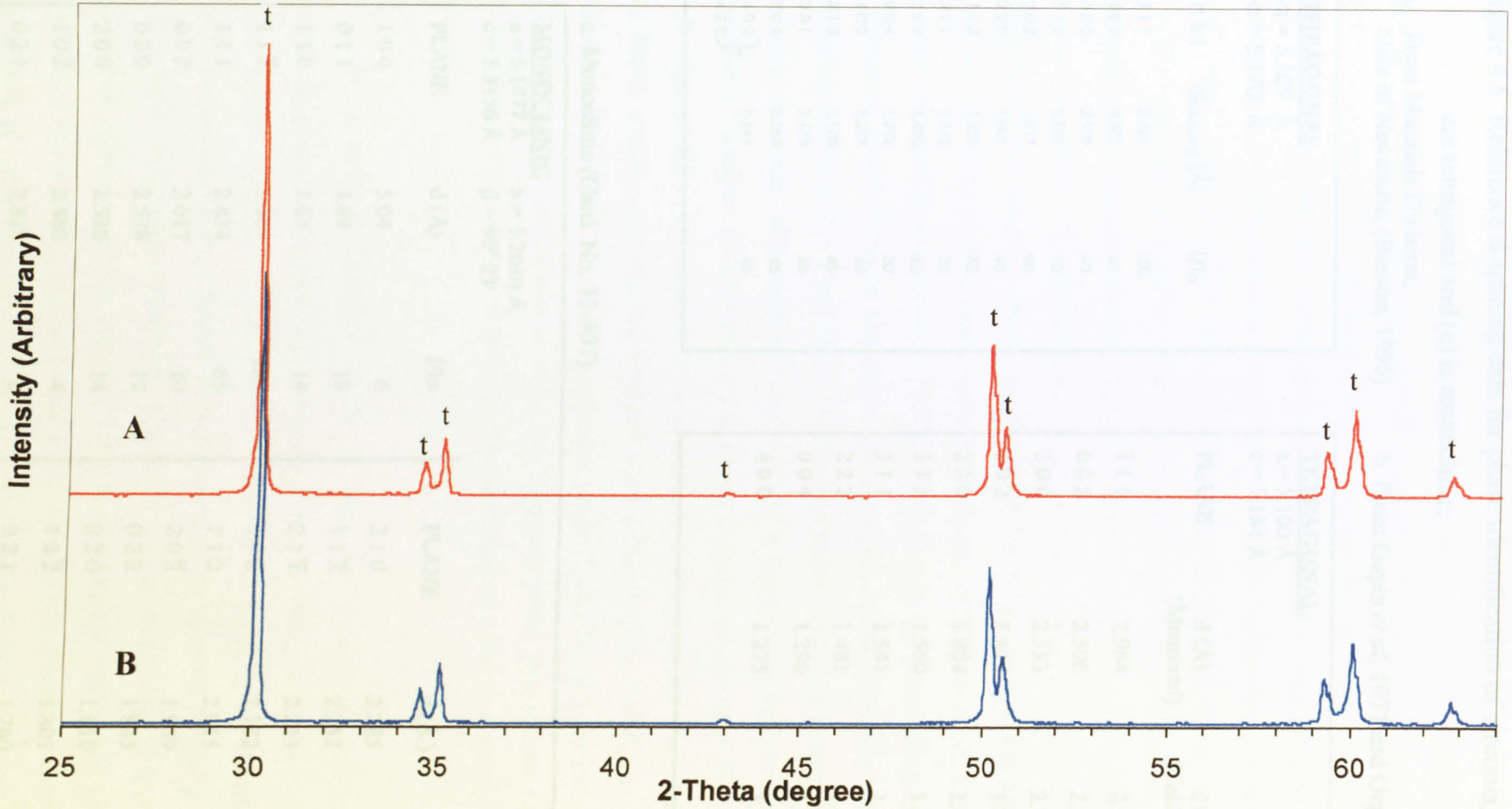

Figure 4.5 X-ray diffraction plot of as-fired zirconia (3Y-TZP) sintered at 1450°C for1h in argon (A), and air (B).

Figure 4.6 Reference d-spacing data for phase identification of zirconia, (a) and (b) are tetragonal and (c) is monoclinic.

a. From Materials Division, Univ of Newcastle, (Besson, 1996)

TETRAGONAL
a = 5.109 Å
c = 5.170 Å

h k l	$d_{spacing}$ (Å)	I/Io
1 1 1	2.964	100
0 0 2	2.585	45
2 0 0	2.555	60
1 1 2	2.101	10
2 0 2	1.817	90
2 2 0	1.806	60
1 1 3	1.552	45
3 1 1	1 542	70
2 2 2	1.480	45
0 0 4	1.292	30
4 0 0	1.277	45
3 1 3	1.178	45
3 3 1	1.173	45
2 0 4	1.153	45
4 0 2 / 4 2 0	1.144	45

b. From Gupta *et al*, 1977 and Gupta, 1978

TETRAGONAL
a = 5.100 Å
c = 5.184 Å

PLANE	d (Å) (Measured)	d (Å) (Calculated)
1 1 1	2.964	2.960
0 0 2	2.596	2.592
2 0 0	2.553	2.550
2 0 2	1.819	1.818
2 2 0	1.804	1.803
1 1 3	1.560	1.556
3 1 1	1.541	1.540
2 2 2	1.481	1.480
0 0 4	1.296	1.296
4 0 0	1.275	1.275

c. Monoclinic (Card No. 13-307)

MONOCLINIC
a = 5.1477 Å b = 5.2030 Å
c = 5.3156 Å β = 99° 23'

PLANE	d (Å)	I/Io	PLANE	d (Å)	I/Io
1 0 0	5.04	6	2 1 0	2.285	2
0 1 1	3.69	18	1 1 $\bar{2}$	2.252	4
1 1 0	3.63	14	2 1 $\bar{1}$	2.213	14
1 1 $\bar{1}$	3.16	100	1 0 2	2.182	6
1 1 1	2.834	65	1 1 2	2.015	8
0 0 2	2.617	20	2 0 $\bar{2}$	1.989	8
0 2 0	2.598	12	0 2 2	1.845	18
2 0 0	2.538	14	2 2 0	1.818	12
1 0 $\bar{2}$	2.488	4	1 2 $\bar{2}$	1.801	12
0 2 1	2.328	6	2 2 1	1.780	6

The results of the experiment show tetragonal phase d-spacing that are in good agreement with the d-spacing data for tetragonal zirconia phase given by the Materials Division of the University of Newcastle [Besson, 1996] and Gupta *et al* (1977) or Gupta (1978). Although 3Y-TZP is classified as tetragonal zirconia, some researchers reported that some amount of cubic phase was present in varying amounts such as 37% (samples contained 5.4 wt% Y_2O_3 sintered at 1600°C) [Ruhle *et al*, 1984]; 18% (3Y-TZP - hot-pressed at 1450°C) [Besson, 1996]; small amount (3Y-TZP sintered at 1600°C) [Lange[a], 1982]; 0% (3Y-TZP sintered at 1350°C) [Haberko and Pampuch, 1983]. These different findings can be understood since there are a number of contradictions in the literature regarding to the position of tetragonal (t) and cubic (c) phase boundaries in the ZrO_2 - Y_2O_3 phase diagram in the range of 1300°C to 1600°C (see Figure 2.3) [Scott, 1975; Ruh *et al*, 1984; Ruhle *et al*, 1984; Nettleship and Stevens, 1987]. According to the phase diagram, sintering temperature also influences the phase composition. In addition, the small angular difference between $(111)_t$ and $(111)_c$ diffraction peaks results in an apparent overlap, so that a slow scan with small increment angle is required to analyse such material. Quantitative analysis of polymorphic zirconia is therefore not easy [Schmid, 1987]. High angle analysis is required to do quantitative analysis, but the peaks are weak and broad making quantitative analysis also difficult [Lee, 1994]. In this present work slow scan with a very small increment angle (0.003°) and 5 seconds of counting time was carried out. Some of the slow scanned peaks are shown in Figure 4.7 indicating that only tetragonal peaks are present and no cubic peaks are found in this material.

In as-sintered samples, there is also no monoclinic phase. However monoclinic phase can be found in samples after a mechanical stress is applied. This is due to the presence of metastable tetragonal at room temperature which can transform to monoclinic. Careful work/machining on sintered samples is necessary so that such transformation can be minimised during preparation. Figure 4.8 shows monoclinic peaks on some samples after a mechanical stress has been applied. Mechanical stress during cutting samples may cause t - m transformation. In samples that are cut at low cut feeding (15 μm/s), low force and 3000 rpm speed monoclinic

phase is not found (Figure 4.8(B)). However, at a higher cut feeding (20 μm/s), monoclinic phase appears (Figure 4.8(A)). It also appears on the tension surface of fracture samples after four point bending tests (Figure 4.8(C)). The metastable tetragonal that can be retained at room temperature will improve both fracture toughness and strength of zirconia by stress-induced transformation [Garvie *et al*, 1975].

The amount of transformation from metastable tetragonal to monoclinic is influenced by the amount of yttria and the grain size of the tetragonal phase [Lange[a], 1982].

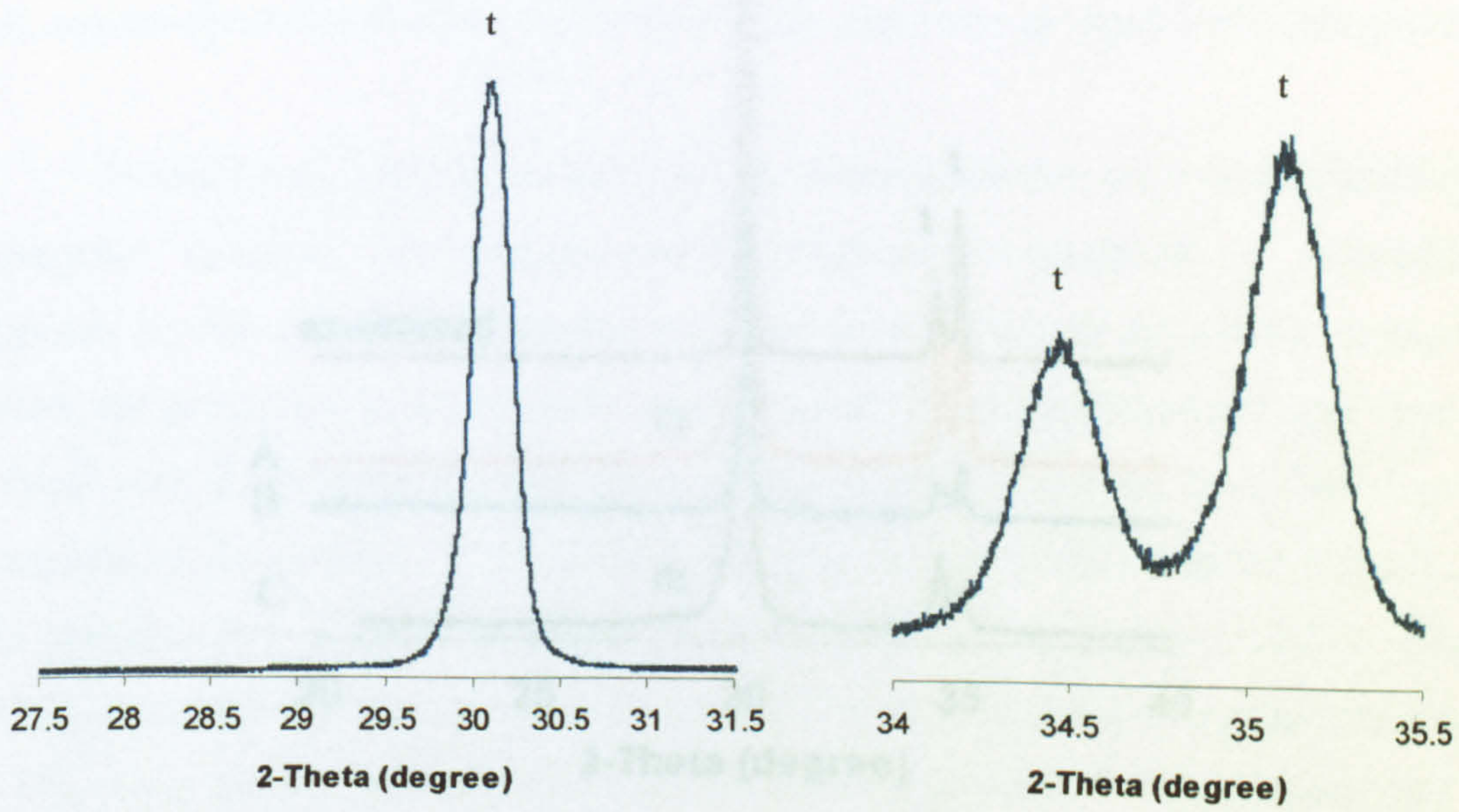

Figure 4.7 XRD plot at slow scan of the sample in Figure 4.2(A)

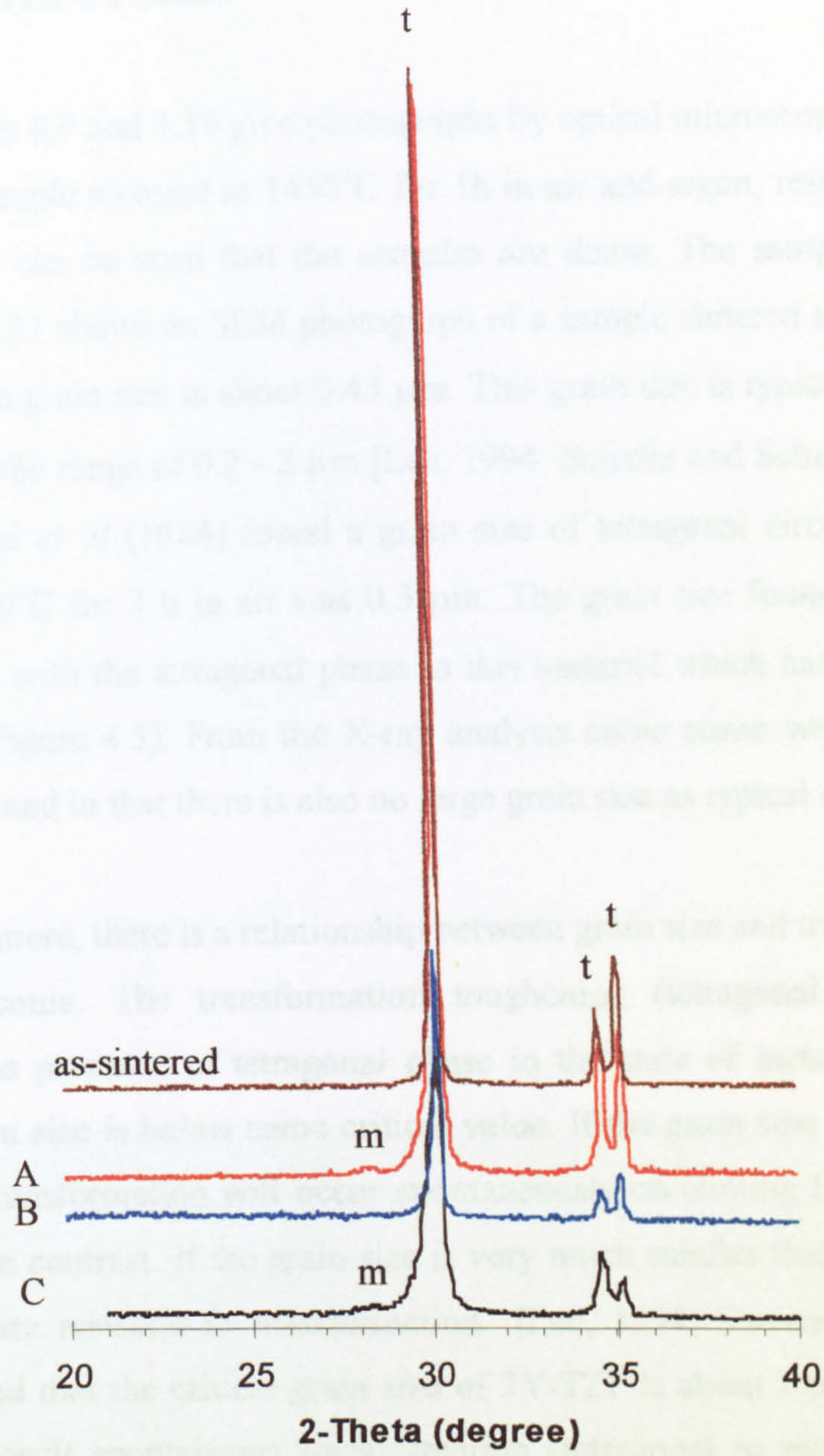

Figure 4.8 Effect of mechanical stress to phase transformation, (A) after cutting at 3000 rpm, 20 μm/s feeding speed with low force, (B) after cutting at 3000 rpm, 15 μm/s feeding speed with low force, and (C) at tension surface near the fracture after bending tests.

4.2.3. MICROSTRUCTURES

Figures 4.9 and 4.10 give photographs by optical microscopy of a polished and unetched sample sintered at 1450°C for 1h in air and argon, respectively. From those Figures it can be seen that the samples are dense. The samples have white colour. Figure 4.11 shows an SEM photograph of a sample sintered at 1450°C for 1h in air. The mean grain size is about 0.45 μm. This grain size is typical for tetragonal zirconia, i.e. in the range of 0.2 - 2 μm [Lee, 1994; Schafer and Schubert, 1998]. For example, Matsui *et al* (1984) found a grain size of tetragonal zirconia in 3Y-TZP sintered at 1400°C for 3 h in air was 0.5 μm. The grain size found in this present work coincides with the tetragonal phase in this material which has been examined using X-rays (Figure 4.5). From the X-ray analysis cubic phase was not found and this was confirmed in that there is also no large grain size as typical of cubic phase.

Furthermore, there is a relationship between grain size and transformability of tetragonal zirconia. The transformation toughening (tetragonal to monoclinic) depends on the presence of tetragonal phase in the state of metastable tetragonal where the grain size is below some critical value. If the grain size is larger than the critical size, transformation will occur spontaneously on cooling from the sintering temperature. In contrast if the grain size is very much smaller than the critical size, the particles are resistant to transformation [Lee, 1994; Stevens, 1994]. Lange[a] (1982) reported that the critical grain size of 3Y-TZP is about 1 micron (see Figure 2.11). As a result spontaneous transformation (tetragonal to monoclinic) did not occur on cooling during sample fabrication yielding no monoclinic phase as shown by the x-ray results in Figure 4.5. However, since the mean grain size (about 0.45 micron) is below the critical grain size (1 micron), transformation from tetragonal to monoclinic may occur when an appropriate mechanical stress is applied as discussed in Section 4.2.2 and shown in Figure 4.8.

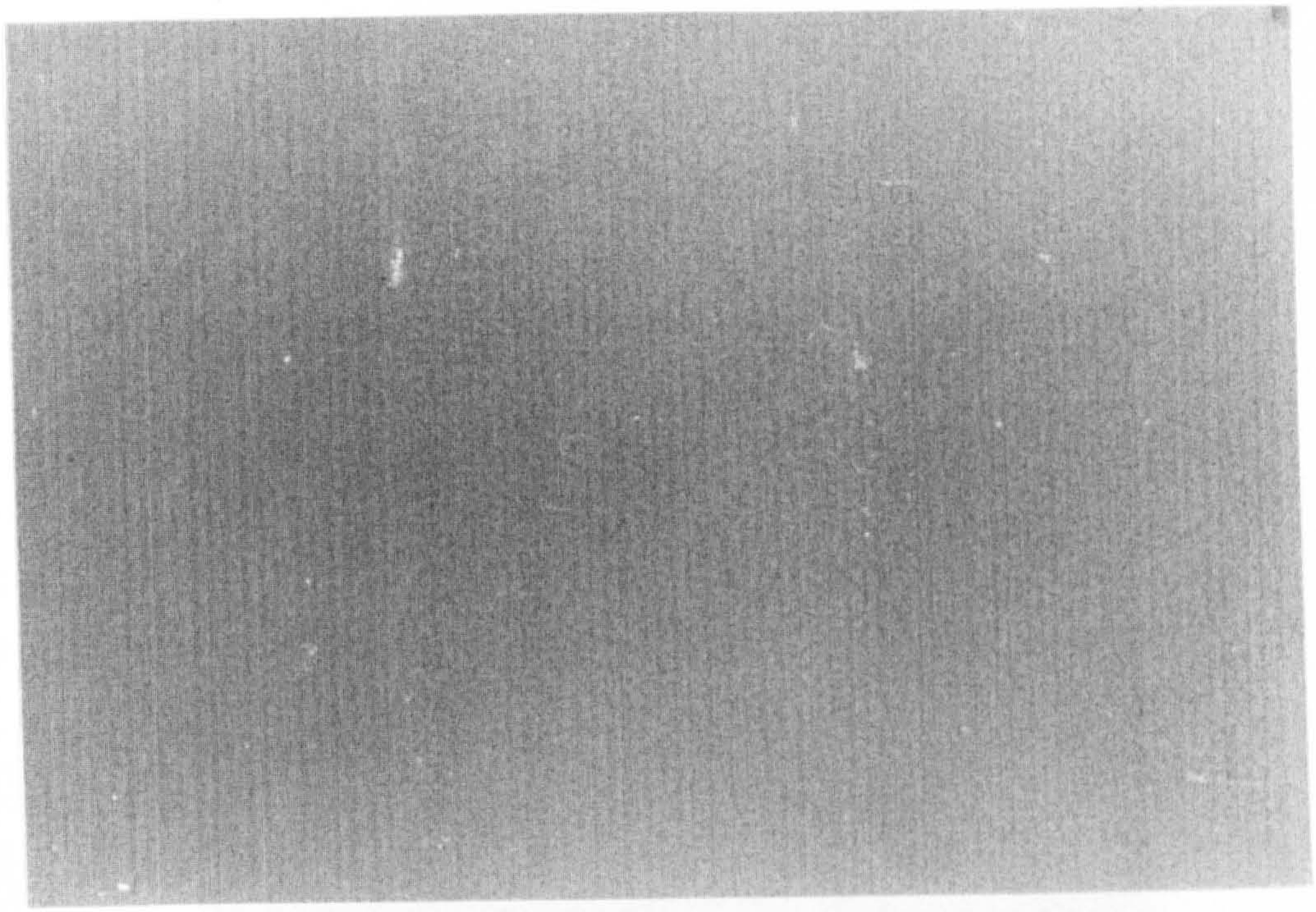

Figure 4.9 Optical micrograph of 3Y-TZP pressureless sintered at 1450°C for 1h in air (un-etched).

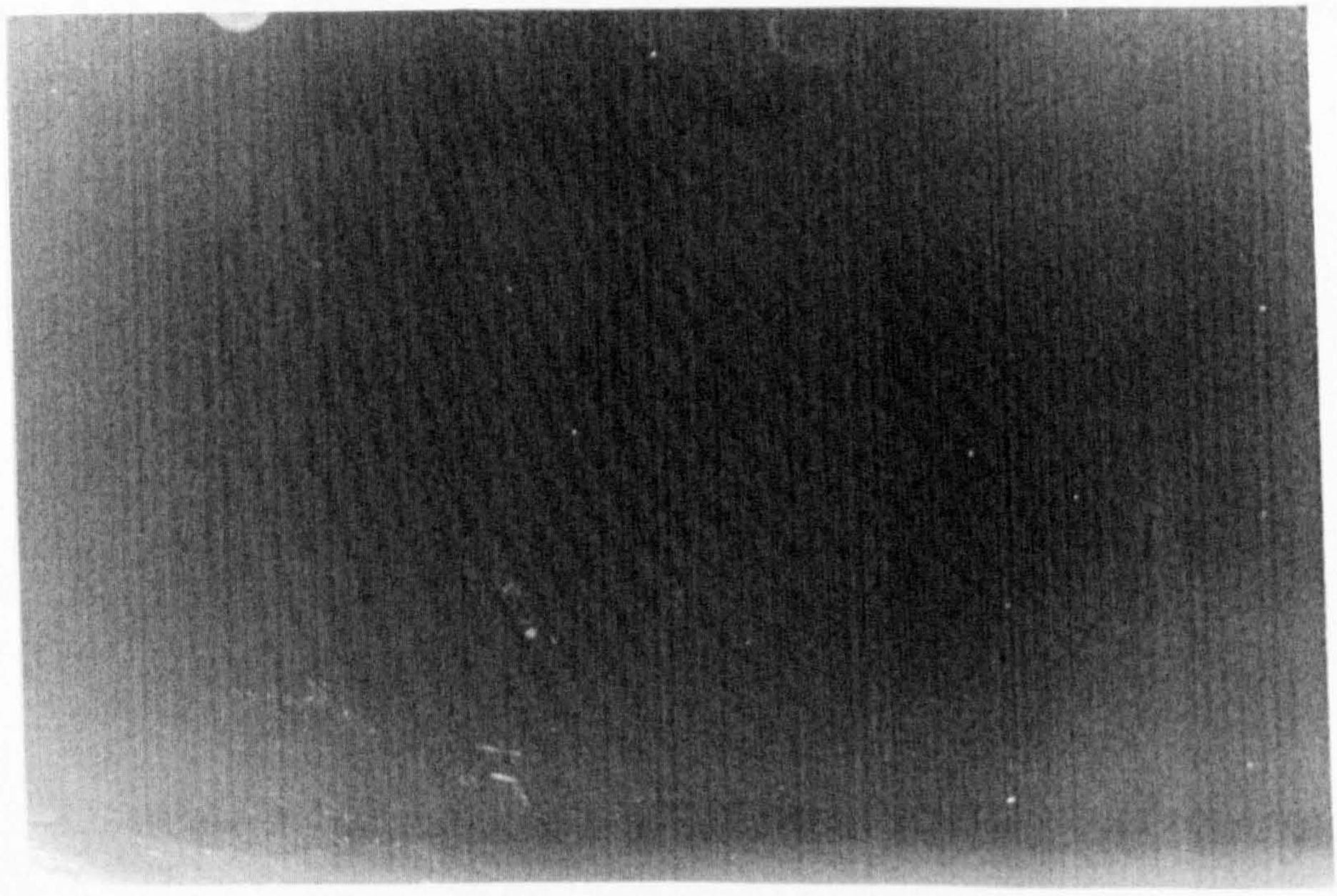

Figure 4.10 Optical micrograph of 3Y-TZP pressureless sintered at 1450°C for 1h in argon (un-etched)

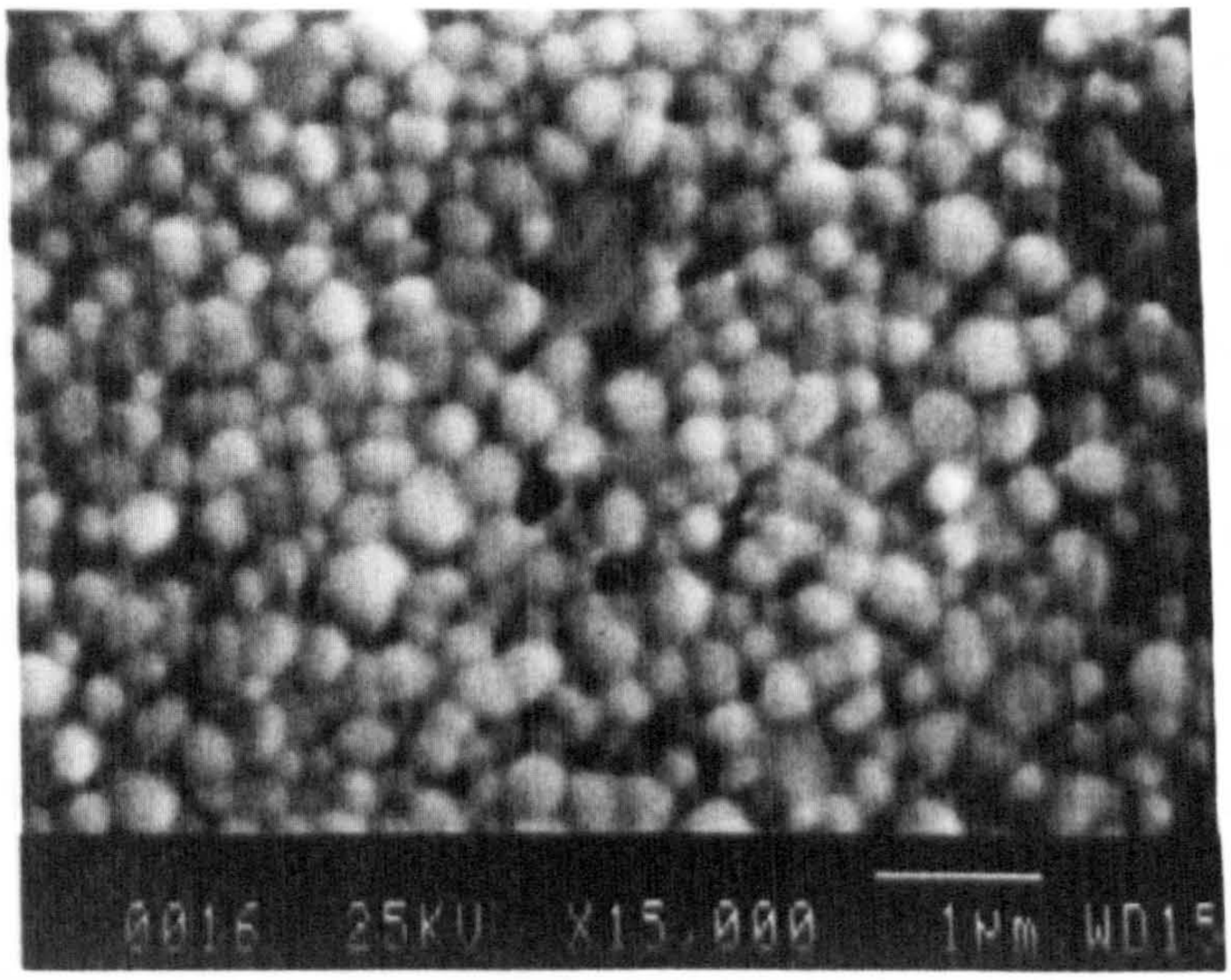

Figure 4.11 SEM photograph of 3Y-TZP sintered at 1450°C for 1h in air after polishing and thermal etching at 1450°C for 1h in air.

4.3. MECHANICAL PROPERTIES

4.3.1. VICKERS HARDNESS AND FRACTURE TOUGHNESS

Ten indents were made at representative locations of the whole polished surface of samples. Indent diagonals and crack length propagating from each indent corner were measured. Applied load of 5 kg for 15 seconds was enough to produce cracks, and this load was also safe enough not to deform the samples in the resin in which the samples were mounted for ease in handling, polishing and testing. The Vickers hardness and fracture toughness were calculated using Equations 3.5 (in Chapter 3) and 3.6 (equation given by Shetty *et al*, 1985 for Palmqvist crack type - in Chapter 3) respectively.

Table 4.4 shows Vickers hardness and fracture toughness values of samples sintered in air and in argon gas. There is no significant effect of either air or argon gas sintering atmosphere on the hardness and fracture toughness. The low standard deviation, ≤ 2.5% for Vickers hardness and ≤ 3.8% for fracture toughness of both samples indicate very uniform structure of the samples.

Table 4.4 Results of Vickers hardness and fracture toughness of 3Y-ZrO_2.

Samples sintered at	Vickers Hardness (Hv)		Fracture Toughness (Kic)	
	Hv (kg/mm^2)	Standard deviation	Kic ($MPa.m^{0.5}$)	Standard Deviation
1450°C / 1h / Air	1342.96	25.22 (1.9%)	5.95	0.15 (2.5%)
1450°C / 1h / Argon gas	1374.46	34.25 (2.5%)	5.89	0.22 (3.7%)

These results are close to those reported by other researchers as shown in Table 4.6. High hardness is typical for Y-TZP [Barsoum, 1997].

Determination of the fracture toughness using the indentation method is easy, simple, and non-destructive in nature, but errors may appear. The error may come from the measurement of crack length that sometimes is not very accurate because the end of the crack is not very clear. Moreover, with many equations available from the literature each can give a different value of fracture toughness. Various fracture toughness values of Y-TZP are presented in Table 4.5 with their material processing and measurement methods. Those various values may be due to the different method of the measurement, particularly the indentation method since it has advantages and disadvantages as mentioned above. Another thing that can influence the value is the transformation toughening effect as it is known in Y-TZP that the metastable tetragonal can transform to monoclinic due to mechanical stress which will improve the toughness of the zirconia. However it depends on the amount of metastable tetragonal that can be transformed to monoclinic, amount of yttria stabiliser, grain size, processing and sample preparation for the fracture test. Above all, fracture toughness of 3Y-TZP is high compared to other oxide ceramic materials, and it can be enhanced using transformation toughening [Barsoum, 1997].

Table 4.5 Data of Vickers hardness and fracture toughness reported by other researchers.

Authors	Material (Processing)	Hv (kg/mm^2)	Kic ($MPa.m^{0.5}$)	Method for Kic
Gupta (1978)	Y-TZP, (PS)	-	6.4	PDBC
Lange[a] (1982)	3Y-TZP, (PS)	-	5.8	IFM
Haberko and Pampuch, 1983	3Y-TZP, (PS, 1350°C, 2h)	-	4.0	-
Tsukuma *et al* (1984)	3Y-TZP, (PS, 1400°C, 2h, air)	-	5.5	IFM
Masaki (1986)	3Y-TZP, (HIP 1450°C, 1.5h)	1320	5.7	IFM
Nawa *et al* (1996)	3Y-TZP, (HP,1400°C, 30 MPa, 1h)	1250	4.5 4.0	SEVNB IFM
Zhan *et al* (1996)	3Y-TZP, (HP, 1700°C, 30 MPa)	1200	12.25	FPBT (Pre-crack)

PS = Pressureless sintered
HP = Hot pressed
HIP = Hot Isostatic Pressed
SEVNB = Single Edge V Notch Beam
IFM = Indentation Fracture Method
PDBC = Pre-cracked Double Beam Cantilever

Figures 4.12 and 4.13 show photographs by optical microscopy of the Vickers indent of the polished surface of 3Y-TZP sintered in air and argon respectively. Cracks generated from each corner of the indent are clearly seen on both samples. The crack length of each indent seems to be similar and means that the samples are homogeneous.

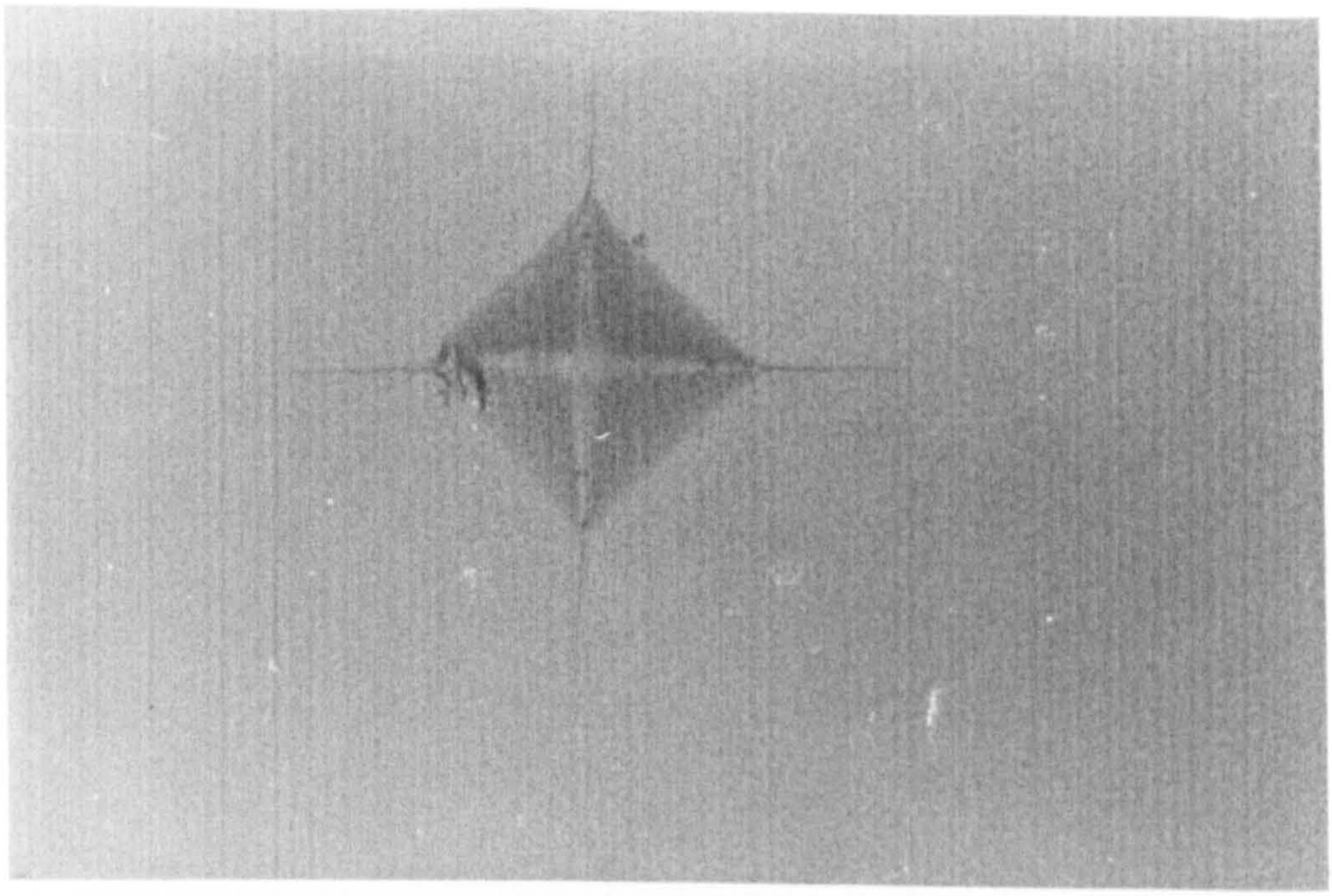

25 μm

Figure 4.12 Optical micrograph of Vickers indent (5 kg load) on 3Y-TZP sintered at 1450°C for 1h in air.

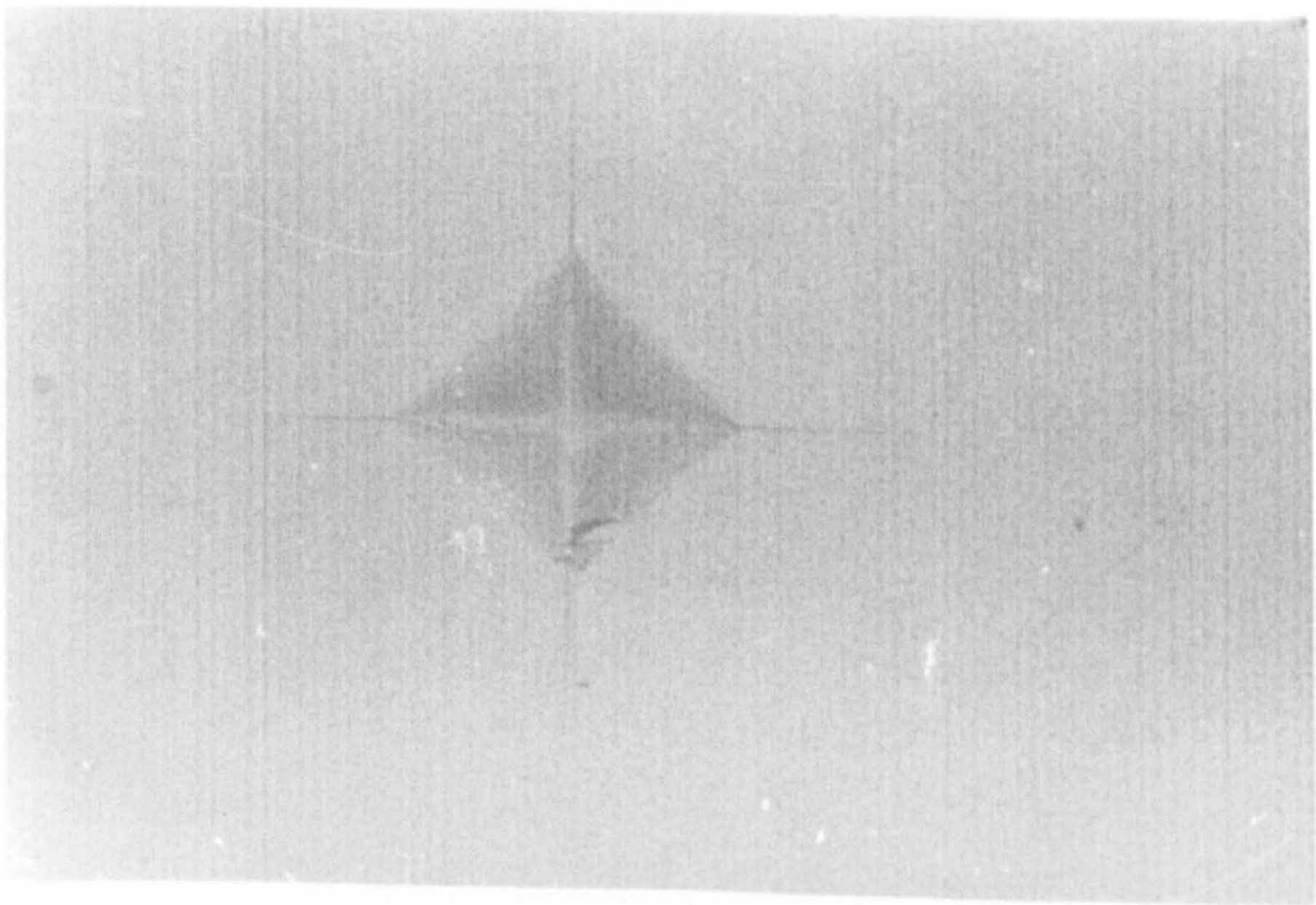

25 μm

Figure 4.13 Optical microscope of Vickers indent (5 kg load) on 3Y-TZP sintered at 1450°C for 1h in argon.

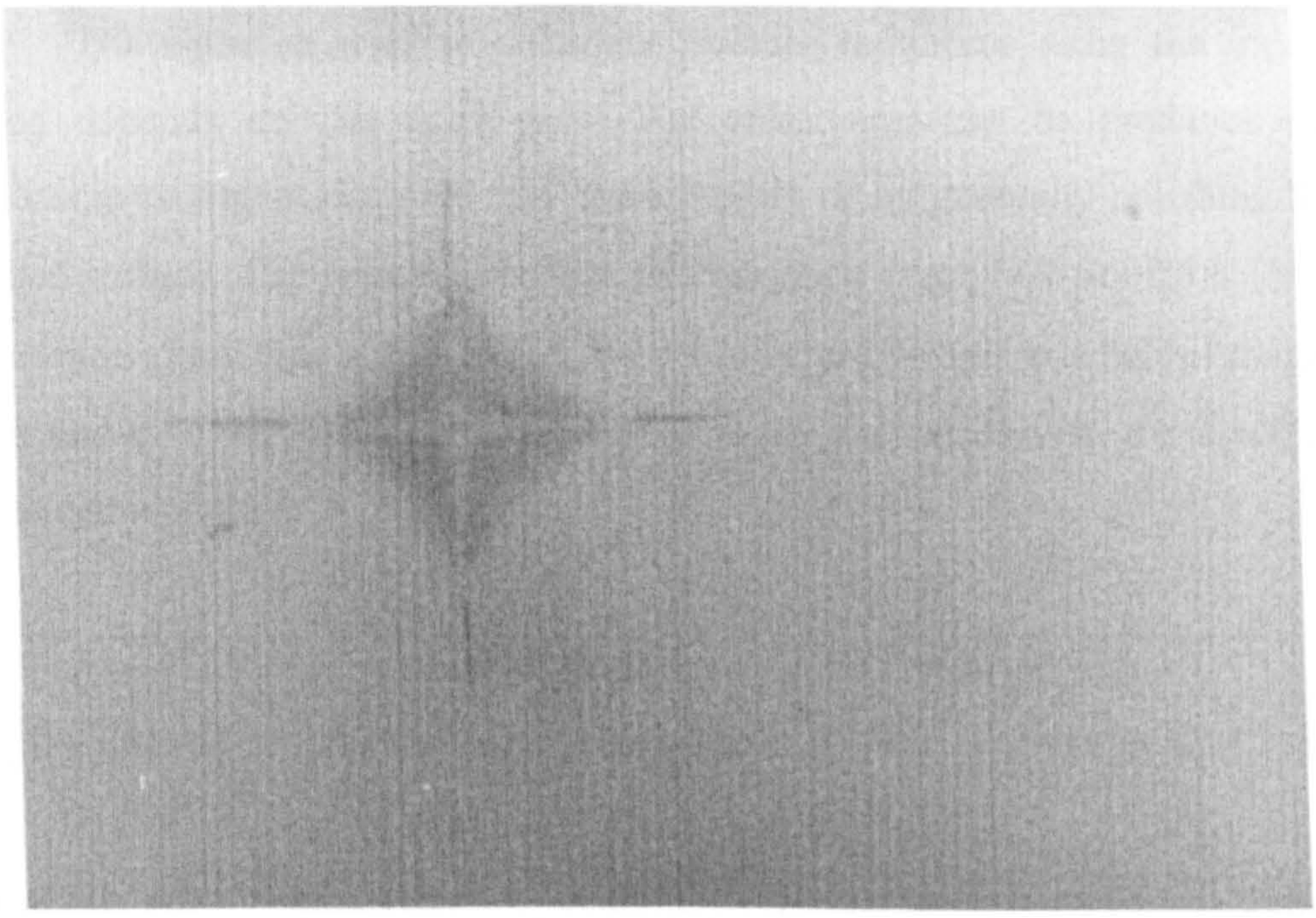

Figure 4.14 Optical micrograph of polished surface of a pre-Vickers indented (5 kg load) on 3Y-TZP sintered at 1450°C for 1h in air.

The equation used to calculate fracture toughness using the indentation method depends on the crack type. The crack type can be predicted using a relationship of indent diagonal and crack length, or by gradually polishing the pre-indented surface. The typical condition of Palmqvist crack type is $0.25 \leq (l/a) \leq 2.5$ and Median crack type is $(c/a) \geq 2.5$, where l is crack length, a is half of diagonal of indent and $c = l+a$ [Niihara *et al*, 1982]. From the test results, the crack type is determined as follow:

Samples sintered at	Vickers Indentation		*l*/a	(*l*+a)/a	Crack type
	Average of a (μm)	Average of *l* (μm)			
1450°C /1h/ Air	41.55	39.45	0.950	1.950	Palmqvist
1450°C /1h / Ar gas	41.075	41.325	1.006	2.006	Palmqvist

To confirm the crack type calculated from the above Table, polishing the pre-indented surface was performed, and clearly the samples have Palmqvist type as indicated in Figure 4.14.

4.3.2. BENDING STRENGTH

Bending strength of the materials was determined using four point bending tests. Six samples of each material were tested. The strength was calculated using Equation 3.7, the results and their standard deviation were presented in Table 4.6. Sintering of the samples in air and argon give similar strength, about 700 MPa. This value is close to that reported by other authors who used similar material, processing and strength measurement methods (Table 4.7). However, the different value of strength can be seen in Table 4.7 when different methods are used. Some strength data taken using TPBT (Three Point Bending Tests) is higher than that using FPBT (Four Point Bending Tests).

In TPBT the maximum bending moment only occurs on a point or very narrow region of the specimen i.e. on the position of the central load anvil. This will reduce the role of flaws, particularly if there are flaws away from the region of the maximum bending moment. In that case higher stress is required to break the specimen, and gives higher bending strength values. In contrast, FPBT gives more accurate results, because in FPBT the maximum bending moment of the test specimen occurs on a certain length of the specimen and depends on the position of the load anvils.

Other parameters that can influence the value of bending tests are condition of the specimen, specimen dimension and specimen preparation. Specimen condition has a big influence since any flaw or defect on the surface, particularly on the tension surface, will be the failure origin where the fracture can start and develop quickly.

Table 4.6 Results of four point bending test of 3Y-ZrO_2.

Sample sintered at	Bending strength (MPa)	Standard deviation (MPa)
1450°C / 1h / Air	706.58	174.40 (24.6%)
1450°C / 1h / Argon gas	691.96	75.47 (10.9%)

Table 4.7 Data of strength of zirconia reported by other researchers.

Researchers	Materials (Processing)	Bending strength (MPa)	Method
Gupta (1978)	Y-TZP, (PS)	700	Disc Method
Matsui *et al* (1984)	3Y-TZP, (PS 1450°C,3h, air)	880	FPBT
Tsukuma *et al* (1984)	3Y-TZP, (HIP, 1400°C, 150MPa)	1500	TPBT
Masaki (1986)	3Y-TZP, (HIP, 1450°C, 1.5h)	1530	TPBT
Nawa *et al* (1996)	3Y-TZP, (HP, 1400°C, 30 MPa, 1h)	1100	TPBT
Besson (1996)	3Y-TZP, (HP, 1450°C, 1h, 20 bar)	570	FPBT
Zhan *et al* (1996)	3Y-TZP, (HP, 1700°C, 30 MPa)	1025	TPBT

TPBT = Three Point Bending Tests

FPBT = Four Point Bending Tests

The fracture surface of the samples sintered in air can be seen in Figure 4.15. Further, Figures 4.15(a-1) and 4.15(a-2) show the microstructures of the fracture surface in Figure 4.15 for the region near the upper surface (under compression) and the region near the bottom surface (under tension) respectively.

Both samples sintered in air and argon give typical brittle fracture surfaces. The microstructures on the tension and compression sides in a sample seem to be different. On the tension region cracks seem to be larger and rougher (Figure 4.15a-2) than that of the compression side (Figure 4.15a-1). The mechanism of the bending test can be illustrated in Figure 4.16a. When a load is applied to a specimen, the upper surface of the specimen will experience compression and the lower surface will be in tension. For homogeneous specimens with square cross-section, the neutral axis is on the middle of the sample along the specimen. The distribution of stress

caused by the bending moment on the cross section of the specimen is illustrated in Figure 4.16. Maximum compressive stress is on the upper surface. This stress decreases in the downward direction until zero value at the neutral axis. Then from the neutral axis downward, the stress is tensile and increases to a maximum value on the lower surface. This tensile stress causes a lot of cracks on the lower region (Figure 4.15a-2) and because the grain size is very small (Figure 4.11), it is difficult to identify crack type whether transgranular (a crack passes across the grain) or intergranular (between the grain).

Two failure origins can be seen clearly on Figure 4.15(a) on the lower surface indicated as a small shiny and smooth region. The left one is clearer than the right one. This failure origin may be caused by a pore or inclusion from impurities in the sample. Fracture of the sample could be initiated from this failure origin.

(a-1) 10μm >>>>

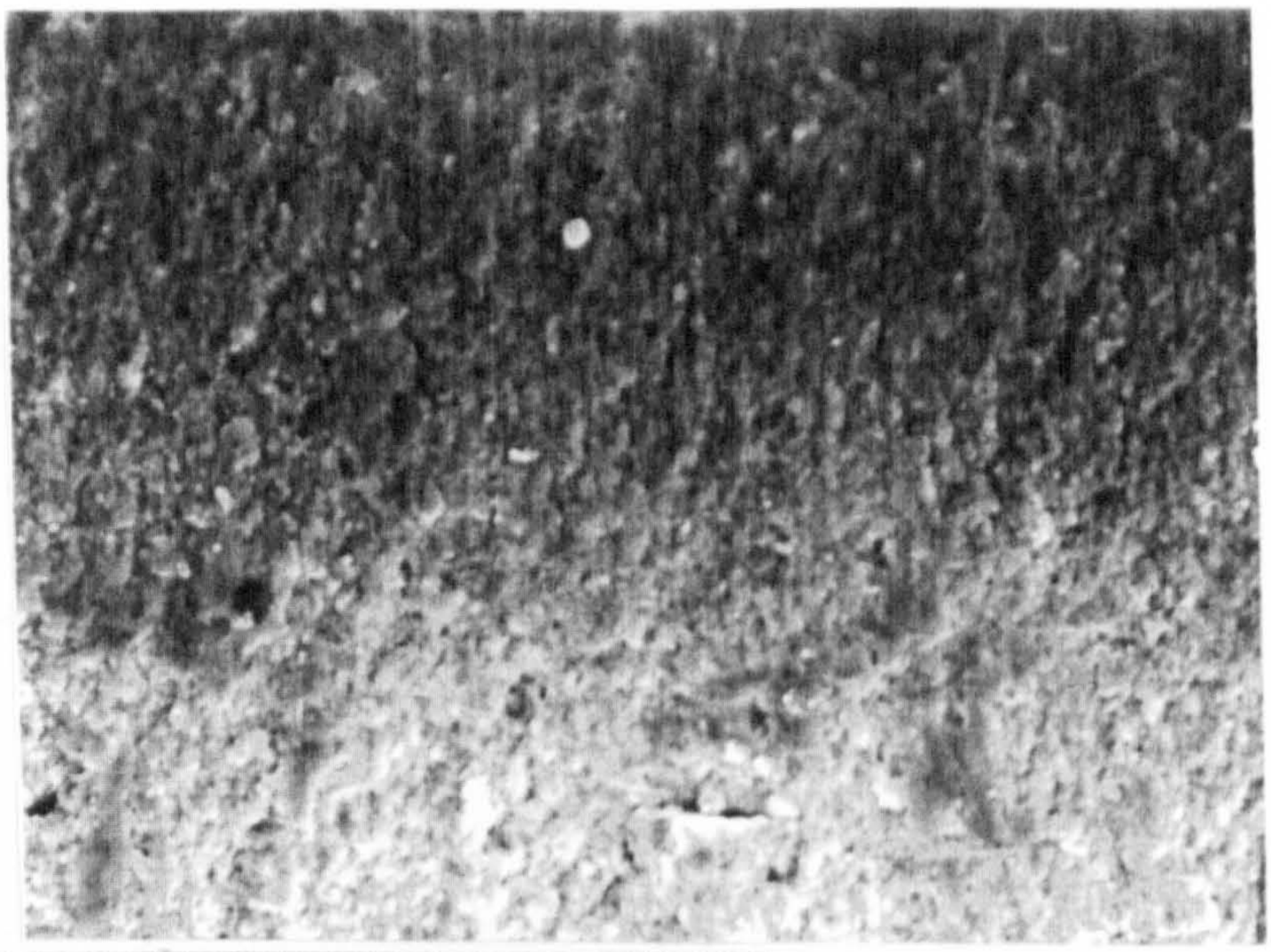

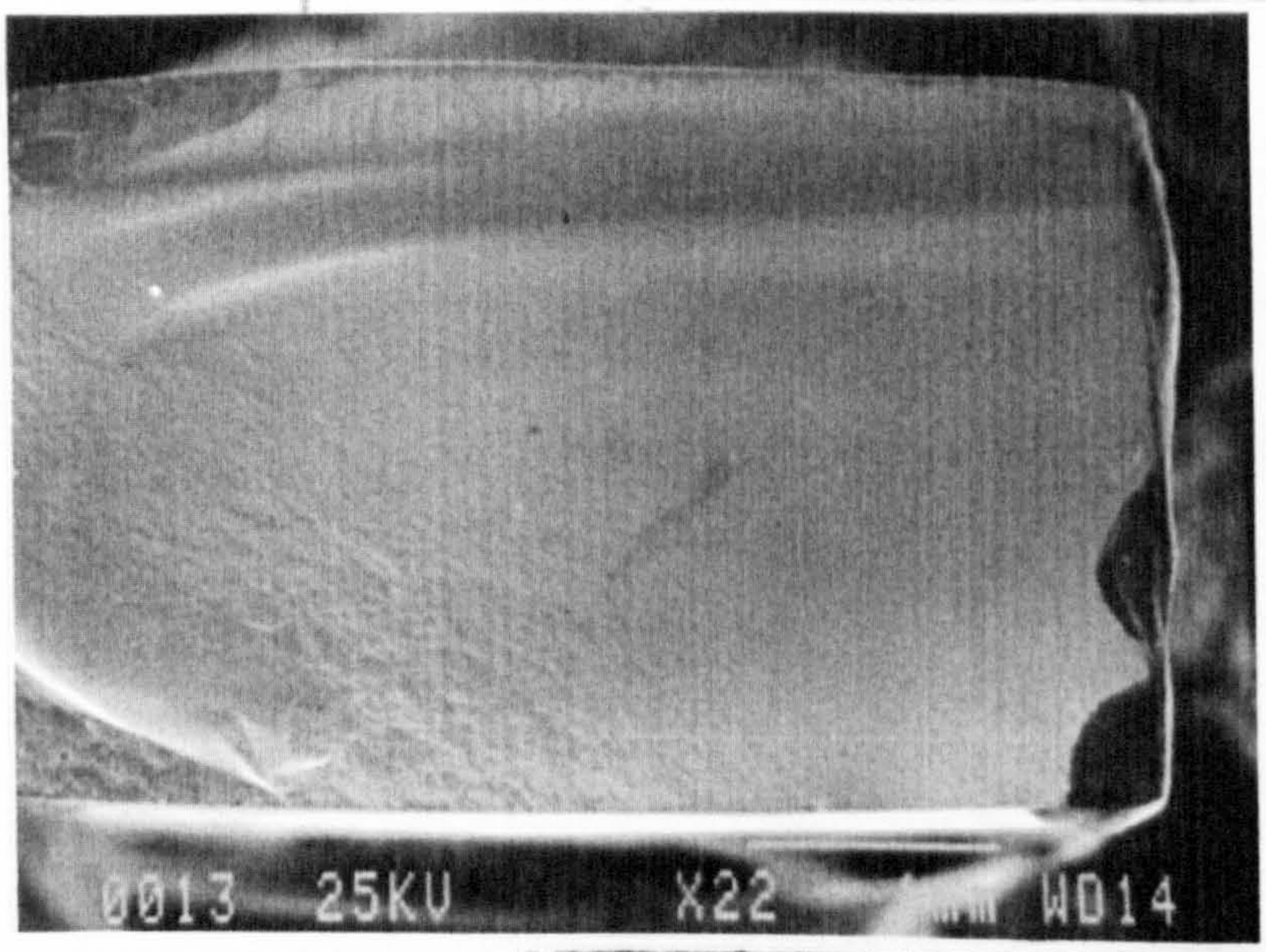

<<<< (a). 1 mm

(a-2) 10μm >>>>

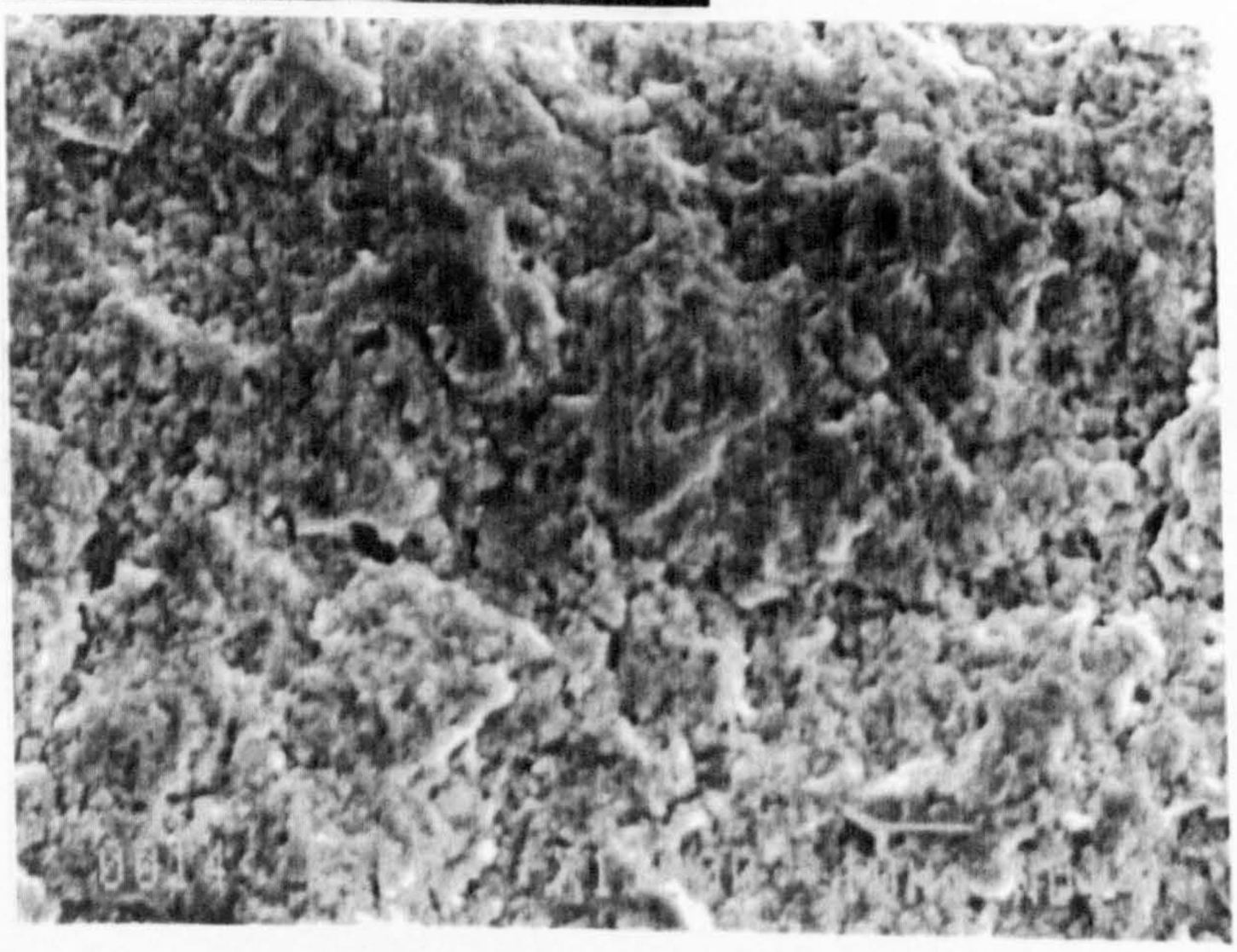

Figure 4.15 (a) SEM photographs of fracture surface after four point bending tests of 3Y-TZP sintered at 1450°C for 1h in air, (a-1) is near to the upper surface (compression) and (a-2) is near to the lower surface (tension surface).

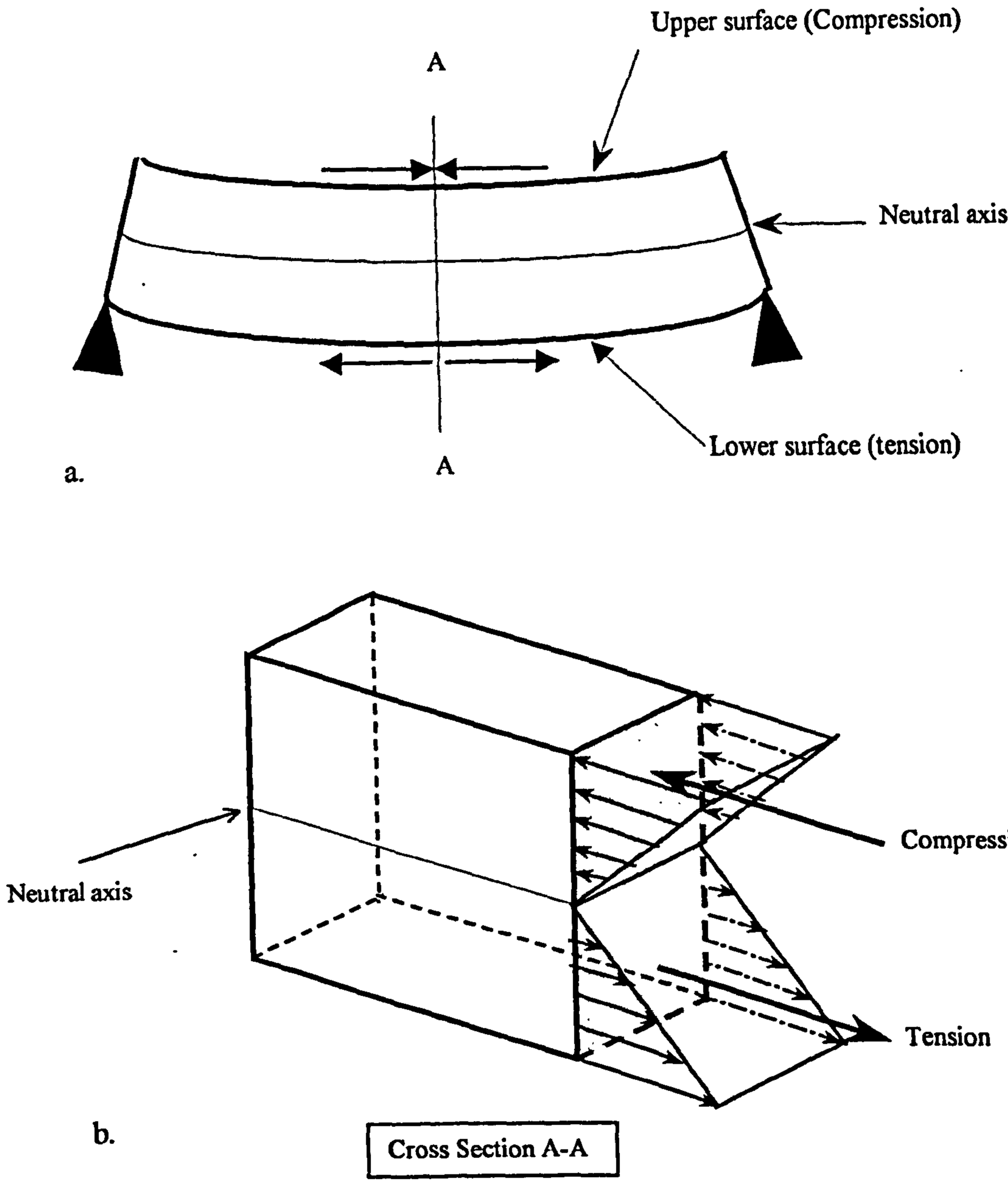

Figure 4.16 A schematic of mechanism of bending moment in bending test (a) and stress distribution on the cross section area where the maximum bending moment is.

4.4. THERMAL PROPERTIES

4.4.1. COEFFICIENT OF THERMAL EXPANSION (CTE)

TMA was used to measure the thermal expansion coefficient of the samples. Two results are presented in Figure 4.17 and 4.18 for zirconia samples sintered at 1450°C for 1h in air and in argon respectively. In Figure 4.17 the measurement was carried out from room temperature up to 1200°C (heating and cooling) in argon and the thermal expansion value of the sample is (10.73 x 10^{-6} /°C) on heating and (10.18 x 10^{-6} /°C) on cooling; the average value is (10.45 x 10^{-6} /°C).

The thermal expansion coefficient of the sample in Figure 4.18 was measured from room temperature to 1400°C in argon. The thermal expansion coefficient value is (11.40 x 10^{-6} /°C) on heating and (9.86 x 10^{-6} /°C) on cooling; and the average value is (10.63 x 10^{-6} /°C). This value is a little higher than that measured up to 1200°C.

Those average values are very close to the thermal expansion coefficient for tetragonal zirconia as reported by several authors with a typical value of thermal expansion about ((10.0 - 10.6) x 10^{-6} /°C) at 20 - 1000°C as shown in Table 4.8.

Table 4.8 Data of CTE of Y-TZP reported by other researchers

Authors	Material and processing	α (ave.) x 10^{-6} /°C	Temp. (°C)	Remarks
Matsui *et al* (1984)	3Y-TZP (PS, 1400°C,3h, air)	10.4**	20 - 900	Tetragonal (grain size 0.5.μm)
Matsui *et al* (1984)	3Y-TZP (PS 1300°C, 3h, air)	10.4**	20 - 900	Tetragonal (grain size 0.2μm)
Adams *et al* (1985)	5 wt%Y_2O_3-ZrO_2 (from skull melting)	10.99	20 - 1500	-
Schubert (1986)	3Y-TZP	10.1 10.6	20 - 600 20 - 800	Tetragonal Tetragonal
Green 1998	3Y-TZP	10.6	20 - 800	Tetragonal
Goodfellow UK (the supplier of the present material)	3Y-TZP	10.0	20 - 1000	Tetragonal

** data were calculated from the thermal expansion diagrams from their paper.

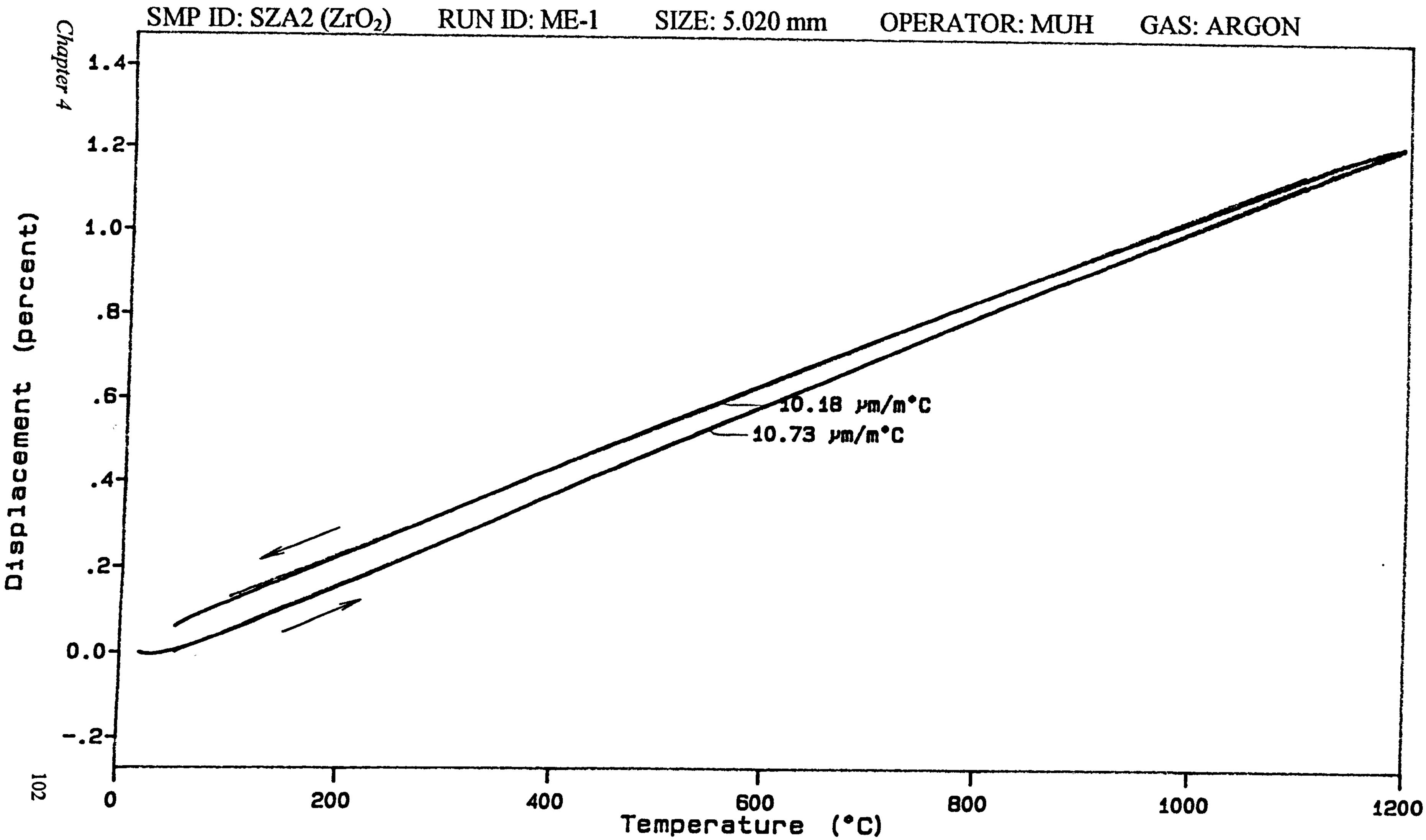

Figure 4.17 Thermal expansion of zirconia (3Y-TZP sintered at 1450°C for 1h in air)

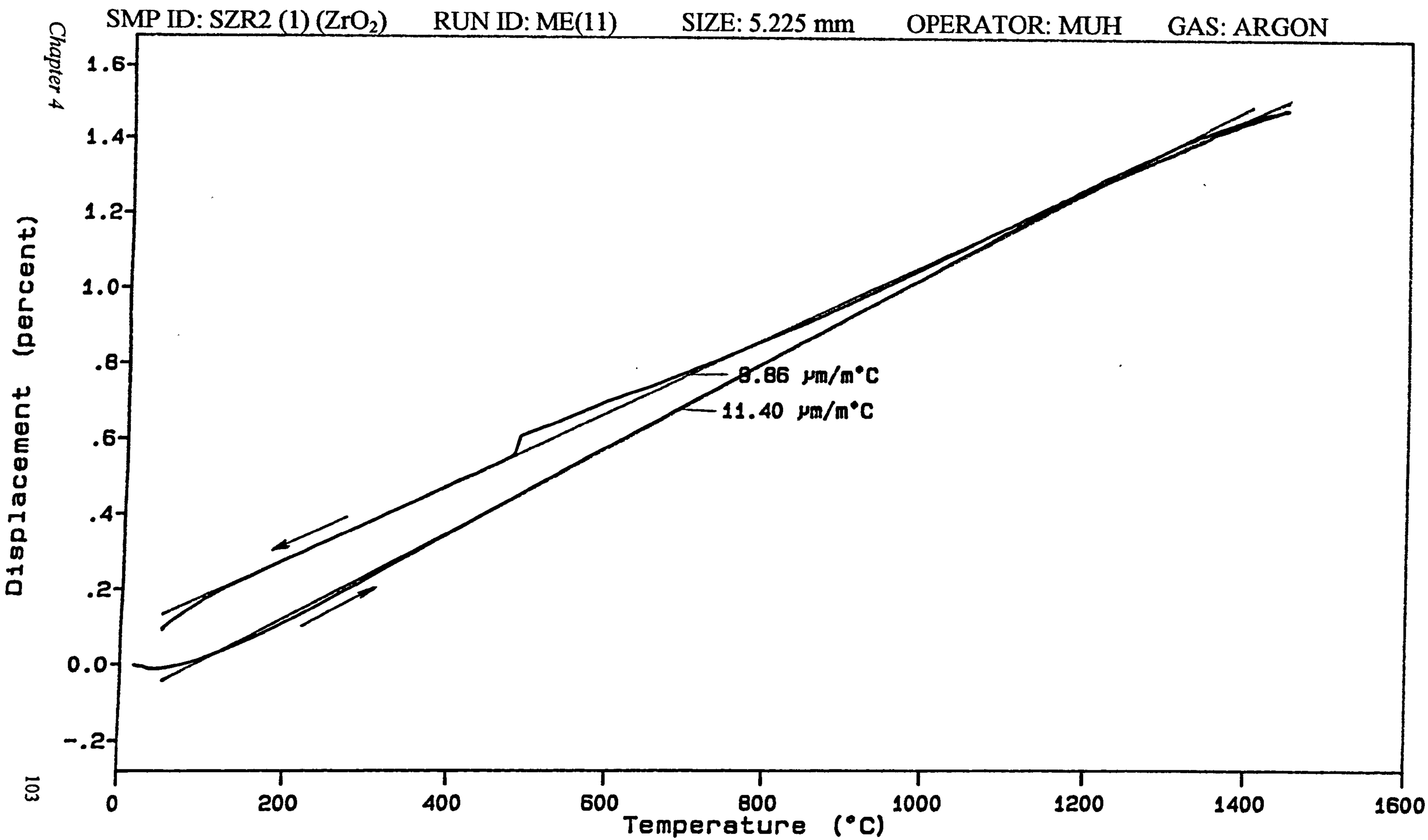

Figure 4.18 Thermal expansion of zirconia (3Y-TZP sintered at 1450°C for 1h in argon)

4.4.2. THERMAL DIFFUSIVITY AND CONDUCTIVITY

Thermal diffusivity of zirconia samples was measured using the laser-flash method. The samples were coated using graphite spray, because the zirconia samples were translucent. Measurement was performed every 100°C from room temperature until 600°C in argon. Above 600°C the equipment did not work properly due to burning out of the carbon coating resulting in the samples becoming translucent again. The oxygen that burns the carbon coating comes from the impurities in the protective gas atmosphere.

The results of the measurement are presented in Figure 4.19. Measurement was taken three times at each designed temperature and the data points in Figure 4.19 are the mean value. The standard deviation at each point (designed temperature) is very small (0.0003 - 0.00007 cm/s^2) or (0.4 - 0.8%) and can not be drawn in the Figure.

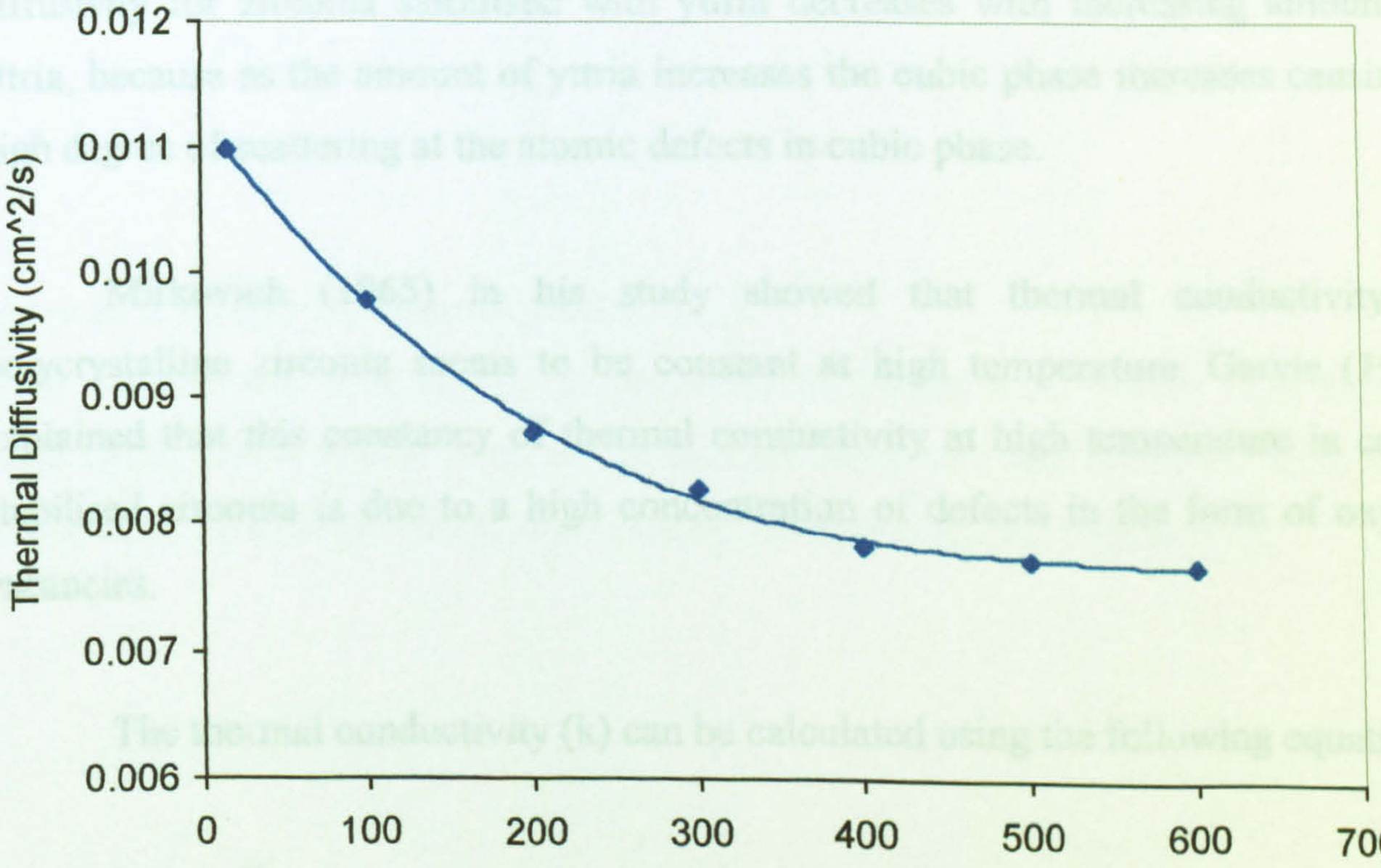

Figure 4.19 Thermal diffusivity of 3Y-TZP (sintered at 1450°C for 1 h in air) as a function of temperature.

Author	Material	Thermal Diffusivity at RT (cm/s^2)	Method
Hasselman *et al* (1987)	ZrO_2 (with 5.4w%Y_2O_3)	0.0119	Laser Flash

The result of this experiment at room temperature is close to that reported by Hasselman *et al* (1987) for similar material. At high temperature, they did not report the thermal diffusivity value for that material, but they observed thermal diffusivity at high temperature up to 1000°C for zirconia with different amount of yttria (2.4 wt% and 5.3 wt%) and up to 1400°C for zirconia with 4 wt% and 9 wt% yttria. At high temperature the results found in this present work have similar trend to that found by Hasselman *et al* (1987) where for zirconia stabilised with yttria, the thermal diffusivity decreases gradually with temperature up to 500°C and then remains almost constant. Hasselman *et al* (1987) also show that at room temperature thermal diffusivity for zirconia stabilised with yttria decreases with increasing amount of yttria, because as the amount of yttria increases the cubic phase increases causing a high degree of scattering at the atomic defects in cubic phase.

Mirkovich (1965) in his study showed that thermal conductivity of polycrystalline zirconia seems to be constant at high temperature. Garvie (1976) explained that this constancy of thermal conductivity at high temperature in calcia stabilised zirconia is due to a high concentration of defects in the form of oxygen vacancies.

The thermal conductivity (k) can be calculated using the following equation:

$$k = \rho \,.\, Cp \,.\, a \qquad \ldots\ldots\ldots\ldots\ldots\ldots\ldots\ldots\ldots\ldots\ldots\ldots\ldots\ldots \quad (4.2)$$

where ρ, Cp and *a* are density, heat capacity and thermal diffusivity, respectively. The data of the heat capacity was obtained from Hasselman *et al* (1987) for similar material (5.3 wt% Y_2O_3) as follows:

Temperature (°C)	25	100	200	300	400	500	600
Heat capacity (J/kg K)	460	509	546	575	591	600	604

The effect of temperature on density was taken into account because zirconia expands with increasing temperature. The CTE of zirconia was taken from the experiments ($\alpha = 10.4 \times 10^{-6}/°C$). The density of the samples at temperature T (ρ_t) can be estimated using the following equation:

$$\rho_t = \frac{\rho_o}{(1+3.\alpha.(T-T_o))} \qquad \ldots\ldots\ldots\ldots\ldots\ldots\ldots\ldots\ldots\ldots (4.3)$$

where ρ_o is density at room temperature (T_o).

Then the thermal conductivity is presented in Figure 4.20 below. The thermal conductivity has a similar trend to the thermal diffusivity and decreases from room temperature up to about 500°C and remains constant at higher temperature.

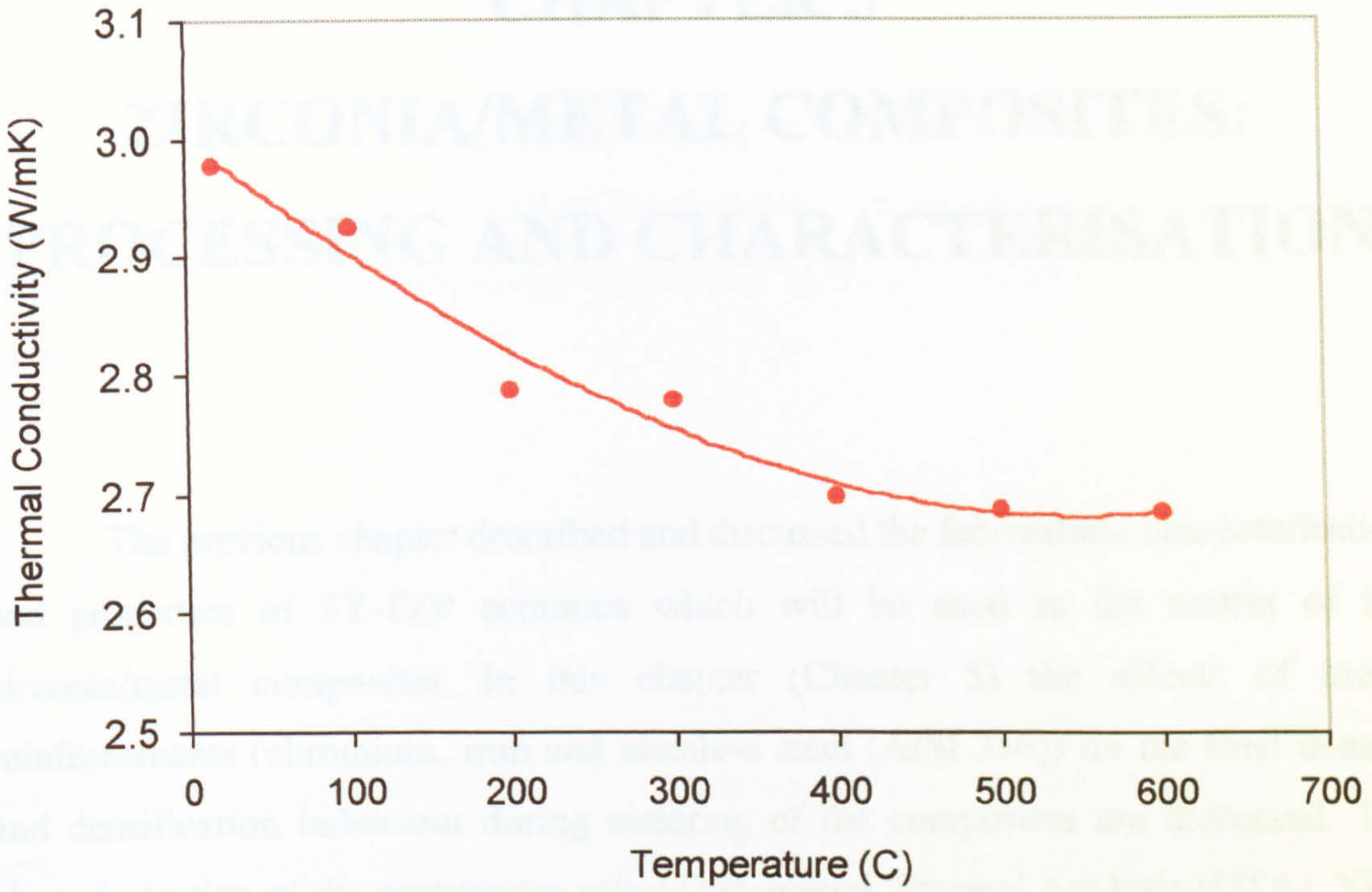

Figure 4.20 Thermal conductivity of 3Y-TZP as a function of temperature.

CHAPTER 5

ZIRCONIA/METAL COMPOSITES: PROCESSING AND CHARACTERISATION

The previous chapter described and discussed the fabrication, characterisation and properties of 3Y-TZP ceramics which will be used as the matrix of the zirconia/metal composites. In this chapter (Chapter 5) the effects of metal reinforcements (chromium, iron and stainless steel (AISI 316)) on the final density and densification behaviour during sintering of the composites are discussed. The characterisation of the composites using Differential Thermal Analysis (DTA), XRD and optical microscopy are also discussed.

The processing techniques used for ceramic-matrix composites can be classified as conventional and novel. The conventional techniques include cold pressing and pressureless sintering, hot pressing, and reaction bonding while examples of novel techniques are liquid infiltration, directed oxidation, in situ reaction, sol-gel, and self propagating high temperature synthesis (SHS) [Chawla, 1993]. The simplest way to produce ceramic particulate composites is by using powder processing techniques used for traditional ceramics, i.e. mixing of constituents in powder form followed by compaction and pressureless sintering (Warren, 1992). This method was used in the present study to fabricate zirconia/metal composites.

5.1. ZIRCONIA/CHROMIUM COMPOSITES

The chromium powder (Goodfellow UK) used in these composites has maximum particle size 38 μm and 99.0+ % purity. Typical chemical analysis given by the supplier shows impurity contents of Al < 0.2%, C < 0.02%, Fe < 0.6% and Si < 0.01%.

5.1.1. DENSIFICATION

Samples of zirconia/chromium composites of 15 mm diameter were prepared using uniaxial pressing with 130 MPa pressure. The composites were sintered at various temperatures between 1300°C and 1500°C for 1 hour in argon and heated and cooled at 10°C/minute. After sintering all samples experienced weight reduction of about 0.3% due to the loss of moisture. Figure 5.1 shows the density of sintered samples of zirconia reinforced with 5, 10 and 25 vol% of chromium powder. The density increases with temperature and almost 100% densification was achieved on all samples sintered at 1400°C and above. The lower density of samples sintered at below 1400°C is due to incomplete densification.

TMA equipment was used to monitor the linear shrinkage behaviour during sintering. In the case of ceramic matrix composites the presence of particles as a second phase may influence the behaviour on sintering. The final linear shrinkage of composites can be predicted using a model proposed by Edrees and Hendry (1999) as follows:

$$\left(\frac{\delta L}{L_o}\right)_c = 1-\left[\left(1-\left(\frac{\delta L}{L_o}\right)_m\right)^3 + f\left(1-\left(1-\left(\frac{\delta L}{L_o}\right)_m\right)^3\right)\right]^{1/3} \qquad \ldots\ldots\ldots\ldots (5.1)$$

where ($\delta L/L_o$) is the linear dimension change, f is the volume fraction of reinforcing phase, the subscripts c and m refer to composite and matrix. This model is only applicable to composites where the volume fraction of reinforcement does not change during sintering or there is no interfacial reaction on the second phase, and the densification only occurs in the matrix.

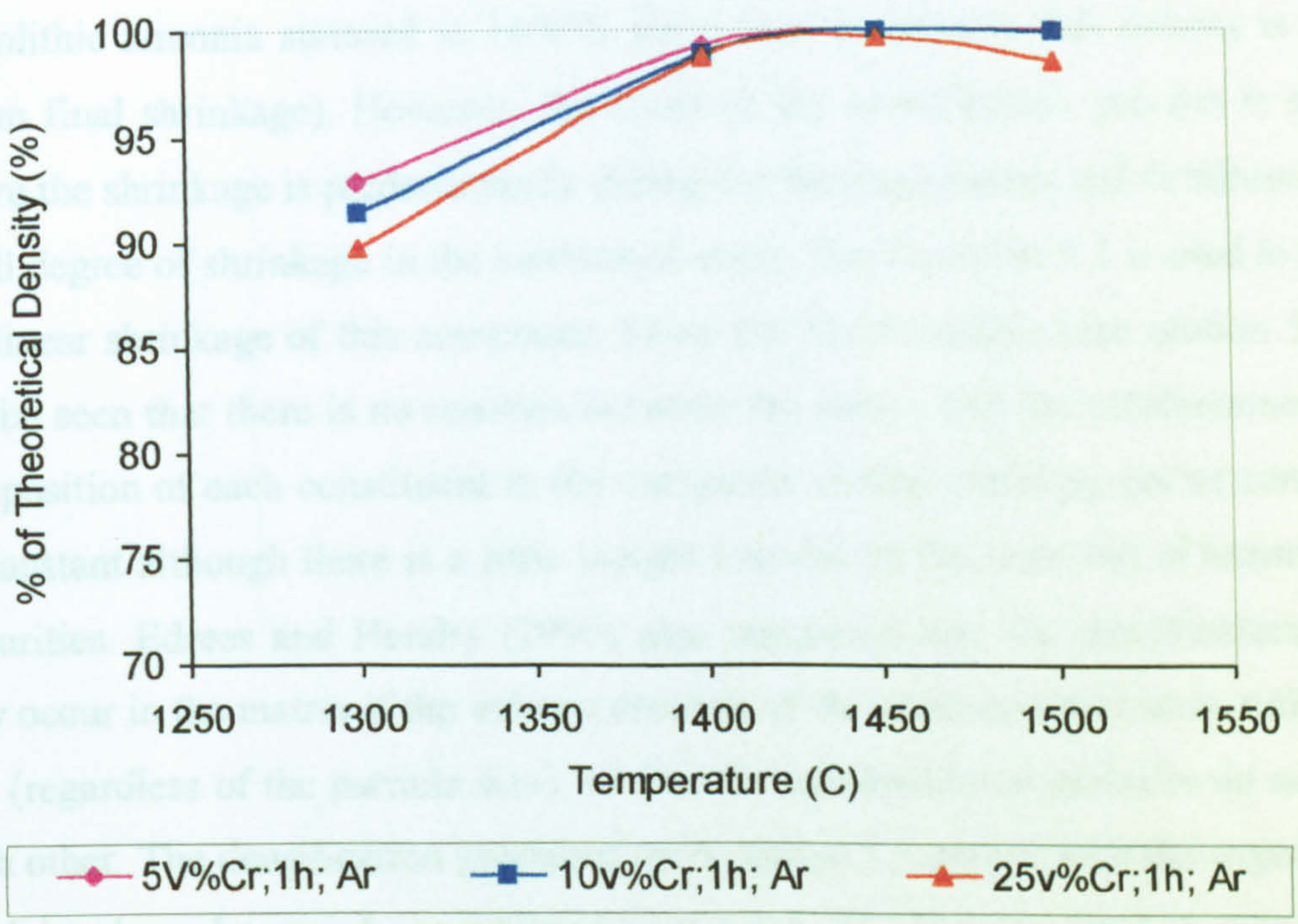

Figure 5.1. The effect of temperature and chromium content on final density of sintered samples.

TMA sintering analysis was performed on samples of 10 vol% Cr + ZrO_2 and 25 vol% Cr + ZrO_2 at a sintering temperature of 1450°C for 1 hour in argon heated at 10°C/minute. The samples of 5 mm diameter were prepared using uniaxial pressing with 130 MPa pressure. With these sintering conditions the sample may be considered as full density as seen in Figure 5.1. Figure 5.2 represents the TMA sintering analysis and shows the curve of linear dimensional changes during sintering and the densification rate of the sample of 25 vol% Cr + ZrO_2. It can be seen in this

figure that the sample slightly shrinks below 300°C due to the loss of moisture and this is followed by thermal expansion of 2.5% up to 1150°C. From 1150°C to 1450°C the sample shrinks quickly (about 17.5%) and this is followed by slow shrinkage (about 1.2%) during isothermal holding at 1450°C for 1 hour; the final linear shrinkage is 16.2%. In comparison with the linear shrinkage of monolithic zirconia (Chapter 4), it is clear that the presence of chromium reinforcement influences the sintering behaviour. As discussed in Chapter 4, the final linear shrinkage for monolithic zirconia sintered at 1450°C for 1 hour to achieve full density is 23.2% (mean final shrinkage). However, the trend of the densification process is similar, where the shrinkage is predominantly during the heating process and is followed by a small degree of shrinkage in the isothermal stage. The Equation 5.1 is used to predict the linear shrinkage of this composite. From the XRD analysis (see section 5.1.3) it can be seen that there is no reaction between the matrix and the reinforcement. The composition of each constituent in the composite during sintering can be considered as constant although there is a little weight loss due to the burn out of moisture and impurities. Edrees and Hendry (1999) also suggested that the densification would only occur in the matrix if the volume fraction of the reinforcement were sufficiently low (regardless of the particle size), so that the reinforcement particles do not touch each other. The densification predicted by Equation 5.1 agrees with the experimental results and can be seen by comparing Figure 4.4 (23.2% mean final shrinkage) with Figure 5.2 (16.2% shrinkage for 25 vol% Cr).

Figure 5.2 also shows the densification rate of the sample of 25 vol% +ZrO_2 and the maximum densification rate of this composite which occurs at 1302°C is lower than that of monolithic zirconia. This is similar to the study of clay/SiC composite by Edrees and Hendry (1999) where the shrinkage rate decreased with increasing reinforcement fraction. The second step of the densification rate between 1285°C and 1415°C in Figure 5.2 may be due to the effect of the re-arrangement of chromium particles (which have maximum size 38 μm) and of the angular and irregular shape on the whole densification process in the composites.

TMA 1500 *(VERSION V5.12)*

SMP ID : 25vol%Cr+ZrO_2 RUN ID : MWW-20 SIZE : 2.110 mm OPERATOR : MUH GAS : ARGON

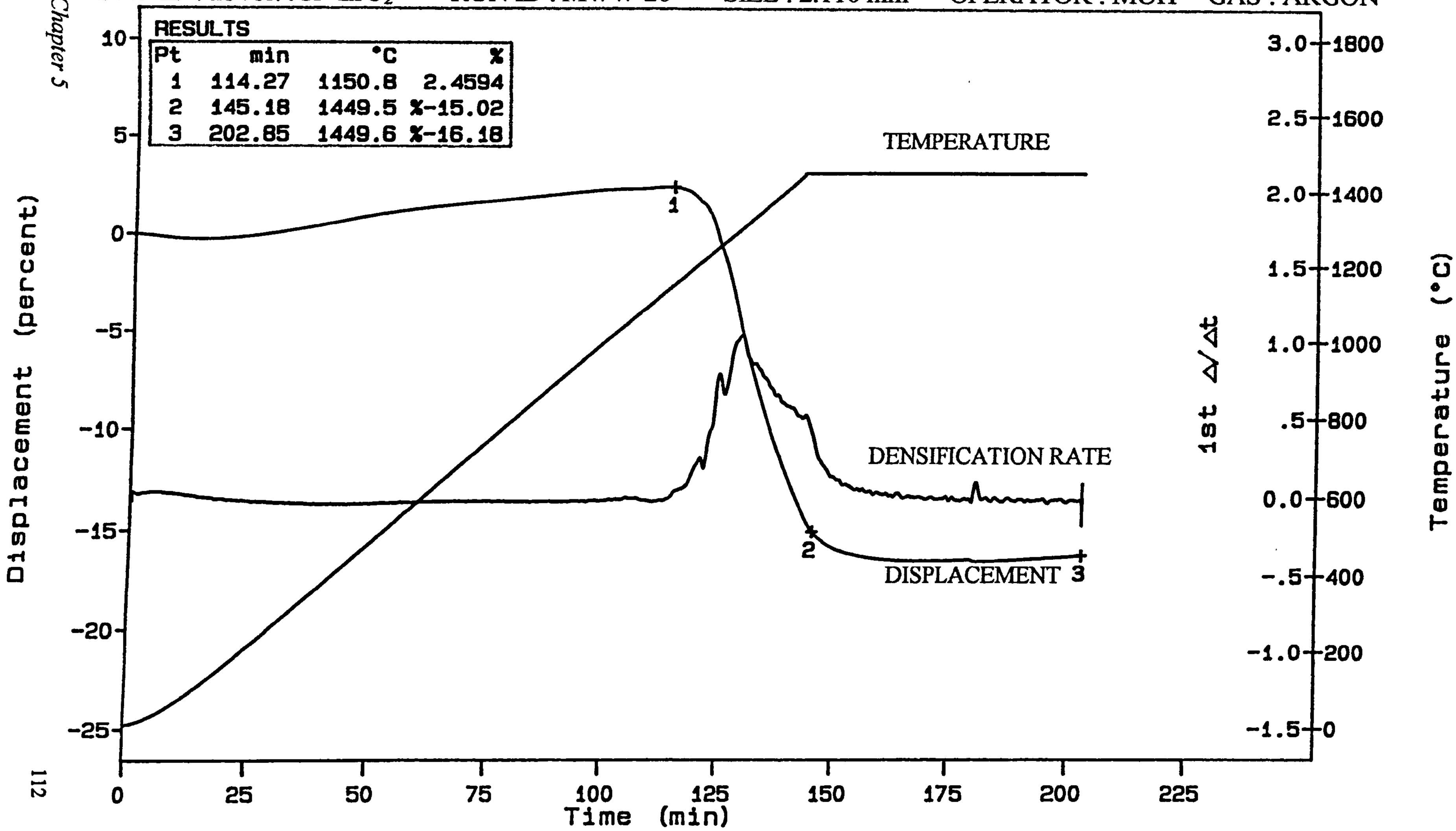

Figure 5.2 Densification behaviour of (25 vol%Cr + ZrO_2) sintered in argon

5.1.2. THERMAL ANALYSIS

Figure 5.3 represents DTA and TGA traces of a zirconia/chromium composite containing 25 vol% Cr. It can be seen in the Figure that there is an increase of sample weight about 7.0% from 1000°C to 1450°C which may be due to reaction between the chromium and the impurity (oxygen) in the argon gas used in this experiment. This weight gain corresponds to a broad and weak exothermic reaction at 1350°C indicating such a reaction. This reaction may occur because the sample was in loose powder form, whereas the compact samples sintered in a horizontal furnace at various temperatures (as shown in Figure 5.1) show weight decrease of about -0.3% due to the loss of moisture content and such a reaction does not occur. The reaction in Figure 5.3 was slow and weak compared to similar samples heated in air where a weight increase of 15% occurred between 900°C and 1200°C coinciding with a strong exothermic peak indicating an oxidation reaction.

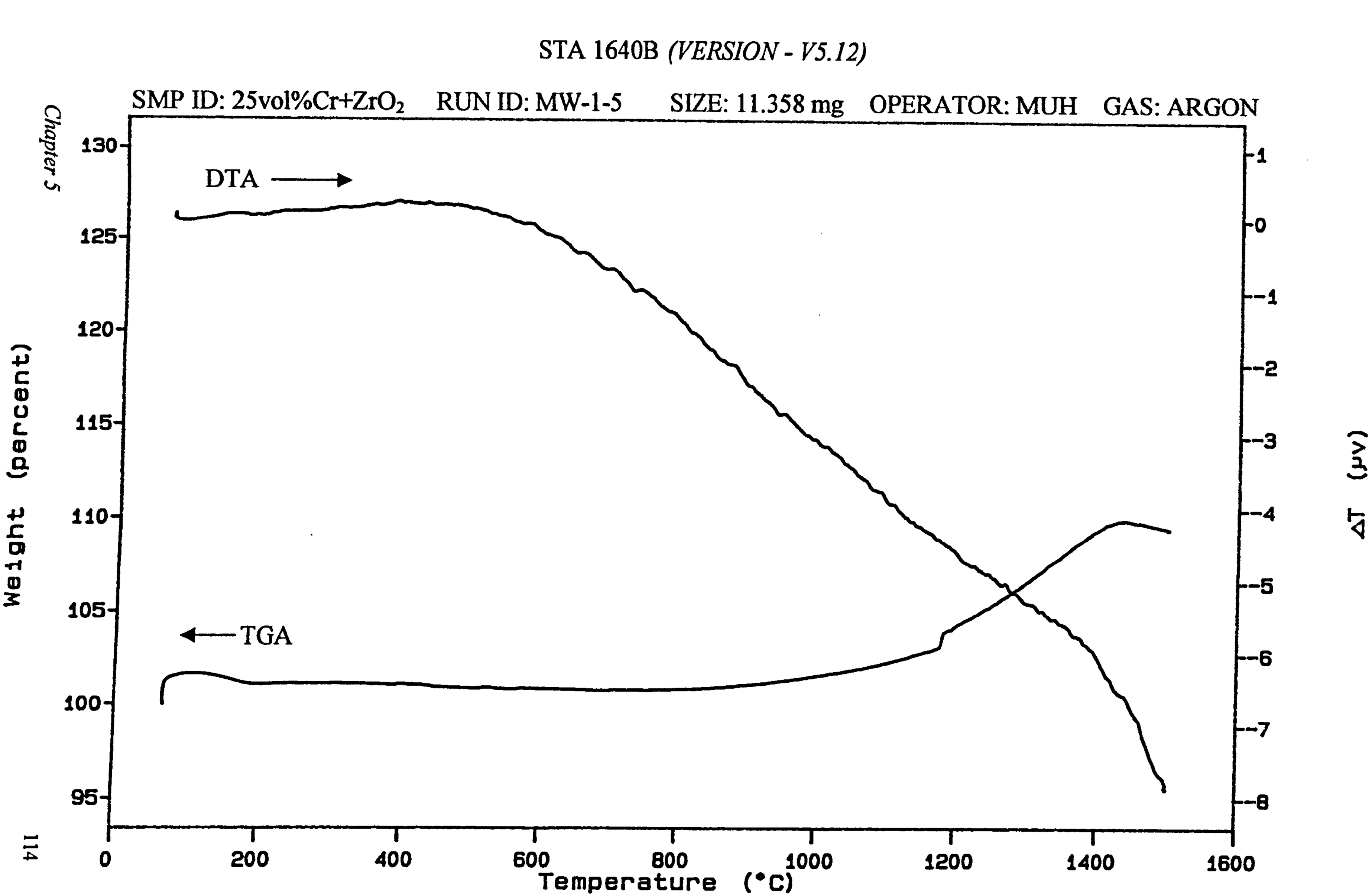

Figure 5.3 DTA and TGA curves of (25 vol% Cr + ZrO_2) sintered in argon

5.1.3. PHASE IDENTIFICATION

X-ray diffraction was used to analyse the crystalline phases present in the samples. Figure 5.4 shows the plots of XRD of as-sintered samples containing (A) 10 vol% Cr and (B) 25 vol% Cr sintered at 1450°C for 1 hour in argon. The d-spacing data measured from the XRD analysis is presented in Table 5.1. There are two phases found in the samples, tetragonal zirconia and chromium. As expected, the zirconia matrix is in the tetragonal form as mentioned in Chapter 4, so there is no effect of chromium reinforcement on the matrix crystal structure. As mentioned in Section 5.1.2, the chromium may react with impurity in the gas used during the course of experiments as indicated in TGA and DTA curves, but from the XRD analysis such reaction is not found. This is due to the fact that the samples used for XRD were in compacted state and not in loose powder as used in TGA and DTA analysis. In compact samples such reaction may not occur since most of the porosity is rapidly closed and there will be no easy path of oxygen to the chromium particles.

Similar to monolithic zirconia as discussed in Chapter 4, the zirconia matrix in this composite also contains metastable tetragonal at room temperature that can transform to monoclinic by applying mechanical stress as shown in Figure 5.5. This will be useful as a toughening mechanism. Furthermore, combined toughening mechanisms such as crack tip interactions, crack tip shielding and matrix compression in ceramic matrix composites may be operated simultaneously [Warren, 1992]. Details of the mechanical properties of this composite will be discussed in Chapter 6.

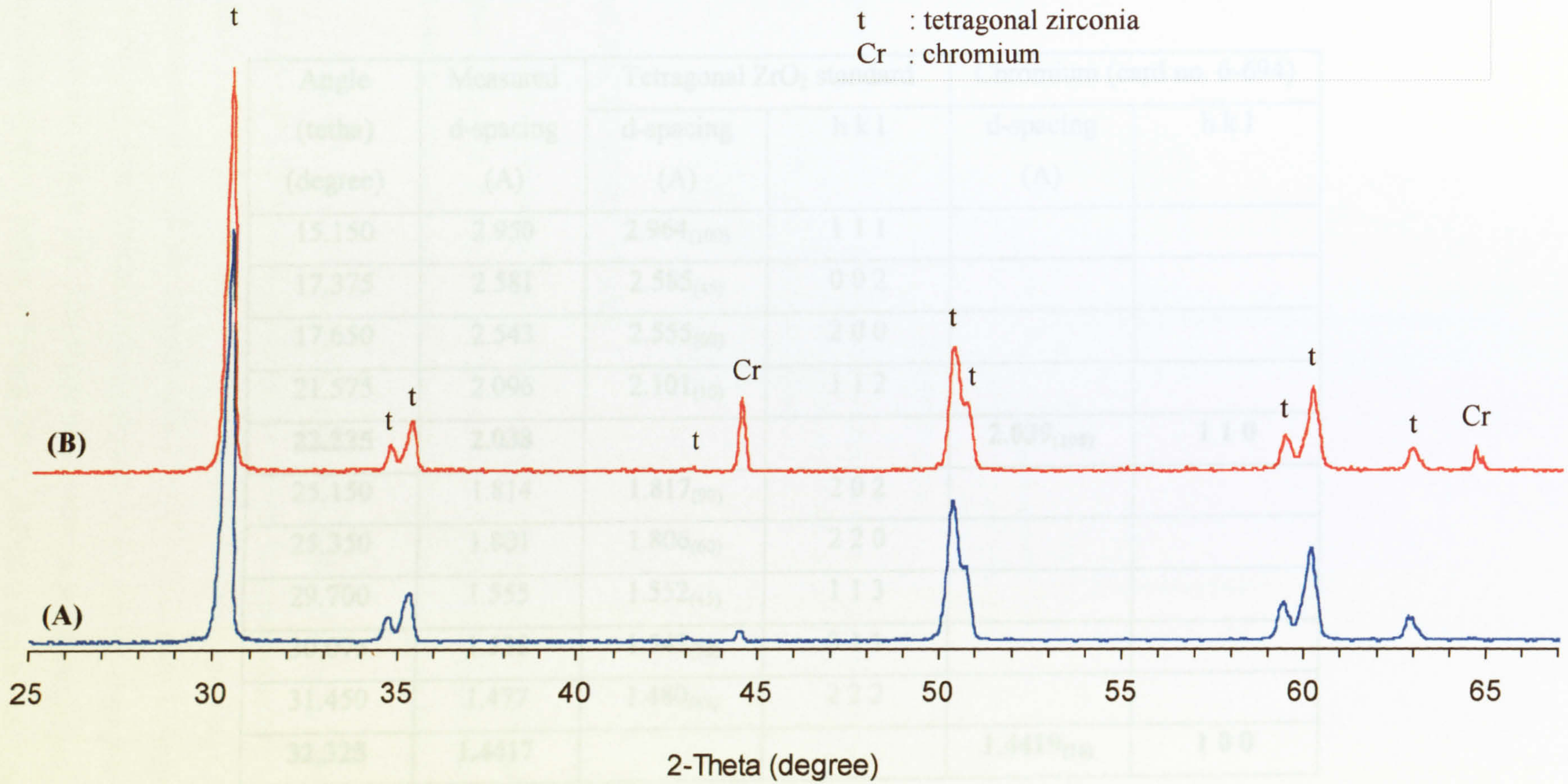

Figure 5.4 X-ray diffraction plot of as-sintered samples of (A) 10V%Cr+ZrO_2 and (B) 25V%Cr+ZrO_2 composites sintered 1450°C for 1h in argon.

Table 5.1. The measured d-spacing of XRD analysis of zirconia/chromium composites as shown in Figure 5.4

Angle (tetha) (degree)	Measured d-spacing (A)	Tetragonal ZrO_2 standard		Chromium (card no. 6-694)	
		d-spacing (A)	h k l	d-spacing (A)	h k l
15.150	2.950	$2.964_{(100)}$	1 1 1		
17.375	2.581	$2.585_{(45)}$	0 0 2		
17.650	2.543	$2.555_{(60)}$	2 0 0		
21.575	2.096	$2.101_{(10)}$	1 1 2		
22.225	**2.038**			**$2.039_{(100)}$**	**1 1 0**
25.150	1.814	$1.817_{(90)}$	2 0 2		
25.350	1.801	$1.806_{(60)}$	2 2 0		
29.700	1.555	$1.552_{(45)}$	1 1 3		
30.075	1.538	$1.542_{(70)}$	3 1 1		
31.450	1.477	$1.480_{(45)}$	2 2 2		
32.325	**1.4417**			**$1.4419_{(16)}$**	**1 0 0**

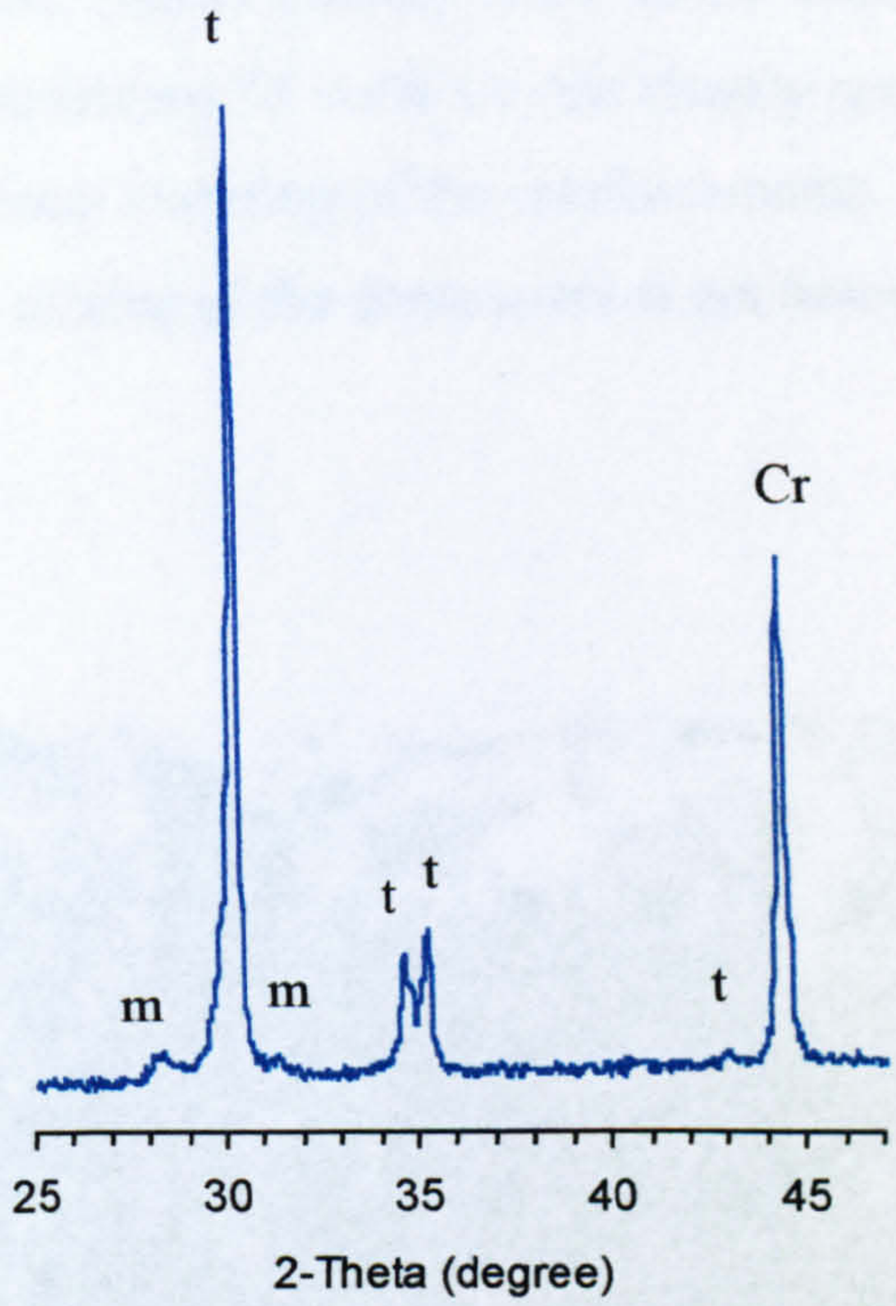

Figure 5.5 Effect of mechanical stress from cutting on phase tetragonal to monoclinic transformation on sample of 25 vol% Cr + ZrO_2 sintered at 1450°C for 1 hour in argon.

5.1.4. MICROSTRUCTURES

Figure 5.6 shows a SEM micrograph of as-received chromium powder used in this composite. It may be clearly seen that the particle shape is angular, irregular and varies in size with maximum diameter 38 micron (as given by the supplier).

Figures 5.7 and 5.8 show optical micrographs of samples containing 10 vol% Cr and 25 vol% Cr sintered at 1450°C for 1 hour in argon respectively. It can be seen in those Figures that the matrix of the samples looks almost fully dense with very little porosity although the sample with 25 vol% Cr as seen in Figure 5.8 contains more porosity (black colour) causing slightly lower density than that of 10 vol% Cr as indicated in Figure 5.1. The shape of chromium particles (angular and irregular) remains the same as before sintering which indicates that no melting has occurred.

The chromium particles (white colour) seem to be embedded effectively in the matrix. For samples containing 25 vol% Cr, the closely spaced particles start to join each other leading to local sintering of the reinforcements. It is also clear that due to large particle size, the mixing of the composites is not homogeneous.

Figure 5.6. SEM photograph of as-received chromium powder.

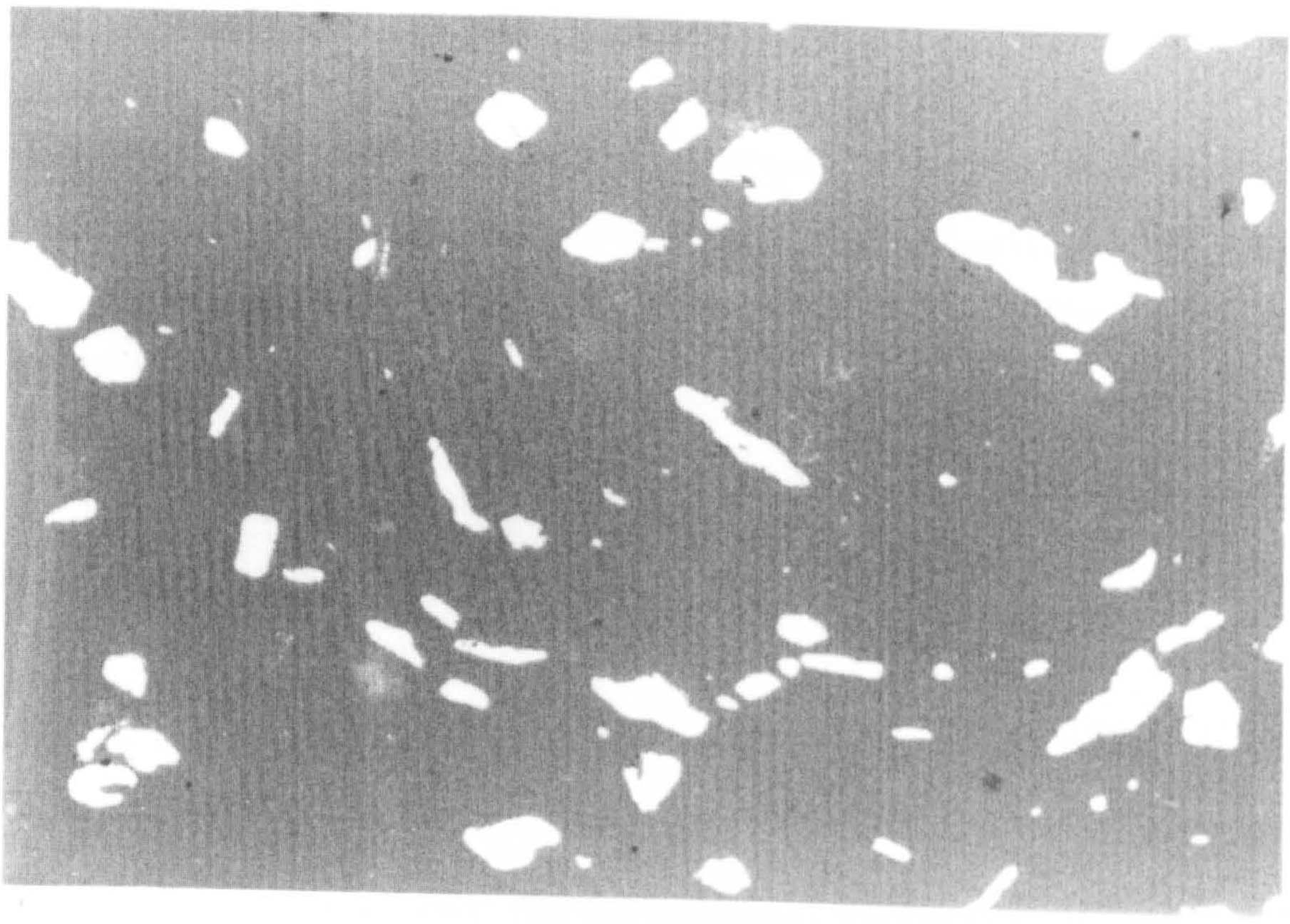

25 μm

Figure 5.7 Optical micrograph of (10 vol%Cr + ZrO_2) sintered at 1450°C for 1 h in argon

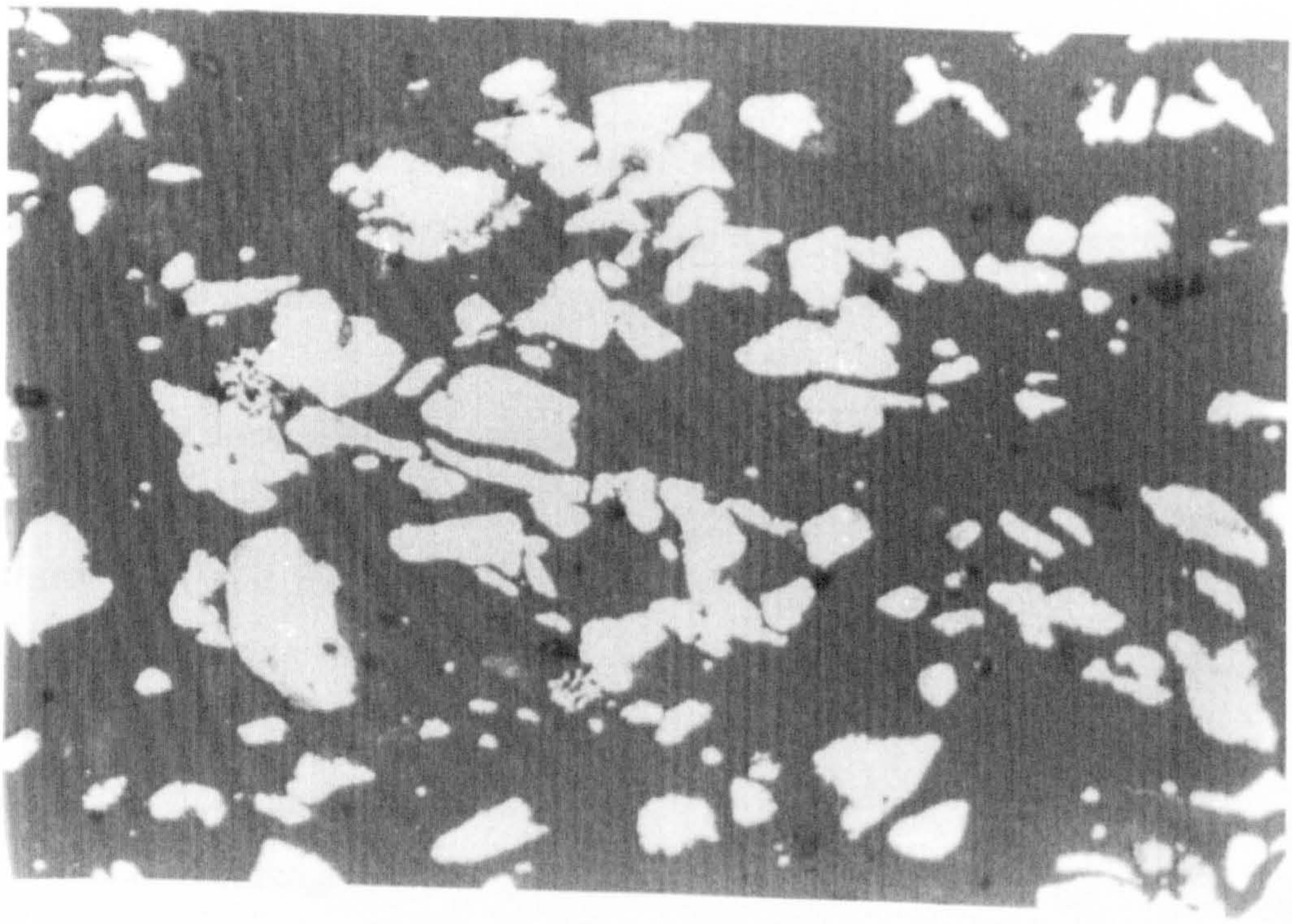

25 μm

Figure 5.8 Optical micrograph of (25 vol%Cr + ZrO_2) sintered at 1450°C for 1 h in argon

5.2. ZIRCONIA/IRON COMPOSITES

The iron powder used in this composite was carbonyl iron powder with purity 99.0+% and mean particle size 6 μm. The typical analysis given by the supplier shows impurity contents of Si < 0.14%, C < 0.2%, P < 0.015%, H-loss < 0.3%, and S < 0.015%.

5.2.1. DENSIFICATION

The percentage of theoretical density of zirconia/iron composites containing 10 vol% and 25 vol% iron sintered for 1 hour in argon at various temperatures (between 1200°C and 1500°C) heated and cooled at 10°C/minute are shown in Figure 5.9. All samples achieved more than 95% of theoretical density at all those temperatures. From 1200°C to 1450°C the density increased with temperature then decreased at 1500°C. Experimental results indicated that densification of the zirconia/iron composites started at a temperature of 900°C (Figure 5.10), which was lower than that of monolithic zirconia and zirconia/chromium composites, and the high density was achieved at low sintering temperature (1200°C). The decrease of density of samples sintered at 1500°C (Figure 5.9) may be due to cracks which occurred in the samples. After sintering all samples experienced weight reduction of about -0.3% due to the loss of moisture from the samples.

The linear dimensional changes and densification rate of sample of (25 vol% Fe + ZrO_2) during sintering at 1450°C for 1 hour in argon are shown in Figure 5.10. It is clearly seen that the sample slightly shrinks until 300°C due to the loss of moisture content and is followed by thermal expansion of 2.0% up to 900°C. The densification starts at 900°C with slow rate, but as the temperature increases the rate of sintering becomes faster and the maximum rate of densification occurs at about 1200°C. Linear shrinkage of 17.7% is achieved up to 1250°C followed by almost constant linear dimensions up to 1370°C where a little sudden change of the dimension occurred. This sudden change of shrinkage rate and the sample dimension

at 1370°C (Point 3) in Figure 5.10 indicates the melting point of the iron particles. This low melting point of the iron used in this experiment is explained in Section 5.2.2. The final shrinkage of (25 vol% Fe + ZrO_2) after sintering at 1450°C for 1 hour is 21.5%.

The presence of iron in the composites has reduced the densification temperature as seen in TMA analysis in Figure 5.10 (200°C lower that that of monolithic zirconia). This effect also occurs in the composites with lower iron content (5 vol% and 10 vol% of Fe). The lower densification temperature and higher densification rate may be the result of the combination of the liquid phase sintering of the matrix (Chapter 4) and the presence in principle of some liquid phase as a result of the impurity contents of the iron (Section 5.2). Figure 5.11 shows phase diagrams of (Fe–Si), (Fe–P) and (Fe-S) systems in which a liquid phase may be formed at the eutectic temperature, (Fe-Si) system at 1212°C, (Fe-P) system at 1048°C and at 988°C for the (Fe-S) system. However, the concentration of these impurities in both iron and zirconia powder is very low and a further more important effect of interfacial reaction is discussed later.

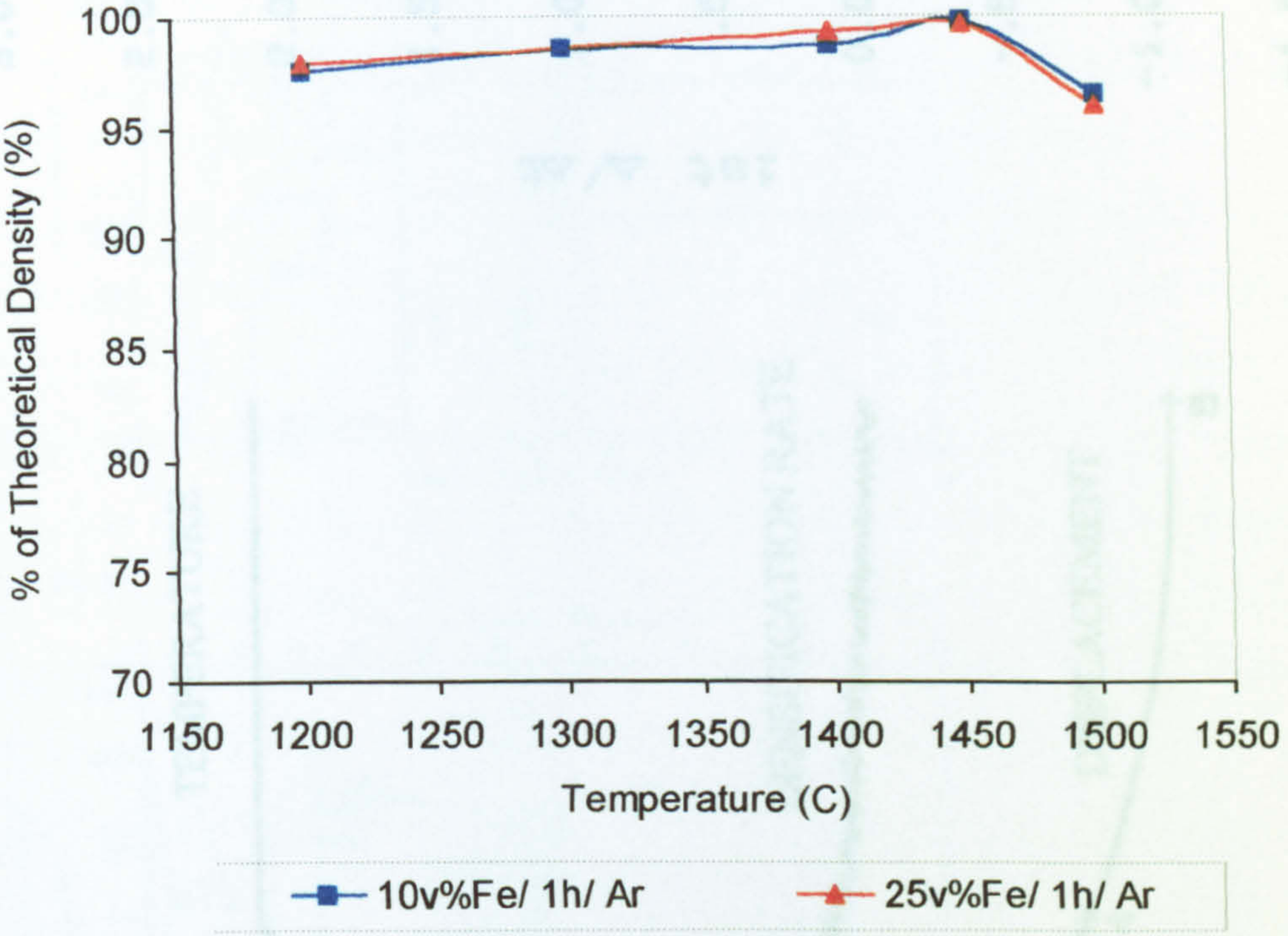

Figure 5.9. Percentage of theoretical density of (10 vol% Fe + ZrO_2) and (25 vol% Fe + ZrO_2) sintered at various temperatures for 1 hour in argon

TMA 1500 *(VERSION V5.12)*

SMP ID : 25vol%Fe+ZrO_2 RUN ID : MWW-22 SIZE : 2.045 mm OPERATOR : MUH GAS : ARGON

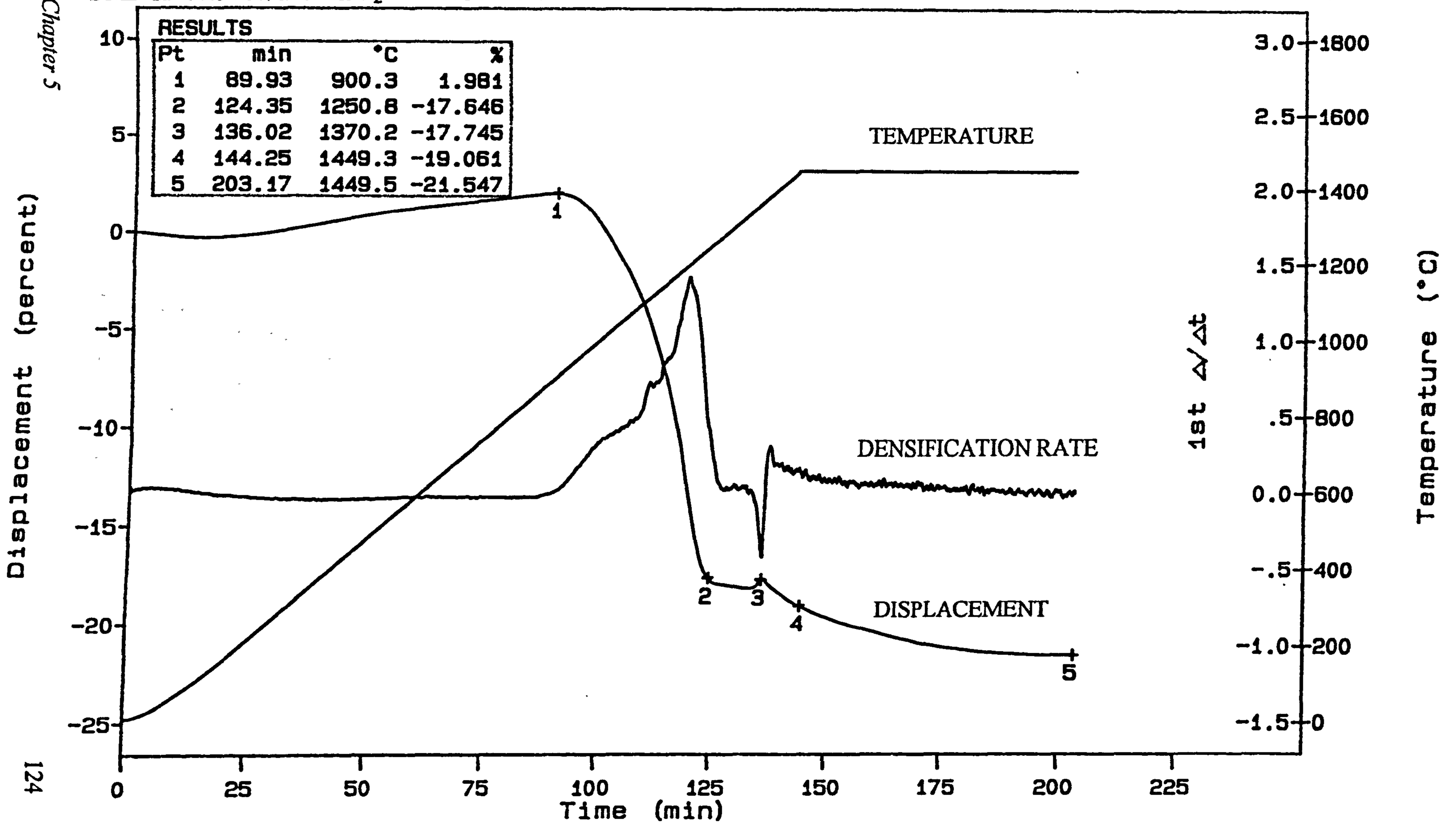

Figure 5.10 Densification behaviour of (25 vol% Fe + ZrO_2) sintered in argon

Fe-Si

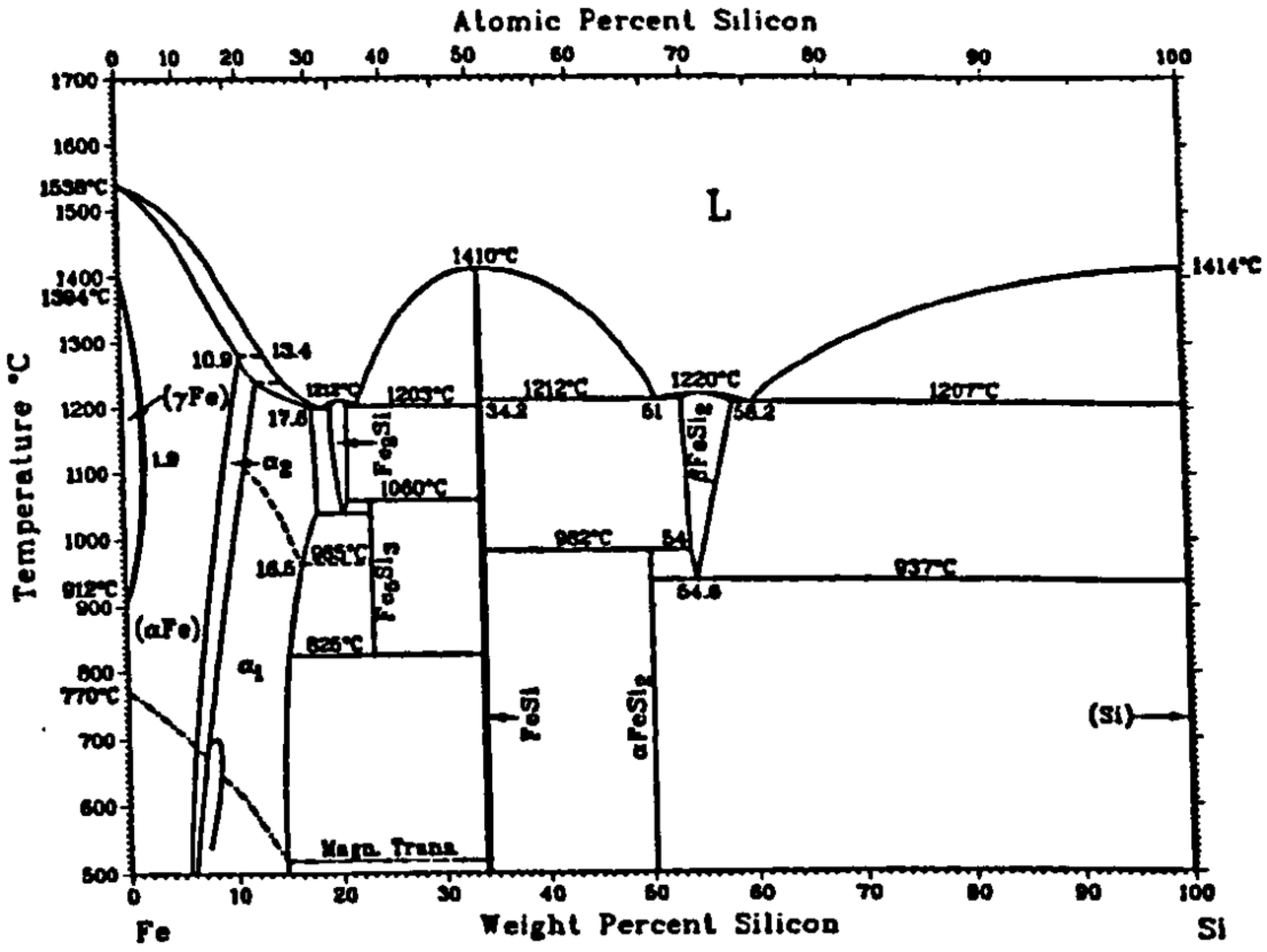

Fe-P

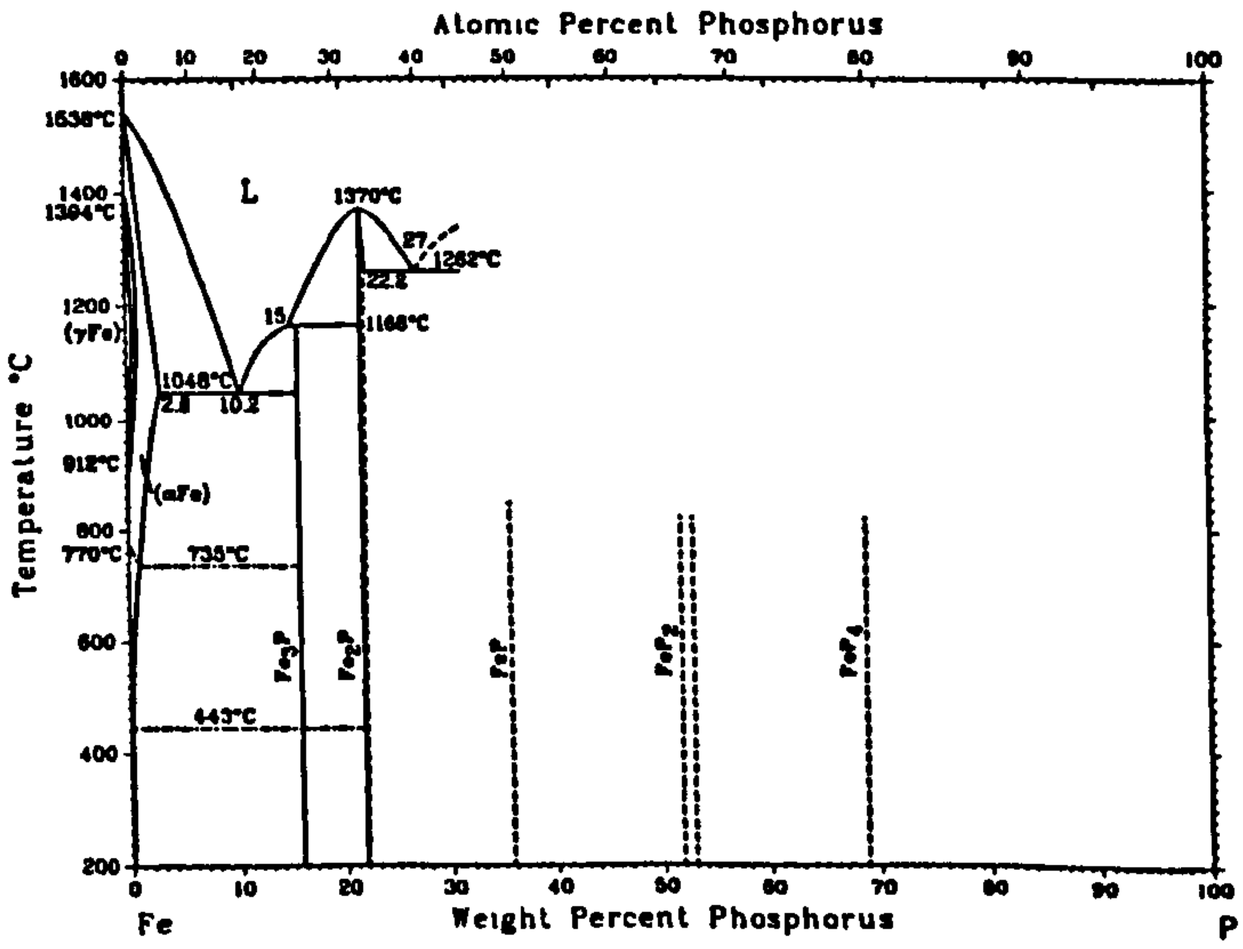

Fe-S

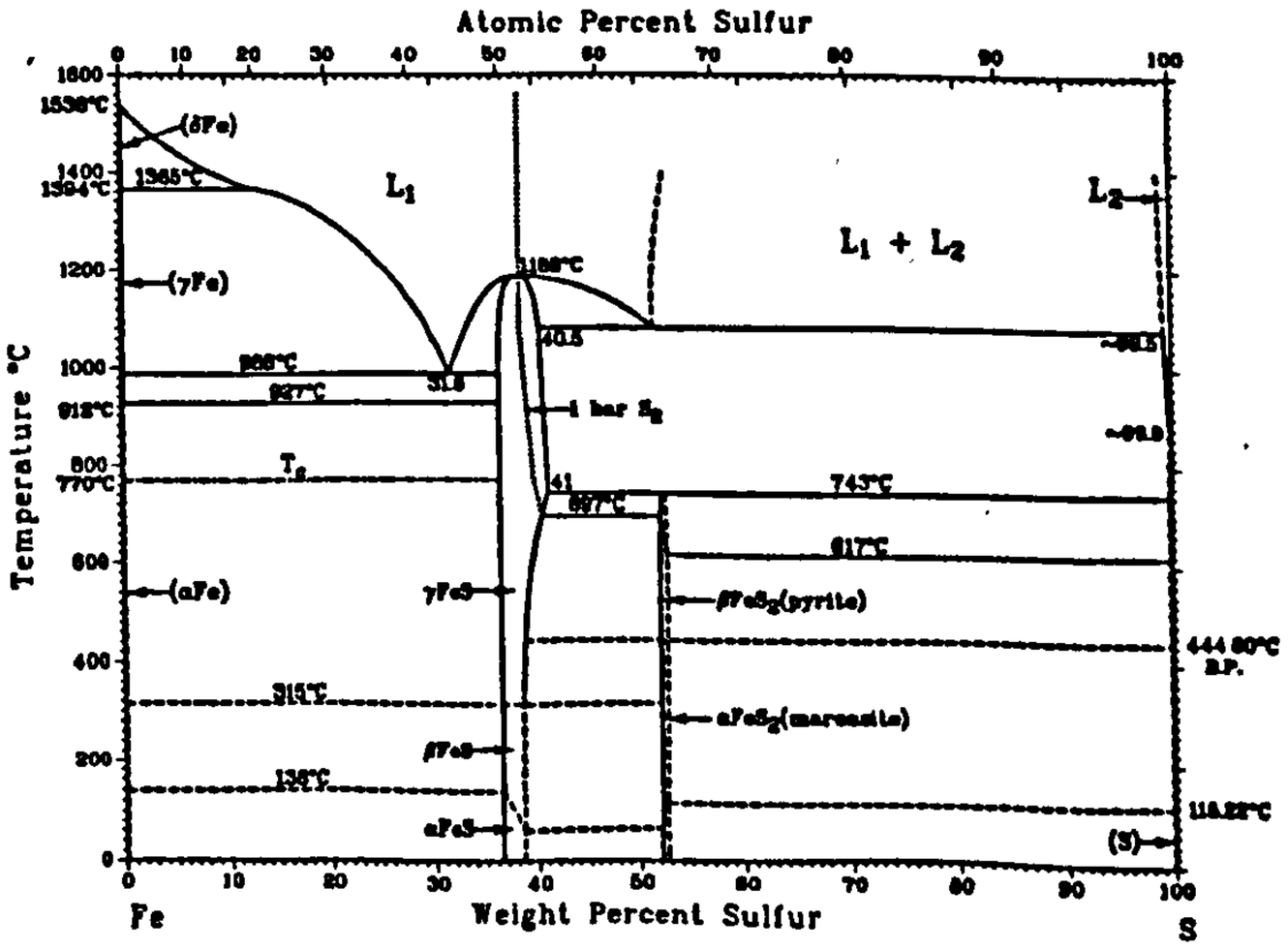

Figure 5.11 Phase diagrams of (Fe-Si), (Fe-P) and (Fe-S) [Baker *et al*, 1992]

5.2.2. THERMAL ANALYSIS

Figure 5.12 show the TGA and DTA curves of sample of 25 vol% Fe + ZrO_2 heated up to 1500°C with a heating rate of 10°C/minute. The TGA curve shows a little weight increase of 6% from 700°C to 1500°C that may be due to the reaction of the iron particles and the impurity of argon gas (oxygen). This reaction may occur since the sample was in loose powder. A DTA analysis of the same composition heated in air as expected showed a quick increase of weight of 16% between 350°C and 600°C coinciding with a strong and sharp exothermic peak at 500°C indicating an oxidation reaction. However for sintering of samples in argon the weight of the sample starts to increase slowly at much higher temperature (700°C) until 1500°C yielding a weak and slow reaction where the oxidation peak did not appear. This weight increase did not appear on compacted samples sintered in a furnace in argon meaning that an oxidation reaction did not occur.

The DTA curve in Figure 5.12 shows a sharp endothermic peak at 1350°C indicating the melting point of the iron (iron particles were found to be melted in the crucible). This melting point seems to be too low for iron with 0.2% carbon as given by the supplier. To confirm this melting point, the iron powder was analysed using DTA heated up to 1550°C in argon and the result showed that only a single sharp and strong endothermic peak occurred at 1370°C and the iron was found to be melted in the crucible. Furthermore a piece of gold was tested to recheck the performance of the DTA and the result showed that the temperature calibration was accurate. It is concluded that the iron used in this present study has low melting point (1350°C - 1370°C) and that this is due to the actual carbon content being higher than that informed by the supplier. Chemical analysis of the iron by combustion method indicated a total carbon content of about 1.5% which is consistent with the melting points determined.

STA 1640B *(VERSION - V5.12)*

SMP ID: 25vol%Fe+ZrO_2 RUN ID: MW-1-9 SIZE: 13.534 mg OPERATOR: MUH GAS: ARGON

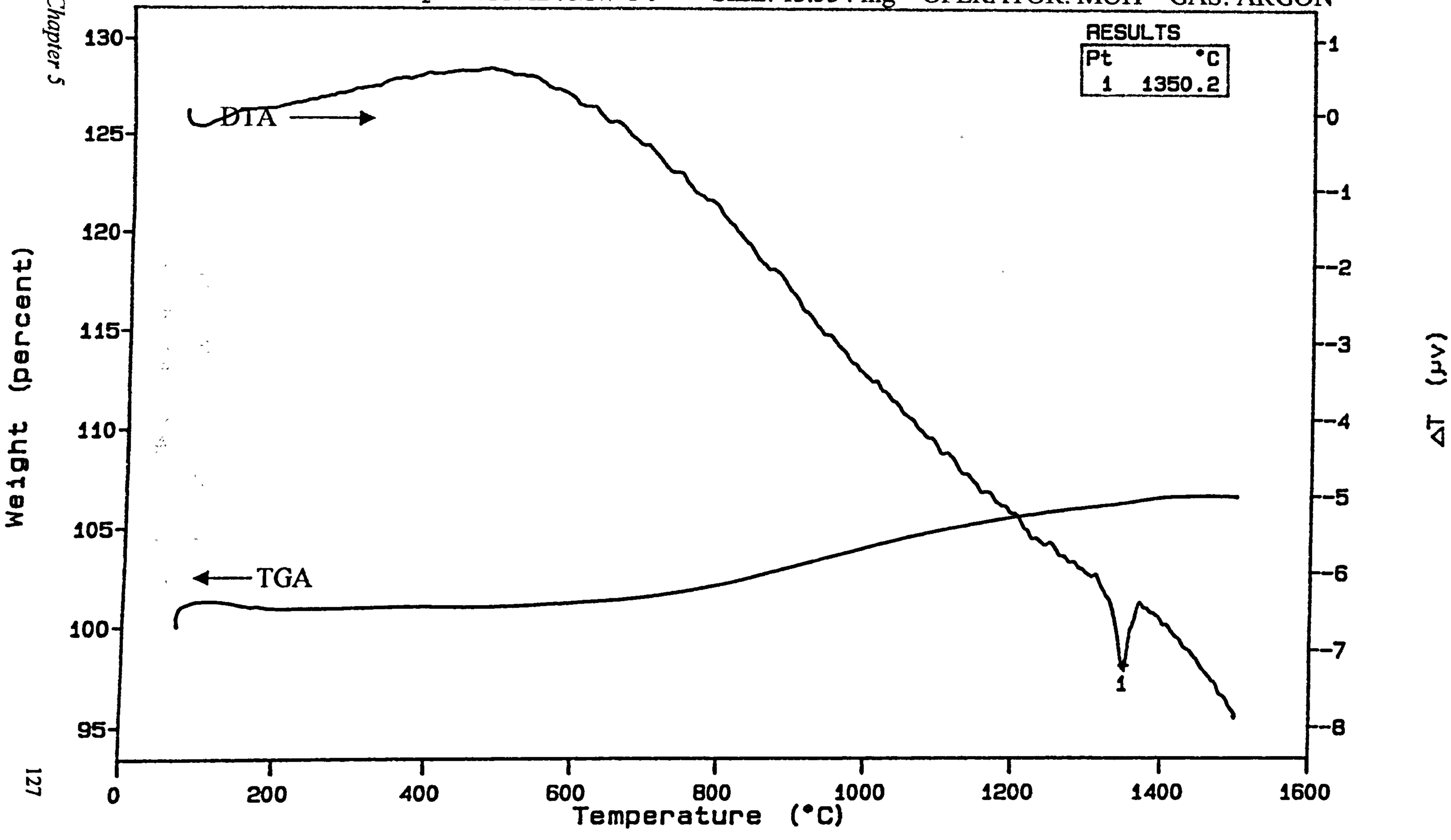

Figure 5.12 DTA and TGA curves of (25 vol% Fe + ZrO_2) sintered in argon

5.2.3. PHASE IDENTIFICATION

X-ray diffraction was used to identify the crystalline phases present in the samples of zirconia/iron composites. Figure 5.13 shows the XRD plots of as-sintered samples of zirconia/iron composites containing 5 vol%, 10 vol% and 25 vol% Fe sintered at 1450°C for 1 hour in argon. The d-spacings of the samples in Figure 5.13 are presented in Table 5.2. It can be seen in Figure 5.13 that the crystal structure of the matrix are in the form of tetragonal and monoclinic zirconia. In fact, monolithic zirconia sintered in the same conditions resulted in only tetragonal phase as discussed in Chapter 4. Consequently there is an effect of iron reinforcement on the matrix. One of the possible reasons to explain this phenomenon is reaction between the iron powder as the reinforcement and some of the yttria (as the stabiliser of zirconia) leading to de-stabilising the 3Y-TZP.

Previous researchers such as Kosco and Koss (1993) and Ogawa (1993) have reported the study of Fe-Y_2O_3 alloys. Kosco and Koss (1993) reported that the microstructures of the Fe-Y_2O_3 alloys (1-10 vol% Y_2O_3) examined using TEM contained iron phase, yttria phase and a new phase (about 10% volume) with unidentifiable diffraction pattern. They did not find yttrium iron garnet phase in the sample. Furthermore, in his study of Fe-Y_2O_3 Ogawa (1993) reported that investigating the microstructures using X-ray diffraction and electron probe microanalysis (EPMA) shows no chemical reaction layers formed in the boundary between iron and yttria. He added, however that unknown spots in the interface between iron and yttria have been found by using high-resolution electron microscope (HREM). This indicates that there is a chemical reaction layer in the boundary. However due to lack of information about such reaction and no thermodynamic data in the literature, it is still difficult to explain the mechanism of the de-stabilising of 3Y-TZP (as a solid solution) caused by a reaction of iron and yttria.

Nevertheless, a simple experiment was performed to observe this phenomenon. Two mixtures of yttria/iron containing 33 wt% Fe and 50 wt% Fe were

sintered at 1450°C for 1 hour in argon. The XRD analysis of these as-sintered samples showed peaks of α-Fe, Y_2O_3 and some unknown peaks as shown in Figure 5.14 and their d-spacings are presented in Table 5.3. Other analysis using DTA and TGA of 50 vol% Fe + 50 vol% Y_2O_3 heated at 10°C/minute until 1500°C show four endothermic peaks at 1142°C, 1265°C, 1275°C, and 1330°C on the DTA curve and a little weight increase of about 7% from 700°C to 1500°C on the TGA curve as shown in Figure 5.15. The little increase of weight may be due to a reaction of the iron with oxygen (impurity in the argon gas). Moreover, the sample was found completely melted in the crucible. According to the phase diagram of (Fe-Y_2O_3-Fe_2O_3) as shown in Figure 5.15(a), some compounds of yttrium-iron-oxide may be formed depending on composition, oxygen pressure and temperature. All those compounds can be formed at a very low oxygen pressure, so in the case of these simple mixtures of (Fe + Y_2O_3) where there is little amount of oxygen (impurity in the argon gas) some of yttrium-iron-oxide compounds may exist, but cannot be detected.

Above all, the mechanism of de-stabilising of 3Y-TZP due to the presence of iron still remains unclear and needs further investigation, because from the phase diagram in Figure 5.15(a) the formation of yttrium-iron-oxide compounds require oxygen, while Kosco and Koss (1993) reported in their study that no yttrium iron garnet was formed in Fe-Yttria alloys, however unidentifiable phase was found in the interface. In fact, in the present study, a very little amount of iron oxide (Fe_2O_3) is only found in the sample containing 25 vol% Fe as indicated by a very weak peak in the XRD as seen in Figure 5.13. This is due to an oxidation reaction of iron particles on the sample surfaces, because as the iron content increased more iron particles will distribute near or on the sample surfaces and are oxidised with oxygen from the impurity in the argon gas. Monoclinic and tetragonal zirconia are present in all the zirconia/iron and α-iron is also detected, increase with increasing iron content in the composites (Figure 5.13).

The experiments reported above show that iron melts during sintering possibly due to the high carbon content and it is clear that iron reacts with the

zirconia matrix. The evidence from the literature and the experiments with Fe and Y_2O_3 shows that reaction between these components produces a liquid phase but also depends on oxygen pressure in the system. It is concluded from these observations therefore that in the zirconia/iron composites during densification iron melts and reacts to form an Fe-Y-O liquid phase which on cooling precipitates an unidentified crystalline phase (XRD results Table 5.3) leaving destabilised zirconia matrix which partially transforms to monoclinic on cooling from sintering temperature.

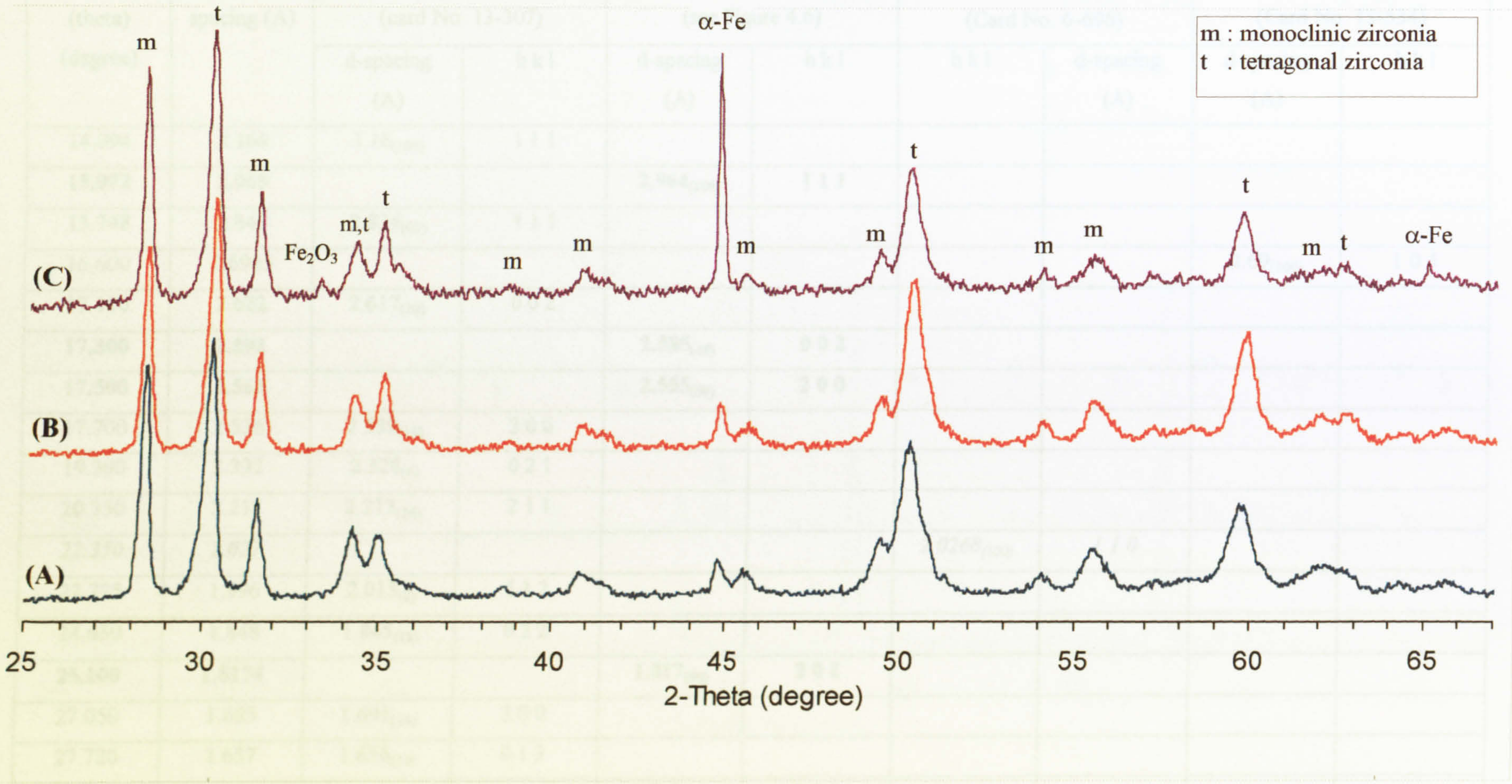

Figure 5.13 X-ray diffraction plot of as-sintered of (A). 5V%Fe+ZrO_2; (B). 10V%Fe+ZrO_2 and (C) 25V%Fe+ZrO_2 composites sintered at 1450°C for 1h in argon

Figure 5.2. The measured d-spacing of XRD analysis of zirconia/iron composites as shown in Figure 5.13.

Angle (theta) (degree)	Measured d-spacing (A)	Monoclinic zirconia (card No. 13-307)		Tetragonal zirconia (see Figure 4.6)		α-Fe (Card No. 6-696)		Fe_2O_3 (Card No. 13-534)	
		d-spacing (A)	h k l	d-spacing (A)	h k l	h k l	d-spacing (A)	d-spacing (A)	h k l
14.094	3.166	$3.16_{(100)}$	1 1 1						
15.072	**2.965**			**$2.964_{(100)}$**	**1 1 1**				
15.748	2.840	$2.834_{(65)}$	1 1 1						
16.600	2.6985							$2.69_{(100)}$	1 0 4
17.100	2.622	$2.617_{(20)}$	0 0 2						
17.300	**2.592**			**$2.585_{(45)}$**	**0 0 2**				
17.500	**2.563**			**$2.555_{(60)}$**	**2 0 0**				
17.700	2.536	$2.538_{(14)}$	2 0 0						
19.300	2.332	$2.328_{(6)}$	0 2 1						
20.350	2.217	$2.213_{(14)}$	2 1 1						
22.350	*2.027*					*$2.0268_{(100)}$*	*1 1 0*		
22.725	1.996	$2.015_{(8)}$	1 1 2						
24.650	1.848	$1.845_{(18)}$	0 2 2						
25.100	**1.8174**			**$1.817_{(90)}$**	**2 0 2**				
27.050	1.695	$1.691_{(14)}$	3 0 0						
27.720	1.657	$1.656_{(14)}$	0 1 3						
29.880	**1.547**			**$1.542_{(70)}$**	**3 1 1**				
31.020	1.496	$1.495_{(10)}$	2 1 3						
31.250	**1.486**			**$1.480_{(45)}$**	**2 2 2**				
32.530	*1.4336*					*$1.4332_{(20)}$*	*2 0 0*		

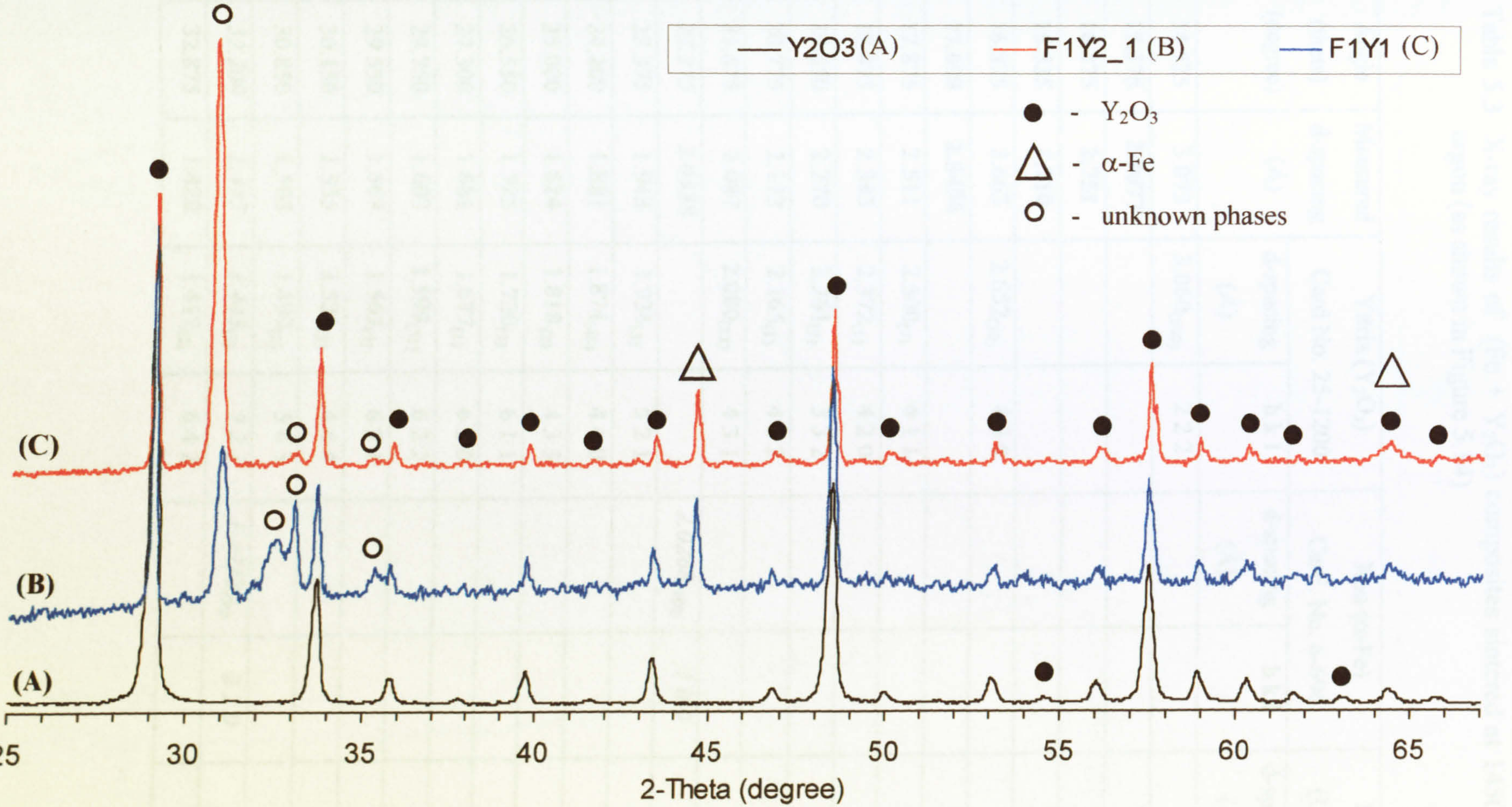

Figure 5.14 XRD plot of (A) Y_2O_3, (B) 50 wt% Fe + Y_2O_3, and (C) 33 w% Fe + Y_2O_3 (B and C were sintered at 1450°C for 1h in argon).

Table 5.3 X-ray results of (Fe + Y_2O_3) composites sintered at 1450°C for 1 h in argon (as shown in Figure 5.14)

Angle (theta) (degree)	Measured d-spacing (Å)	Yttria (Y_2O_3) Card No. 25-1200		Iron (α-Fe) Card. No. 6-696		New Phases (UNKNOWN)	
		d-spacing (Å)	h k l	d-spacing (Å)	h k l	d-spacing (Å)	h k l
14.525	3.073	$3.060_{(100)}$	2 2 2				
15.375	**2.9077**					**V**	
16.275	**2.751**					**V**	
16.525	**2.710**					**V**	
16.825	2.663	$2.652_{(30)}$	4 0 0				
17.600	**2.5496**					**V**	
17.875	2.511	$2.500_{(7)}$	4 1 1				
18.875	2.383	$2.372_{(1)}$	4 2 0				
19.850	2.270	$2.261_{(8)}$	3 3 2				
20.775	2.173	$2.165_{(1)}$	4 2 2				
21.675	2.087	$2.080_{(12)}$	4 3 1				
22.275	*2.0338*			*$2.0268_{(100)}$*	*1 0 0*		
23.375	1.943	$1.936_{(3)}$	5 2 1				
24.200	1.881	$1.874_{(46)}$	4 4 0				
25.000	1.824	$1.818_{(2)}$	4 3 3				
26.550	1.725	$1.720_{(5)}$	6 1 1				
27.300	1.681	$1.677_{(1)}$	6 2 0				
28.750	1.603	$1.599_{(31)}$	6 2 2				
29.550	1.563	$1.563_{(7)}$	6 3 1				
30.150	1.535	$1.531_{(5)}$	4 4 4				
30.850	1.503	$1.499_{(2)}$	5 4 3				
32.200	*1.447*	*$1.443_{(3)}$*	*7 2 1*	*$1.4332_{(20)}$*	*2 2 0*		
32.875	1.420	$1.417_{(2)}$	6 4 2				

STA 1640B *(VERSION - V5.12)*

SMP ID: 50vol%Fe+50vol%Y_2O_3 RUN ID: MW-1-10 SIZE: 12.977 mg OPERATOR: MUH GAS: ARGON

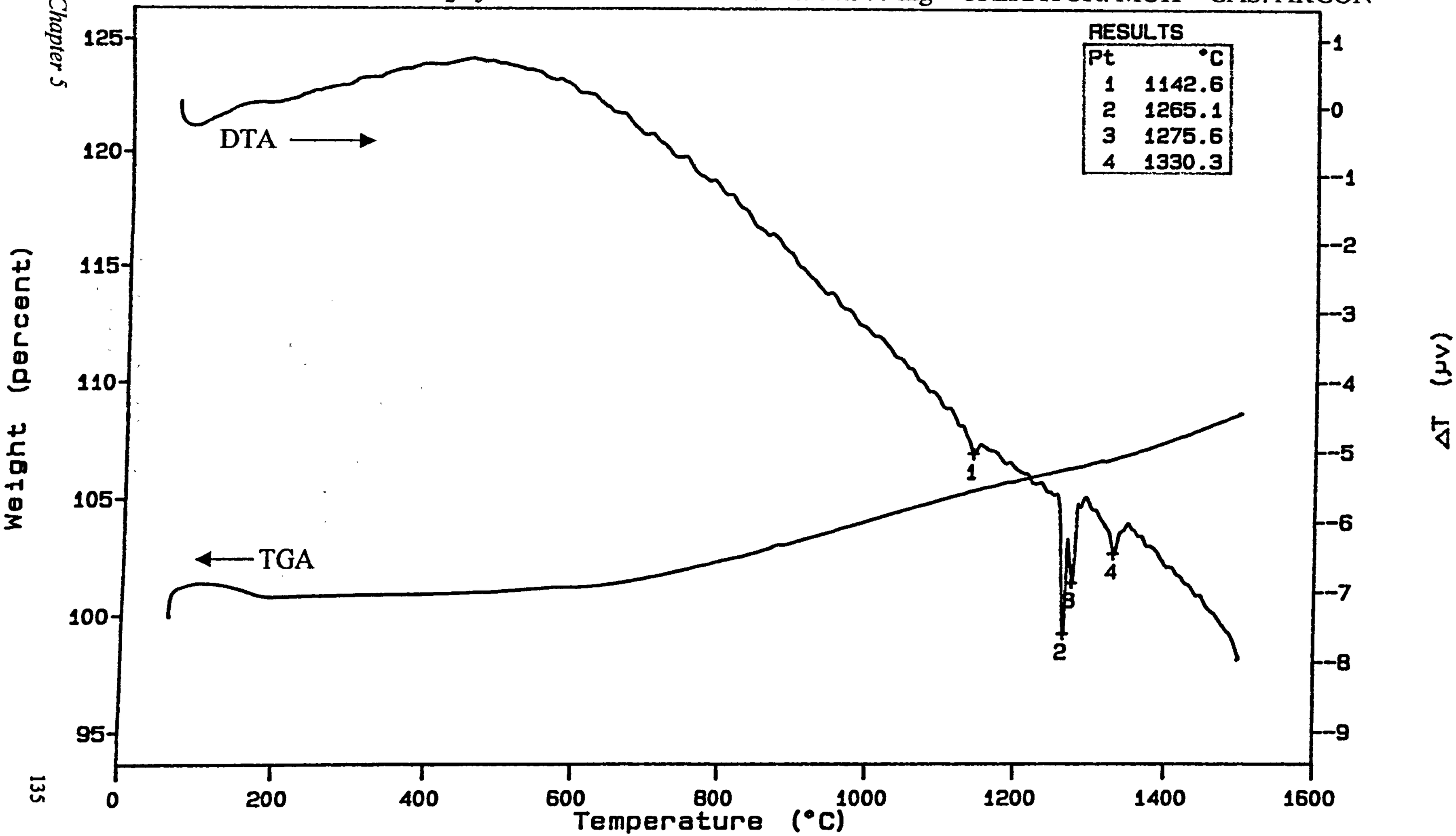

Figure 5.15 DTA and TGA curves of (50 vol% Fe + 50 vol%Y_2O_3) sintered in argon

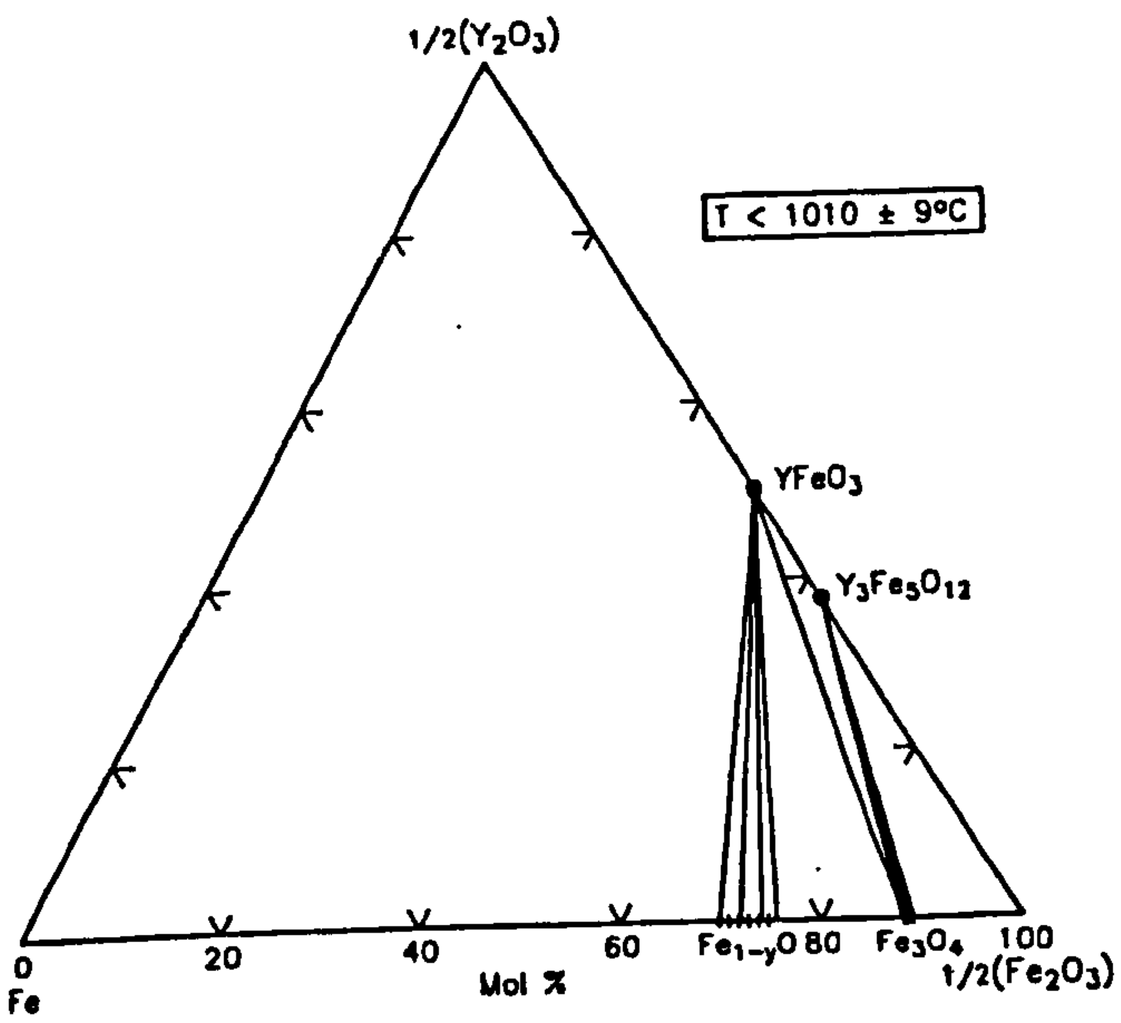

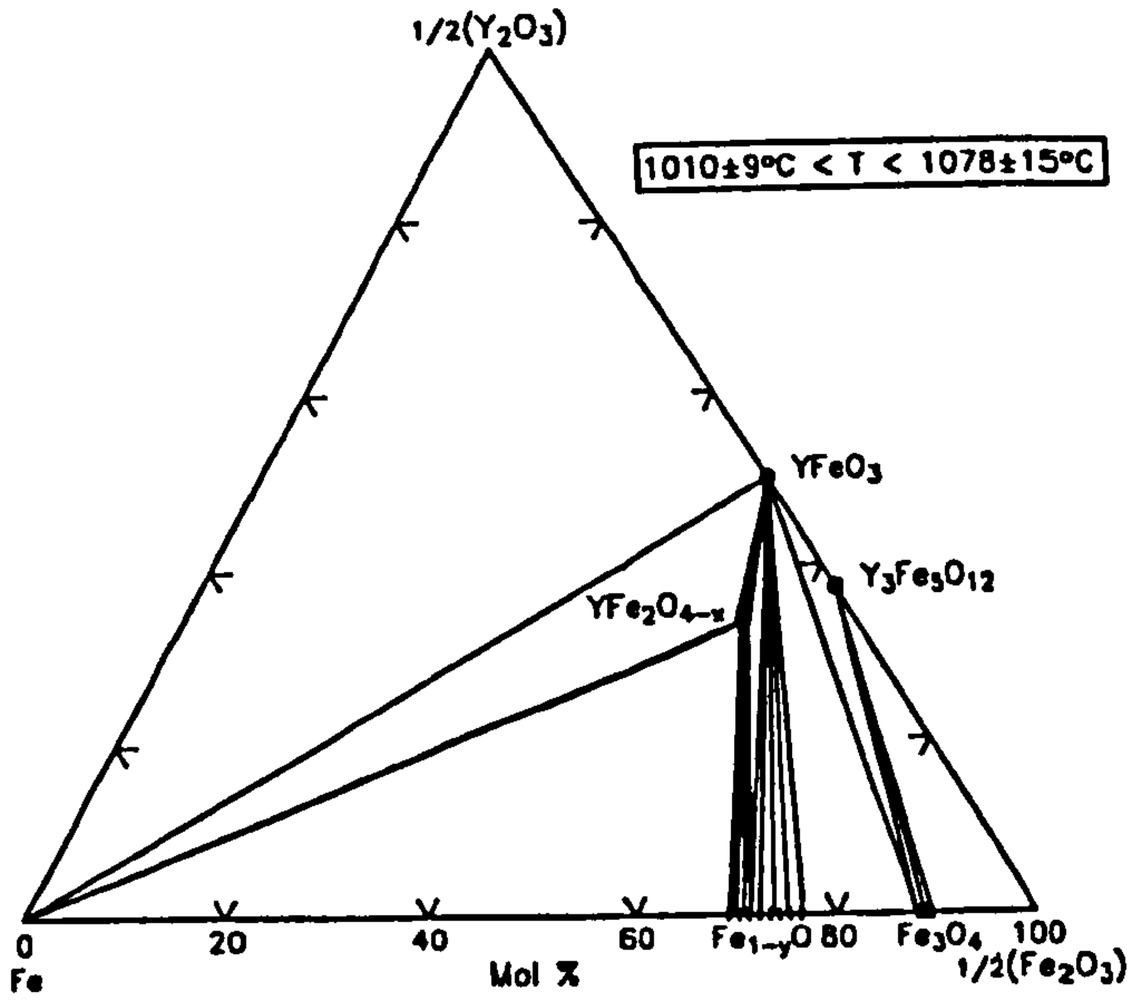

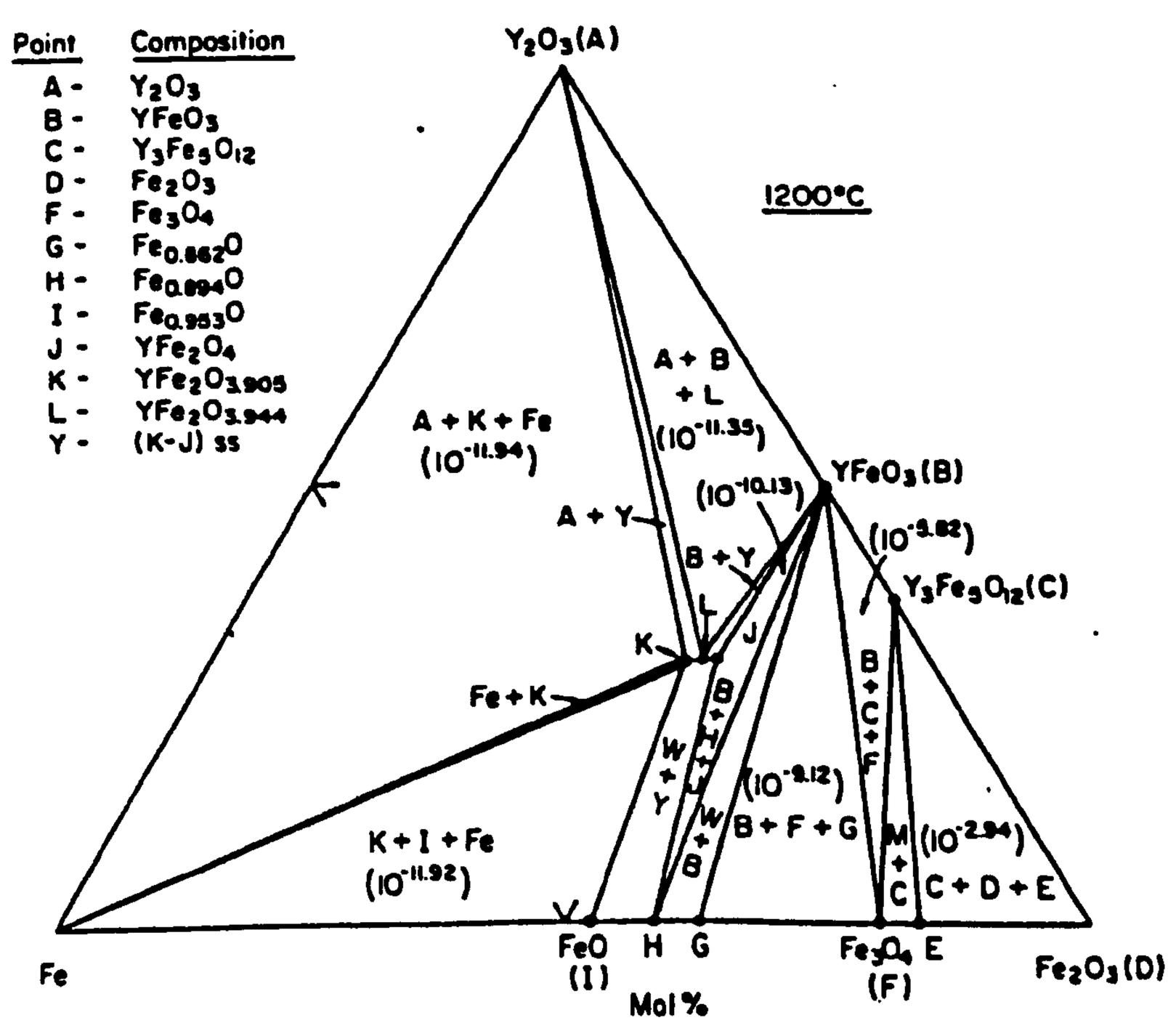

Figure 5.15(a) Phase diagram of (Fe-Fe_2O_3-Y_2O_3) system at 1200°C [Kimizuka and Katsura, 1975; Levin *et al*]

5.2.4. MICROSTRUCTURES

The as-received iron powder used in the present work has rounded or spherical shape with mean particle sizes 6 -8 micron as shown in Figure 5.16. This shape and fine particle size are typical for iron made by the carbonyl process. It can be seen in the Figure that some particles seem to be chained or agglomerated.

The microstructures of zirconia/iron composites containing 10 vol% Fe and 25 vol% Fe are shown in Figures 5.17 and 5.18 respectively. It can be seen in both Figures that the particles are well distributed. Some particles that are close to each other join and form larger particles. For the sample of 25 vol% Fe + ZrO_2 more iron particles are joined together as the distance between particles is smaller. At this condition where the iron particles are small (6 micron) and the distances between them are small, the sintering process is not only in the matrix but also occurs in the reinforcement. This phenomenon plus the possible reaction between iron and yttria cause the prediction of linear shrinkage, given by Edrees and Hendry (1999) (Equation 5.1) to be inaccurate. The linear shrinkage of zirconia/iron composites is much greater than that calculated using Equation 5.1.

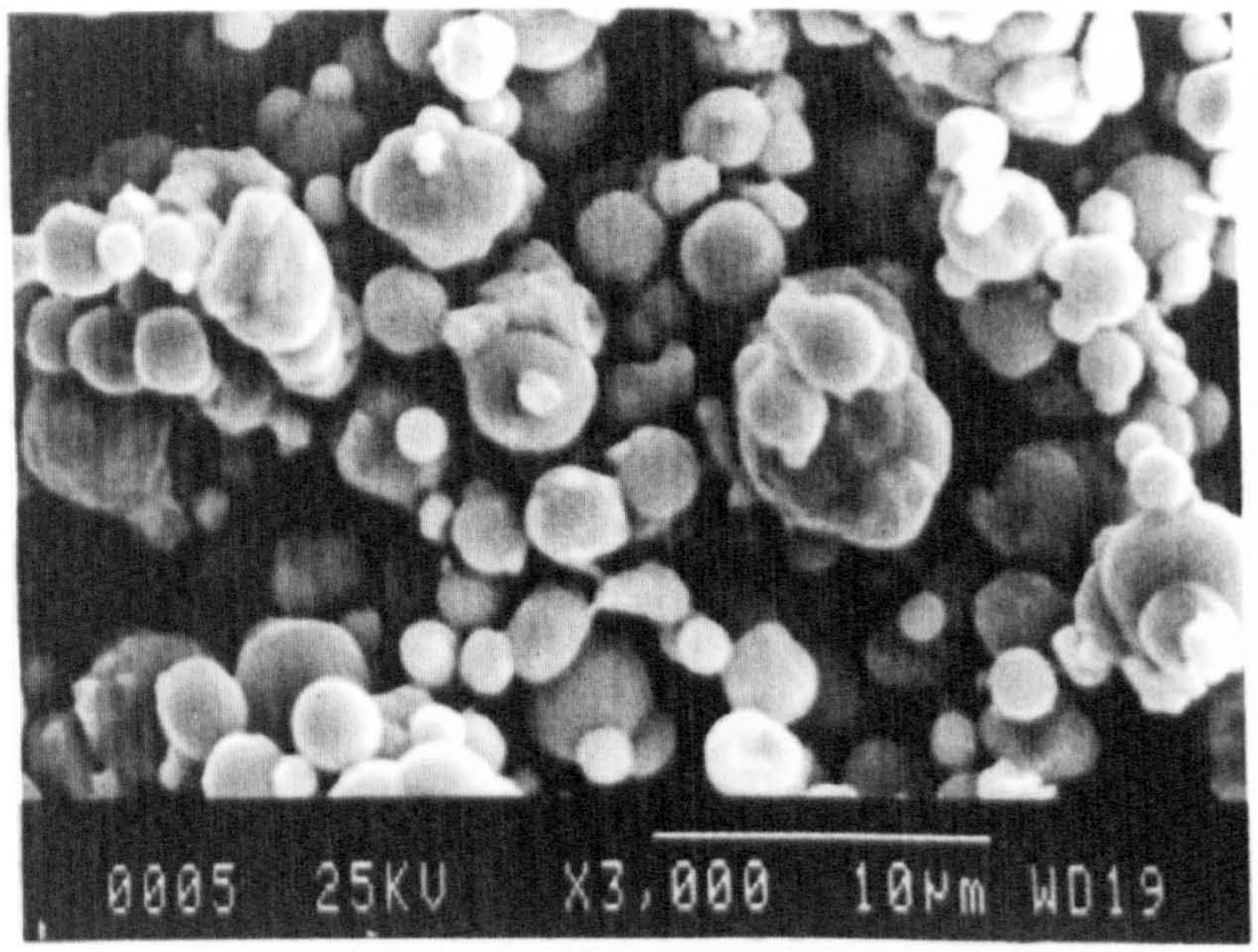

Figure 5.16. SEM photograph of as-received iron powder.

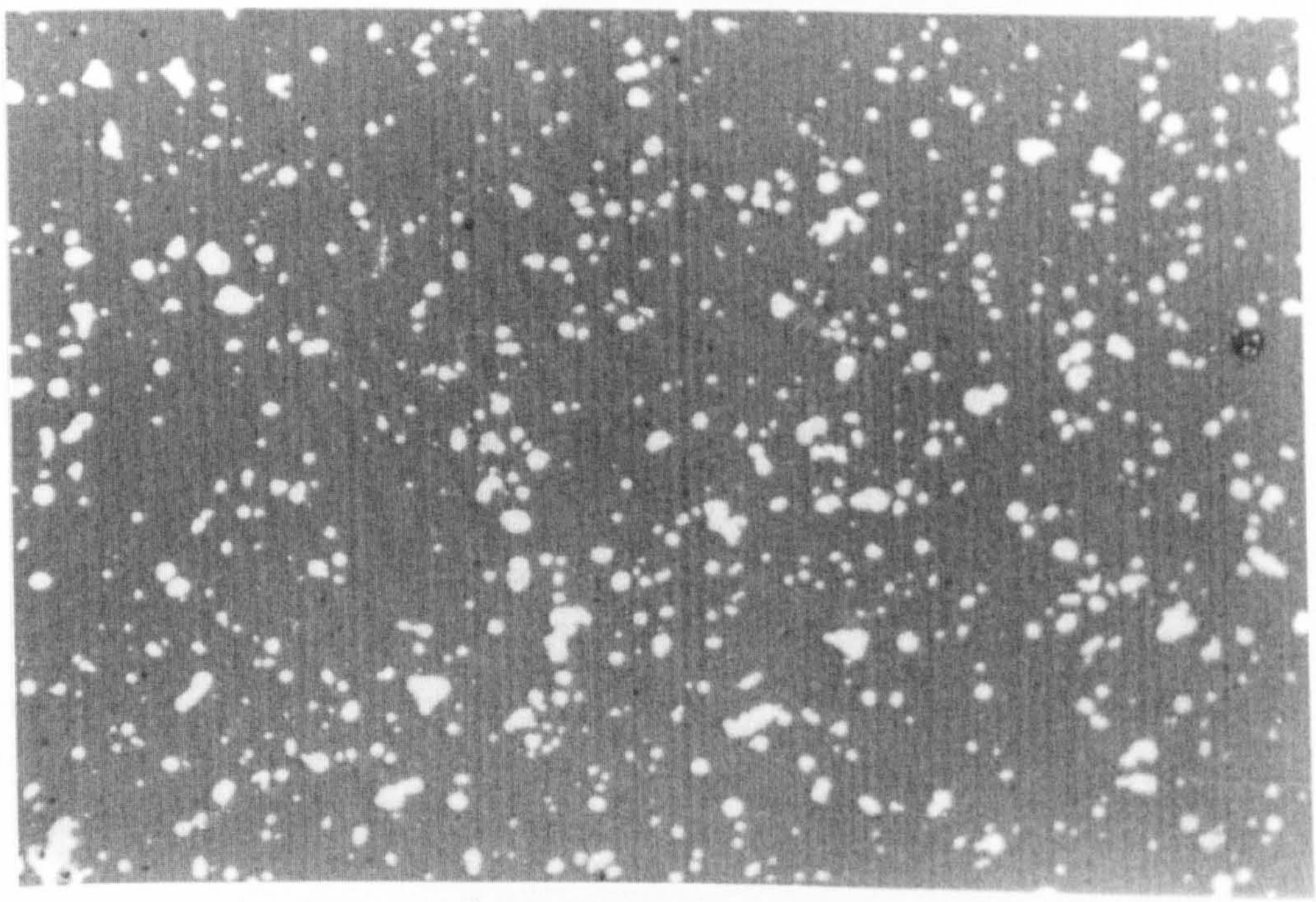

Figure 5.17. Optical micrograph of (10 vol%Fe+ZrO_2) sintered at 1450°C for 1 h in argon

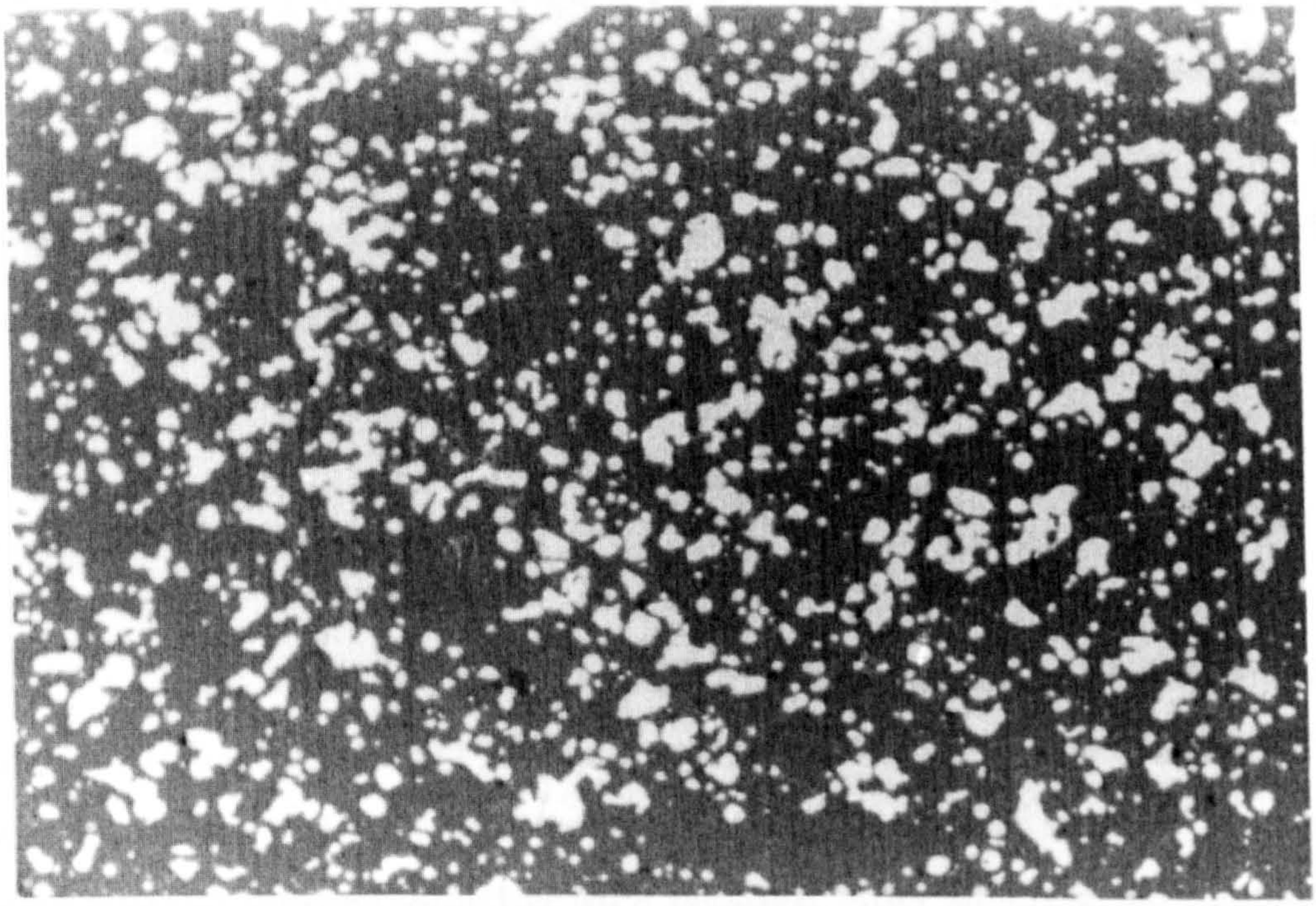

Figure 5.18. Optical micrograph of (25 vol%Fe+ZrO_2) sintered at 1450°C for 1 h in argon

5.3. ZIRCONIA/STAINLESS STEEL AISI 316 COMPOSITES

The stainless steel used in this experiment was AISI 316 type, which has the composition of 17.8% Cr, 13.0% Ni, 2.8% Mo, Fe balance and C < 0.03%. The maximum particle size is 45 micron.

5.3.1. DENSIFICATION

Samples of composites of zirconia/AISI 316 containing 10 vol% and 25 vol% of AISI 316 were sintered at various temperatures between 1300°C and 1500°C for 1 hour in argon and heated and cooled at 10°C/minute. The samples were prepared using uniaxial pressing with 130 MPa pressure. After sintering the samples weight decreased about -0.2% due to the loss of moisture content. The relative density of those samples is presented in Figure 5.19. The samples sintered at 1300°C are about 83% of theoretical density, but sintering at 1400°C and above resulted in a density greater than 95% of the theoretical.

The linear dimensional changes of samples during sintering were observed using TMA equipment. Figure 5.20 shows the linear shrinkage of a sample of 25 vol% AISI 316 + ZrO_2 during sintering at 1450°C for 1 hour in argon. As for the other composites reported above, very little shrinkage occurs below 300°C and the sample then expands by 2% up to 1100°C. A linear shrinkage of 19% occurs during heating between 1100°C and 1450°C and during isothermal processing at 1450°C a further shrinkage of 1.5% occurs in the sample. So the final linear shrinkage at this sintering condition is 18.5% and leads to almost fully dense samples where the shrinkage is predominantly during the heating process (92%). The maximum densification rate occurs at 1353°C. In comparison to monolithic zirconia, the starting densification temperatures are similar, but the final linear shrinkage of this composite was lower than that of monolithic zirconia because of the presence of AISI 316 particles.

The densification rate of the composites containing 25 vol% AISI 316 is the same with that of monolithic zirconia. This differs from the model proposed by Edrees and Hendry (1999) where the maximum densification rate would decrease with increasing amount of reinforcement. This difference may be due to the melting and local sintering in the particles where the particles start to join together and does therefore not conform to the conditions required for Equation 5.1.

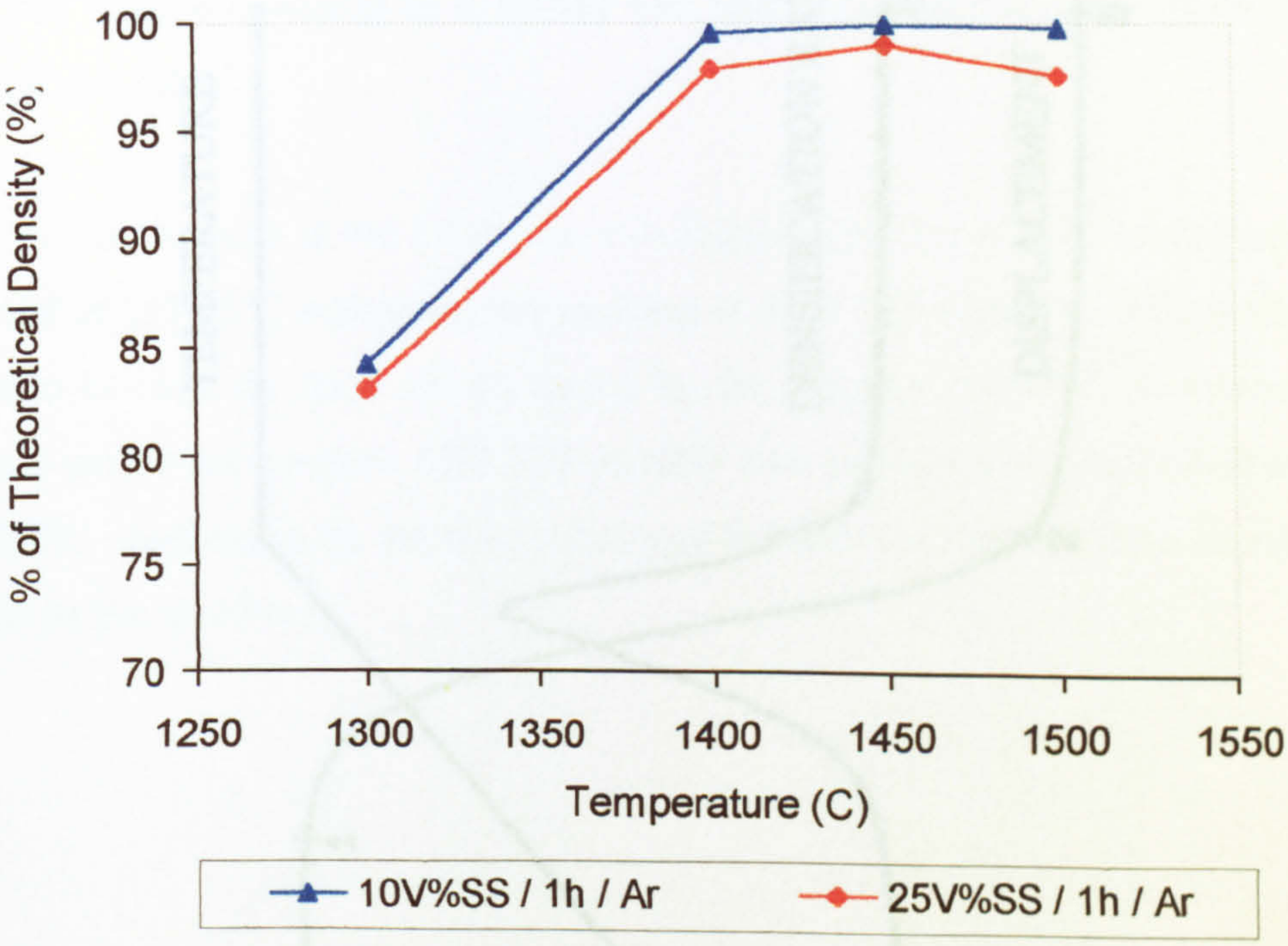

Figure 5.19. The effect of temperature and stainless steel content on final density of sintered samples

TMA 1500 *(VERSION V5.12)*

SMP ID: 25vol%AISI316+ZrO_2 RUN ID: MWW-19 SIZE: 2.293 mm OPERATOR: MUH GAS: ARGON

RESULTS

Pt	min	°C	%
1	109.77	1100.7	2.045
2	144.82	1449.7	-17.034
3	203.32	1449.7	-18.501

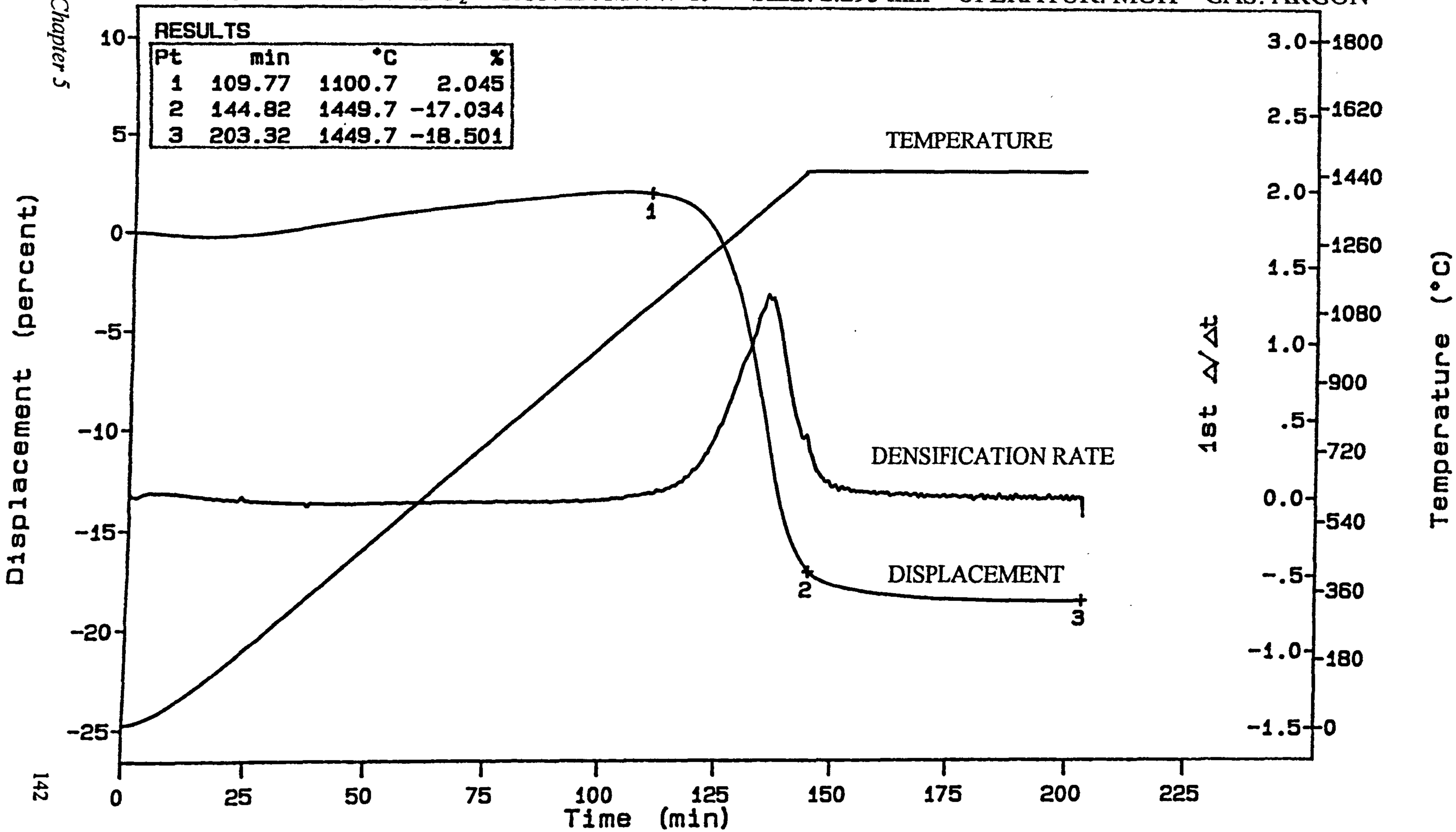

Figure 5.20 Densification behaviour of (25 vol% AISI 316 + ZrO_2) sintered in argon

5.3.2. THERMAL ANALYSIS

DTA and TGA curves of sample of 25 vol% AISI 316 + ZrO_2 heated to 1500°C in argon with a heating rate 10°C/minute are presented in Figure 5.21. As mentioned in the other two composites, this TGA curve also shows a slow weight increase of 5% from 1100°C to 1500°C due to a slow and weak reaction of the AISI 316 particles with impurity (oxygen) in the argon gas. In a similar sintering of the same composition in air, a rapid weight increase of 14% occurred between 900°C and 1200°C corresponding to a strong and sharp exothermic peak of an oxidation reaction at 1150°C.

It can be seen in the DTA curve in Figure 5.21 that a sharp endothermic peak occurred at 1450.5°C indicating the melting of AISI 316 particles. This melting point seems to be high for AISI 316 as stated by the supplier (1400°C). However, a DTA analysis performed on pure AISI 316 powder also showed a single endothermic peak at 1465°C confirming its melting point and the sample was found to be completely melted in the crucible.

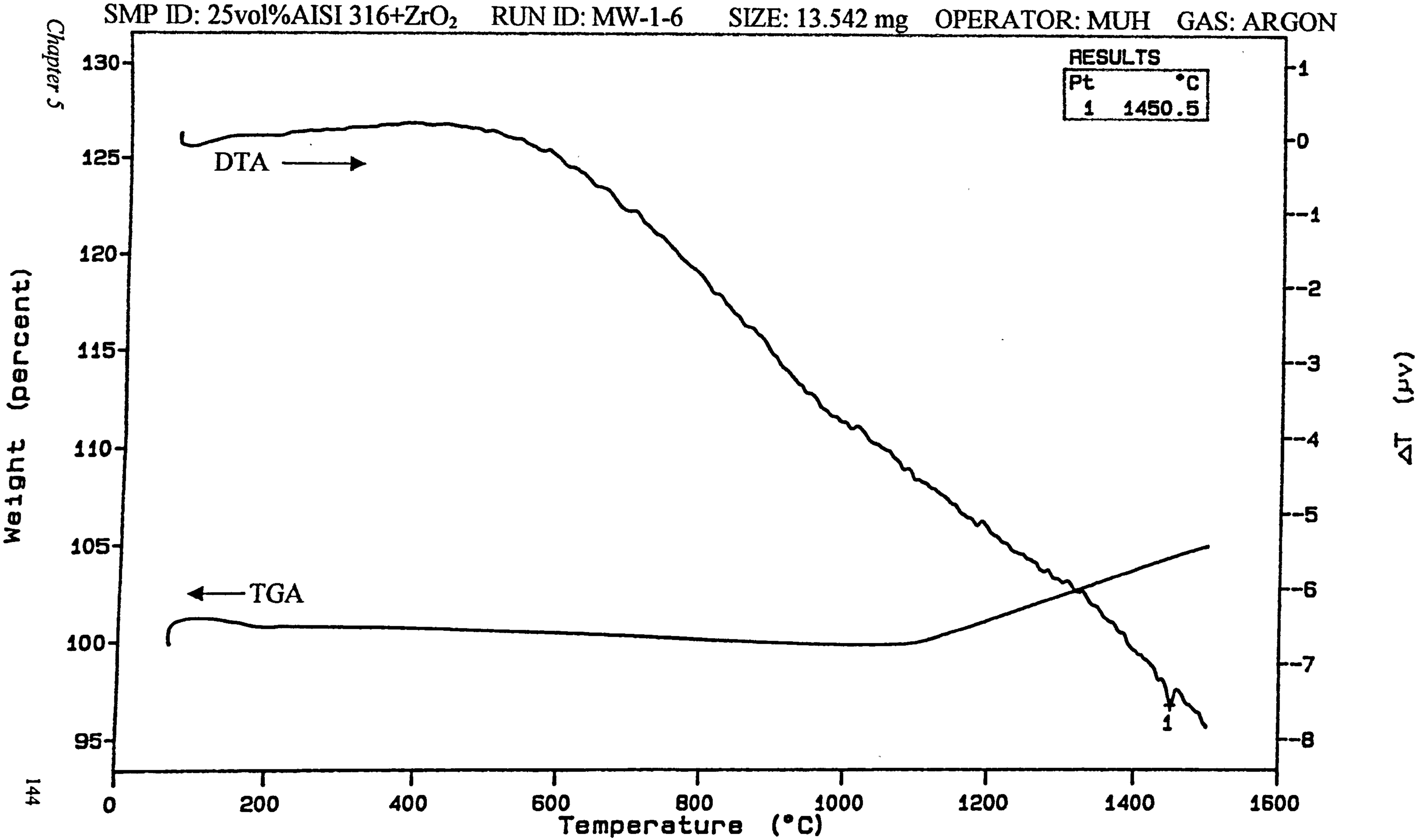

Figure 5.21 DTA and TGA curves of (25 vol% AISI 316 + ZrO_2) sintered in argon

5.3.3. PHASE IDENTIFICATION

Phase identification performed using XRD analysis showed the presence of tetragonal zirconia and AISI 316 peaks as indicated in Figure 5.22. The values of the d-spacing of those peaks and the matching phases are shown in Table 5.4. As expected, only tetragonal zirconia is present in these samples as discussed in Chapter 4 and in these composites the AISI 316 does not affect the structure of the matrix. A mechanical stress applied to these composites can transform the tetragonal zirconia to monoclinic form because of the presence of metastable tetragonal in the materials. Figure 5.23 shows this phenomenon where a mechanical stress from cutting the sample can cause such transformation.

It can also be seen in Figure 5.22 that the phenomenon of a reaction between iron and yttria which causes de-stabilising zirconia does not occur in zirconia/AISI 316 composites, although AISI 316 contains about 69% iron. This is due to the chemical stability of AISI 316 (lower activity of iron), and different structure and properties from α-iron. Moreover, AISI 316 exhibits passivity and therefore reduces the chemical reactivity due to the presence of high chromium content. This passive behaviour results from the formation of very thin oxide film on the metal surface which serves as barrier or protection. Finally, as seen from the DTA data, iron in the composites melts at 1350°C (Figure 5.12) while the stainless steel remains solid up to 1450°C (Figure 5.21). Combination of all of these factors results in no Fe-Y-O reaction in the stainless steel composites and the zirconia remains in the tetragonal form.

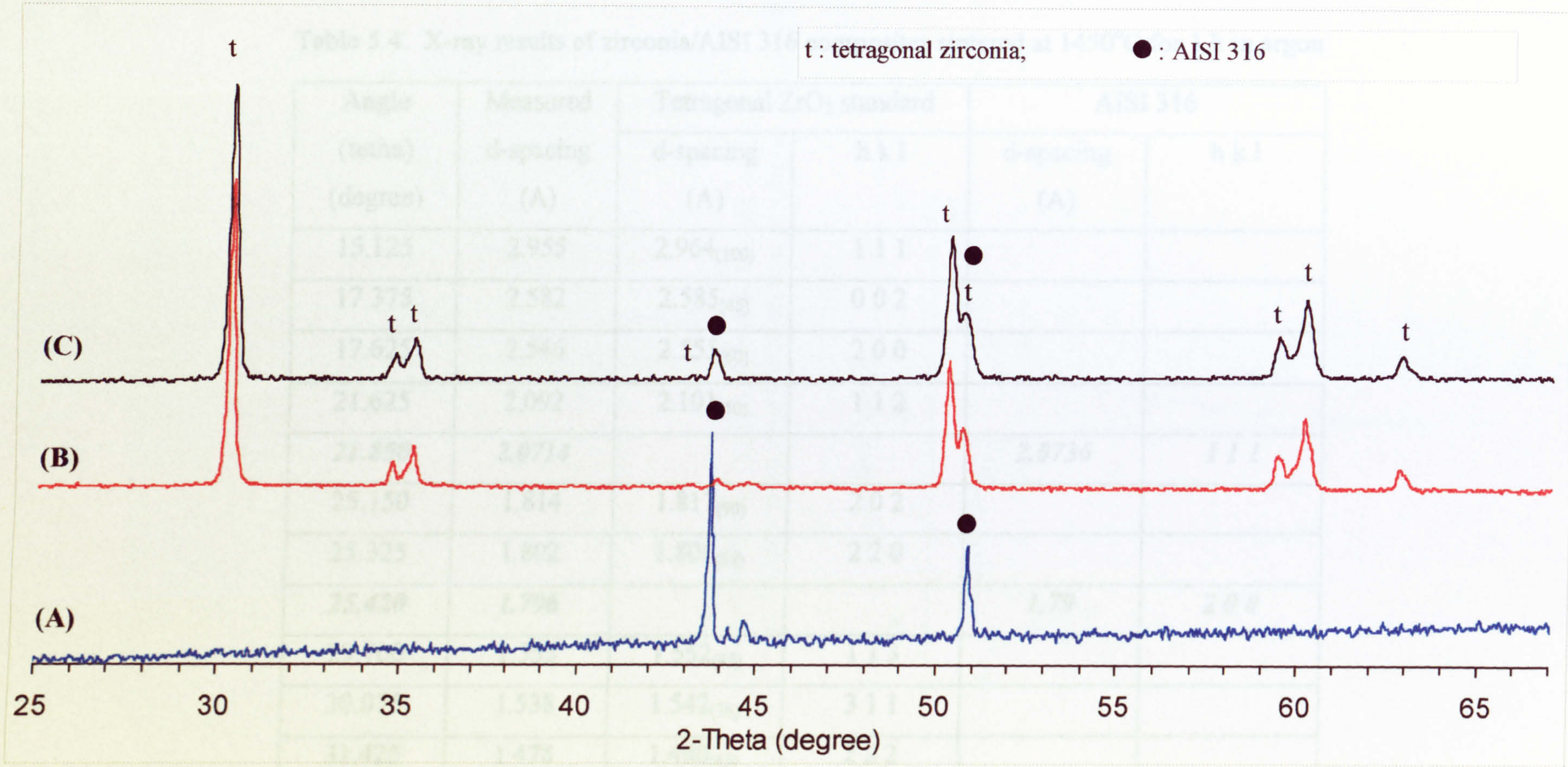

Figure 5.22 XRD plot of (A) AISI 316, (B) 10 vol% AISI 316 + ZrO_2, and (C) 25 vol% AISI 316 + ZrO_2 (B and C were sintered at 1450°C for 1h in argon).

Table 5.4. X-ray results of zirconia/AISI 316 composites sintered at 1450°C for 1 h in argon

Angle (tetha) (degree)	Measured d-spacing (A)	Tetragonal ZrO_2 standard		AISI 316	
		d-spacing (A)	h k l	d-spacing (A)	h k l
15.125	2.955	$2.964_{(100)}$	1 1 1		
17.375	2.582	$2.585_{(45)}$	0 0 2		
17.625	2.546	$2.555_{(60)}$	2 0 0		
21.625	2.092	$2.101_{(10)}$	1 1 2		
21.850	***2.0714***			***2.0736***	***1 1 1***
25.150	1.814	$1.817_{(90)}$	2 0 2		
25.325	1.802	$1.806_{(60)}$	2 2 0		
25.420	***1.796***			***1.79***	***2 0 0***
29.700	1.555	$1.552_{(45)}$	1 1 3		
30.075	1.538	$1.542_{(70)}$	3 1 1		
31.425	1.478	$1.480_{(45)}$	2 2 2		

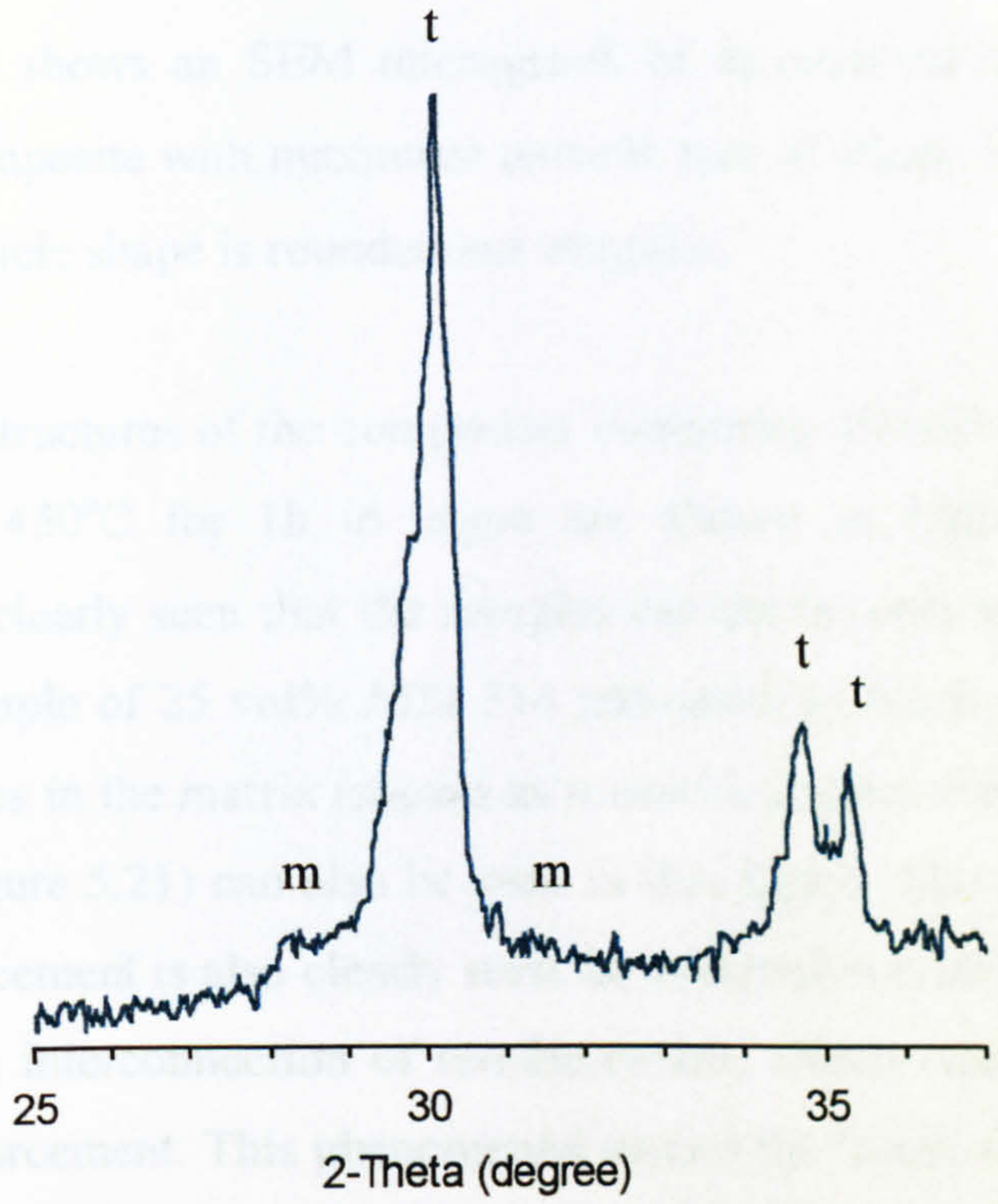

Figure 5.23 Effect of mechanical stress from cutting of sample of (25 vol% AISI 316 + ZrO_2) sintered at 1450°C for 1hour in argon

5.3.4. MICROSTRUCTURES

Figure 5.24 shows an SEM micrograph of as-received stainless steel AISI 316 used in the composite with maximum particle size of 45μm. It can be seen in the Figure that the particle shape is rounded but irregular.

The microstructures of the composites containing 10 vol% and 25 vol% AISI 316 sintered at 1450°C for 1h in argon are shown in Figures 5.25 and 5.26 respectively. It is clearly seen that the samples are dense, only a very little porosity appears in the sample of 25 vol% AISI 316 indicated by black areas. Furthermore, the melted particles in the matrix (shown as rounded, regular shapes) as indicated in DTA analysis (Figure 5.21) can also be seen in this figure. The variation of particle size of the reinforcement is also clearly seen. In composites containing 25 vol% AISI 316 there is some interconnection of reinforcement, which causes sintering also to occur in the reinforcement. This phenomenon causes the linear shrinkage of 25 vol% AISI 316 + ZrO_2 is to be greater than that calculated using the model given by Edrees and Hendry (1999) in Equation 5.1.

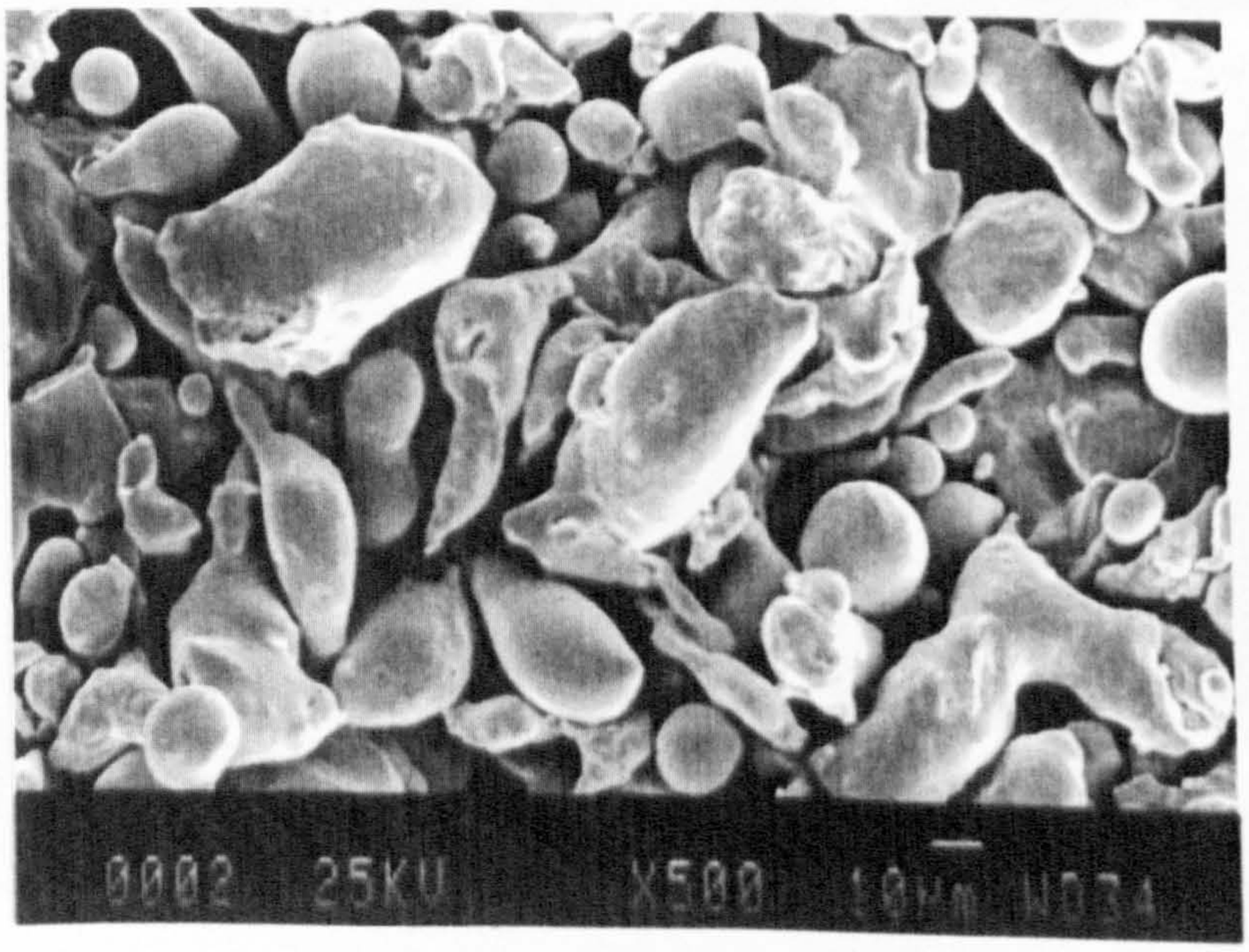

Figure 5.24. SEM photograph of as-received stainless steel AISI 316 powder.

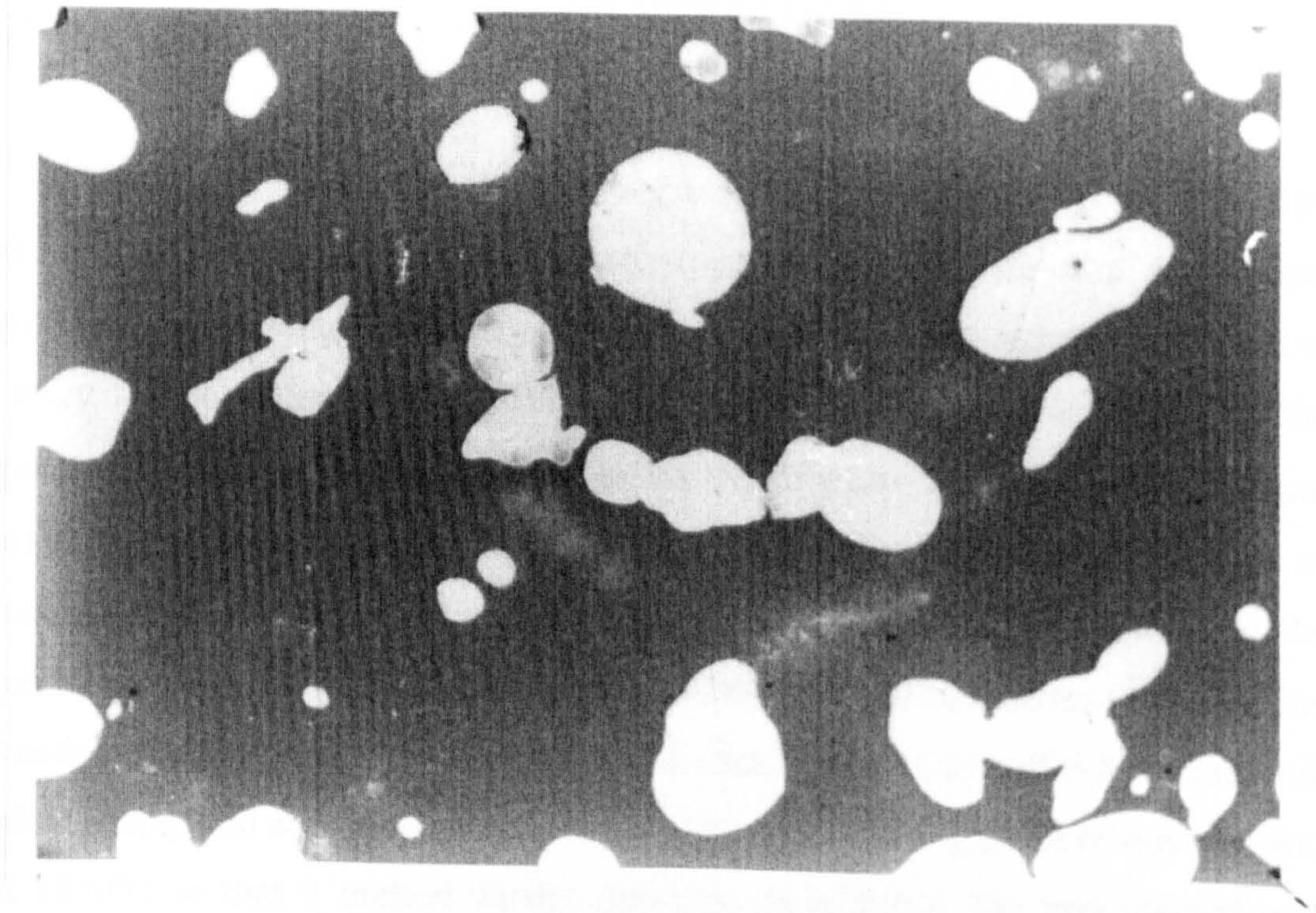

25 μm

Figure 5.25. Optical micrograpgh of (10 vol%AISI 316 + ZrO_2) sintered at 1450°C for 1 h in argon

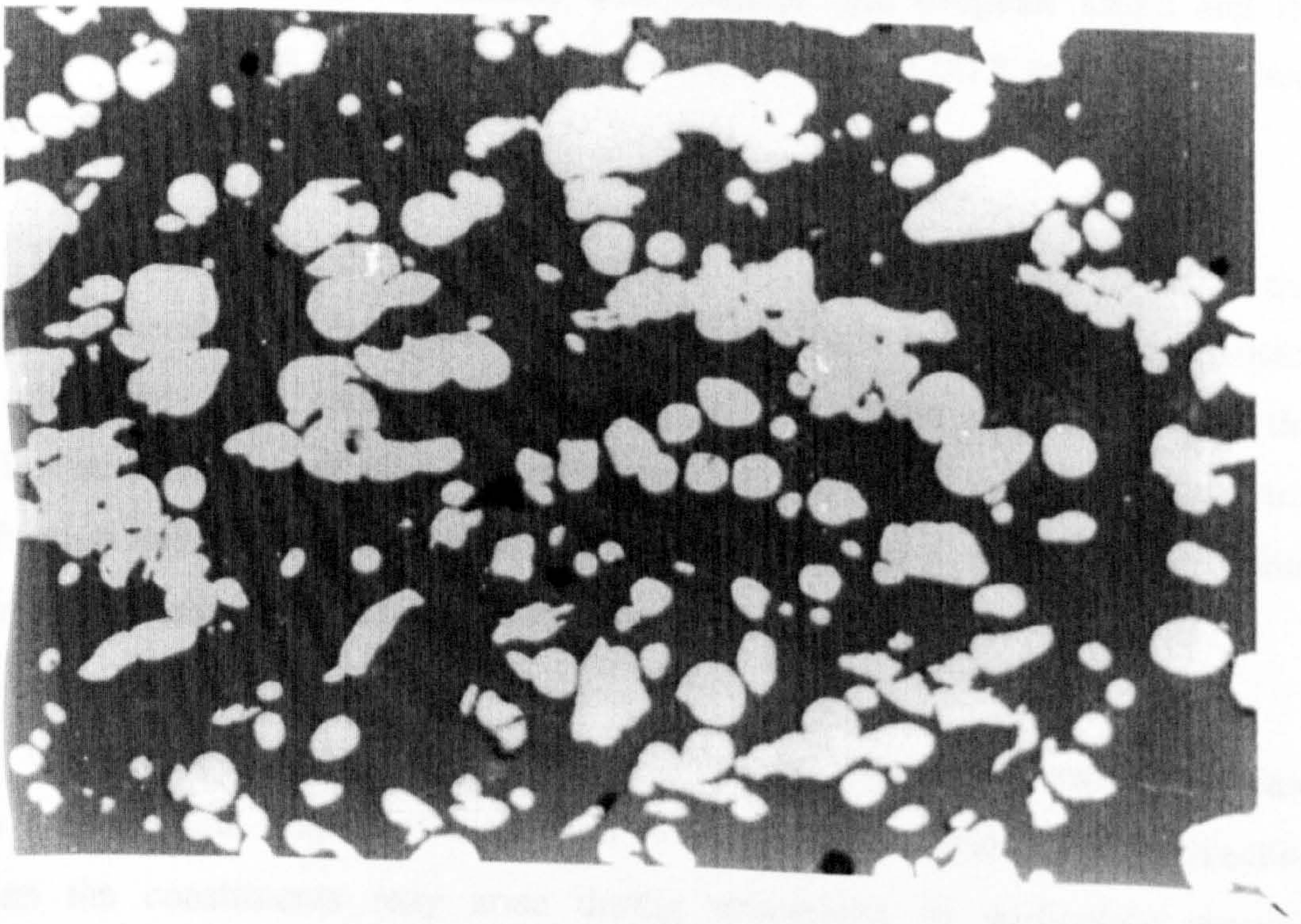

50 μm

Figure 5.26 Optical micrograph of (25 vol%AISI 316 + ZrO_2) sintered at 1450°C for 1 h in argon

5.4. DISCUSSION

Three different metallic reinforcements (chromium, iron and AISI 316 powders), which have different characteristics such as particle size and shape, transformability, melting point and chemical reactivity with the matrix, were used in this study. These characteristics affect the processing and characterisation of the composites. In zirconia/chromium composites the structure and morphology (38 μm maximum size) of the chromium did not change up to the sintering temperature of the composites, and it did not melt. Moreover under standard conditions the chromium also did not react with the matrix. In the second composites (zirconia/iron composites) the iron powder was smaller with mean particle size of 6-8 micron with spherical shape, and according to the DTA analysis the melting point of this iron was about 1370°C so that it melted during sintering. In addition, the iron reacted with yttria in the zirconia causing de-stabilisation of the zirconia. However the mechanism of this phenomenon remains unclear and still needs further investigation. In the last composites (zirconia/stainless steel AISI 316) the austenitic stainless steel had maximum particle size of 45 micron with rounded and irregular shape and its structure did not change during sintering but according to the DTA analysis it melted in the composites at about 1450°C.

The particle size, shape and the amount of reinforcement will influence the degree of connectivity of the reinforcement in the matrix. If the particles interconnect each other, they may cause local sintering of the reinforcement affecting the densification behaviour of the composites including the final linear shrinkage and densification rate. The particle shape will also influence the densification behaviour in term of how easy the re-arrangement of the particles in the matrix can occur.

Fantozzi and Olagnon (1993) point out that the phenomena such as decrease in the densification, degree of dispersion of the particles, and chemical reaction between the constituents may arise during processing of particulate ceramic composites. Exter *et al* (1993) in their study of Y-TZP/20 wt% alumina composites

stated that the densification behaviour depended on the crystal structure of the constituent and the dispersion of the particle reinforcement in the matrix. More specifically Edrees and Hendry (1999) in the study of clay/SiC composites proposed a model as shown in Equation 5.1 to predict the total linear shrinkage of ceramic-matrix composites. This equation can be applied in ceramic composites with the conditions that volume fraction does not change, there is no chemical reaction between the constituents and shrinkage only occurs in the matrix. They found that the particle size did not affect the degree of shrinkage, but the degree of the dispersion of particle in the matrix would have such effects, because if the particles interconnect then sintering may occur in the particles as well. Furthermore they stated that the rate of densification was dependent on heating rate, particle volume fraction, and reinforcement particle size.

The comparison of final linear shrinkage of the composites in the present study and the prediction using Equation 5.1 are described in Table 5.5. From this Table it can be seen that the final linear shrinkage of the composites decreases with increasing reinforcement content. It can also be seen that when the particles cluster and melt in the matrix then the final linear shrinkage will be much greater than that calculated using equation 5.1 as seen in composites containing 25 vol% Fe and 25 vol% AISI 316. The densification temperature of zirconia/chromium and zirconia/AISI 316 are close to that of monolithic zirconia (at about 1100°C). However, for zirconia/iron composites the densification starts 200°C lower than that of monolithic zirconia due to combination of liquid phase sintering of the zirconia matrix and liquid phase formed by the impurity of the iron. Edrees and Hendry (1999) showed that the maximum densification rate decreased as the volume fraction of particle increased. This phenomenon is only found in the zirconia/chromium composites, and does not apply to zirconia/iron and zirconia/AISI 316.

Table 5.5. Comparison of total linear shrinkage after heating up to 1450°C and isothermal for 1 hour of the samples measured using TMA equipment and calculated using Equation 5.1.

Material	Final Linear Shrinkage measured using TMA analysis (%)	Final Linear Shrinkage calculated using Equation 5.1 (%)
ZrO_2 (in air or argon)	23 (mean final shrinkage)	23
10 vol Cr + ZrO_2 in argon	18	20
25 vol Cr + ZrO_2 in argon	16	16
25 vol Fe + ZrO_2 in argon	22	16
10 vol AISI 316 + ZrO_2 in argon	19	20
25 vol AISI 316 + ZrO_2 in argon	18	16

All the samples of the composites sintered at between 1400°C and 1500°C yielded a density greater than 95% of theoretical. This range of sintering temperature is the typical temperature for 3Y-TZP monolithic to produce full density where the sintering is usually liquid-phase sintering because of the presence of impurities such as SiO_2 and Al_2O_3 in the material [Mecartney, 1987; Besson, 1996]. Sintering at lower than those temperatures for zirconia/chromium and zirconia/AISI 316 composites gave lower density as the densification process was still underway. However for zirconia/iron composites sintering at 1200°C have resulted in more than 95% of theoretical density because the densification started at 900°C or 200°C lower than that of monolithic zirconia as seen in the TMA analysis.

The high density of the all composites samples sintered at 1450°C for 1 hour in argon is represented by the optical micrographs in which they look dense and the

particles are embedded well in the matrix. Only very little porosity is present in samples containing 25 vol% of reinforcement.

The XRD analysis showed that there was no reaction between the matrix and the reinforcement found in the composites of zirconia/chromium and zirconia/AISI 316. Furthermore, the presence of such reinforcements did not influence the structure of the zirconia matrix (in the form of tetragonal) which correspond to the tetragonal structure in monolithic zirconia as discussed in Chapter 4. However a significant effect of iron on the zirconia matrix was detected using XRD analysis i.e the zirconia matrix was in the form of tetragonal and monoclinic. This is due to iron reacting with yttria and de-stabilising the zirconia. However, this reaction does not occur in zirconia/AISI 316 where the AISI 316 contains about 69% iron because the AISI exhibits passivity which reduces the chemical reactivity. The passive behaviour is due to the presence of high chromium content and a very thin oxide film as a surface protection in AISI 316.

CHAPTER 6

ZIRCONIA/METAL COMPOSITES: MECHANICAL PROPERTIES

Mechanical properties tests are required to understand the performance of ceramic composites and to analyse the effects of the reinforcement. The applications of ceramic materials in structural engineering require dense materials, because any porosity in such materials can be the initial failure defect. Since ceramic materials usually have low toughness, such flaws may propagate quickly. Therefore, from results of the processing and characterisation of monolithic zirconia and zirconia/metal composites as mentioned in Chapters 4 and 5 respectively, sintering conditions of 1450°C for 1 hour in argon were used to produce dense samples for mechanical properties analysis. In this chapter (Chapter 6) the mechanical properties of Vickers hardness, fracture toughness and bending strength of zirconia/metal composites are presented and discussed. The effect of thermal stress due to thermal expansion mismatch is also discussed.

6.1. VICKERS HARDNESS

Vickers hardness tests were used to measure the hardness of zirconia/metal composites. Ten Vickers indentations using 5 kg load and 15 seconds loading time were performed on the polished samples.

6.1.1. ZIRCONIA/CHROMIUM COMPOSITES

Figure 6.1 shows the effect of chromium content on the Vickers hardness of the composites. The curves of the linear rule of mixtures (upper bound) and inverse

rule of mixtures (lower bound) are also shown in Figure 6.1. The general formulas of the rule of mixtures are [Warren, 1992]:

a. Linear rule of mixtures:

$$k_c = V_m k_m + V_p k_p \qquad \ldots\ldots\ldots\ldots\ldots\ldots\ldots\ldots\ldots\ldots\ldots\ldots\ldots\ldots (6.1)$$

b. Inverse rule of mixtures:

$$\frac{1}{k_c} = \frac{V_m}{k_m} + \frac{V_p}{k_p} \qquad \ldots\ldots\ldots\ldots\ldots\ldots\ldots\ldots\ldots\ldots\ldots\ldots\ldots\ldots (6.2)$$

where k is the property (here, hardness), V is particle volume fraction and the subscripts **m** and **p** represent matrix and particle respectively. The rule of mixtures curves are calculated using the experimental data of the 3Y-TZP monolithic (see Chapter 4) and the data of chromium given by the supplier (Goodfellow UK).

It can be seen in the Figure that as expected the Vickers hardness decreases with increasing chromium content. This decrease is due to chromium having lower Vickers hardness than that of monolithic zirconia. The Vickers hardness of the composites lies between the upper and lower bounds of the rule of mixtures. It is suggested by Lee and Gurland (1978) and Warren (1983) that the lower hardness value of the composites than that of the upper bound of the mixture rule is due to the influence of particle size and/or interparticle spacing.

Optical micrographs of Vickers indentation on samples containing 10 vol% Cr and 25 vol% Cr are shown in Figures 6.2 and 6.3 respectively. It can be seen in these Figures that the indent diagonal increases with increase of chromium content

indicating a decrease of Vickers hardness. The standard deviation of the measurement was small (< 5%) and indicates that the reinforcement particles were well dispersed in the samples.

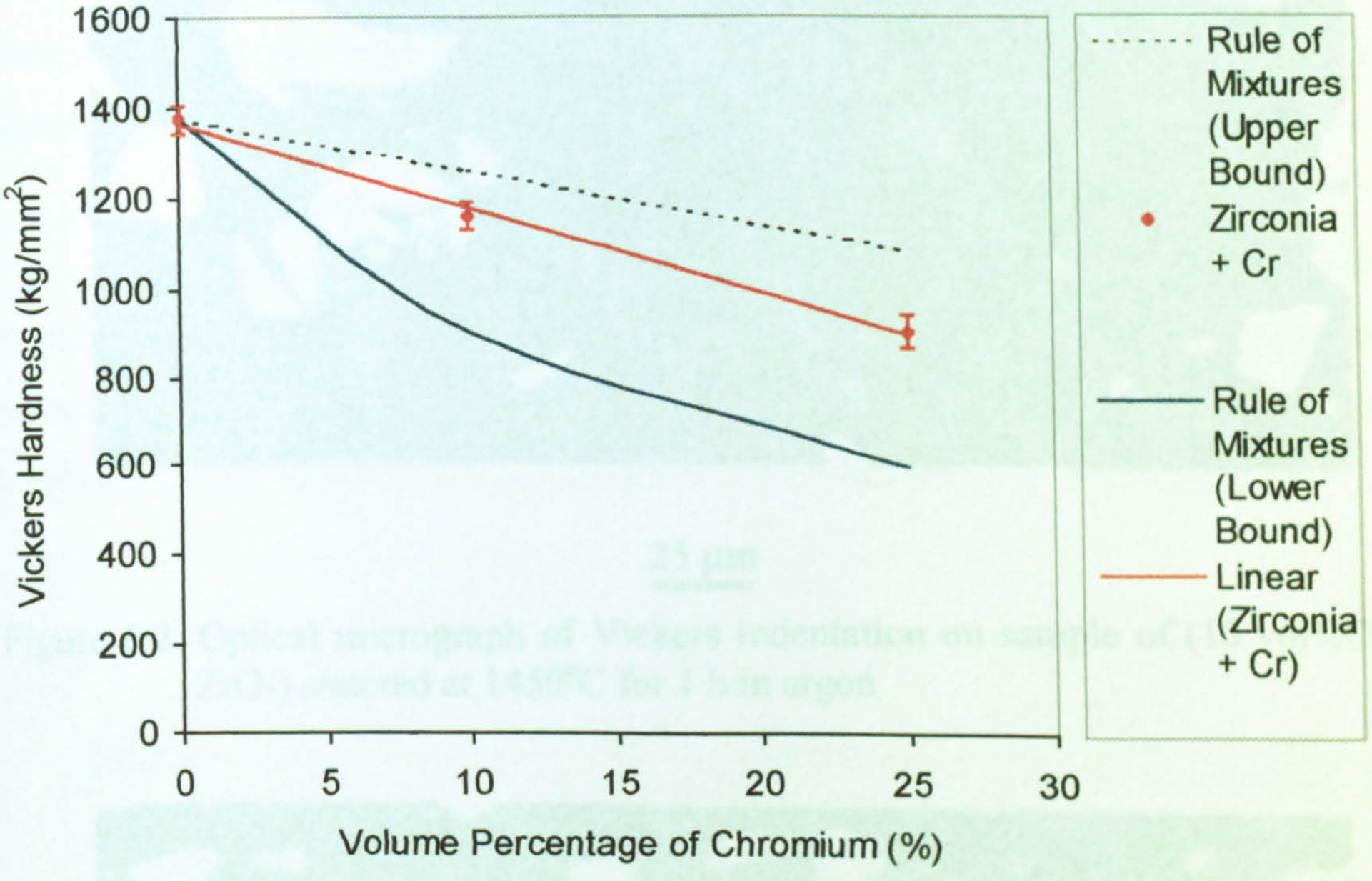

Figure 6.1. The effect of chromium content on Vickers hardness of zirconia/chromium composites sintered at 1450°C for 1 hour in argon

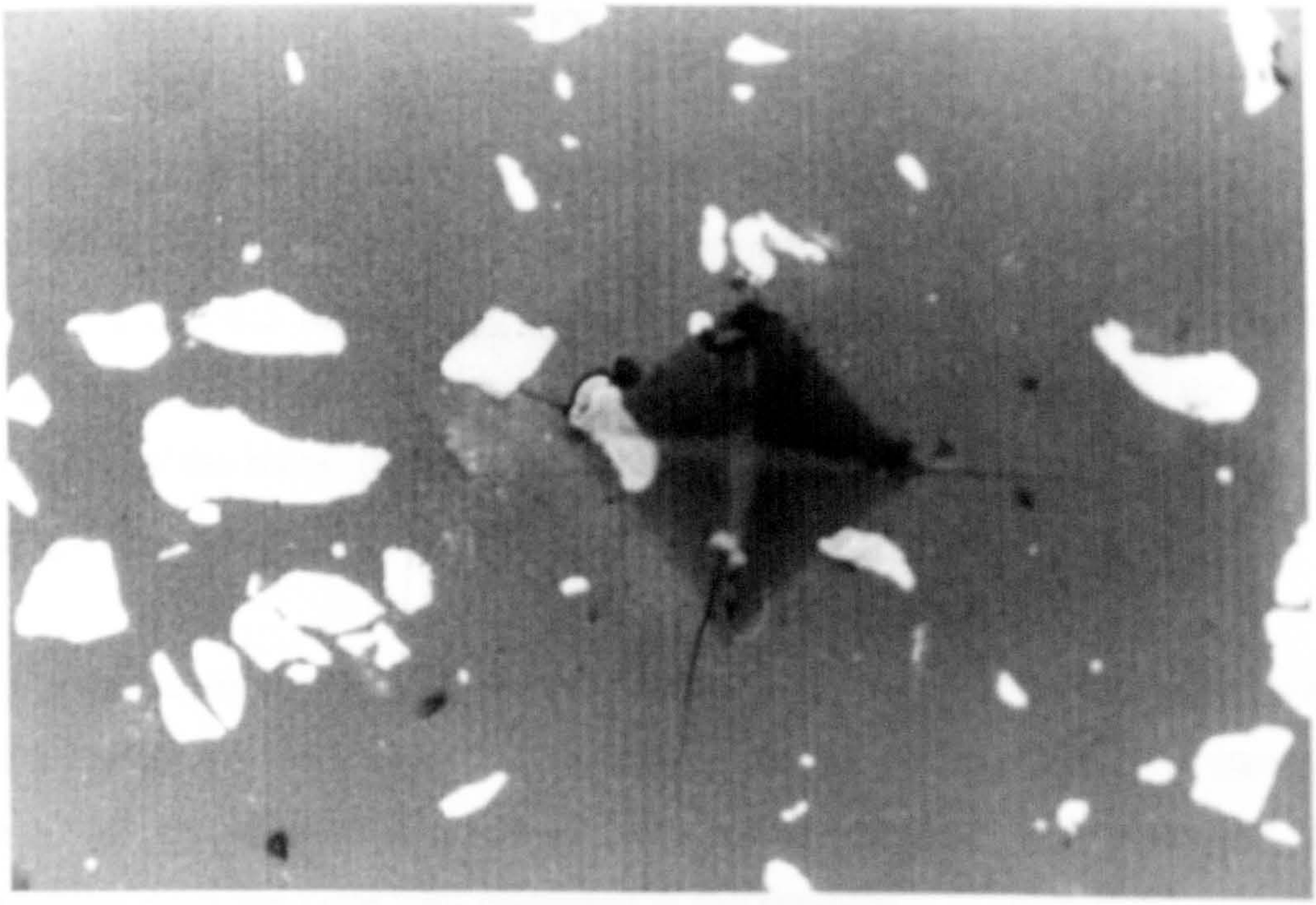

25 μm

Figure 6.2. Optical micrograph of Vickers Indentation on sample of (10 vol%Cr + ZrO_2) sintered at 1450°C for 1 h in argon

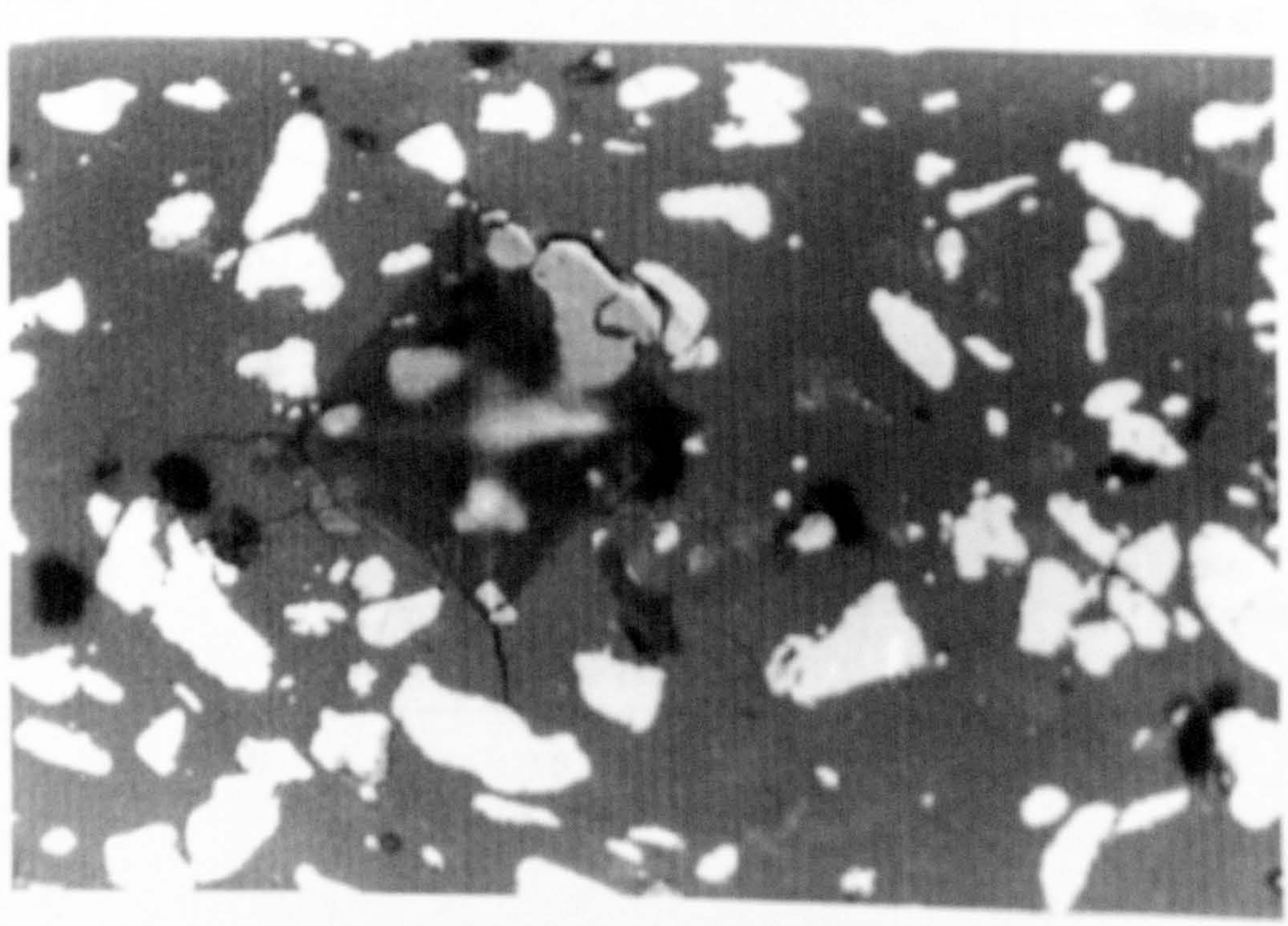

25 μm

Figure 6.3. Optical micrograph of Vickers Indentation of sample of (25 vol%Cr + ZrO_2) sintered at 1450°C for 1 h in argon

6.1.2. ZIRCONIA/IRON COMPOSITES

The Vickers hardness of zirconia/iron composites as a function of iron content is shown in Figure 6.4. The rule of mixtures curves calculated using Equations 6.1 and 6.2 representing upper and lower bounds respectively are also drawn in that Figure. As discussed in the previous section, due to the softer characteristic of the metal particles than that of zirconia, the hardness decreases on increasing the iron content.

An optical micrograph of Vickers indentation on samples containing 10 vol% Fe and 25 vol% Fe are shown in Figures 6.5 and 6.6 respectively. The standard deviation of the measurements was very small (< 3%) indicates that the reinforcement particles were well dispersed in the samples.

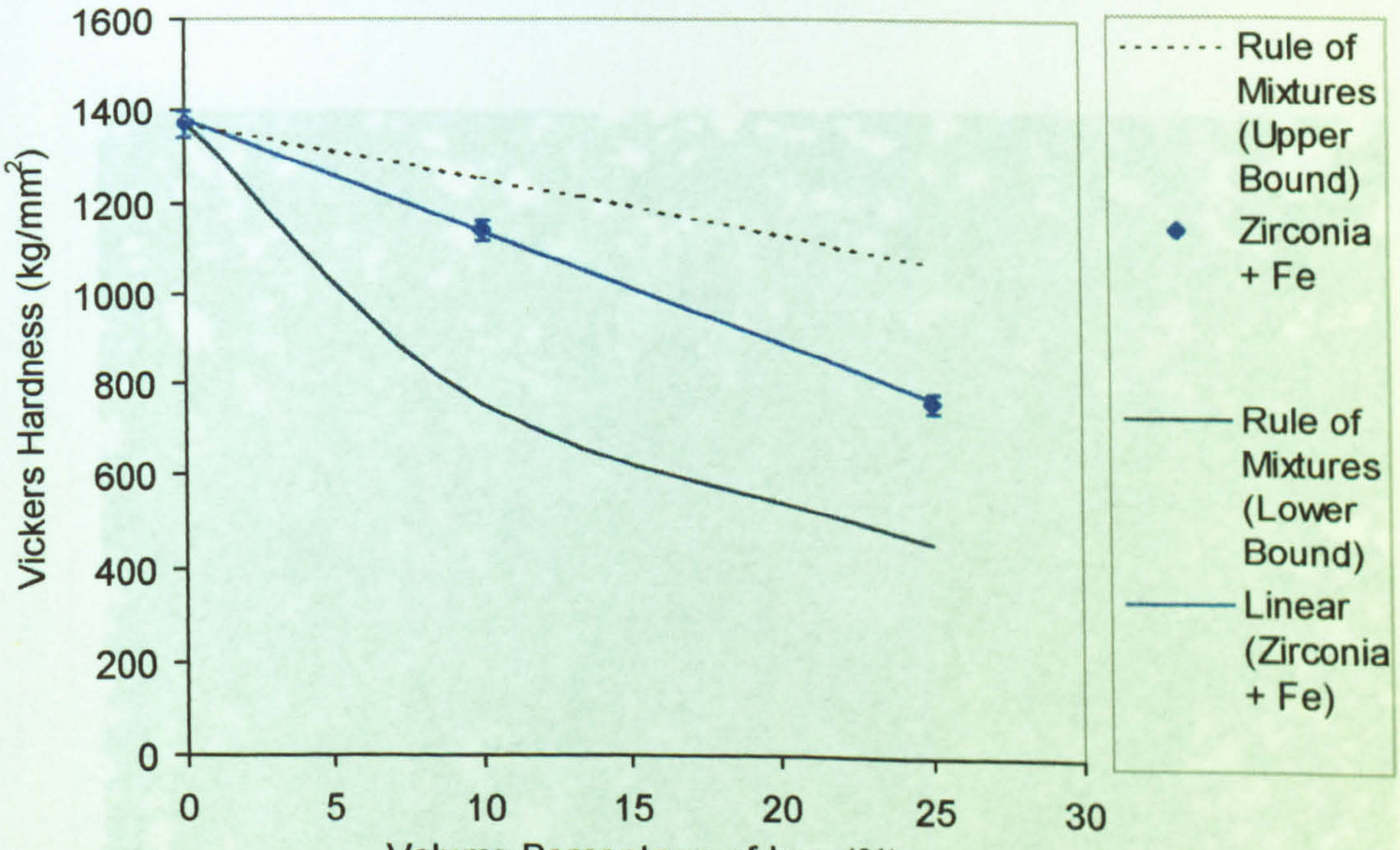

Figure 6.4. The effect of iron content on Vickers hardness of zirconia/iron composites sintered at 1450°C for 1 hour in argon.

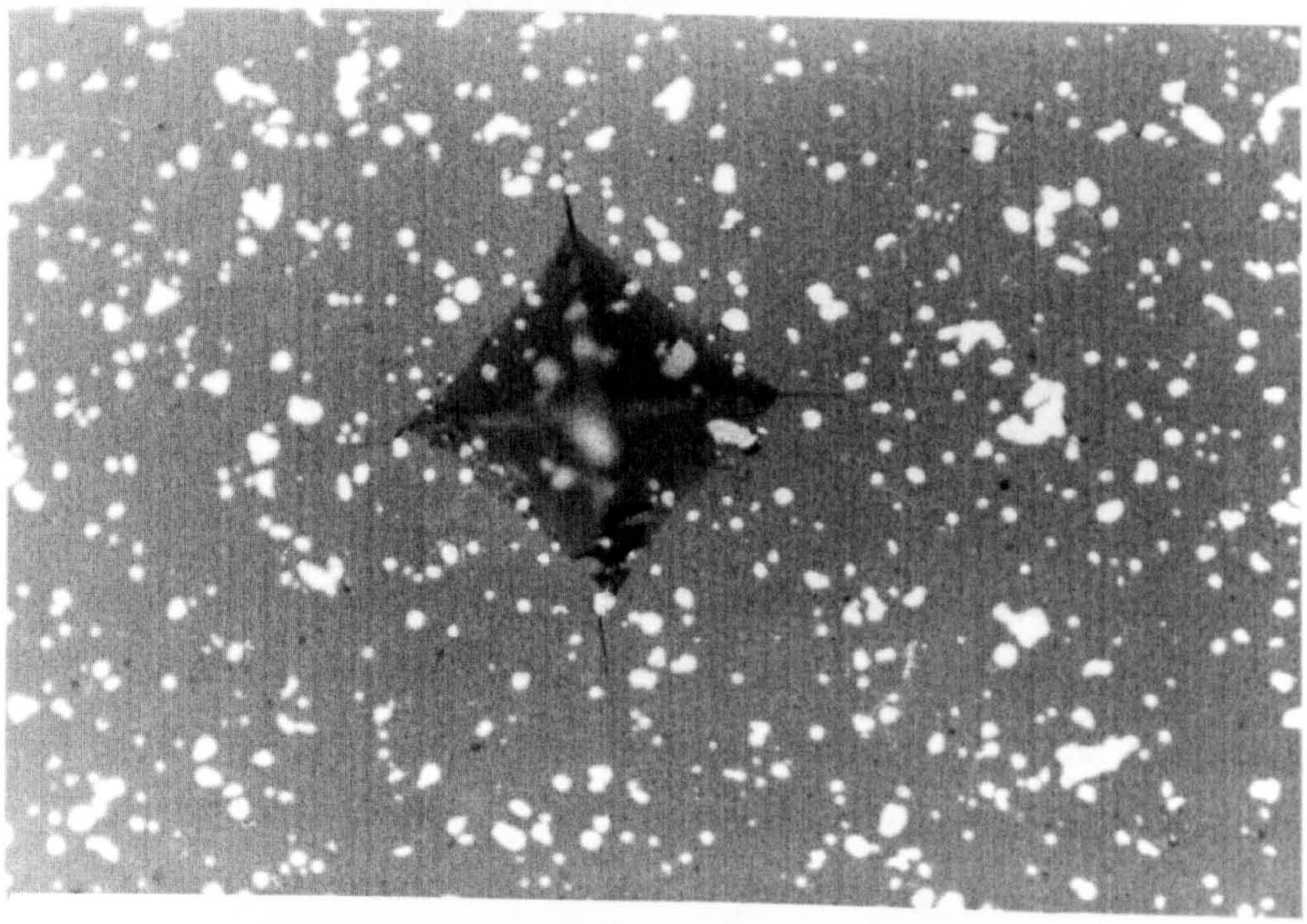

25 μm

Figure 6.5 Optical micrograph of Vickers Indentation on sample of (10 vol% Fe+ ZrO_2) sintered at 1450°C for 1 h in argon

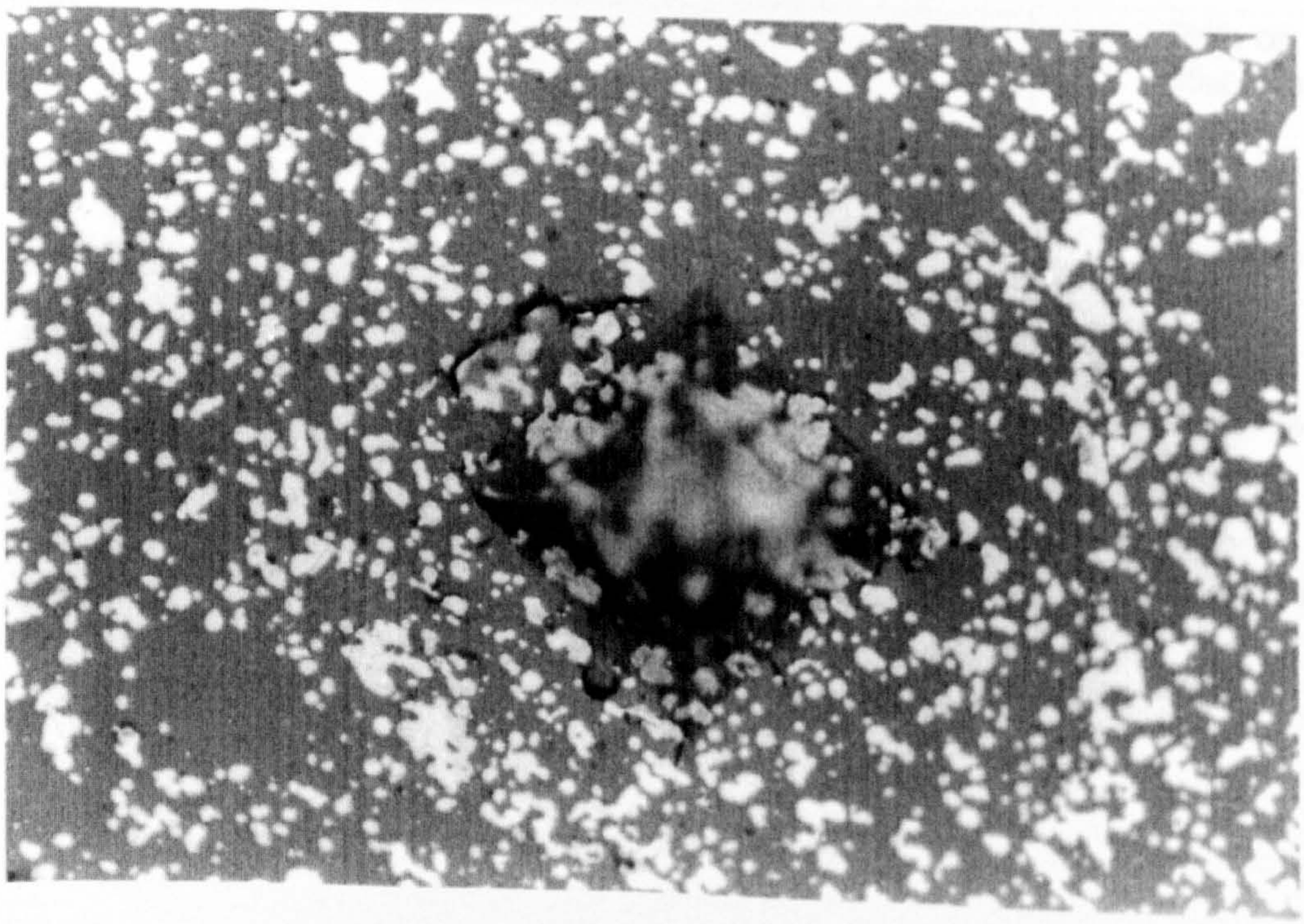

25 μm

Figure 6.6 Optical micrograph of Vickers Indentation of sample of (25 vol% Fe + ZrO_2) sintered at 1450°C for 1 h in argon

6.1.3. ZIRCONIA/AISI 316 COMPOSITES

Figure 6.7 shows the effect of AISI 316 content on Vickers hardness of zirconia/AISI 316 composites and the rule of mixture curves. Equations 6.1 and 6.2 were used to calculate the rule of mixtures curves. In these composites the Vickers hardness has the same trends as with the previous two composites because of the softer AISI 316 than that of monolithic zirconia.

An optical micrograph of the Vickers indentation on samples containing of 10 vol% AISI316 is shown in Figure 6.8. It can be seen in this figure that the particle size and distribution of the particles may influence the accuracy of the measurement and the location of the indentation influences the indent diagonal and therefore the hardness value. In this composite the maximum particle size was 45 μm and larger than that of the reinforcements of the other two composites. This may cause less uniform distribution of the particles in the matrix resulting in larger standard deviation of the measurement (< 22%).

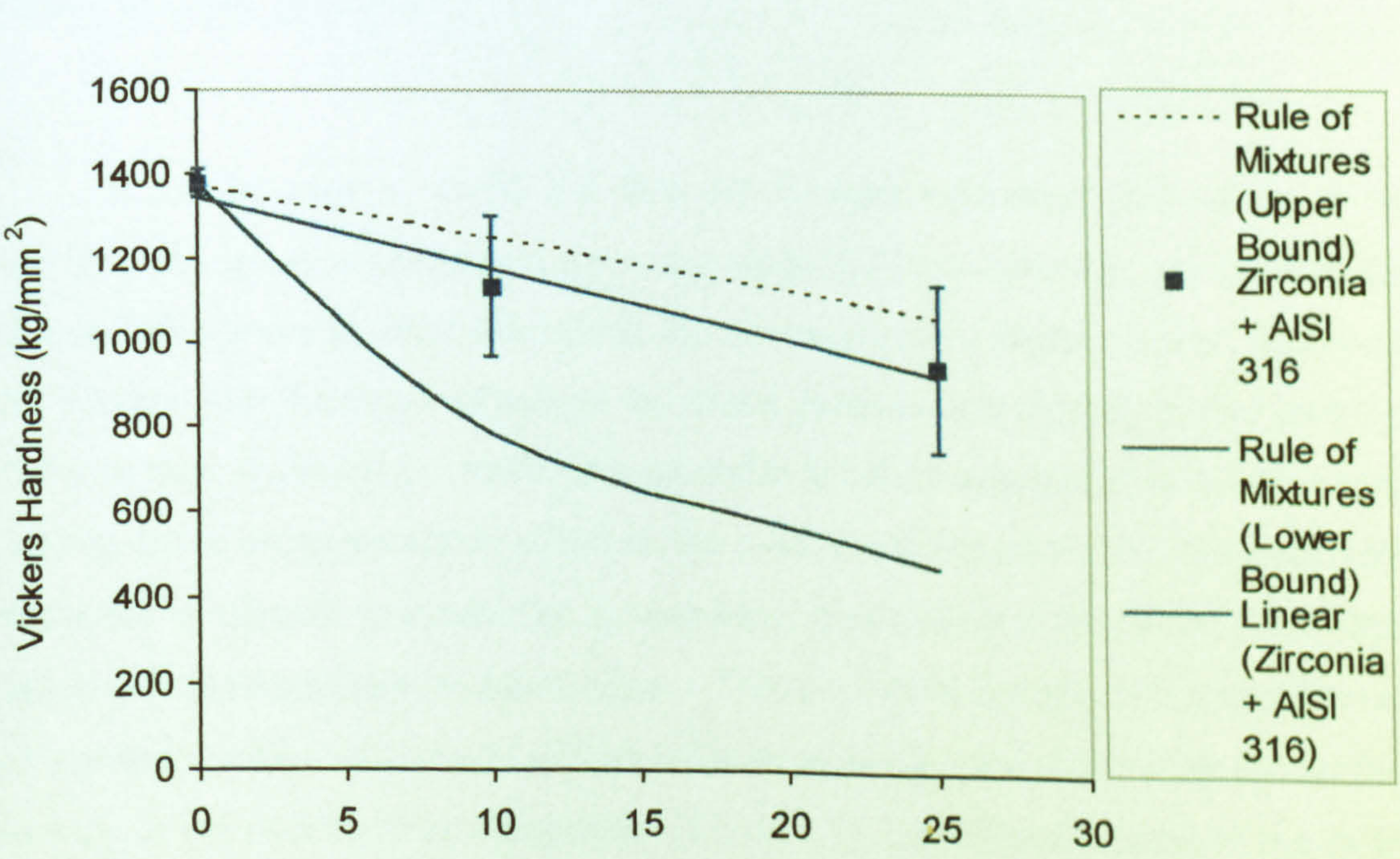

Figure 6.7 The effect of AISI 316 content on Vickers hardness of zirconia/AISI 316 composites sintered at 1450°C for 1 hour in argon.

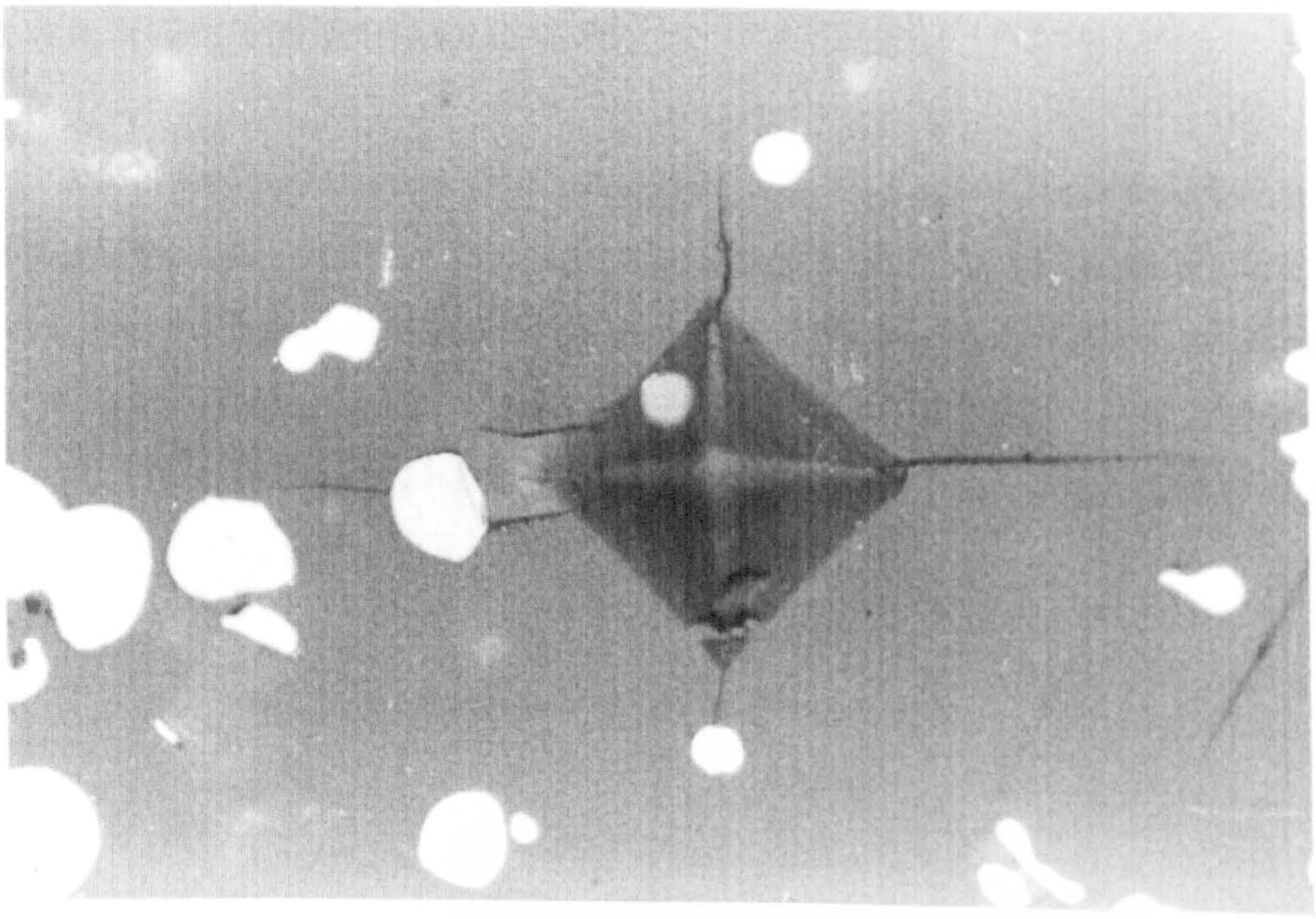

25 μm

Figure 6.8 Optical micrograph of Vickers Indentation on sample of (10 vol% AISI 316 + ZrO_2) sintered at 1450°C for 1 h in argon

6.1.4. VICKERS MICROHARDNESS

Vickers microhardness tests using 50 gram load and 5 seconds loading time were performed on specific areas of the samples such as the matrix, the metal particles, and the boundary between the matrix and the particles. Optical micrographs of the Vickers microhardness of (10 vol%Cr + ZrO_2), (10 vol% Fe + ZrO_2) and (25 vol% AISI 316 + ZrO_2) are shown in Figures 6.9, 6.10 and 6.11 respectively, and the values are presented in Table 6.1.

Table 6.1 Vickers microhardness values of the composites

Material	Vickers Microhardness (kg/mm^2) in	
	The Matrix	The Particles
10 vol% Cr + ZrO_2	1367 ± 10	287 ± 9
10 vol% Fe + ZrO_2	1268 ± 21	215 ± 55
25 vol% AISI 316 + ZrO_2	1349 ± 22	215 ± 17
Monolithic zirconia (3Y-TZP) sintered in argon (Chapter 4)	1374 ± 34	-

It can be seen in Table 6.1 that the Vickers microhardness values of the matrix of the zirconia/chromium and zirconia/AISI 316 composites are close to that of monolithic zirconia, while the value for zirconia/iron is slightly lower. Moreover, the Vickers microhardness values of the metal particles are slightly higher than that of the metals. It should be noted that microhardness measurement in specific areas (matrix, particles, or boundary between the matrix and the particles) in a particulate composite is difficult to obtain the actual value, particularly if the particles are small and distributed uniformly, because when a Vickers indent is applied to a specific area on a sample surface, the result will be influenced by the structure under the surface. As seen in the zirconia/iron composites (Table 6.1), the microhardness of the matrix is slightly lower than that of monolithic zirconia because the iron particles are small and well distributed, so the indent which is applied to the matrix area may be influenced by the hidden and dispersed small particles under the surface.

In general the relative hardness of a specific area can be represented by the indent size of the microhardness as seen in Figures 6.9, 6.10 and 6.11.

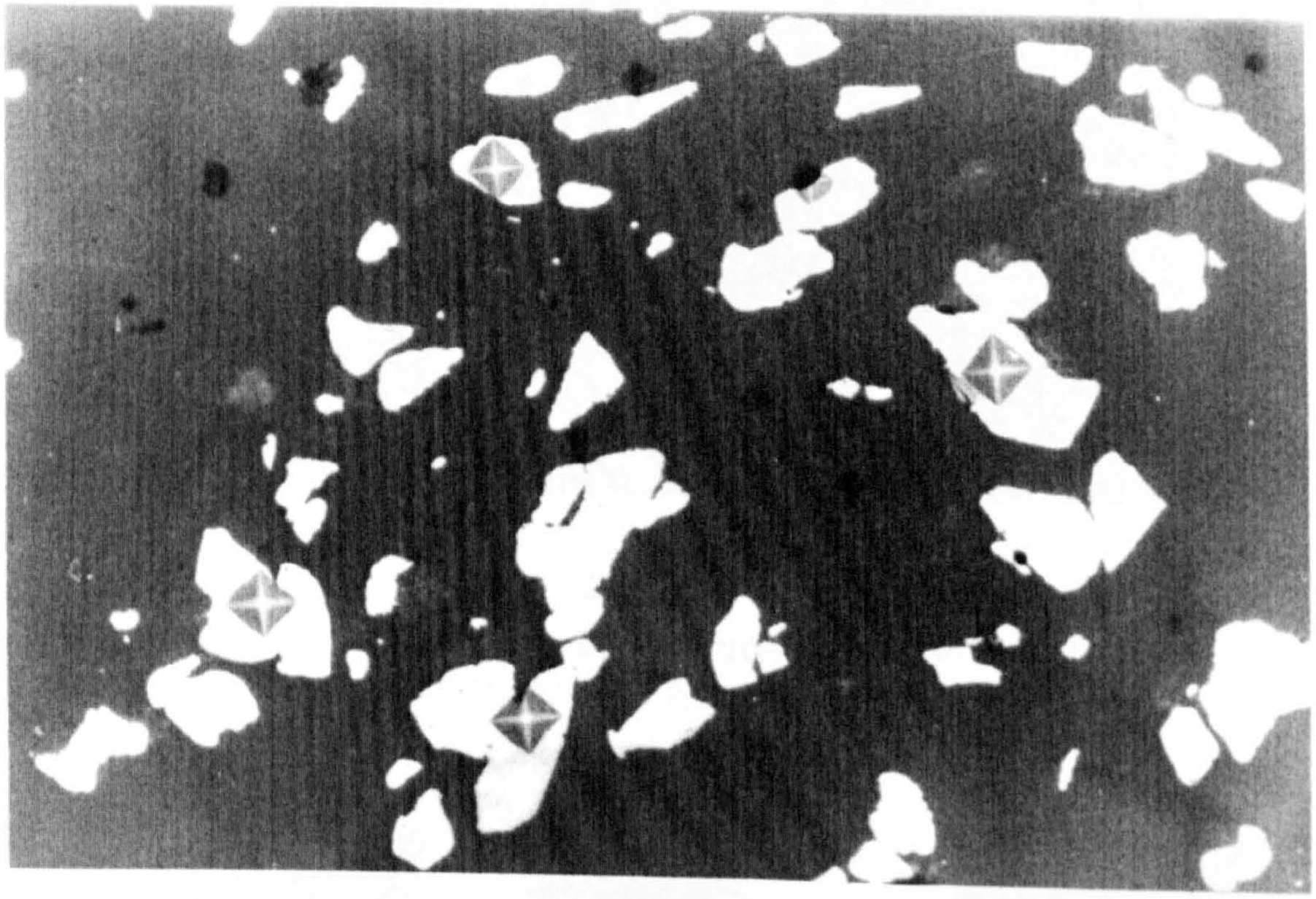

Figure 6.9 Optical micrograph of Vickers Microhardness on sample of (10 vol% Cr + ZrO_2) sintered at 1450°C for 1 h in argon

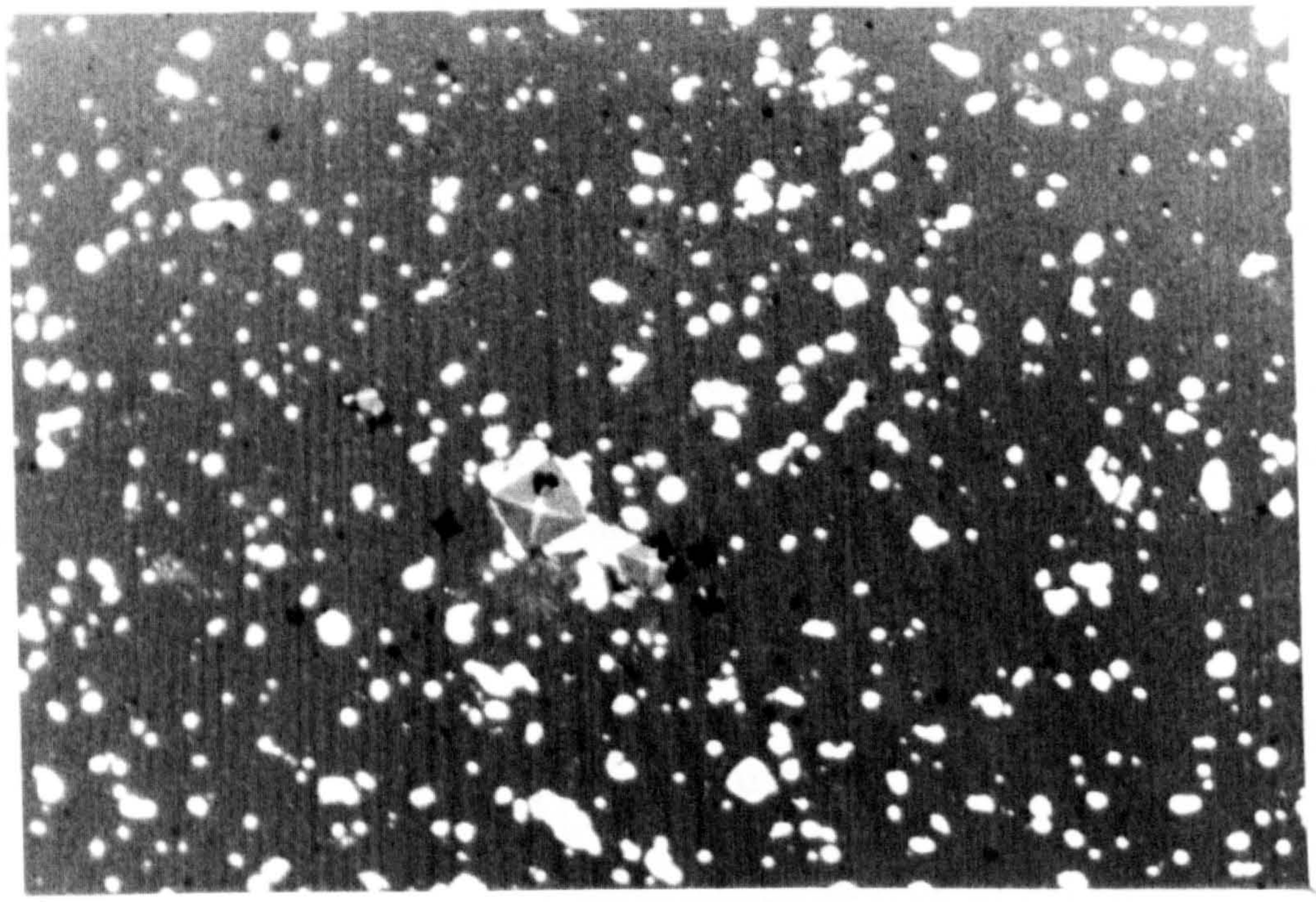

25 μm

Figure 6.10 Optical micrograph of Vickers Microhardness on sample of (10 vol% Fe + ZrO_2) sintered at 1450°C for 1 h in argon

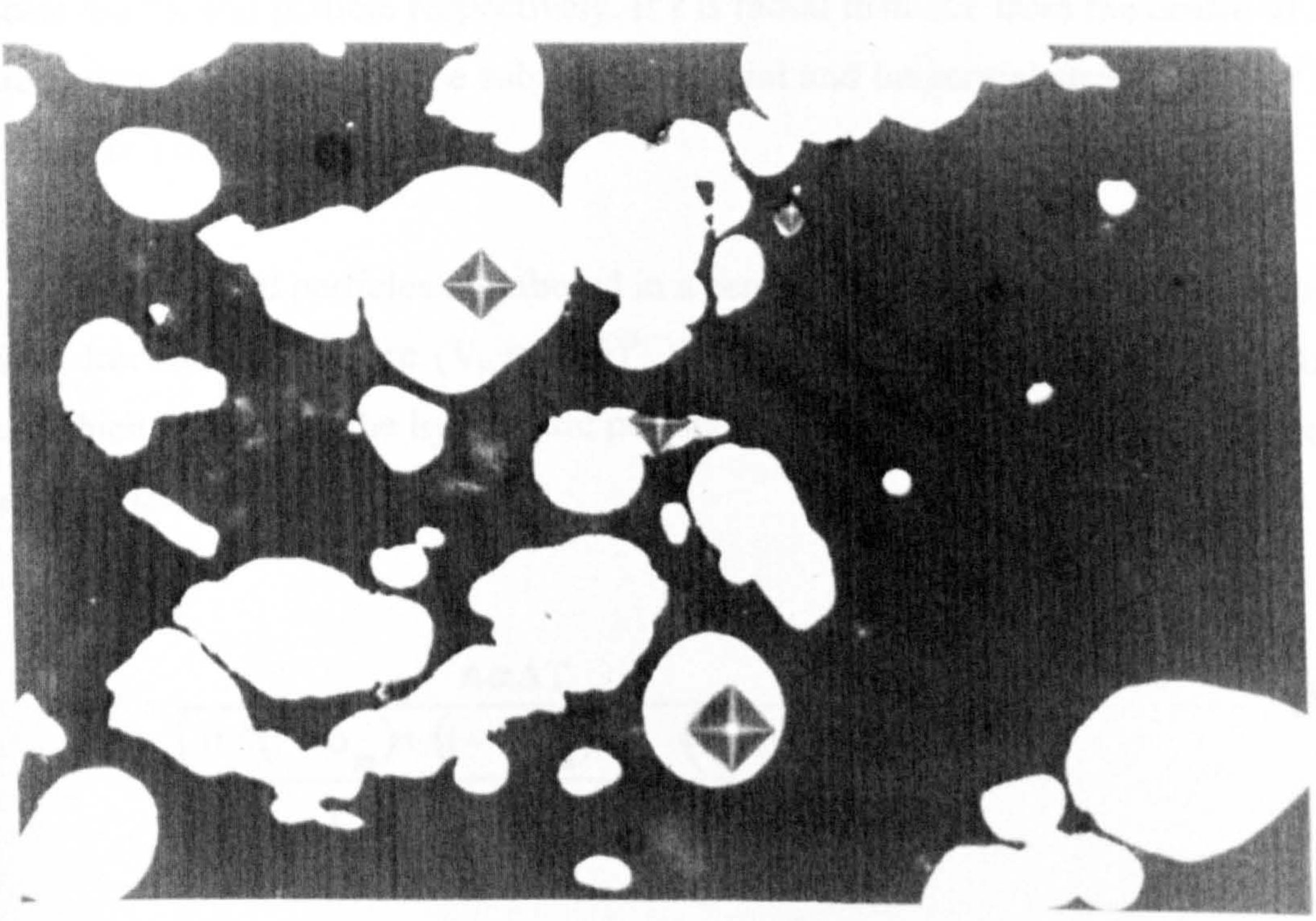

25 μm

Figure 6.11 Optical micrograph of Vickers Microhardness on sample of 25 vol% AISI 316 + ZrO_2 sintered at 1450°C for 1 h in argon

6.2. THERMAL STRESSES

Thermal expansion mismatch between matrix and reinforcement in composites can cause residual stresses within the particles and the matrix around the particles when the composites cool down from the fabrication temperature. For the case of a single spherical particle radius *a* embedded in an isotropic matrix of radius *b*, a hydrostatic stress will be created in the particle [Selsing, 1961]. This stress is equal to the hydrostatic pressure (P) in the particle.

$$\sigma_{rp} = \sigma_{tp} = P = \frac{\Delta\alpha.\Delta T}{\left[\frac{(1+\upsilon_m)}{2E_m}\right]+\left[\frac{(1-2\upsilon_p)}{E_p}\right]} \qquad \ldots\ldots\ldots\ldots\ldots\ldots \quad (6.3)$$

where $\Delta\alpha$ is the thermal expansion coefficient difference of matrix and particle ($\Delta\alpha = (\alpha_m - \alpha_p)$); E is modulus of elasticity; ν is poisson's ratio; and subscript **m** and **p** indicate matrix and particle respectively. If r is radial distance from the centre of the particle, then the matrix will be subjected to radial and tangential stresses of (Pa^3/r^3) and $(-Pa^3/2r^3)$ respectively.

For spherical particles distributed in a ceramic matrix composite with particle volume fraction (V_p) where ($V_p = (a/b)^3$, the particle will be subjected a uniform stress which is equal to the hydrostatic pressure. The hydrostatic pressure, will be as follows [Chawla, 1993]:

$$P = \frac{\Delta\alpha\Delta T}{\left[\frac{0.5(1+\upsilon_m)+(1-2\upsilon_m)V_p}{E_m(1-V_p)}+\frac{(1-2\upsilon_p)}{E_p}\right]} \qquad \ldots\ldots\ldots\ldots\ldots\ldots \quad (6.4)$$

The stresses generated in the matrix at distance r from the centre of the particle are:

- the radial stress:

$$\sigma_{rm} = \frac{P}{(1 - V_p)}\left[\left(\frac{a}{r}\right)^3 - V_p\right] \qquad \ldots\ldots\ldots\ldots\ldots\ldots\ldots\ldots \quad (6.5)$$

- the tangential stress:

$$\sigma_{tm} = -\frac{P}{(1 - V_p)}\left[\frac{1}{2}\left(\frac{a}{r}\right)^3 + V_p\right] \qquad \ldots\ldots\ldots\ldots\ldots\ldots\ldots\ldots \quad (6.6)$$

From those Equations, it can be seen that the maximum stresses in the matrix (radial or tangential) occur at the interface between matrix and particle, then the stresses in the matrix will decrease with distance from the particle centre.

According to the above equations, if the strength of the matrix is lower than the stresses developed by thermal stress, cracking may occur in the matrix independently of the particle size. In fact, in their study experimentally and theoretically, Davidge and Green (1968) point out that the critical particle size should be taken into account in prediction of cracking caused by thermal stress. They found that cracking only occurs in the matrix around particles greater than a critical size. Therefore crack formation depends on both the magnitude of the stress and the critical size. They proposed a model to predict a critical radius size as follows:

$$r_c = \frac{8\gamma_s}{P^2\left(\frac{1+\upsilon_m}{E_m} + 2\frac{1-2\upsilon_p}{E_p}\right)} \qquad \ldots\ldots\ldots\ldots\ldots\ldots\ldots\ldots\ldots\ldots (6.7)$$

Where r_c is critical radius size above which matrix cracking will take place, γ_s is the surface energy of the matrix, P is pressure around the particle due to thermal expansion mismatch, ν is Poisson's ratio, subscript m and p are matrix and particle respectively.

In the present study, the prediction of the residual stress due to thermal expansion mismatch and the critical size of each composite will be discussed below.

6.2.1. ZIRCONIA/CHROMIUM COMPOSITES

The thermal stress in zirconia/chromium composites generated during cooling from fabrication at 1450°C can be estimated by assuming that the particles are spherical and distributed orderly in the matrix. The data for coefficient of thermal expansion (CTE) of 3Y-TZP = 10.45 x 10^{-6}/°C (at 20 -1000°C) was taken from the experiment as discussed in Chapter 4. The other parameters were taken from the data available from the literature and the supplier such as CTE of Cr = 9.4 x 10^{-6} (at 20 - 700°C) [Smithells and Brandes, 1976]; modulus of elasticity of 3Y-TZP and Cr are 200 GPa and 279 GPa respectively; Poisson's ratio of 3Y-TZP and Cr are 0.3 and 0.21 respectively [Goodfellow, UK].

The fracture surface energy of the matrix (3Y-TZP) is estimated using the Equation below [Chiang, 1997; Green, 1998]:

$$K_{Ic} = \sqrt{2E\gamma} \qquad \ldots\ldots\ldots\ldots\ldots\ldots\ldots\ldots\ldots\ldots\ldots\ldots\ldots\ldots\ldots\ldots\ldots\ldots\ldots\ldots\ldots\ldots (6.8)$$

where K_{ic} is fracture toughness. From the experimental data (Chapter 4) the fracture toughness of 3Y-TZP is 5.89 MPa.$m^{0.5}$. Thus, the fracture surface energy of the matrix is 8.673 x 10^{-5} MPa.m (86.73 J/m^2).

The thermal stresses around particles and the critical size of zirconia/chromium composites are described in Table 6.2. The bending strength of the matrix (3Y-TZP) is 692 MPa (see Chapter 4) and the maximum particle size of chromium is 38 μm [Goodfellow, UK].

Table 6.2. Results of thermal stresses and critical diameter size of zirconia/chromium composites

Chromium Content	Stress in the particle (MPa)	Stress in the matrix		Critical Diameter Size (micron)
		Radial stress (MPa)	Tangential Stress (MPa)	
10 vol% Cr	-241.9	-241.9	161.2	2225.6
25 vol% Cr	-202.1	-202.1	202.0	3190.7

The Table reveals that the particle is subjected to a compressive stress and the matrix to radial compressive and tangential tensile stresses. These type of stresses typically occur on a composite where ($\alpha_m > \alpha_p$) [Zhan *et al*, 1996; Barsoum, 1997]. According to those results, cracking should not occur during cooling from fabrication temperature because the stresses developed in the matrix are lower than the matrix strength and the maximum of chromium particle size is lower than the critical size. The optical micrographs of the polished samples shown in Chapter 5 also do not show any cracks around the particles.

6.2.2. ZIRCONIA/IRON COMPOSITES

In these composites the required data of the matrix is as the previous section while the data for iron is taken from the literature and the supplier. The CTE of iron is 14.6 x 10^{-6} /°C (at 20 - 800°C) [Smithells and Brandes, 1976]; the modulus of elasticity and the Poisson's ratio of iron are 211 GPa and 0.293 respectively [Goodfellow, UK]. By using those data, the thermal stress in zirconia/iron

composites generated during cooling from fabrication at 1450°C can be estimated by assuming that the particles are spherical and distributed orderly in the matrix. The results of the thermal stresses around particles and the critical size are described in Table 6.3.

Table 6.3. Results of thermal stresses and critical diameter size of zirconia/iron composites

Iron Content	Stress in the particle (MPa)	Stress in the matrix		Critical Diameter Size (micron)
		Radial stress (MPa)	Tangential Stress (MPa)	
10 vol% Fe	1036.3	1036.3	-690.9	124.0
25 vol% Fe	862.7	862.7	-862.7	178.9

The results show that for particulate composites where ($\alpha_m < \alpha_p$), the particle will be subjected to tensile stress and the matrix to radial tensile and tangential compressive stresses [Barsoum, 1997]. It can be seen in Table 6.3 that the stresses in the matrix are bigger than that of monolithic zirconia (692 MPa), and the particle diameter (mean particle size = 6 - 8 μm) is much lower than that the critical size. In this case, Davidge and Green (1968) suggest that cracks around particles should not occur during cooling from fabrication temperature, because although the stress magnification in the matrix is bigger than that of the monolithic matrix, the reinforcement particle size is much lower than the critical size. Cracks however, may be formed around the particles under applied stress at stresses below the macroscopic fracture stress (stress required for fracture). The optical micrographs of the polished samples shown in Chapter 5 do not show any cracks around the particles. The available data of particle sizes of the iron given by the supplier is only the mean size (6 - 8 μm) and the maximum size is not known. However, as discussed in Chapter 5, some iron particles interconnect each other forming some larger particles, and these larger particles (less than 25 μm) are still smaller than the critical size.

6.2.3. ZIRCONIA/AISI 316 COMPOSITES

The data of AISI 316 available in the literature and given by the supplier are used for these calculations. The CTE of AISI 316 is 19 x 10^{-6} /°C (at 20 - 1000°C) [Deckner and Bernstein, 1977], the modulus of elasticity and the Poisson's ratio are 193 MPa and 0.3 respectively [Goodfellow UK]. The particle size of AISI 316 is varied with the maximum size of 45 micron [Goodfellow UK] and the particle shape is irregular and rounded (see Chapter 5). The results of thermal stresses and the critical size are presented in Table 6.4.

Table 6.4. Results of thermal stresses and critical diameter size of zirconia/AISI 316 composites

AISI 316 Content	Stress in the particle (MPa)	Stress in the matrix		Critical Diameter Size (micron)
		Radial stress (MPa)	Tangential Stress (MPa)	
10 vol% AISI316	2143.2	2143.2	-1428.8	29.3
25 vol% AISI 316	1781.1	1781.1	-1781.1	42.4

Table 6.4 shows that after cooling from fabrication temperature at 1450°C the particle experiences tensile stress and the matrix is subjected to radial tensile and tangential compressive stresses due to the thermal expansion mismatch ($\alpha_m < \alpha_p$) [Barsoum, 1997]. Furthermore, it can be seen in that table that the stresses of the matrix are bigger than the strength of zirconia and the critical size is smaller than the maximum particle size. As a result, these conditions may lead to circumference cracks around the particles after cooling [Davidge and Green, 1968]. Because the particle size varies, such cracks may only occur on particles greater than the critical size on each composition or particles that are clustered. However, cracks may also form on particles smaller than the critical size if stress below the macroscopic fracture stress is applied. Although the optical micrographs (Chapter 5) do not show such cracks around particles greater than the critical size, such cracks may however be seen if methods of higher magnification in optical or electron microscopy were to be done. Moreover, such cracks may influence thermal diffusivity, which will be discussed in Chapter 7.

6.3. FRACTURE TOUGHNESS

Indentation fracture toughness method was used to measure the fracture toughness of the composites. The same data of the Vickers hardness discussed in Section 6.1 plus the data of crack lengths developed from the each indent corners were used to calculate the fracture toughness. The model given by Shetty *et al*, (1985), which is applicable for Palmqvist crack type was used in this present study:

$$\mathbf{Kc} = 0.0316\,\mathbf{x}\,\frac{\mathbf{P}}{\mathbf{a}\sqrt{l}} \qquad \ldots\ldots\ldots\ldots\ldots\ldots\ldots\ldots \quad (3.6)$$

Where P is the indenter load (kg), a is half of the indent diagonal (m) and *l* is the crack length from the indent corner (m).

6.3.1. ZIRCONIA/CHROMIUM COMPOSITES

Figure 6.13 shows the fracture toughness of zirconia/chromium composites as a function of chromium content. It can be seen in this figure that the fracture toughness increases slightly from (5.89 ± 0.22) MPa.m$^{0.5}$ for monolithic zirconia to (7.05 ± 0.36) MPa.m$^{0.5}$ for composites containing 25 vol% chromium. Transformation of the matrix may give a contribution to the toughness as seen in Chapter 5 (Figure 5.5) as some transformation (t - m) occurs in the sample after a mechanical stress is applied. In addition crack deflection [Faber and Evans[a,b], 1983] around chromium particles appears to be another toughening mechanism. It can be seen in Figures 5.2 and 5.3 that cracks developed from the indent corners that reach chromium particles will either stop propagating or be deflected. As mentioned by Faber and Evans[a,b] (1983), the fracture toughness improvement due to crack deflection depends on the volume fraction and the reinforcement geometry. They

show that reinforcement with high aspect ratio will give more effect to toughening than that of spheres and this mechanism is only effective up to about 20 vol% of reinforcement. Such crack deflection may be caused by the local stress at the interface [Green, 1998]. This local stress can be developed by the difference of the stiffness and/or coefficient of thermal expansion [Taya *et al*, 1990]. Moreover, Wei and Becher (1984) consider that residual stress due to thermal expansion mismatch is a major cause of the crack deflection. In the present study, the residual stress developed during the fabrication as mentioned in Section 6.2.1 may be responsible for the crack deflection.

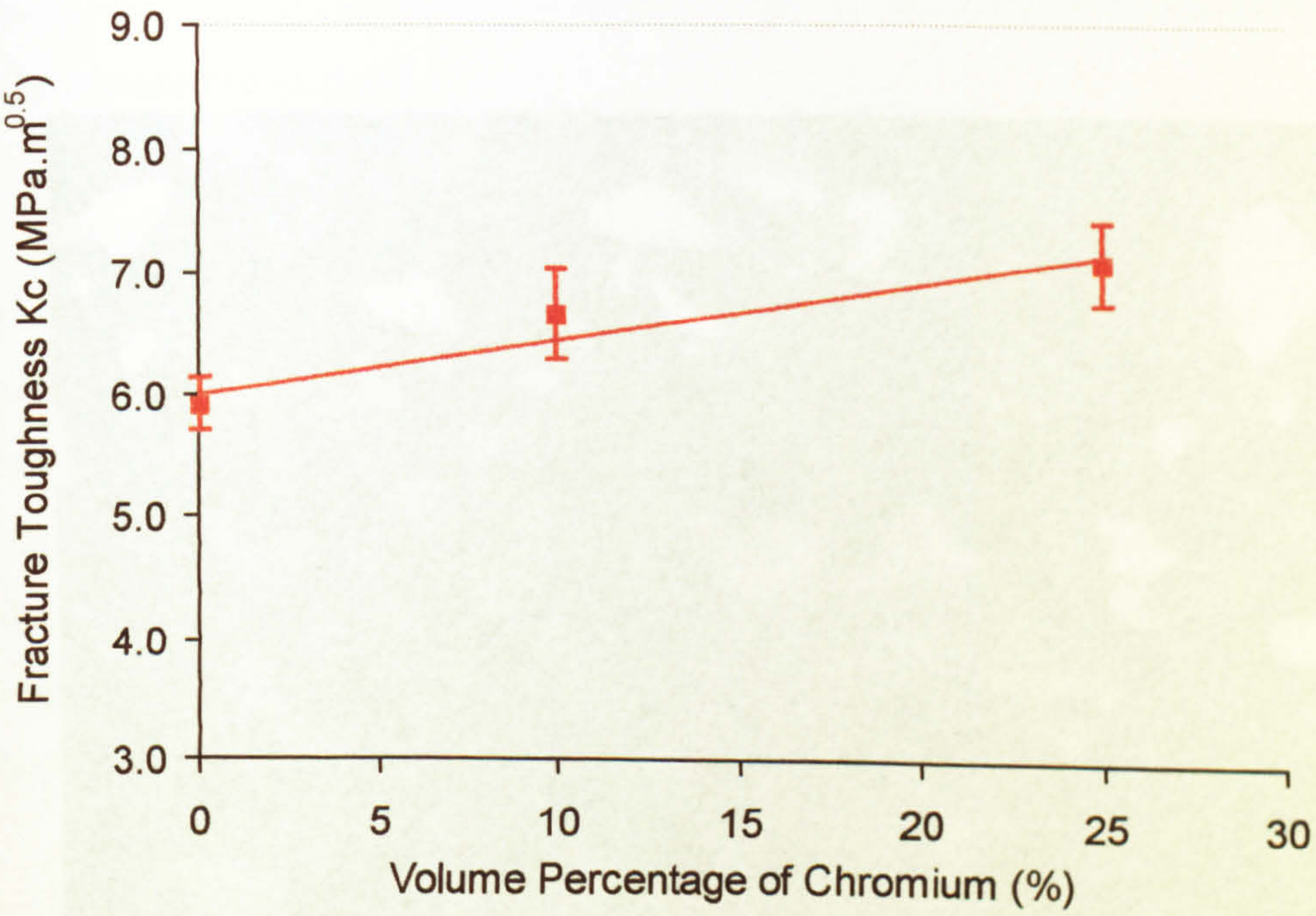

Figure 6.12. Effect of chromium content on fracture toughness of zirconia/chromium composites sintered at 1450°C for 1 hour in argon.

The crack type resulted from Vickers indentation is Palmqvist type as shown in Figure 6.13. This type was confirmed by gradually polishing the pre-indented surface and using a relationship of indent diagonal and crack length, which is $0.25 \leq (l/a) \leq 2.5$ for Palmqvist and $(l+a)/a \geq 2.5$ for Median [Niihara *et al*, 1982].

Material	Vickers Indentation		(l/a)	$(l + a)/a$	Crack Type
	Average of a (μm)	Average of l (μm)			
10 vol% Cr + ZrO_2	44.75	27.68	0.62	1.62	Palmqvist
25 vol% Cr + ZrO_2	50.78	18.95	0.37	1.37	Palmqvist

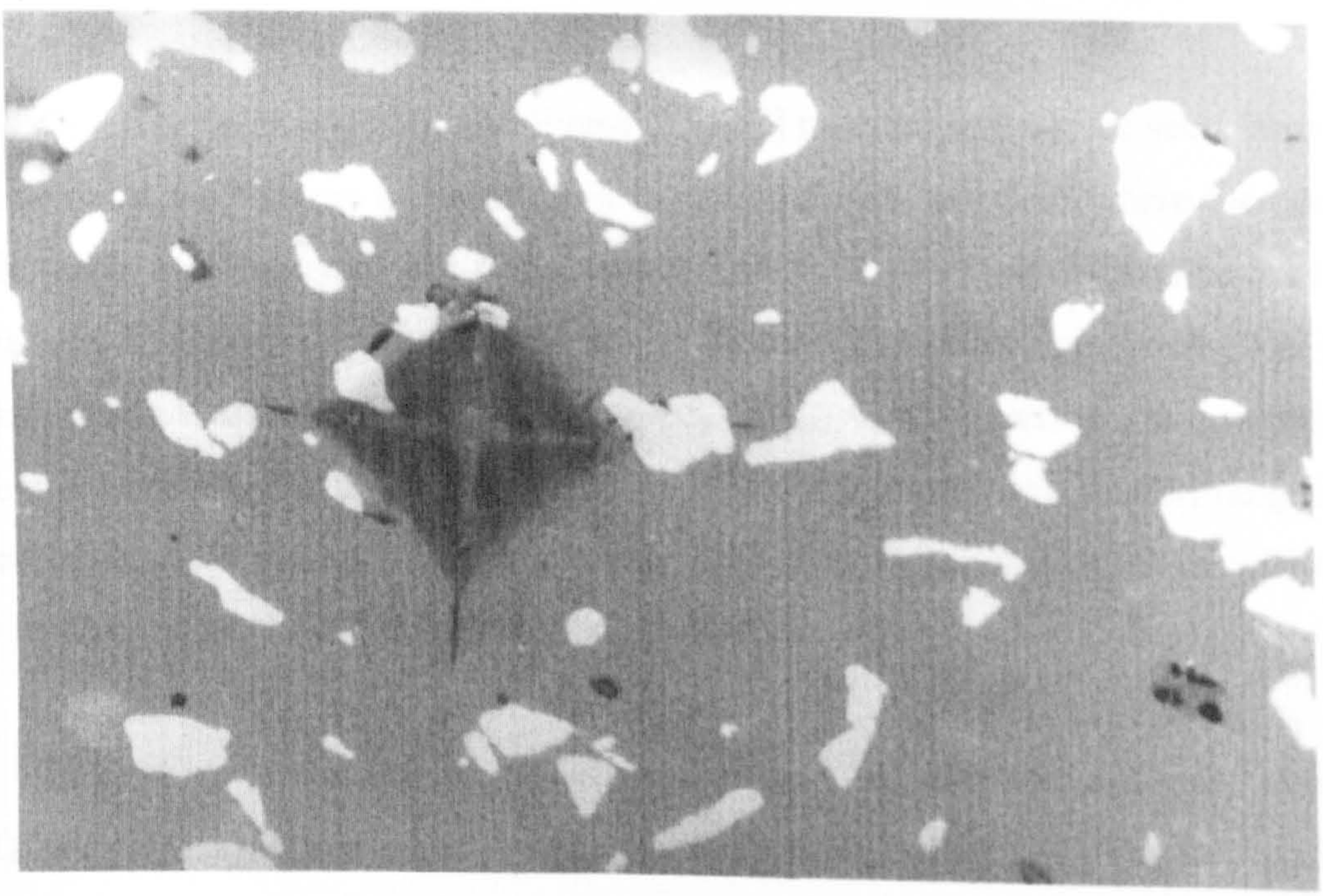

Figure 6.13. Optical micrograph of Palmqvist crack type on sample of (10 vol%Cr + ZrO_2) sintered at 1450°C for 1 h in argon

6.3.2. ZIRCONIA/IRON COMPOSITES

The fracture toughness of zirconia/iron composites as a function of iron content is shown in Figure 6.14. It can be seen that the fracture toughness increases from (5.89 ± 0.2) MPa.m$^{0.5}$ for monolithic zirconia to (7.74 ± 0.40) MPa.m$^{0.5}$ for composites containing 25 vol% Fe. Crack deflection, microcracking, and matrix compression are thought to be the mechanism of the toughening. While transformation toughening of the matrix is difficult to identify because as mentioned in Chapter 5, in these composites transformation of tetragonal to monoclinic occurs during fabrication which may be due to destabilising of 3Y-TZP. Therefore after fabrication, the matrix (zirconia) structures are in the form of tetragonal and monoclinic. This causes difficulty to detect the further stress-induced transformation of the metastable zirconia.

Crack deflection [Faber and Evans[a,b], 1983] mechanisms can be seen from the cracks around the Vickers indentation in Figures 6.5, 6.6, and 6.15 where the cracks which reach iron particles are deflected or ended. This crack deflection may be encouraged by thermal residual stress due to thermal expansion mismatch [Wei and Becher, 1984; Warren, 1992]. In the case ($\alpha_p > \alpha_m$), after sintering the composites will experience tensile stress in the particles while the matrix will exhibit tangential compressive stress and radial tensile stress. Therefore a propagating crack will tend to be led around particles leading to crack deflection.

According to the thermal stress and critical particle size analysis (Section 6.2.2), microcracking may also be responsible for toughening since the iron particle size is below the critical particle size and the thermal stresses at the interface are greater than the strength of the matrix. In this condition, stress-induced microcracking can occur [Davidge and Green, 1968; Green, 1998]. The stress-induced microcracks would be expected to form in a zone around larger cracks leading to a reduction of the stresses near the crack tip and a rise in crack shielding. It is important to keep the particles from clustering and forming larger particles

greater than the critical size, otherwise spontaneously microcracking can take place during fabrication. In these composites although clustering of some iron particles occurs in the sample, their final sizes are still below the critical size.

Another toughening mechanism that may be responsible in these composites is matrix compression. Due to the thermal expansion mismatch ($\alpha_p > \alpha_m$), the thermal residual stress (tangential compressive stress) in the matrix will also give a contribution to the fracture toughness [Taya *et al*, 1990; Warren, 1992]. This compression state will tend to hinder crack propagation.

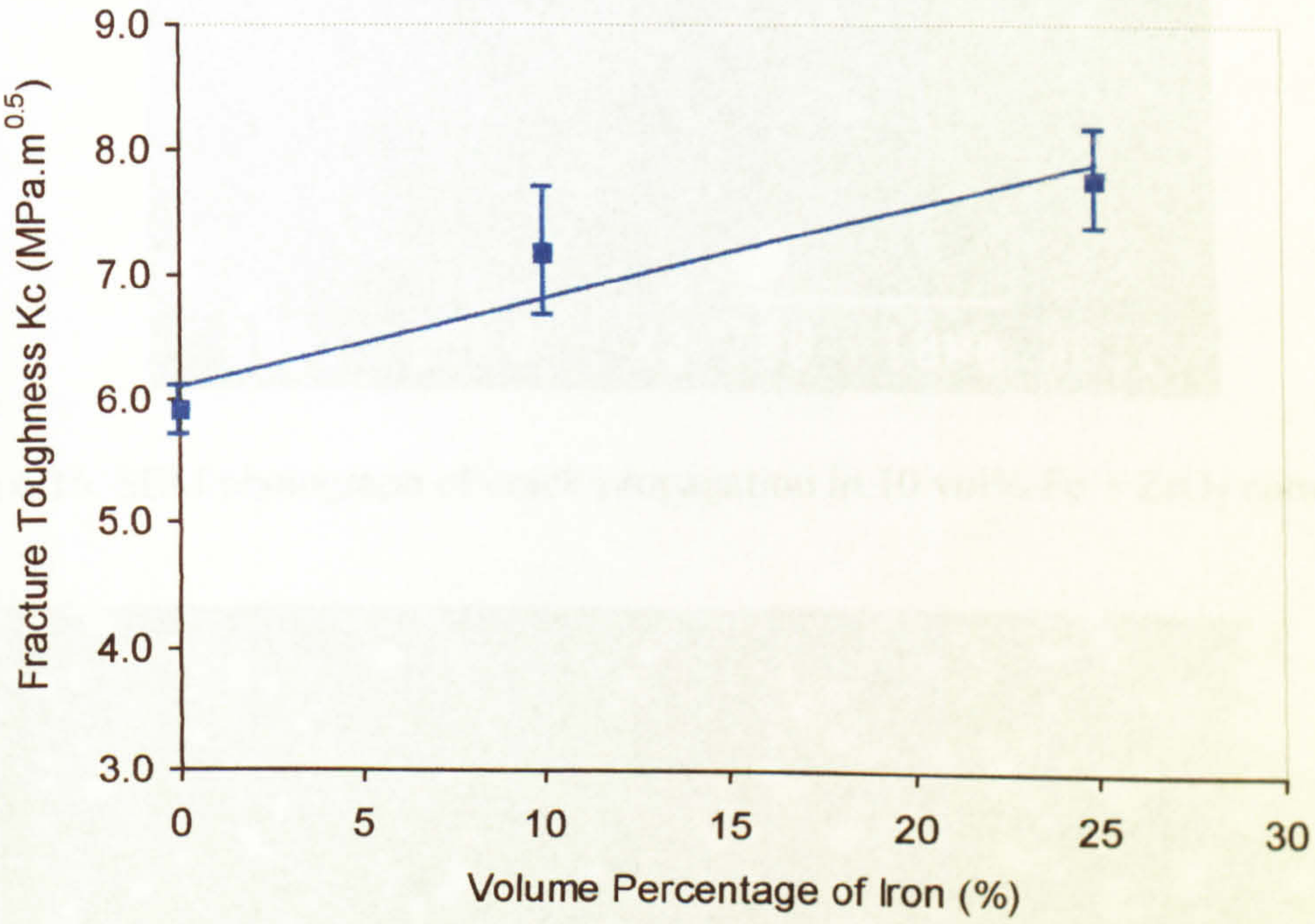

Figure 6.14. Effect of iron content on fracture toughness of zirconia/iron composites sintered at 1450°C for 1 hour in argon

Palmqvist crack type as shown in Figure 6.16 was characterised in the zirconia/iron composites. The pre-indented surface was gradually polished until the Palmqvist crack appeared. This type was also confirmed using a relationship of indent diagonal and crack length given by Niihara *et al*, 1982.

Material	Vickers Indentation		(*l*/a)	(*l* + a)/a	Crack Type
	Average of a (μm)	Average of *l* (μm)			
10 vol% Fe + ZrO_2	45.13	23.43	0.52	1.52	Palmqvist
25 vol% Fe + ZrO_2	54.75	13.53	0.25	1.37	Palmqvist

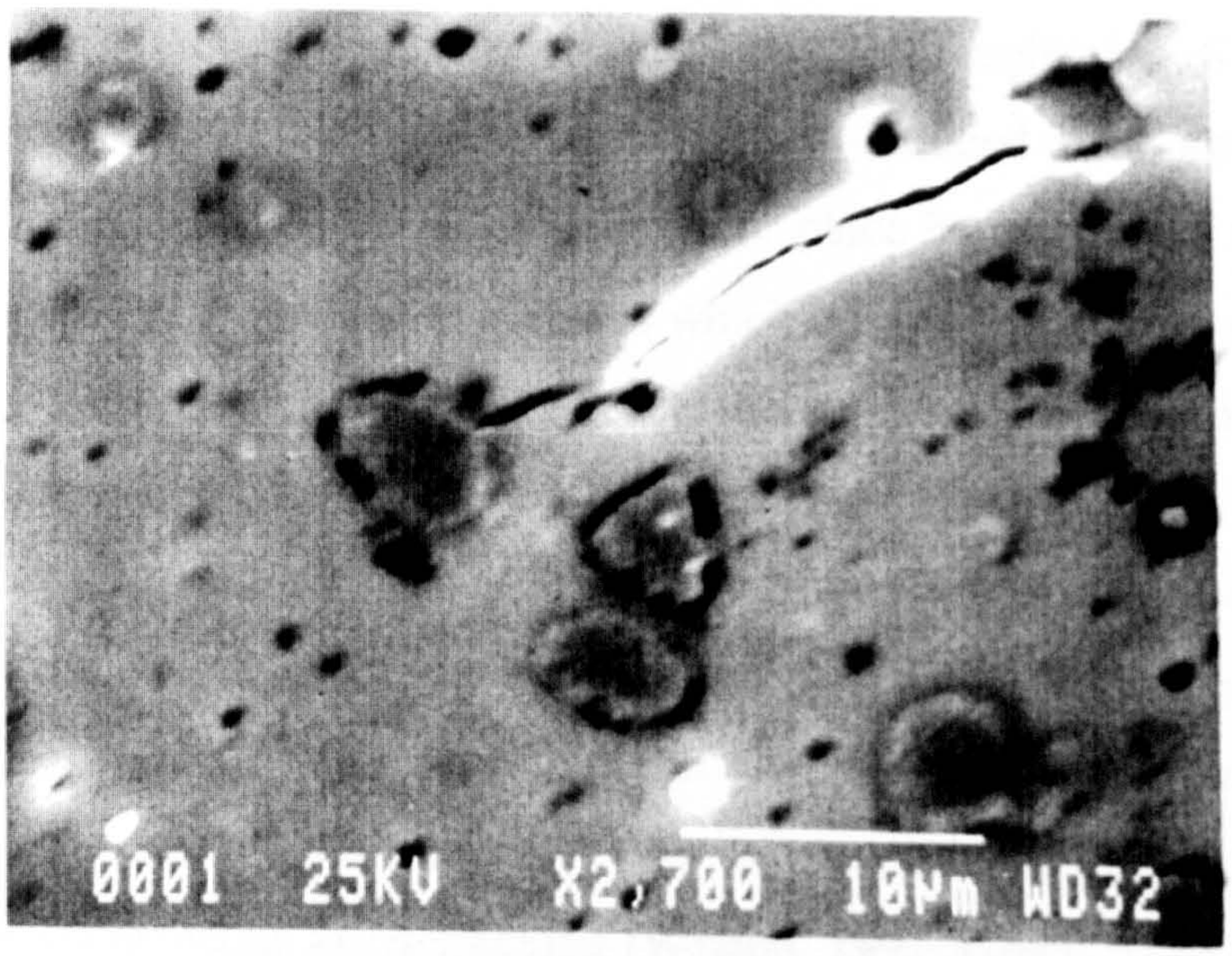

Figure 6.15. SEM photograph of crack propagation in 10 vol% Fe + ZrO_2 composite.

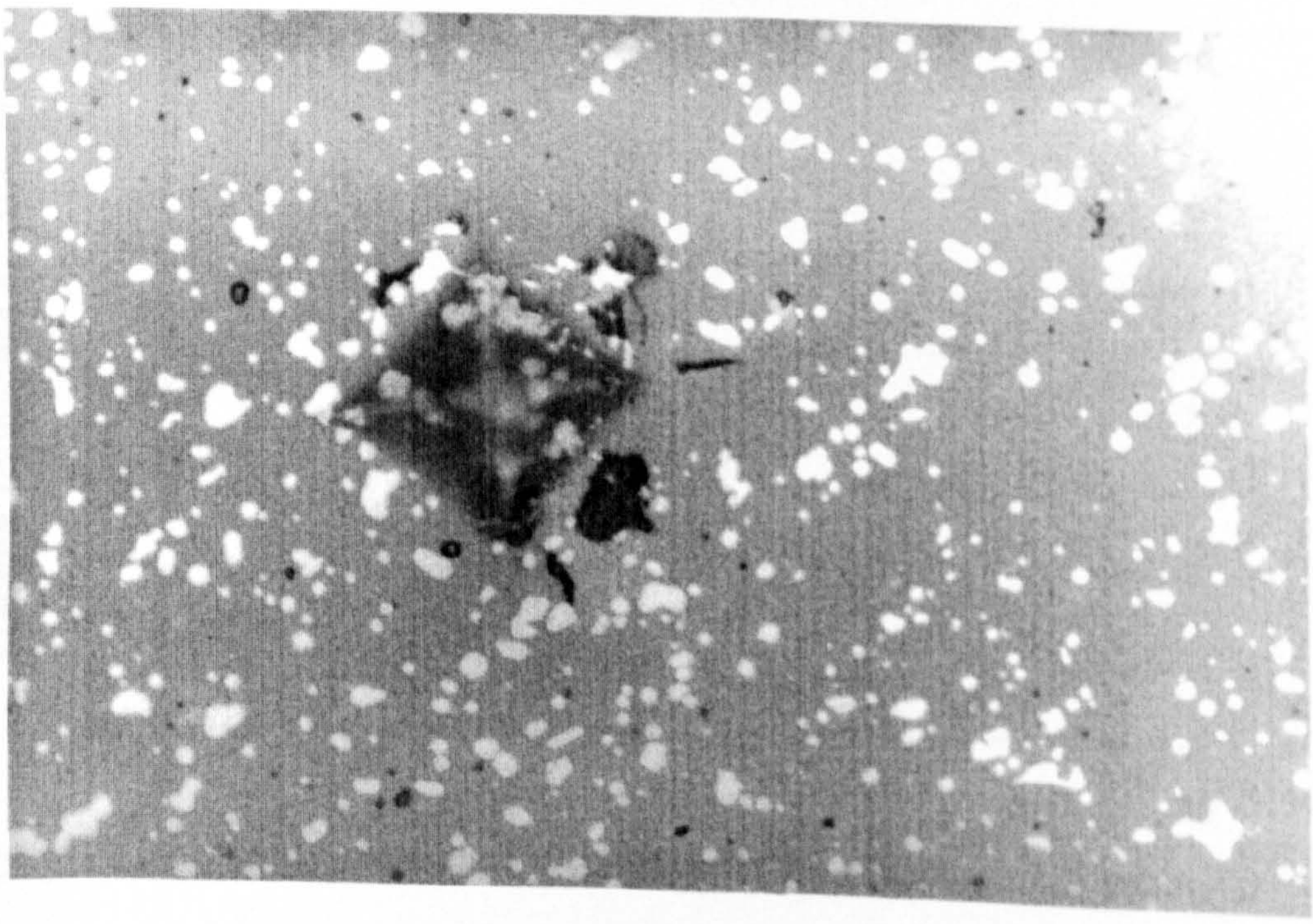

Figure 6.16 Optical micrograph of Palmqvist crack type on sample of (10 vol%Fe + ZrO_2) sintered at 1450°C for 1 h in argon

6.3.3. ZIRCONIA/AISI 316 COMPOSITES

The effect of AISI 316 content on fracture toughness of zirconia/AISI 316 is depicted in Figure 6.17. The toughness shows a little increase from (5.89 ± 0.22) MPa.m$^{0.5}$ to (6.26 ± 0.53) MPa.m$^{0.5}$ for 25 vol% AISI 316 + ZrO_2. The increase in fracture toughness is thought to be due to transformation toughening of the matrix and crack deflection. As mentioned in Chapter 5 stress-induced transformation from tetragonal to monoclinic of this composite can take place by applying a mechanical stress. It can be seen in Figure 5.9 that cracks which are generated from the Vickers hardness indent are deflected when they reach the particles. Furthermore, thermal stress analysis (Section 6.2.3) suggested that cracks are spontaneously formed in these composites during cooling from fabrication temperature, because the thermal stress due to thermal expansion mismatch is greater than the matrix strength and the particle size (the maximum size is 45 μm) is greater than the critical size. The fracture toughness is only expected to increase with particle size up to the critical particle size for spontaneous microcracking [Warren, 1992; Green, 1998]. So in this case the spontaneous microcracking during processing is less of value.

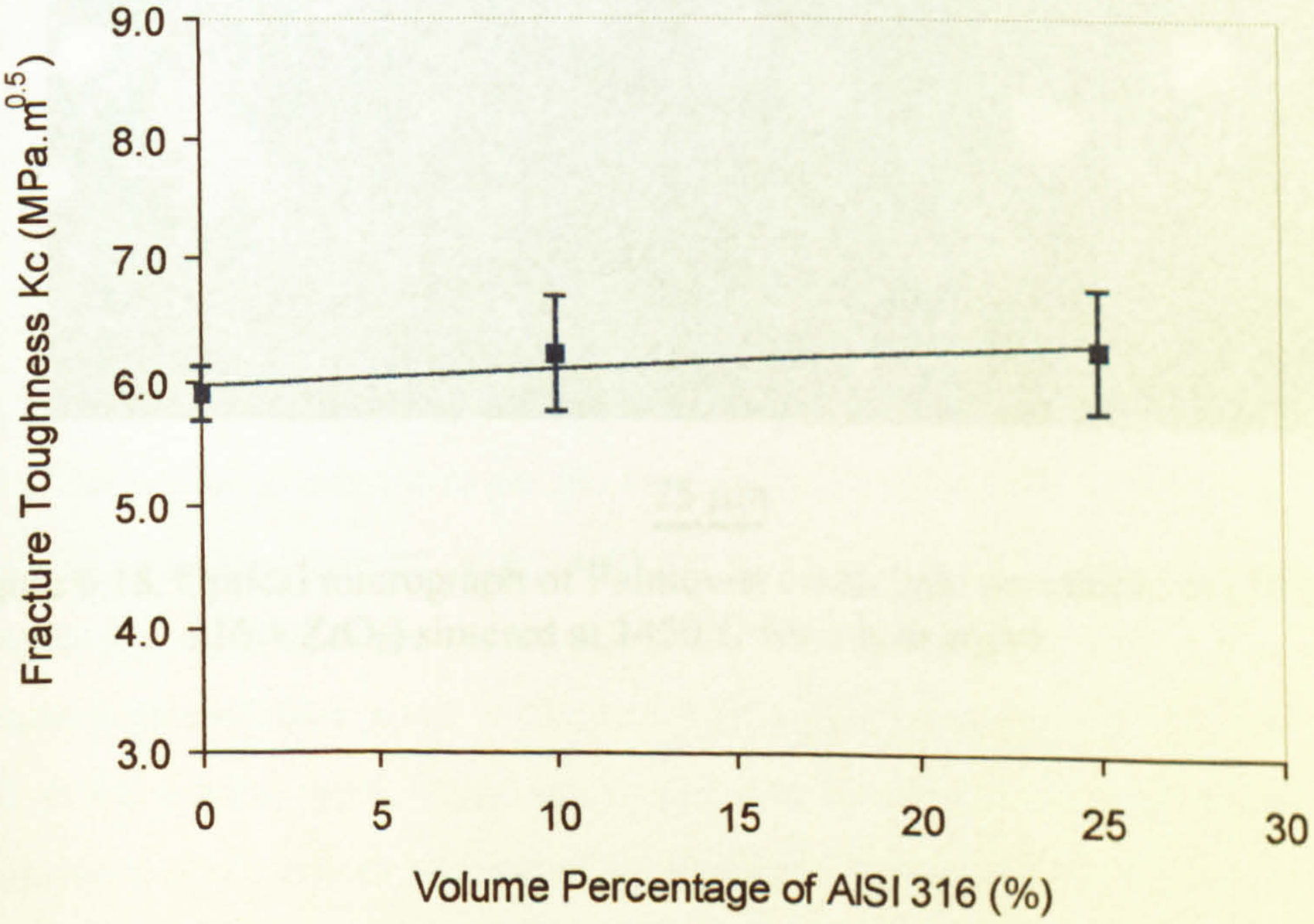

Figure 6.17. Effect of AISI 316 content on fracture toughness of zirconia/AISI 316 composites sintered at 1450°C for 1 hour in argon.

Palmqvist crack type was also marked on zirconia/AISI 316 samples as predicted using relationships given by Niihara, *et al* (1982) and showed in a polished, pre-indented surface of 10 vol% AISI 316 + ZrO_2 in Figure 6.18.

Material	Vickers Indentation		(*l*/a)	(*l* + a)/a	Crack Type
	Average of a (μm)	Average of *l* (μm)			
10 vol% AISI 316 + ZrO_2	45.15	30.03	0.67	1.67	Palmqvist
25 vol% AISI 316 + ZrO_2	51.53	21.14	0.51	1.51	Palmqvist

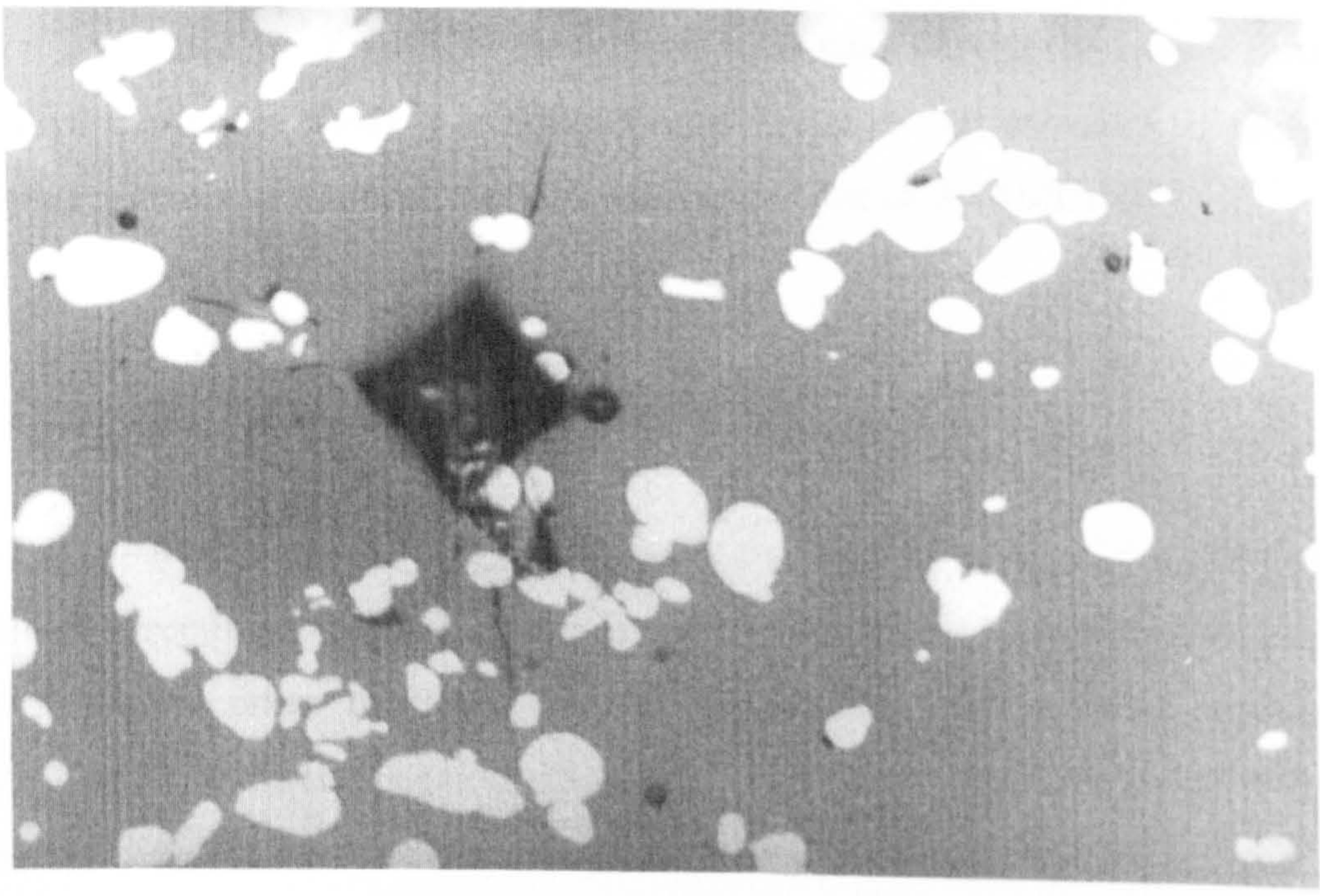

Figure 6.18. Optical micrograph of Palmqvist crack type on sample of (10 vol% AISI 316 + ZrO_2) sintered at 1450°C for 1 h in argon

6.4. BENDING STRENGTH

Four point bending tests were used to measure the sample strengths. Six samples of each material type were tested. For all the composites below, the strength of monolithic zirconia is superior to those of the composites. These phenomena will be analysed using the Griffith Equation [Chiang, 1997]:

$$\sigma = \frac{Kc}{\sqrt{\pi . c}} \qquad \ldots\ldots\ldots\ldots\ldots\ldots\ldots\ldots\ldots\ldots\ldots\ldots\ldots\ldots\ldots\ldots\ldots\ldots (6.10)$$

Where σ is the load at failure, K_c is the fracture toughness and c is the critical flaw or crack size (the largest flaw). According to that Equation the critical flaw size for monolithic zirconia is 23 μm at σ of 692 MPa and at Kic of 5.89 MPa.$m^{0.5}$.

6.4.1. ZIRCONIA/CHROMIUM COMPOSITES

Figure 6.19 shows the bending strength of zirconia/chromium composites as a function of chromium content. It can be seen in this figure that the strength decreases as the chromium content increases (from (692 ± 75) MPa for monolithic zirconia to (348.2±35) MPa for a composite containing 25 vol% Cr). This decrease of strength may be attributed to the residual thermal stress due to thermal expansion mismatch where tangential tensile stress occurs in the matrix around the particles [Claussen *et al*, 1986]. Furthermore the larger particle size (and/or the size of the coalescence between the particles) than the critical flaw (crack) size of the pure monolithic, may introduce greater flaw sizes in the composites [Davidge and Green, 1968]. Figure 6.20 shows critical crack (flaw) sizes in monolithic zirconia and zirconia/chromium composites at the failure stresses of the materials predicted using Equation 6.10. It can also be deduced from Figure 6.20 that the larger critical flaw size of

zirconia/chromium composites than that of monolithic zirconia for a given stress indicates that the composites have an increased fracture toughness as compared to monolithic zirconia [Smith, 1993].

Figure 6.21 is representative of fracture surfaces after bending tests of zirconia/chromium composites. The Figure shows the fracture surface of the composite containing 25 vol% Cr. It can be seen in that figure that cracks not only occur around the chromium particle or cluster, but they connect each other causing strength reduction.

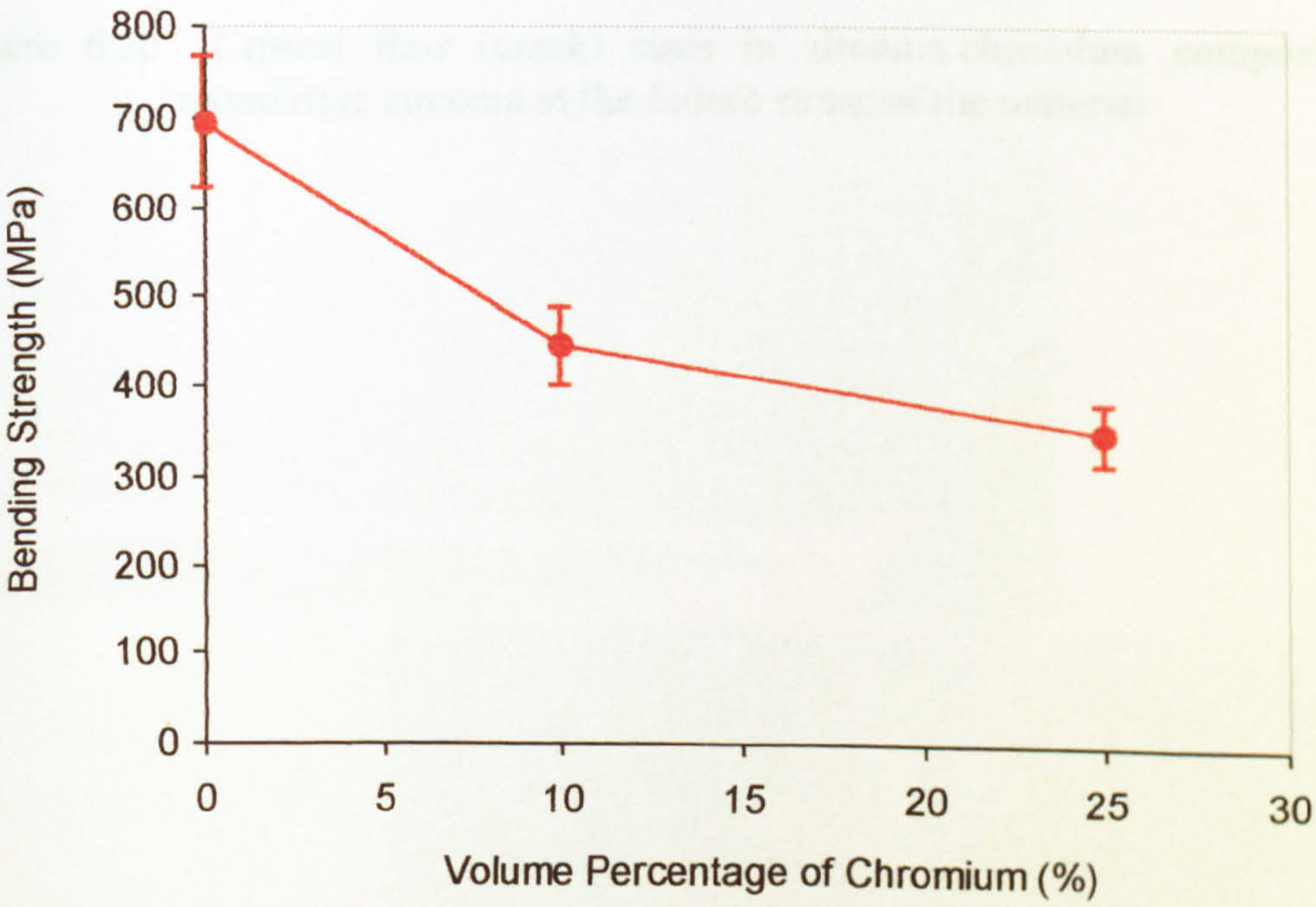

Figure 6.19 Effect of chromium content on bending strength of zirconia/chromium composites sintered at 1450°C for 1 hour in argon.

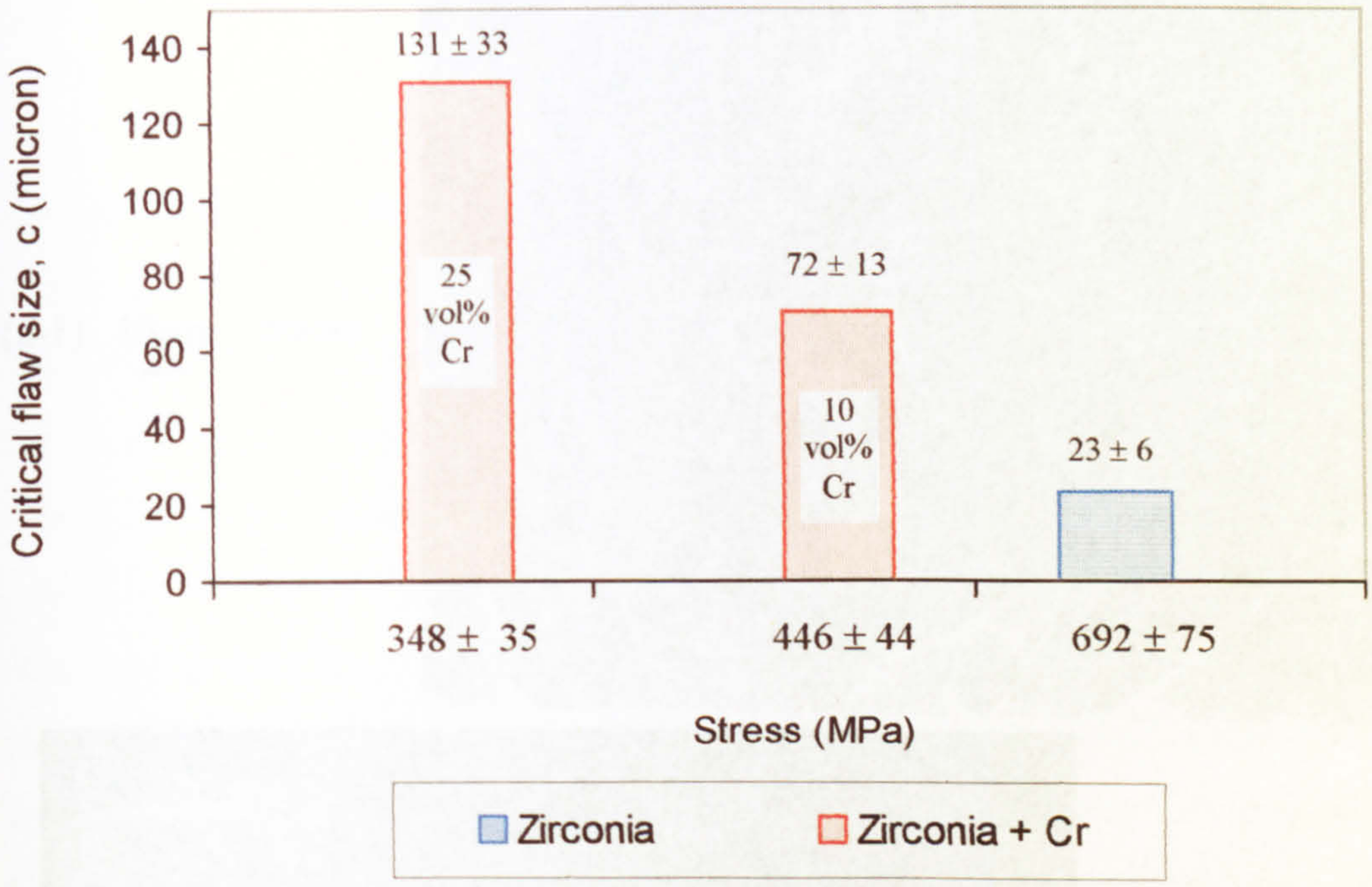

Figure 6.20 Critical flaw (crack) sizes in zirconia/chromium composites and monolithic zirconia at the failure stress of the material

(a-1) 10μm >>>>

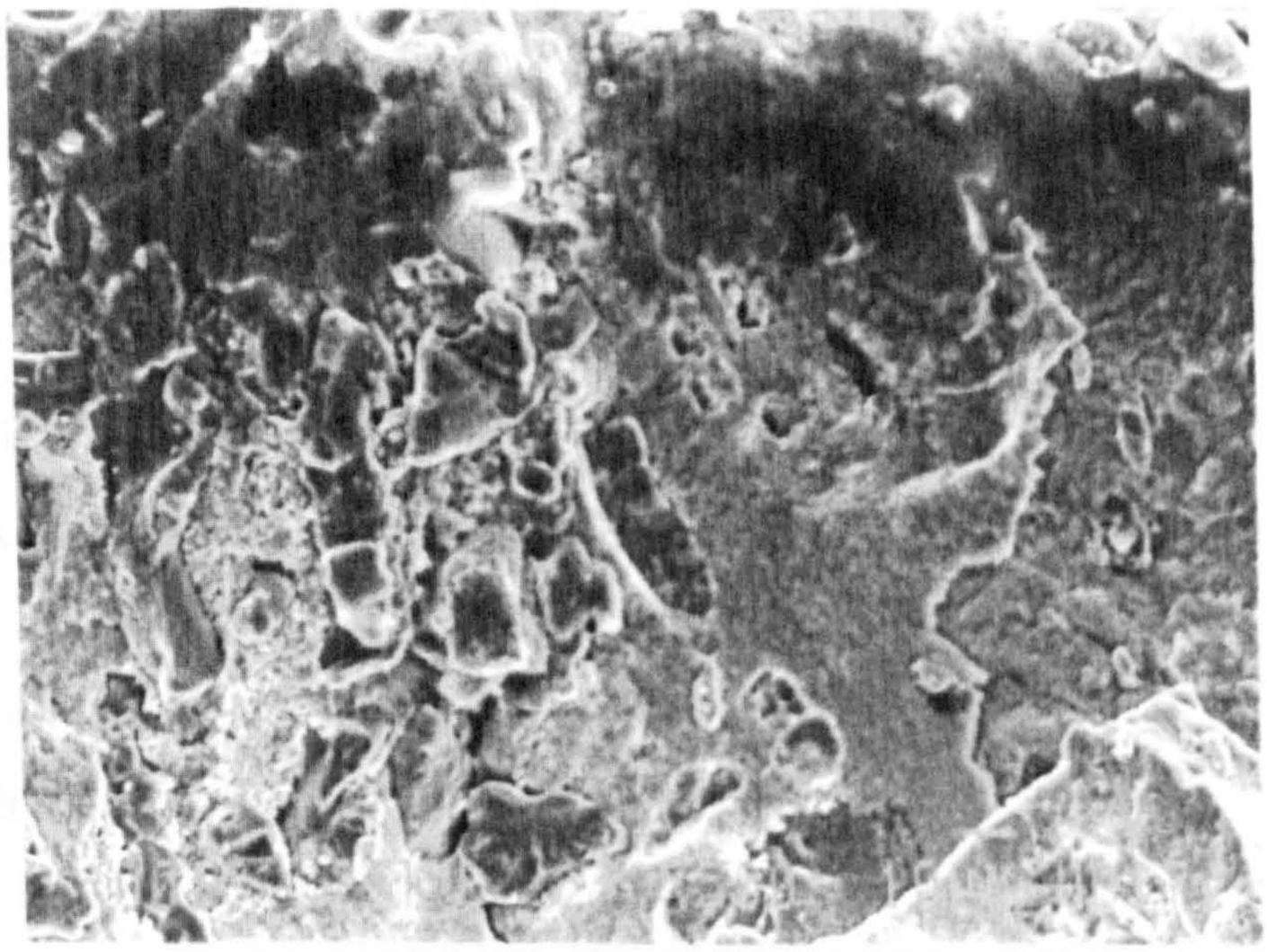

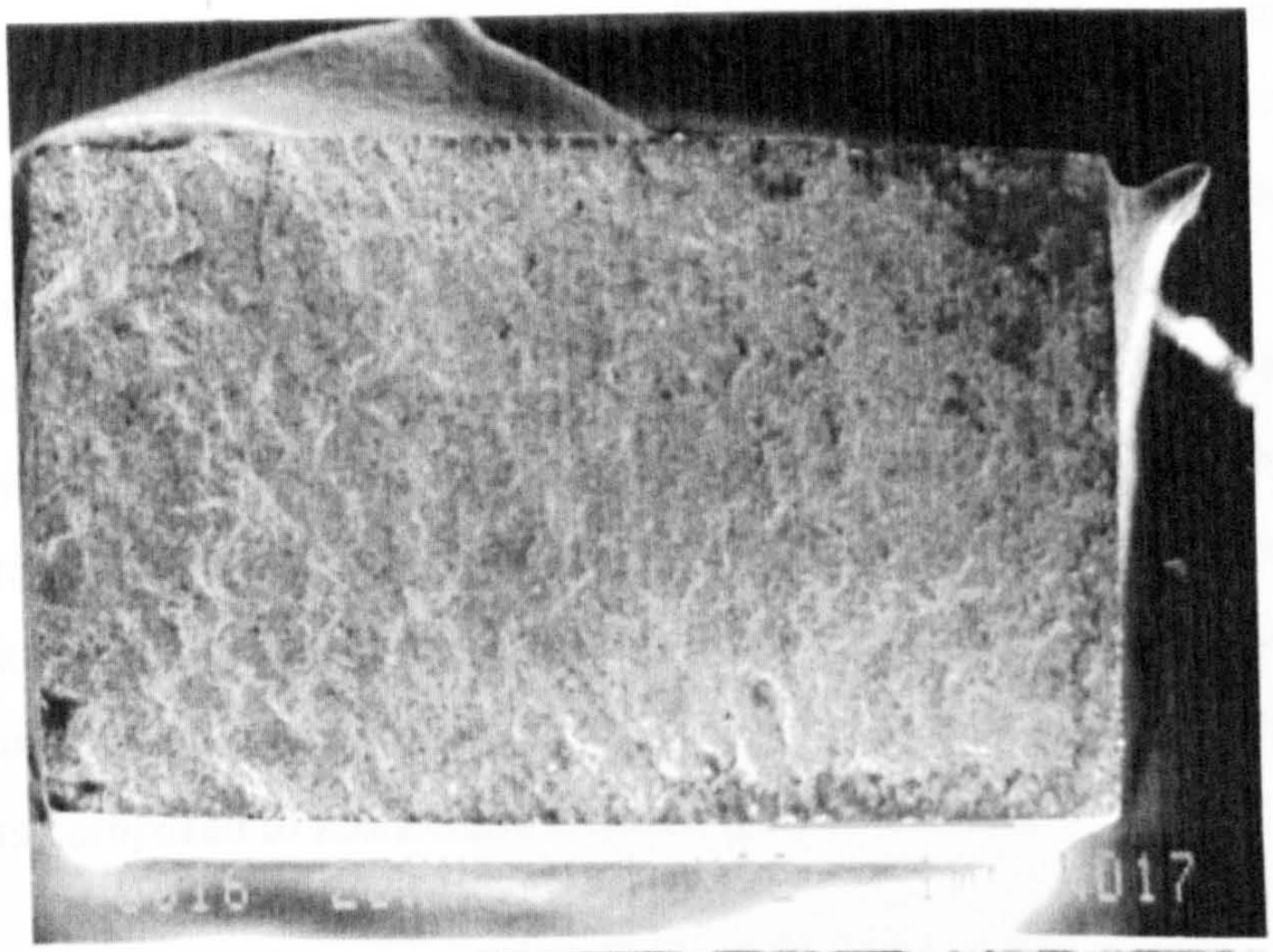

<<<< (a). 1 mm

(a-2) 10μm >>>>

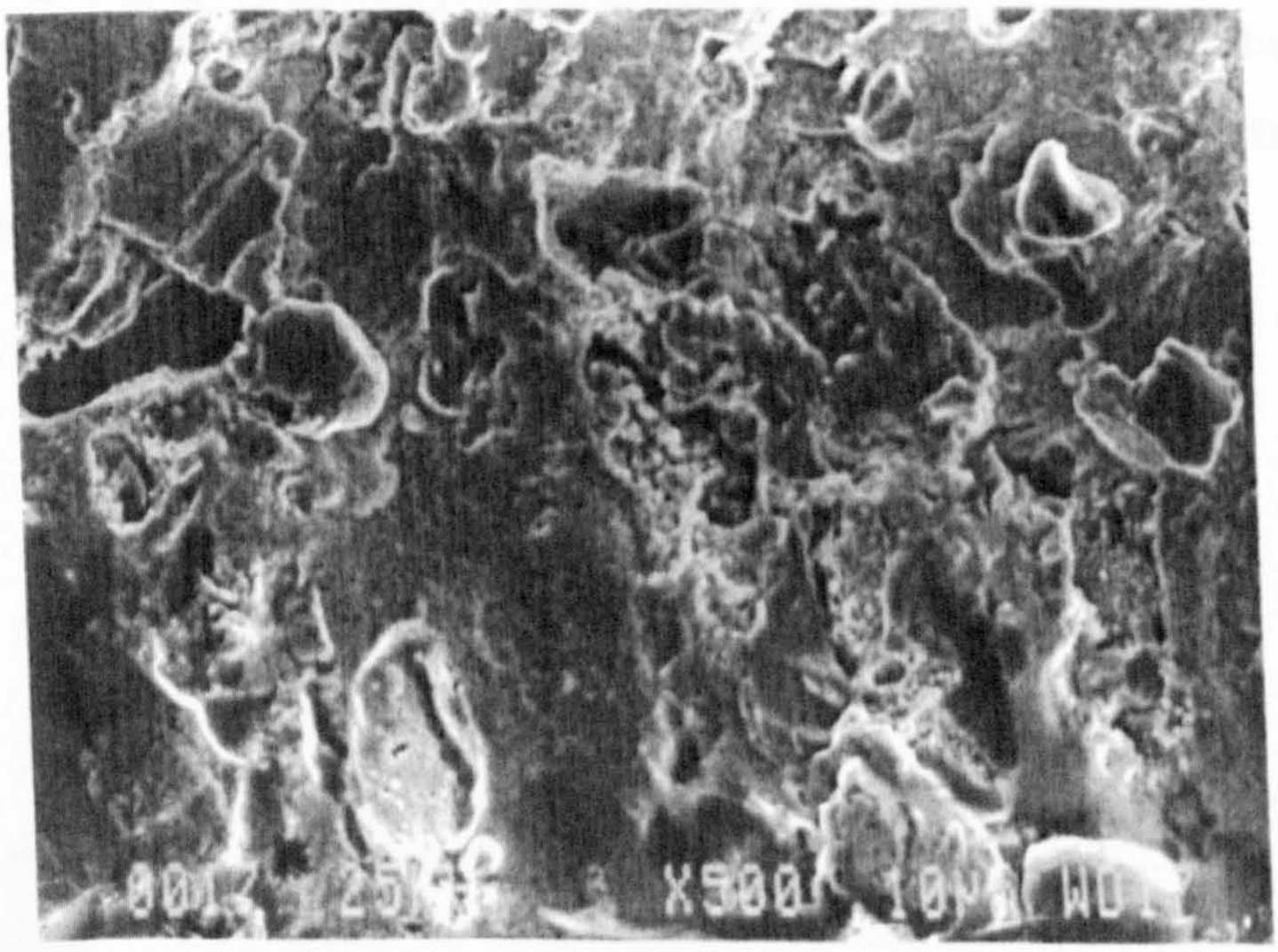

Figure 6.21 (a) SEM photographs of fracture surface after four point bending tests of (25 vol% Cr + ZrO_2) sintered at 1450°C for 1h in argon, (a-1) is near to the upper surface (compression) and (a-2) is near to the lower surface (tension surface).

6.4.2. ZIRCONIA/IRON COMPOSITES

The effect of iron content on strength is shown in Figure 6.22, where the strength decreases with increasing iron content (from (692 ± 75) MPa for monolithic zirconia to (432.5 ± 30) for composites containing 25 vol% Fe). In this case, as discussed in previous sections, cracks can occur around the particles with the stress below the macroscopic fracture stress (failure stress), because the matrix strength is smaller than the residual stresses and the iron particles are smaller than the critical particle size. This condition may lead to a decrease of the strength of the composites [Davidge and Green, 1968]. The coalescence of iron particles which may form a larger size can also be the cause of strength reduction if this size becomes larger than the inherent flaw (crack) size. Figure 6.23 shows the critical crack sizes in monolithic zirconia and zirconia/iron composites at the failure stresses of the composite materials predicted using Equation 6.10. The decrease of strength in these composites is lower than that of zirconia/chromium composites, because the iron particle size is much smaller than that of chromium. So, the smaller particle sizes may reduce the critical (flaw) size. It can also be seen from Figure 6.23 that the larger critical flaw size of zirconia/iron composites than that of monolithic zirconia for a given stress indicates that the composites have an increased fracture toughness as compared to monolithic zirconia [Smith, 1993].

The fracture surface of 25 vol% Fe + ZrO_2 is shown in Figure 6.24. It can be seen that some iron particles are pulled out and cracks occur around the particles or the coalescence of particles.

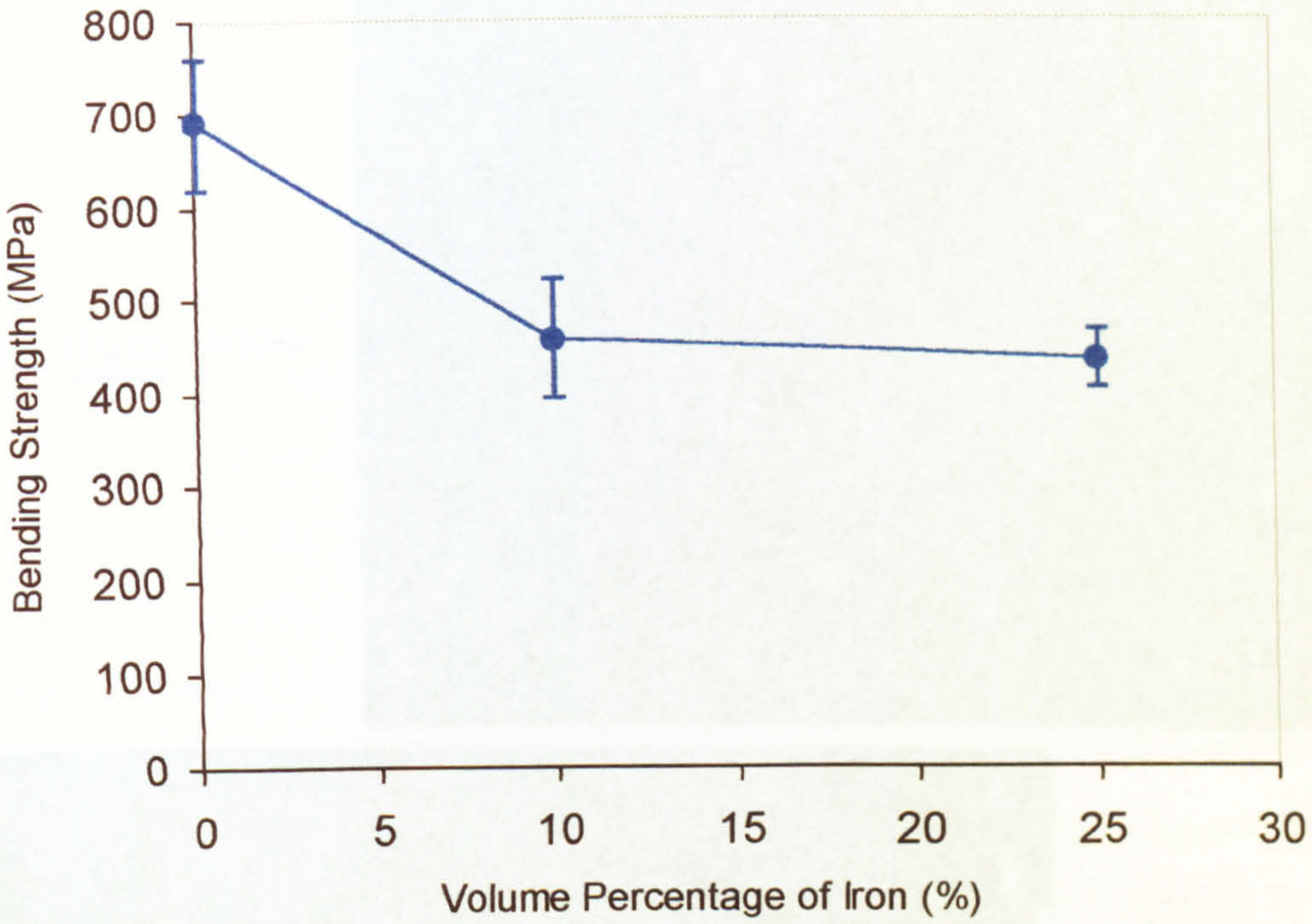

Figure 6.22 Effect of iron content on bending strength of zirconia/iron composites sintered at 1450°C for 1 hour in argon

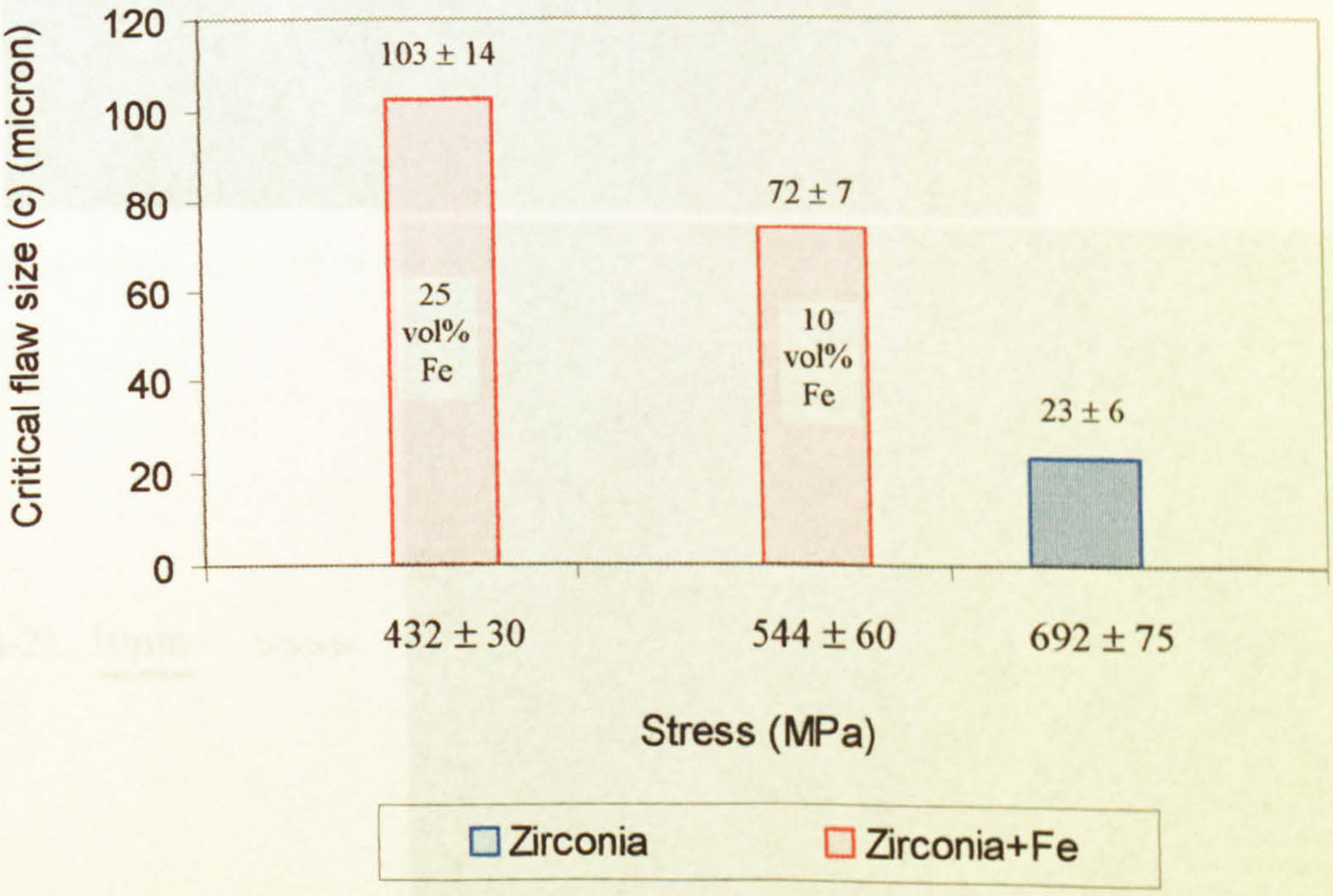

Figure 6.23 Critical crack sizes in zirconia/iron composites and monolithic zirconia at the failure stress of zirconia/iron composites.

(a-1) 10μm >>>>

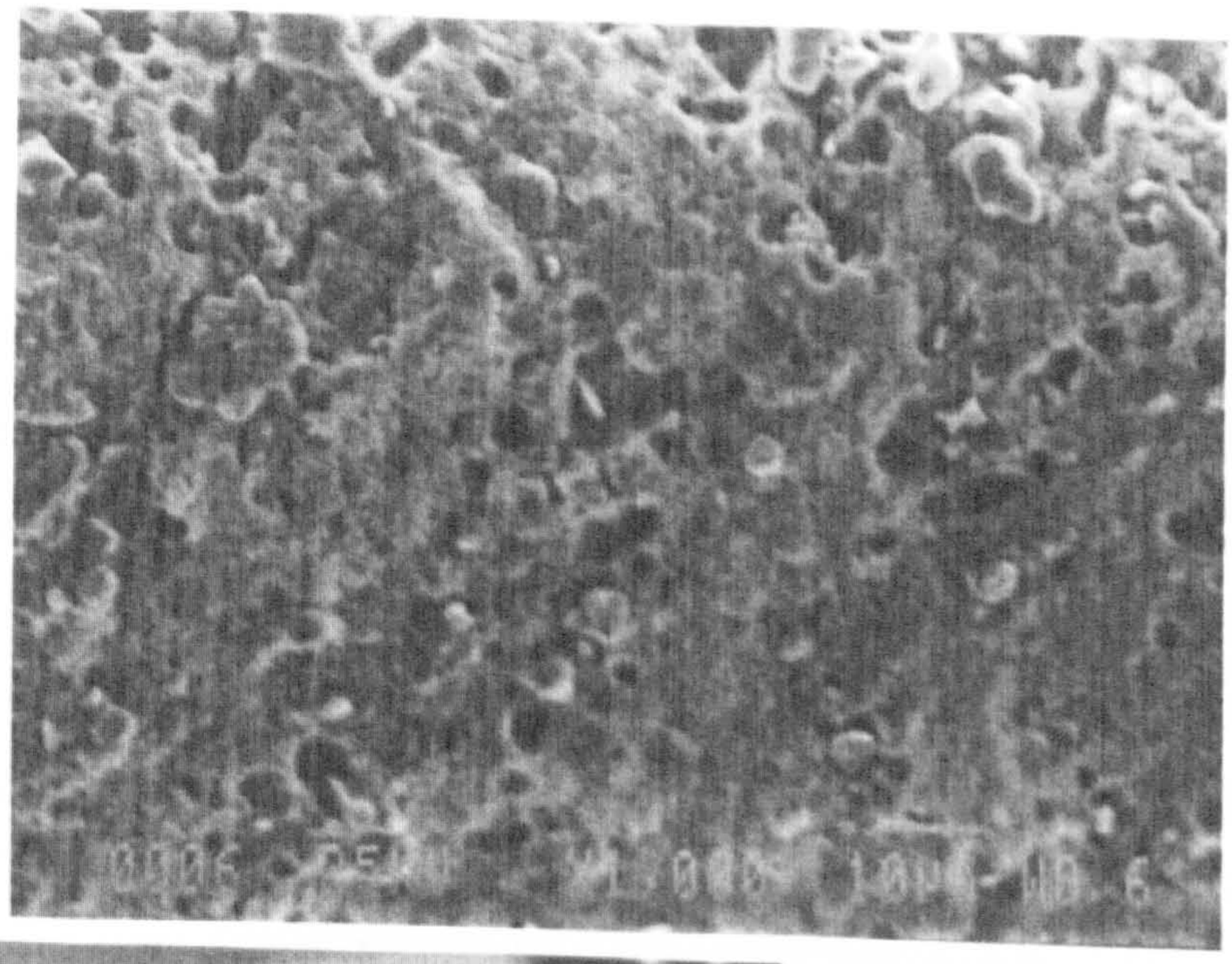

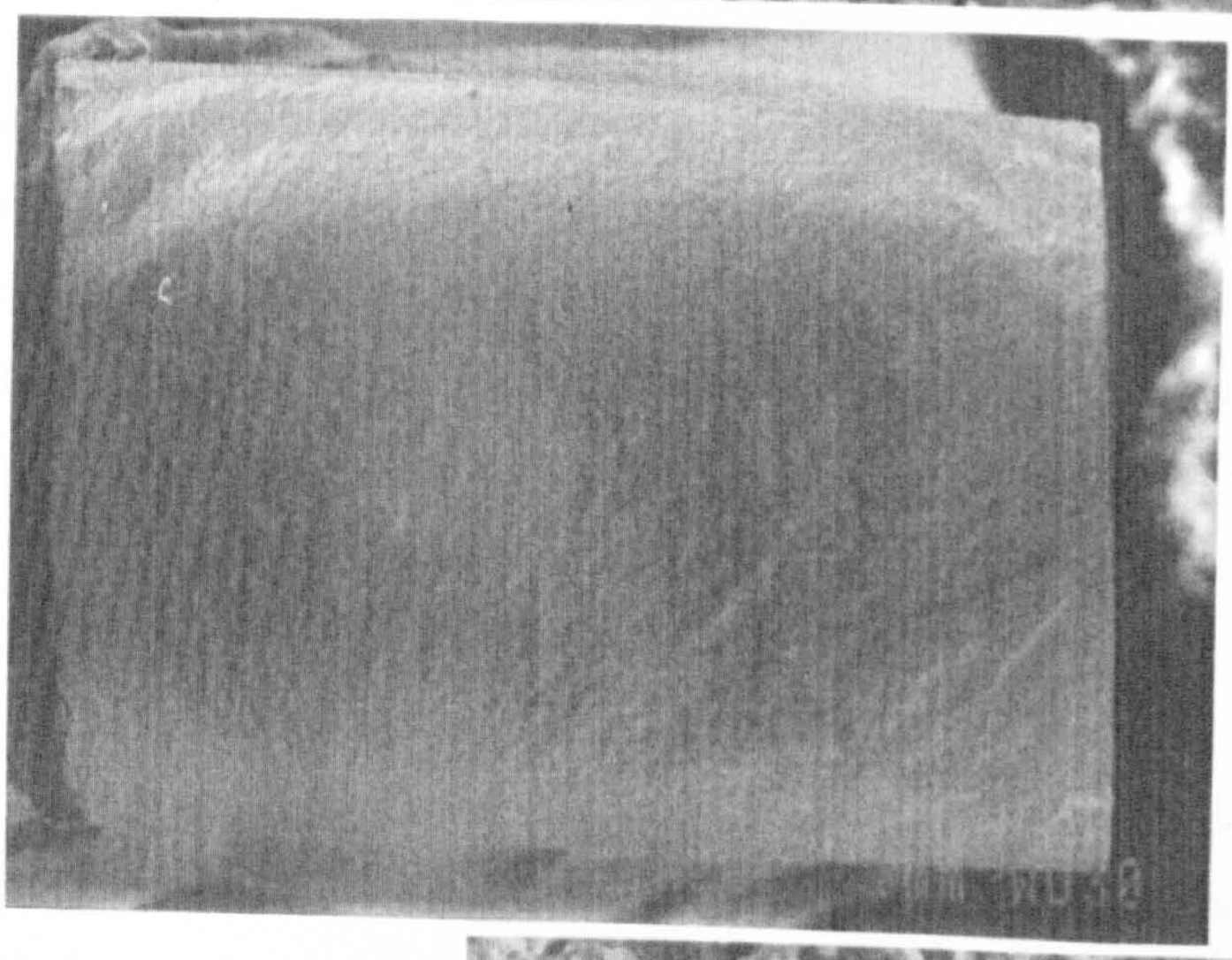

<<<< (a). 1 mm

(a-2) 10μm >>>>

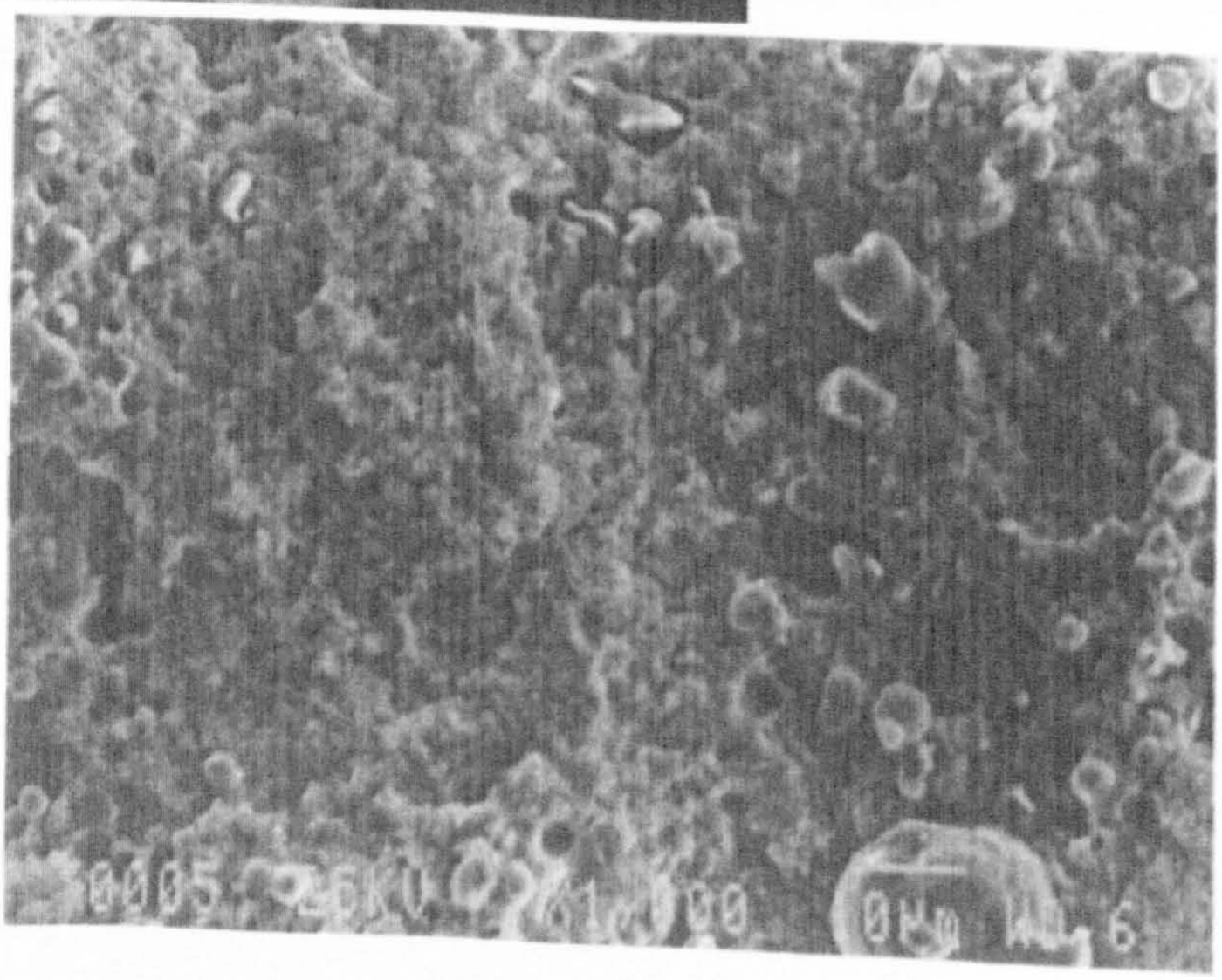

Figure 6.24 (a) SEM photographs of fracture surface after four point bending tests of (25 vol% Fe + ZrO_2) sintered at 1450°C for 1h in argon, (a-1) is near to the upper surface (compression) and (a-2) is near to the lower surface (tension surface).

6.4.3. ZIRCONIA/AISI 316 COMPOSITES

The strength of zirconia/AISI 316 composites decreases drastically with increasing AISI 316 content (from (692 ± 75) MPa for monolithic zirconia to (186.6 ± 37) for the composites containing 25 vol% AISI 316 as shown in Figure 6.25. As mentioned in the earlier sections, in this composite spontaneous microcracking may occur during fabrication due to thermal expansion mismatch and the AISI 316 particles are greater than the critical particle size. If spontaneous microcracking occurs in the whole sample and are interconnected, they will drastically reduce the strength [Warren, 1992; Green, 1998]. Smith, (1993) showed that the strength of sialon/AISI 316 composites decreased drastically as the AISI 316 content increases due to thermal expansion mismatch causing high thermal stress in the matrix. Also if there is coalescence between the particles, it will cause an increase in the flaw (crack) sizes. The critical flaw (crack) sizes of monolithic zirconia and zirconia/AISI 316 composites at the failure stresses of the composite materials predicted using Equation 6.10 is shown in Figure 6.26. It can be seen from Figure 6.26 that there are larger critical flaw sizes for zirconia/AISI 316 composites than that of the other composites or of monolithic zirconia for a given stress.

Figure 6.27 shows the fracture surface of 25 vol% AISI 316 + ZrO_2 where cracks clearly occur around the particles and across the matrix. Some particle pull out also can be seen in that figure.

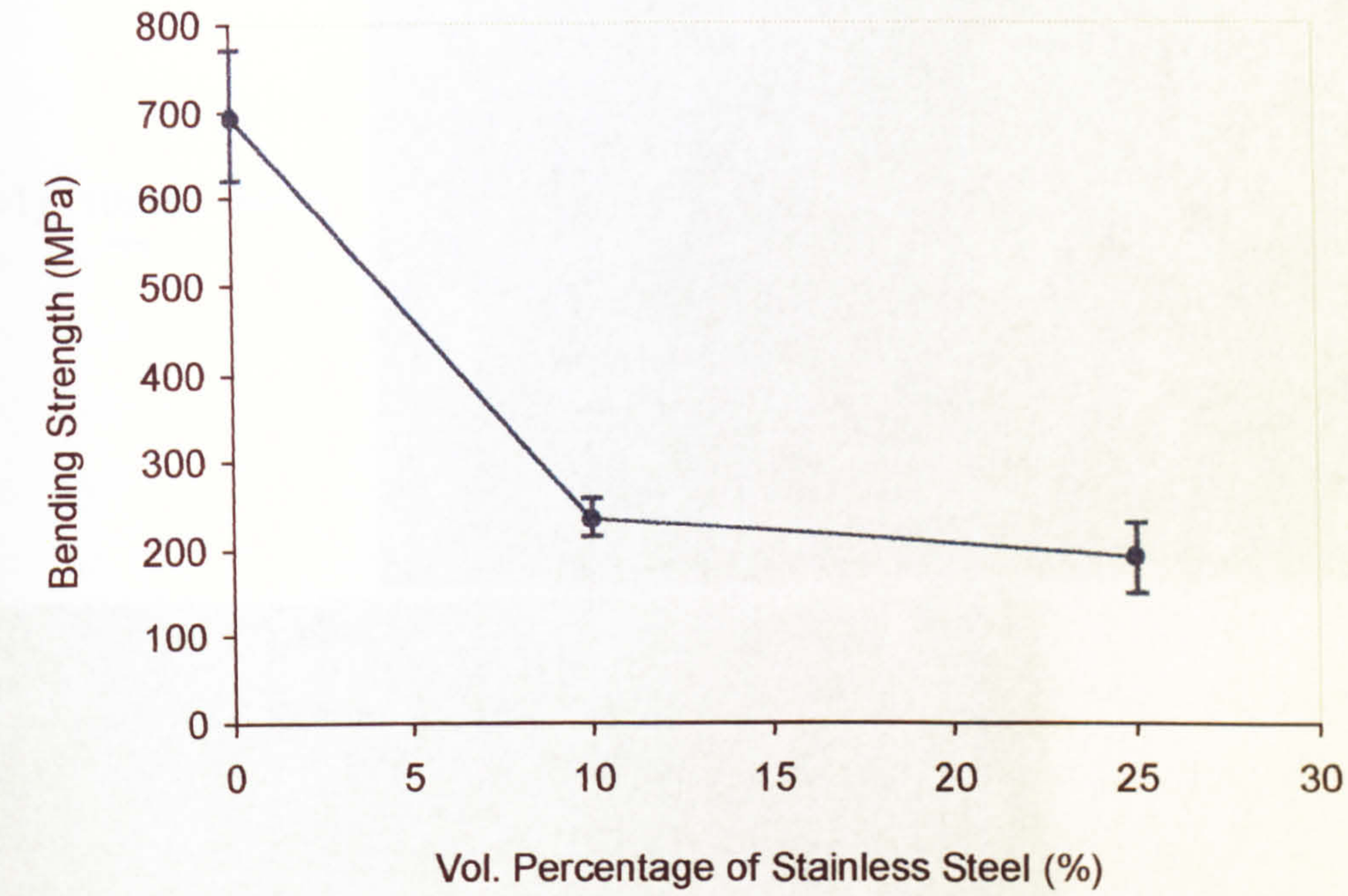

Figure 6.25 Effect of AISI 316 content on bending strength of zirconia/AISI 316 composites sintered at 1450°C for 1 hour in argon

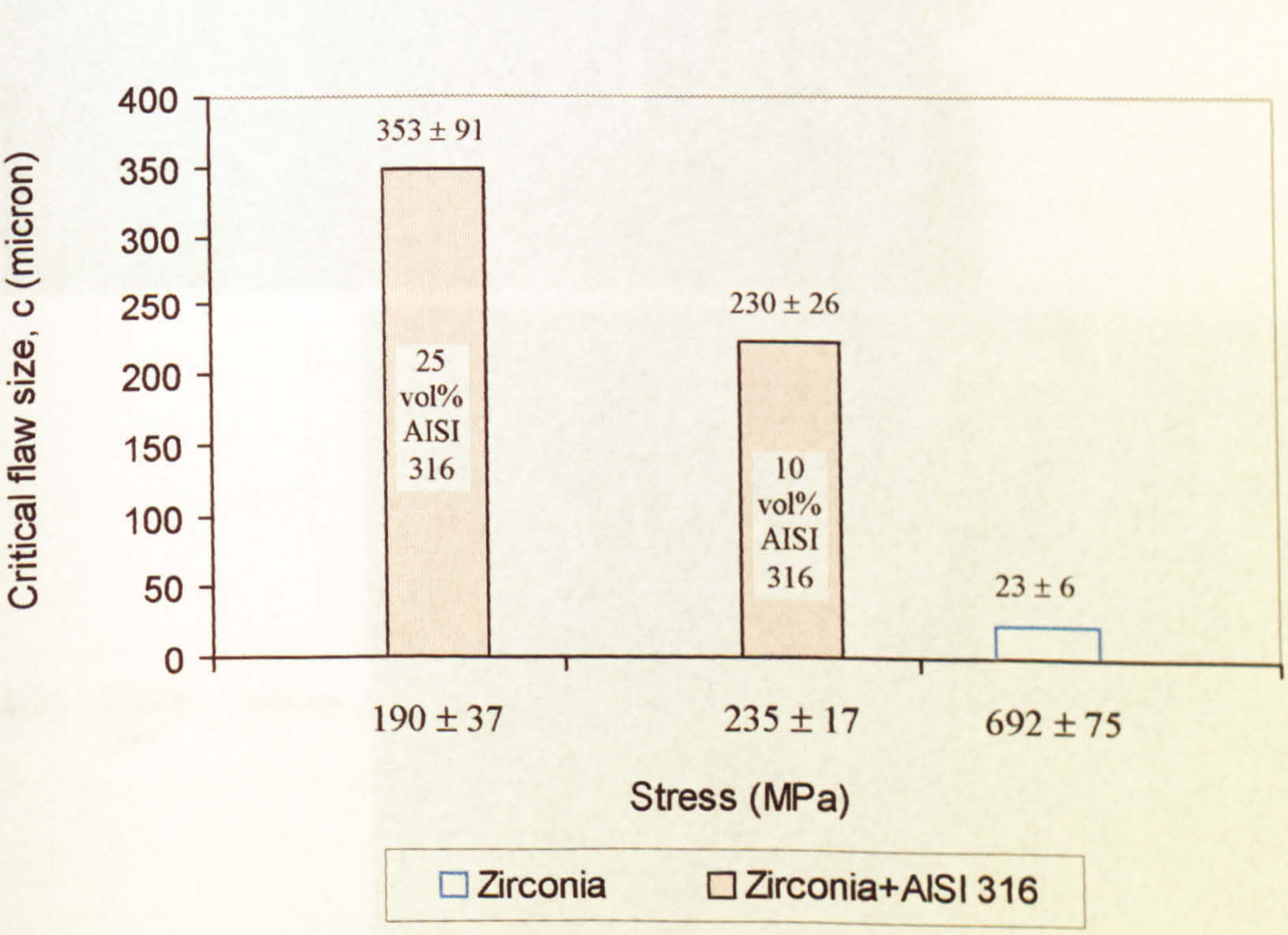

Figure 6.26 Critical crack sizes in zirconia/AISI 316 composites and monolithic zirconia at the failure stress of zirconia/AISI 316 composites.

(a-1) 10μm >>>>

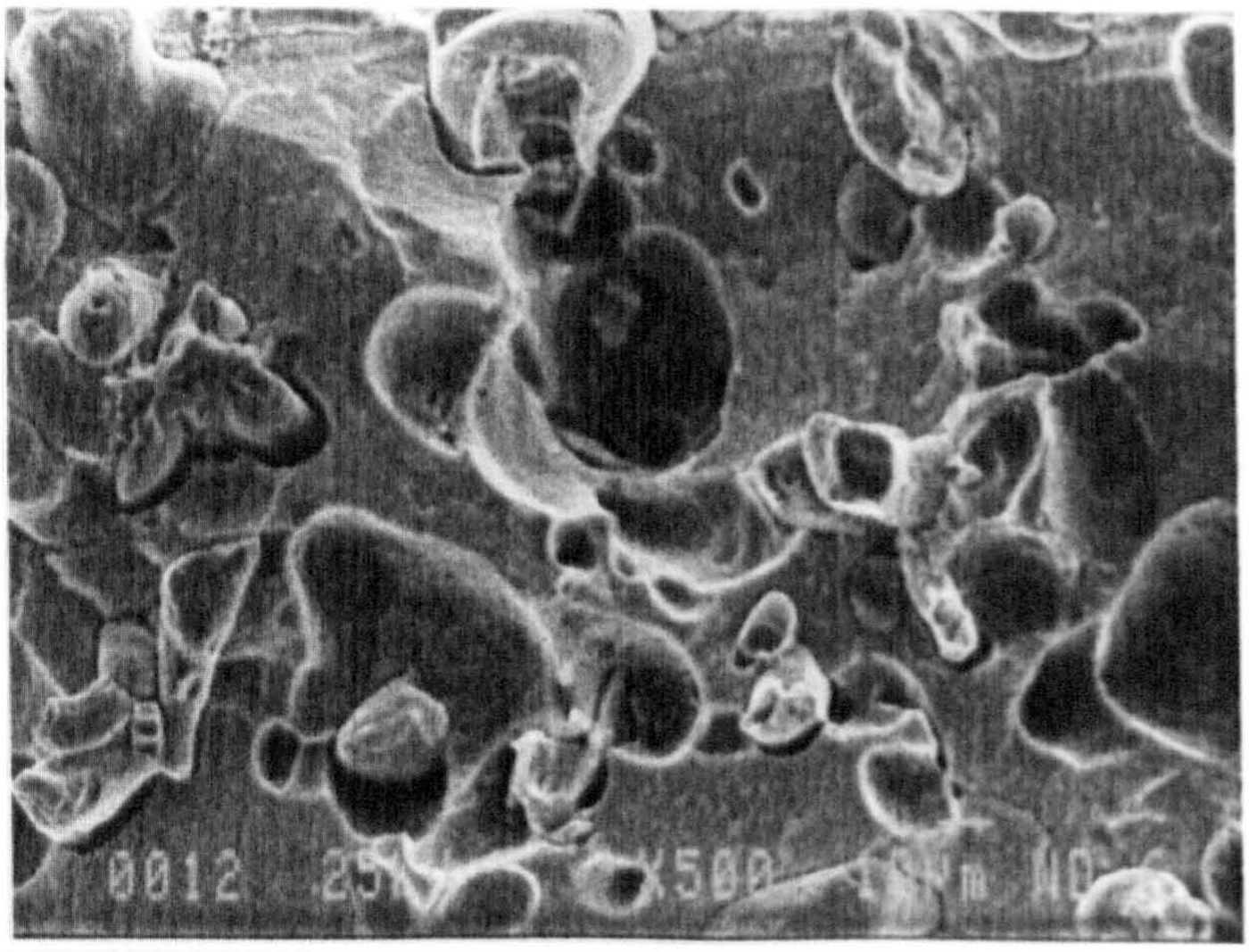

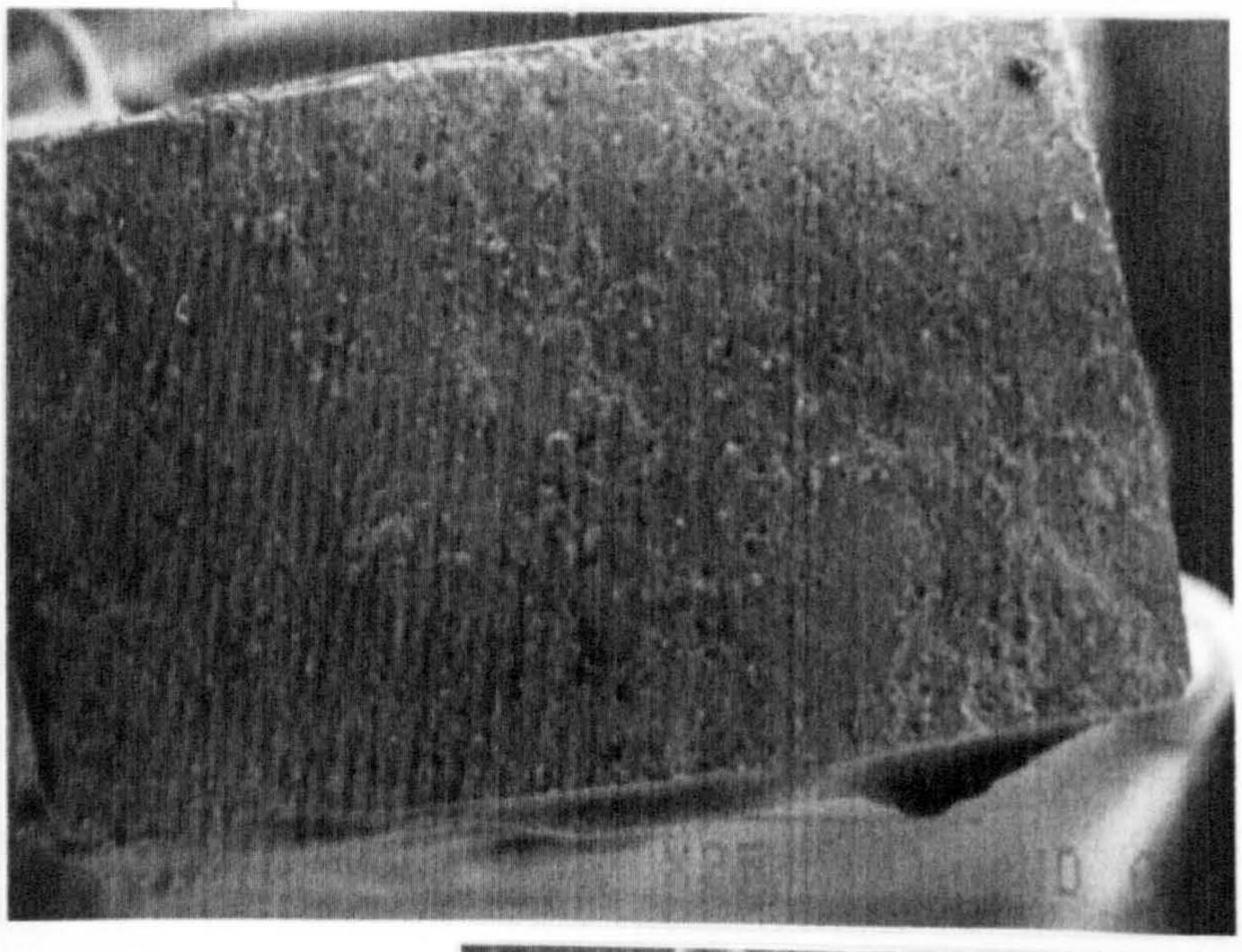

<<<< (a). 1 mm

(a-2) 10μm >>>>

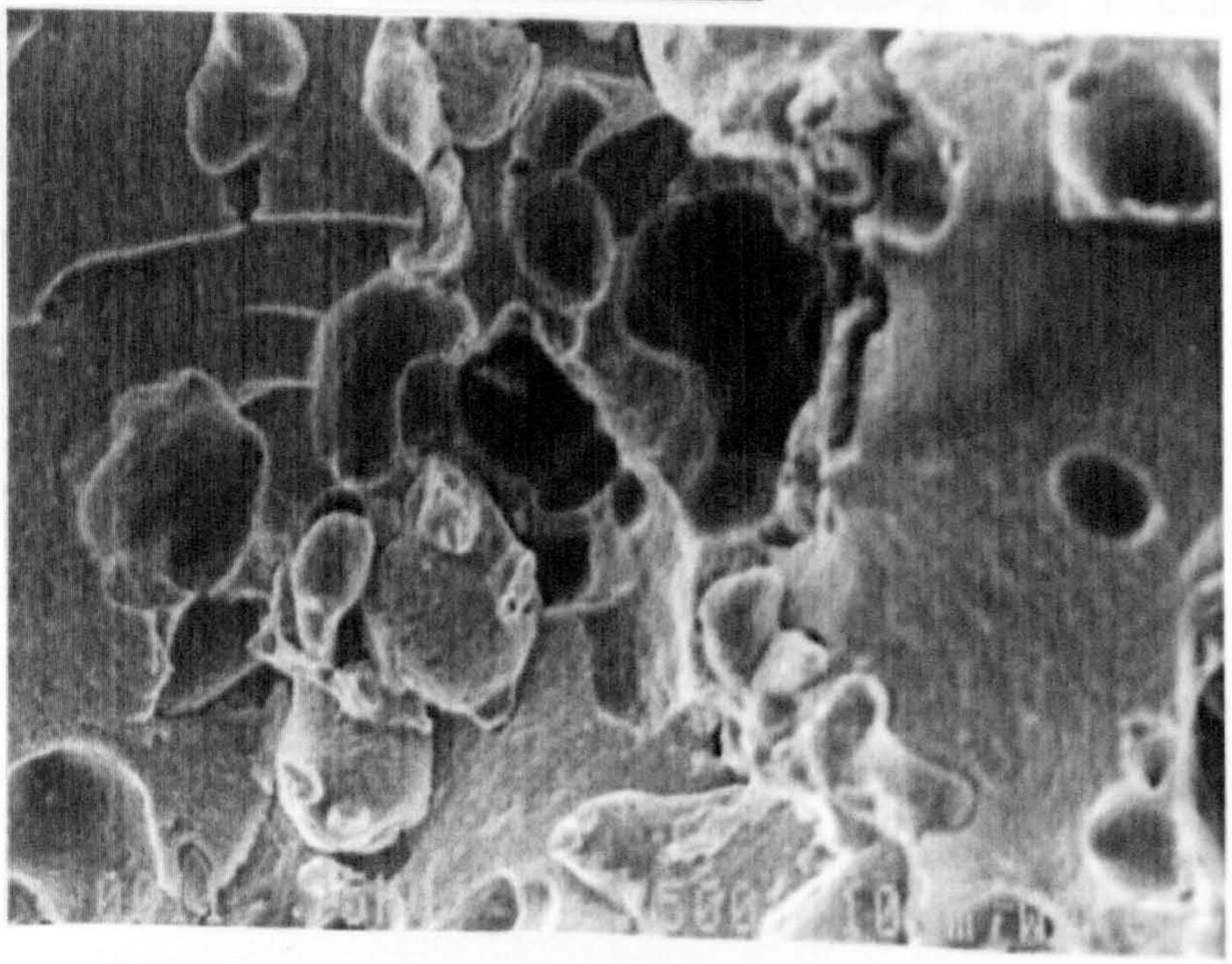

Figure 6.27 (a) SEM photographs of fracture surface after four point bending tests of (25 vol% AISI 316 + ZrO_2) sintered at 1450°C for 1h in argon, (a-1) is near to the upper surface (compression) and (a-2) is near to the lower surface (tension surface).

6.5. DISCUSSION

6.5.1. HARDNESS

Hardness number is a term used to express the resistance of a material to the formation of a permanent surface impression by an indenter. Vickers hardness is the most common method in hardness measurement for ceramics and is one of the requirement parameters in wear and erosion specification [Warren, 1992]. The application of Vickers method in ceramics often causes cracks generated from the indent corners.

The hardness of a composite can be predicted using a simple rule of mixtures. For particulate composites the value will usually lie between the upper bound (linear rule of mixtures) and lower bound (inverse rule of mixtures) which are expressed in Equations 6.1 and 6.2 respectively [Warren, 1992]. Furthermore, Lee and Gurland (1978) and Warren (1983) point out that the hardness value of particulate composites is also influenced by the particle size and/or the connectivity between the particles. In their study on 3Y-TZP/Mo nanocomposites, Nawa *et al* (1996) found that the hardness of the composites containing less than 70 vol% Mo showed slightly lower values than that calculated using a linear rule of mixtures and for the composites containing above 70 vol% Mo showed slightly higher than that calculated using a linear rule of mixtures. This indicates that particulate composites with smaller particle size (nano-sizes) will result in more uniform material, hence the hardness will be close to the linear rule of mixtures. In addition, the connectivity between the particles influences the hardness.

In this present study, the hardness of zirconia matrix composites (zirconia/chromium, zirconia/iron and zirconia/AISI 316 composites) decreases with increasing volume fraction of the reinforcement due to the lower hardness value of the reinforcement than that of the matrix. Nawa *et al* (1996), Jung *et al* (1997), and Guichard *et al* (1997) also found that the softer metal particle reinforcements reduced the hardness of particulate ceramic composites. The hardness values of the present

study were lower than that calculated using a linear rule of mixtures which may be due to the effect of particle size and/or interparticle spacing. The values however, lie between the upper and lower bound (Figures 6.1, 6.5 and 6.9).

It can also be seen in the present study that the particle size influenced the error or standard deviation of hardness measurement. The zirconia/iron composites with mean particle size of iron of (6 - 8 μm) yielded a standard deviation of < 3%. Chromium with the maximum particle size of 38 μm in zirconia/chromium composites resulted in a standard deviation of < 5%, while a standard deviation of < 20% was found in zirconia/AISI 316 composites where the maximum particle size of AISI 316 was 45 μm. This can be understood that at a certain composition, the smaller particle size will be dispersed more uniformly than that of larger size (see the microstructures in Chapter 5).

6.5.2. THERMAL STRESSES, FRACTURE TOUGHNESS AND STRENGTH

Although the model of thermal stresses due to thermal expansion mismatch between matrix and particle given by Selsing (1961) is based on a single spherical particle in infinite matrix and by Chawla (1993) for spherical particulate composites with particle volume fraction V_p, those models (Section 6.2) can be used to estimate such thermal stresses of any particulate composites. Several researchers such as Selsing (1961), Davidge and Green (1968), Powell *et al* (1980), Krstic *et al* (1981) and Zhan, *et al* (1996) have used those models to analyse the residual stresses in particulate ceramic composites. However, they used different approaches in taking the value of coefficient of thermal expansion (α) on the Equations. Some authors such as Powell *et al* (1980), Krstic *et al* (1981) and Zhan *et al* (1996) used the value of α at the range of (20 - 100) °C. Whereas others such as Davidge and Green (1968), and Taya *et al* (1990) took the α value at the range of (20 - annealing temperature) and (20 - processing temperature) °C respectively. According to their models (Selsing (1961) and Chawla (1993)), ΔT is the temperature difference over

which the composite is cooled from T_0 to T_1 and over which no stress relaxation can occur ($\Delta T = T_1 - T_o$), and $\Delta\alpha$ is the thermal expansion mismatch between matrix and particle ($\Delta\alpha = \alpha_m - \alpha_p$). In this present study the value of α_m was taken from experimental measurement, while the thermal expansion of the reinforcements (α_p) were taken from the literature. Thermal expansion is temperature dependent, and so average of α values from T_1 to T_0 should be taken. However, due to the limited data of α at the range of 20 to high temperature (above 1000°C) in the literature, then the data of α was taken for the range of (20 to about 900)°C.

Based on those models the thermal stresses due to thermal expansion mismatch can be illustrated in Figure 6.28 below.

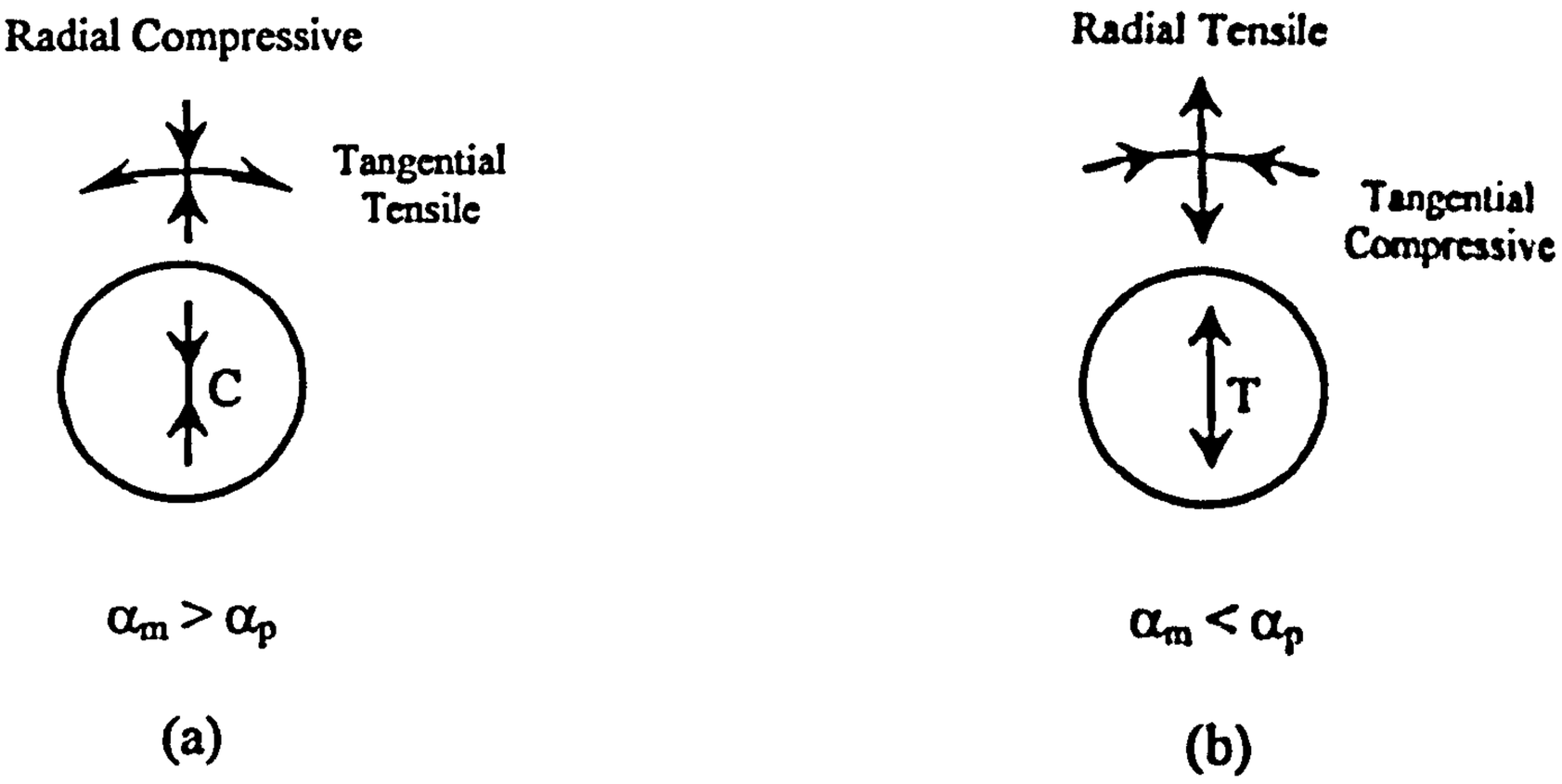

Figure 6.28. Radial and tangential stresses developed upon cooling of embedded particle in a matrix (Barsoum, 1997)

Models of thermal stresses (Selsing, 1961 and Chawla, 1993) together with a model for critical particle size given by Davidge and Green (1968) can be used to estimate the residual stresses in composites and to explain the fracture toughness and strength. Metal reinforcements used in the present study are different in terms of modulus of elasticity, poisson's ratio, particle size and coefficient of thermal expansion. Zirconia/chromium composites (where $\alpha_m > \alpha_p$) will be subjected to compressive stress in the particle; and to radial compressive and tangential tensile

stresses in the matrix. Microcracking will not occur during fabrication because the residual stresses in the particle and the matrix are small (small $\Delta\alpha$ (10.4 - 9.4)x10^{-6}/°C), the stresses in the matrix (interface) are lower than the strength of the matrix, and the chromium particle size is much smaller than the critical size. These residual stresses may help crack deflection as a toughening mechanism [Wei and Becher, 1984]. Combined with transformation toughening of the matrix (see Chapter 5) the fracture toughness of the composites increase with increasing chromium content. However the contribution of crack deflection is only effective up to about 20 vol% reinforcement [Faber and Evans[a,b], 1983].

A significant thermal expansion mismatch occurs in zirconia/iron composites ((10.4 - 14.6) x 10^{-6}). This causes tensile stress in the particle, and radial tensile and tangential compressive stresses in the matrix. The residual stresses developed in the matrix are big enough (greater than the strength of the matrix) to cause cracking during fabrication. However, because the iron particle size is much lower than the critical size, such cracking will not occur during fabrication. Nevertheless, cracking around the particles may occur when the composites are subjected to stress under the macroscopic fracture stress [Davidge and Green ,1968]. In this case, stress-induced microcracking can take place leading to enhanced toughening. This type of thermal stress may also enhance fracture toughness due to matrix compression, because in this case the tangential compressive stress in the matrix will tend to hinder crack propagation [Warren, 1983]. Another toughening mechanism is crack deflection, which is also influenced by the residual stresses.

In comparison with the other two composites, thermal expansion mismatch in zirconia/AISI 316 composites is the biggest ((10.4 - 19)x10^{-6})/°C resulting in a large tensile stress in the particle, and radial tensile and tangential compressive stresses in the matrix which exceed the strength of the matrix. Combined with large particle size (maximum of 45 μm), this results in spontaneously microcracking around the big particles. According to Green (1998) the fracture toughness will increase up to the particle size just below the critical size where the spontaneous microcracking occurs.

It is difficult to make comparisons among those composites in term of fracture toughness, because of the difference of the reinforcement particle size. However, it can be seen in all composites that because of thermal expansion mismatch, residual stresses are developed in the particles and matrix. These residual stresses may contribute to crack deflection as one of the toughening mechanism although it is also considered that transformation toughening of the matrix may contribute to the toughening. In terms of particle size, if the particle size is smaller than the critical size and the residual stresses are greater than the matrix strength, stress-induced microcracking can be the toughening mechanism such as in zirconia/iron composites. However if spontaneous microcracking occurs and/or interlinking of microcracking take place, then this will predominate as in zirconia/AISI 316 composites.

The thermal stresses generated due to thermal expansion mismatch also influence the strength of the composites [Davidge and Green, 1968]. In the case of the present study, if the particle size is larger than the inherent flaw size of the monolithic zirconia (23.1μm), such as in zirconia/chromium and zirconia/AISI 316 composites, the weakening effect on strength is due to flaw sizes which are similar to the particle size. In the case of residual stresses greater than the matrix strength, microcracking can occur in two different ways; spontaneous microcracking due to particle sizes larger than the critical size or microcracking on the smaller particle size. The first case occurs in zirconia/AISI 316 composites and the latter case may occur in zirconia/iron composites. As a result the decrease of strength in zirconia/AISI 316 is bigger than the other two composites. Moreover if the microcracks interlink, they will reduce the strength further. In this present study all the composites have lower strength than the monolithic zirconia. Strength improvement can only be achieved if the residual stresses between the matrix and the particles is small and the particle size is small as shown by Nawa *et al* (1996) in zirconia/Mo nanocomposites.

CHAPTER 7

ZIRCONIA/METAL COMPOSITES: THERMAL PROPERTIES

In order to know the thermal properties of the zirconia/metal composites, thermal diffusivity and coefficient of thermal expansion measurements were performed. In engineering applications, the performance of structural ceramic materials is also influenced by their response to transient or steady state heat flow, which is governed by the value of thermal diffusivity and conductivity. Coefficient of thermal expansion on the other hand is also important, because dimensional changes may occur during heating or cooling and these should also be taken into account in material design.

7.1. THERMAL DIFFUSIVITY

The thermal conductivity of ceramic composites depends on the amount and arrangement of each constituent, and their individual conductivity. Moreover it is also sensitive to porosity, microcracks and interfacial contact. From the rule of mixtures in terms of volume fractions, the thermal conductivity of a linear and inverse unidirectional composite can be described by the upper and lower bounds respectively, as follows [Warren, 1992]:

Upper bound:

$$k_c = V_m k_m + V_r k_r \quad \ldots\ldots\ldots\ldots\ldots\ldots\ldots\ldots\ldots\ldots \quad (7.1)$$

Lower bound:

$$\frac{1}{k_c} = \frac{V_m}{k_m} + \frac{V_r}{k_r}$$

$$k_c = \frac{k_m k_r}{V_m k_r + V_r k_m} \qquad \ldots\ldots\ldots\ldots\ldots\ldots\ldots\ldots\ldots\ldots\ldots\ldots\ldots\ldots (7.2)$$

where k is thermal conductivity, subscript c, m and r represent the composite, matrix and reinforcement respectively.

More specifically, in particulate composites where spherical particles are isolated in a continuous matrix with a good thermal contact, the thermal conductivity of the composite can be approximately calculated using the Eucken model as follows [Kingery, 1976]:

$$k_c = k_{mc} \frac{\left[1 + \frac{2V_{rd}(1-Q)}{(2Q+1)}\right]}{\left[1 - \frac{V_{rd}(1-Q)}{(Q+1)}\right]} \qquad \ldots\ldots\ldots\ldots\ldots\ldots\ldots\ldots\ldots\ldots\ldots\ldots (7.3)$$

Where Q is the ratio of k_{mc} and k_{rd} or ($Q = k_{mc}/k_{rd}$), k is thermal conductivity, V is volume fraction, and subscript mc and rd represent the continuous phase and dispersed phase respectively.

The thermal diffusivity of composites can be calculated from the above Equations if the heat capacity and density of the composites are known. In this case the heat capacity and density are not dependent on transport phenomena but dependent only on the amounts of each component [Warren, 1992], so they can be estimated simply [Hasselman, 1986; and Warren, 1992]:

Heat capacity (C_p) of a composite:

$$C_{pc} = V_m C_{pm} + V_r C_{pr} \qquad \ldots\ldots\ldots\ldots\ldots\ldots\ldots\ldots\ldots\ldots\ldots\ldots (7.4)$$

Density (ρ) of a composite:

$$\rho_c = V_m \rho_m + V_r \rho_r \qquad \ldots\ldots\ldots\ldots\ldots\ldots\ldots\ldots\ldots\ldots\ldots\ldots (7.5)$$

The density of a material however, is not a constant value but depends on the temperature, due to thermal expansion. Therefore, the density of each component as a function of temperature should be taken into account. It can be estimated using the assumption that thermal expansion is isotropic, as follows:

$$\rho_t = \frac{\rho_o}{(1+3.\alpha.(T-T_o))} \qquad \ldots\ldots\ldots\ldots\ldots\ldots\ldots\ldots\ldots\ldots\ldots\ldots (7.6)$$

Where ρ_t is the density at temperature T, ρ_o is the density at room temperature (T_o) and α is the linear coefficient of thermal expansion.

Finally, the thermal diffusivity of composites can be calculated using the following equation [Hasselman, 1986]:

$$a_c = \frac{k_c}{\rho_c . C_{pc}} \qquad \ldots\ldots\ldots\ldots\ldots\ldots\ldots\ldots\ldots\ldots\ldots\ldots (7.7)$$

The above Equations will be used to analyse the thermal diffusivity of zirconia/metal composites below. The thermal diffusivity of samples was measured using the Laser Flash Method in an argon atmosphere.

7.1.1. ZIRCONIA/CHROMIUM COMPOSITES

The effect of chromium content on the thermal diffusivity of zirconia/chromium composites at room temperature is shown in Figure 7.1. It can be seen in this figure that the total thermal diffusivity increases with increasing chromium content. This behaviour is expected since the thermal diffusivity of chromium is greater than that of zirconia. Three models of thermal diffusivity for composites i.e upper bound (linear rule of mixtures), lower bound (inverse rule of mixtures) and the Eucken model in Equation 7.3 are also presented in Figure 7.1. The experimental data are in between the upper and lower bound, but as expected they are much closer to the lower bound because the reinforcement was in particle form and the thermal diffusivity of zirconia (0.01097 cm^2/s) is much lower than that of chromium (0.29 cm^2/s). Therefore at low content of chromium the thermal diffusivity of the composites will be significantly influenced by the value of the zirconia matrix.

The experimental results are in good agreement with the model of Equation 7.3. According to the previous chapter (Chapter 6) spontaneous microcracking due to thermal expansion mismatch between the components should not occur in these composites. In addition, the density of the composites is greater than 99% of theoretical (Chapter 5), and the particles are well embedded in the matrix resulting in a good thermal contact. These conditions lead to the conclusion that the total thermal diffusivity will be influenced only by the thermal diffusivity values of zirconia and chromium. Above 20 vol% of chromium, the difference between the experimental data and the model in Equation 7.3 is greater, which may be due to some particles interconnecting.

Figure 7.2 shows thermal diffusivity of composites containing 10 vol% and 25 vol% of chromium as a function of temperature. The estimation of thermal diffusivity using the model in Equation 7.3 is also presented in this Figure. It is clearly seen that thermal diffusivity of both composites decreases with increasing temperature. This behaviour is expected because the thermal diffusivity of each constituent also decreases with increasing temperature. From the experimental data,

the thermal diffusivity of zirconia decreases from 0.01097 cm^2/s at room temperature to 0.00767 cm^2/s at 600°C (Chapter 4), while the thermal diffusivity of chromium decreases from 0.2884 cm^2/s at room temperature to 0.1208 cm^2/s (see Figure 7. 8) [Incropera and DeWitt, 1996]. It is also expected that the composites containing 25 vol% chromium have higher thermal diffusivity than that of 10 vol% chromium at the temperature range as shown in Figure 7.2. The experimental results of both chromium contents are in good agreement with the model given in Equation 7.3.

To draw the model of Equation 7.3 into a curve in Figure 7.2, the procedures in Section 7.1 (Equations 7.3 to 7.7) were followed. The data required for those calculations were taken from the experiment and literature. Data for thermal diffusivity (20°C - 600°C) and thermal expansion coefficient of zirconia (20°C - 1000°C) were available from experiment as discussed in Chapter 4, while the heat capacity (from 20°C to 600°C) was obtained from a similar material (ZrO_2 with 5.3 wt% Y_2O_3) given by Hasselman *et al* (1987). The data of thermal diffusivity and heat capacity at higher temperature were extrapolated from those available data. The data of chromium were taken from literature given by Smithells and Brandes (1976), and Incropera and DeWitt (1996).

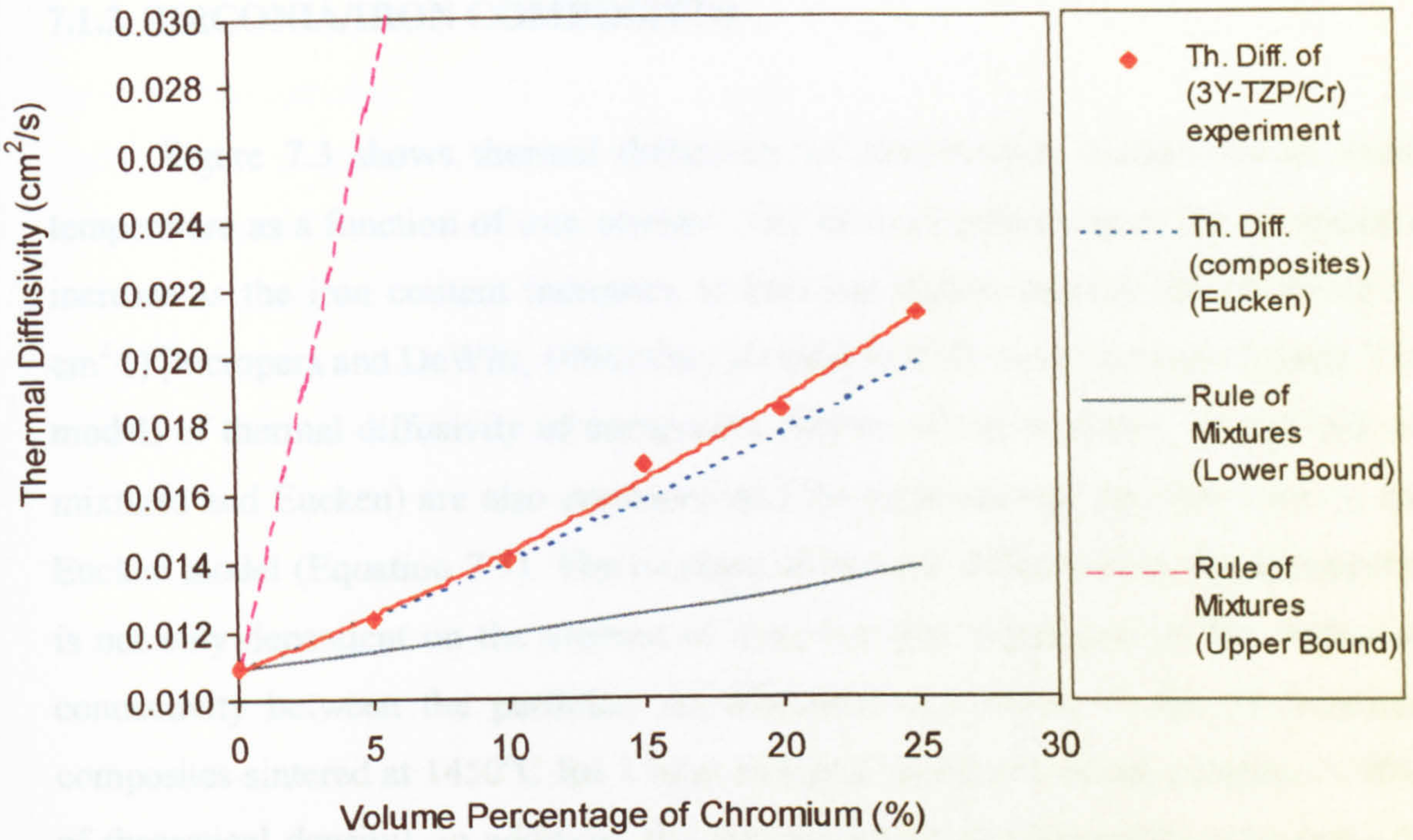

Figure 7.1. Thermal diffusivity at room temperature of zirconia/chromium composites sintered at 1450°C for 1 hour in argon

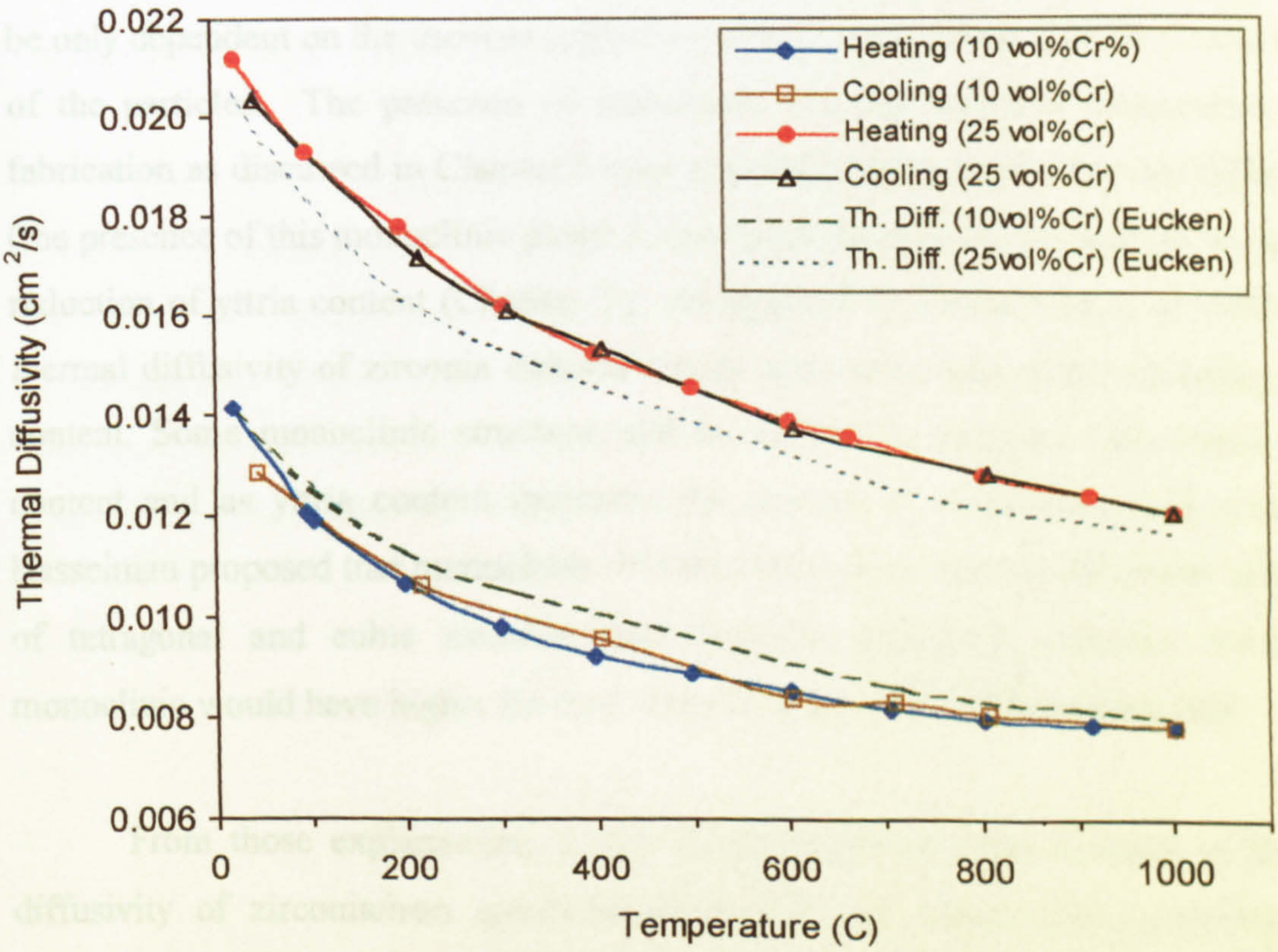

Figure 7.2. The effects of temperature and chromium content on thermal diffusivity of zirconia/chromium composites sintered at 1450°C for 1 hour in argon.

7.1.2. ZIRCONIA/IRON COMPOSITES

Figure 7.3 shows thermal diffusivity of zirconia/iron composites at room temperature as a function of iron content. The thermal diffusivity of the composites increase as the iron content increases as iron has higher thermal diffusivity (0.23 cm^2/s) [Incropera and DeWitt, 1996] than zirconia (0.01097 cm^2/s) [experiment]. The models of thermal diffusivity of composites (linear rule of mixtures, inverse rule of mixtures and Eucken) are also presented and the experimental data are close to the Eucken model (Equation 7.3). The increase of thermal diffusivity in the composites is not only dependent on the amount of iron, but also dependent on the degree of connectivity between the particles. As discussed in Chapter 5, the zirconia/iron composites sintered at 1450°C for 1 hour in argon resulted in dense samples (> 99% of theoretical density). In addition, the microstructure of composites containing 25 vol% iron showed that some particles clustered and formed into larger particles. From Chapter 6, it can be seen that microcracking due to thermal stress should not occur in these composites. Therefore the total thermal diffusivity of zirconia/iron will be only dependent on the thermal diffusivity of each component and the connectivity of the particles. The presence of monoclinic zirconia in these composites after fabrication as discussed in Chapter 5 may also influence the total thermal diffusivity (the presence of this monoclinic phase is due to the reaction of iron and yttria causing reduction of yttria content (Chapter 5)). As reported by Hasselman *et al* (1987) the thermal diffusivity of zirconia stabilised with yttria decreases with increasing yttria content. Some monoclinic structure will be present in zirconia with lower yttria content and as yttria content increases the amount of monoclinic will decrease. Hasselman proposed that monoclinic zirconia had higher thermal diffusivity than that of tetragonal and cubic zirconia, and therefore tetragonal zirconia containing monoclinic would have higher thermal diffusivity than that of fully tetragonal.

From those explanations, it can be concluded that the increase of thermal diffusivity of zirconia/iron composites which is not linear with increasing iron content is due to the higher degree of connectivity of iron particles at higher iron content and the effect of the presence of monoclinic zirconia. The bigger difference

between the experimental data and the model of Equation 7.3 may also be influenced by those phenomena. To calculate the model of Equation 7.3, the value of thermal diffusivity of zirconia was taken from the experiment data (in Chapter 4) where the zirconia was fully tetragonal, but in this case the zirconia component consists of two structures (tetragonal and monoclinic) (Chapter 5). So the zirconia component in these composites should have higher thermal diffusivity than that measured in Chapter 4 (Hasselman *et al*, 1987).

Figure 7.4 shows the effects of temperature on thermal diffusivity of zirconia/iron composites containing 10 vol% iron and 25 vol% iron. It is expected that the trends of the total thermal diffusivity will be influenced by the thermal diffusivity of each constituent as a function of temperature. Thermal diffusivity of each component decreases with increase of temperature (Figure 7.8). However, the thermal diffusivity of iron changes between 700°C and 900°C due to phase change (α to γ) and depending on composition. These effects also influence the thermal diffusivity of zirconia/iron composites, and are clearly seen in Figure 7.4, particularly on higher iron content (25 vol%).

The model of Equation 7.3 was drawn in Figure 7.4 using the similar method as that for zirconia/chromium composites. The data of thermal diffusivity of zirconia was taken from experiment (Chapter 4) and the heat capacity was taken from Hasselman *et al* (1987). These data however, were only available up to 600°C, so the data above that temperature was obtained from extrapolation. The data for iron was obtained from Smithells and Brandes (1976), and Incropera and DeWitt (1996).

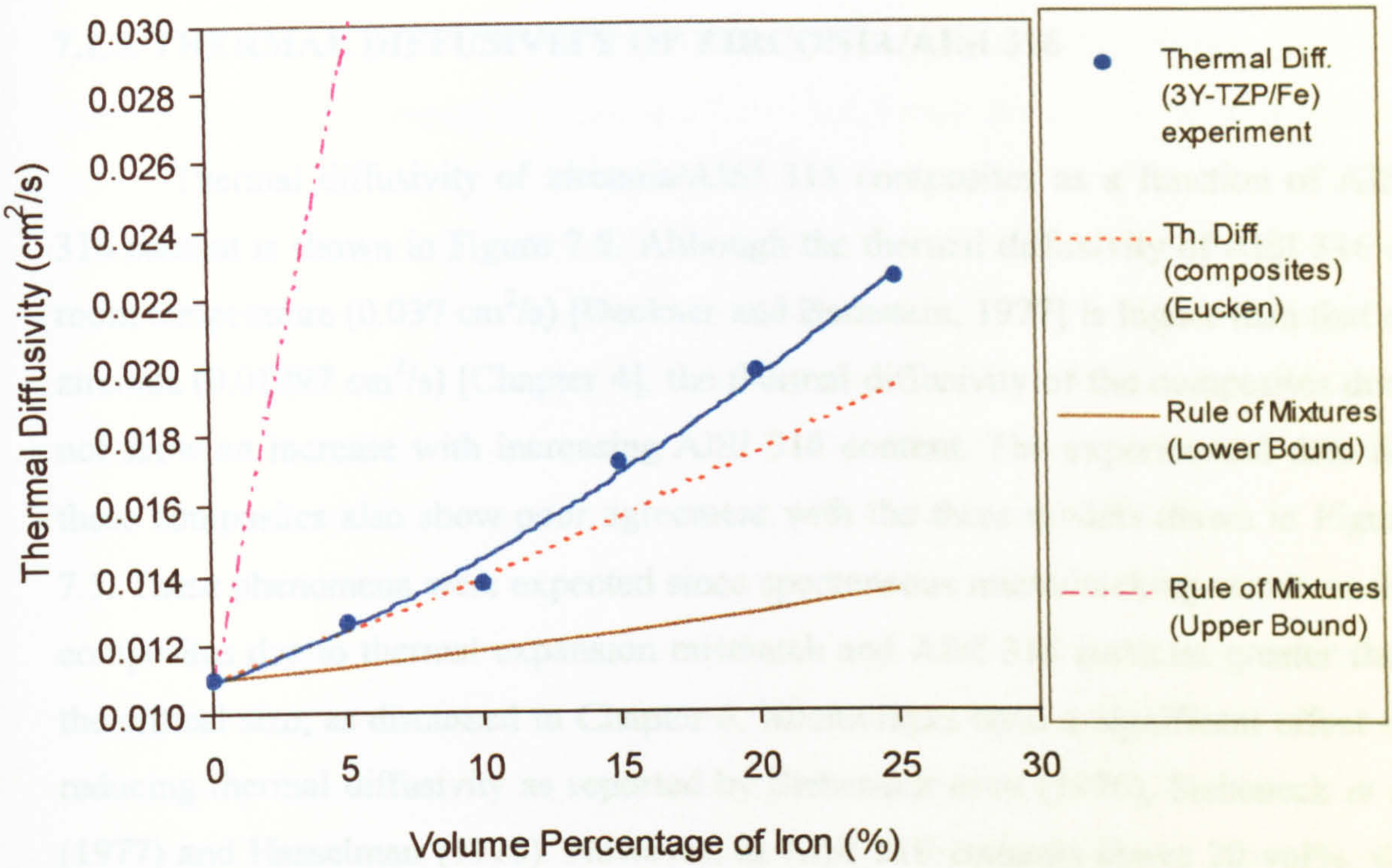

Figure 7.3. Thermal diffusivity at room temperature of zirconia/iron composites sintered at 1450°C for 1hour in argon.

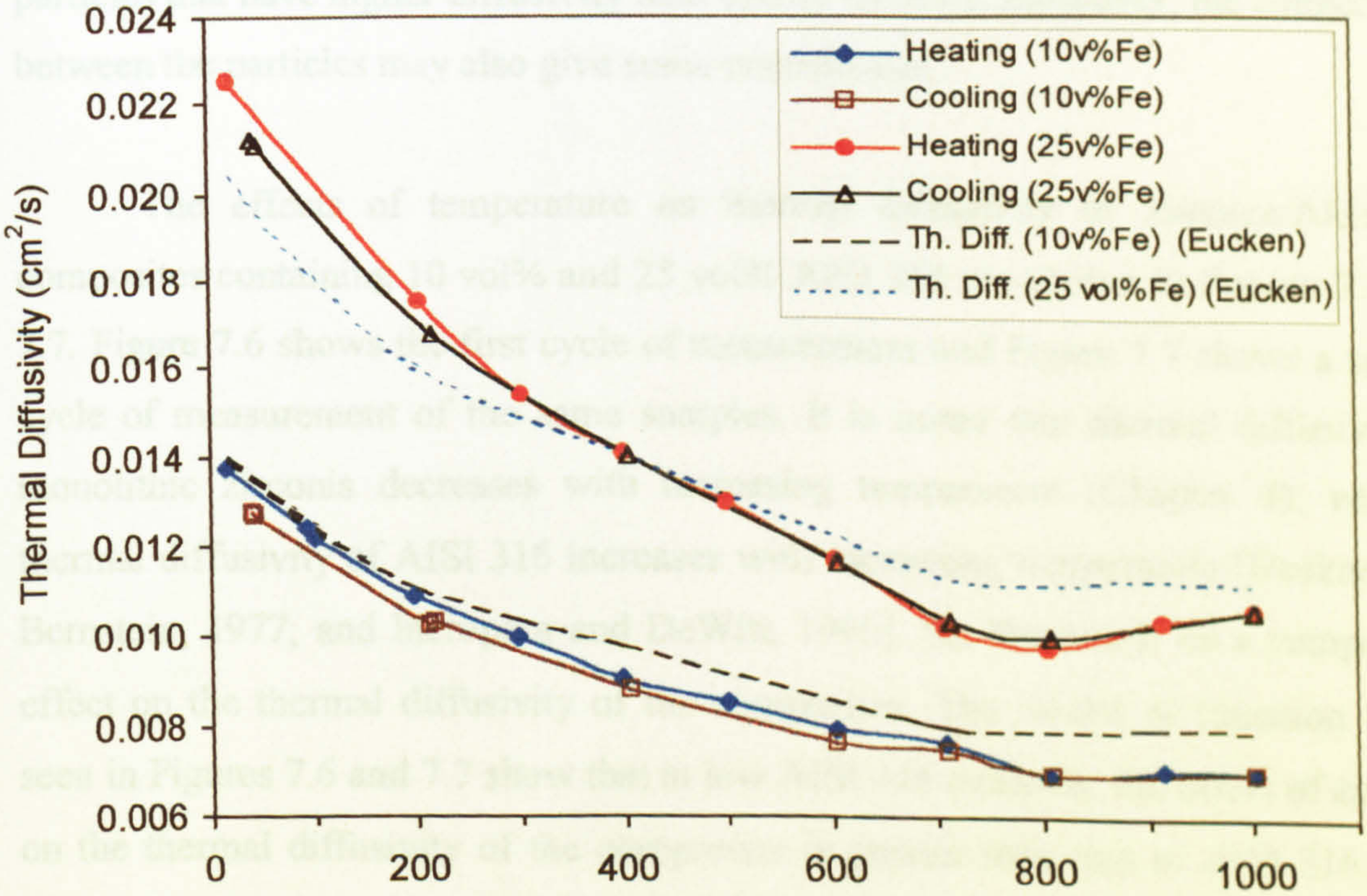

Figure 7.4. The effects of temperature and iron content on thermal diffusivity of zirconia/iron composites sintered at 1450°C for 1 hour in argon.

7.1.3. THERMAL DIFFUSIVITY OF ZIRCONIA/AISI 316

Thermal diffusivity of zirconia/AISI 316 composites as a function of AISI 316 content is shown in Figure 7.5. Although the thermal diffusivity of AISI 316 at room temperature (0.037 cm^2/s) [Deckner and Bernstein, 1977] is higher than that of zirconia (0.01097 cm^2/s) [Chapter 4], the thermal diffusivity of the composites does not show an increase with increasing AISI 316 content. The experimental data for these composites also show poor agreement with the three models drawn in Figure 7.5. These phenomena were expected since spontaneous microcracking occurs in the composites due to thermal expansion mismatch and AISI 316 particles greater than the critical size, as discussed in Chapter 6. Microcracks have a significant effect on reducing thermal diffusivity as reported by Siebeneck *et al* (1976), Siebeneck *et al* (1977) and Hasselman (1978). However, at AISI 316 contents above 20 vol%, the effect of AISI 316 particles seems to be noted where the thermal diffusivity of the composites increases slightly. These may be due to a combination of effects of microcracks that tend to reduce the thermal diffusivity and the presence of AISI 316 particles that have higher diffusivity than that of zirconia. Moreover, the connectivity between the particles may also give some contribution.

The effects of temperature on thermal diffusivity of zirconia/AISI 316 composites containing 10 vol% and 25 vol% AISI 316 are shown in Figures 7.6 and 7.7. Figure 7.6 shows the first cycle of measurement and Figure 7.7 shows a second cycle of measurement of the same samples. It is noted that thermal diffusivity of monolithic zirconia decreases with increasing temperature (Chapter 4), whereas thermal diffusivity of AISI 316 increases with increasing temperature [Deckner and Bernstein, 1977; and Incropera and DeWitt, 1996]. So, there will be a competitive effect on the thermal diffusivity of the composites. The model of Equation 7.3 as seen in Figures 7.6 and 7.7 show that at low AISI 316 contents, the effect of zirconia on the thermal diffusivity of the composites is greater than that of AISI 316. As a result according to the model of Equation 7.3 the thermal diffusivity of the composites decreases with increasing temperature.

In both Figures 7.6 and 7.7 the experimental data are lower than that estimated using the model of Equation 7.3. The reason for this is the presence of microcracks in the samples during fabrication as a result of thermal expansion mismatch (see Chapter 6) [Siebeneck *et al*, 1976; Siebeneck *et al*, 1977; Hasselman, 1978; Bentsen *et al*, 1981]. Furthermore, it can be seen in Figure 7.6 that there is an irreversible behaviour on heating and cooling, especially on samples containing 25 vol% AISI 316 and this is due to irreversible crack closure and healing at the higher level of composition [Siebeneck *et al*, 1976 and Siebeneck *et al*, 1977].

In the second cycle of measurement (Figure 7.7) the thermal diffusivity seems to be higher than that of the first cycle and the irreversibility between heating and cooling is smaller, although the data on cooling still exceed those obtained on heating to high temperature. Again this may be attributable to further crack closure and healing at higher temperature followed by re-formation microcracks at lower temperature on cooling [Bentsen *et al*, 1981 and Hasselman, 1986].

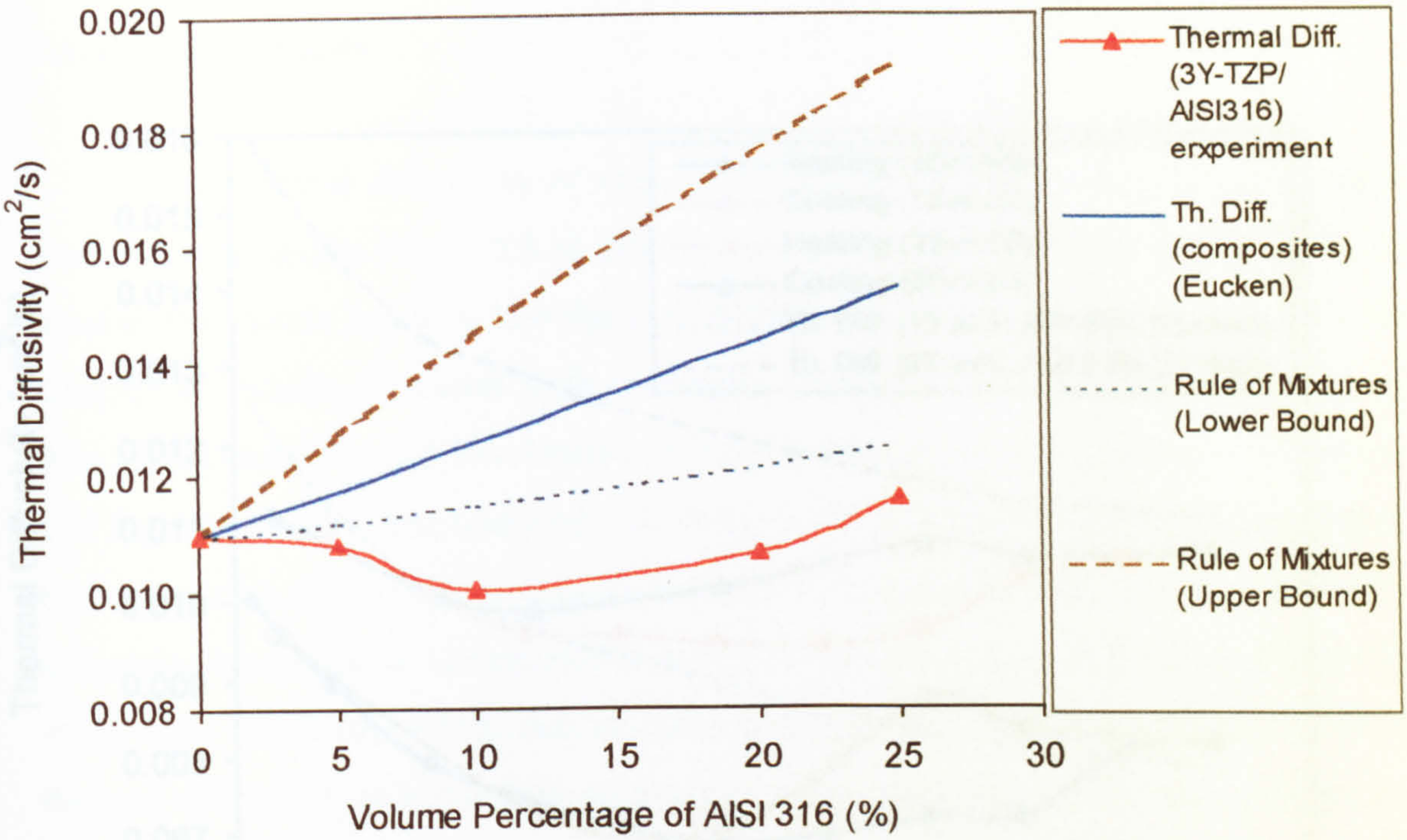

Figure 7.5. Thermal diffusivity at room temperature of zirconia/AISI 316 composites sintered at 1450°C for 1hour in argon.

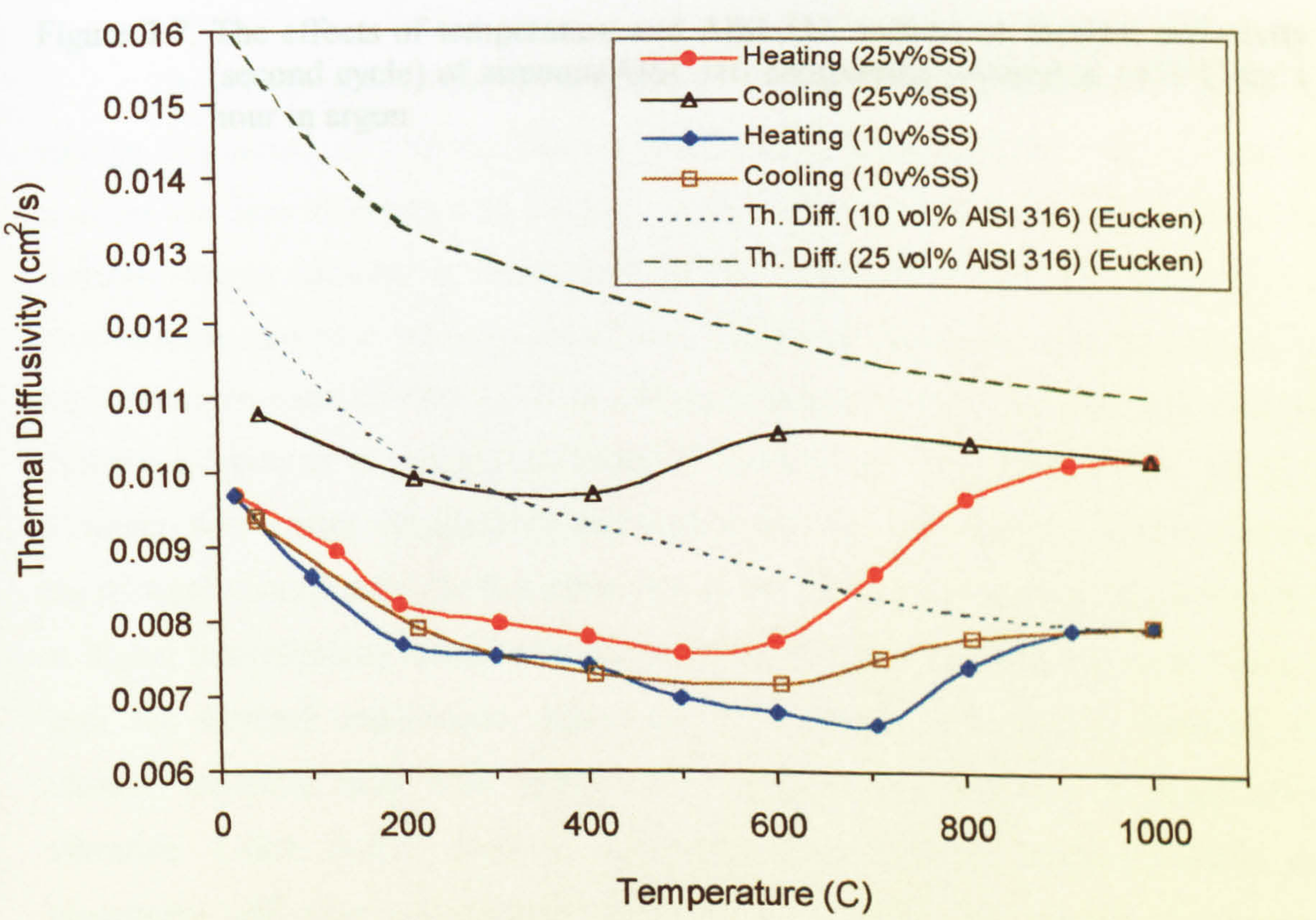

Figure 7.6. The effects of temperature and AISI 316 content on thermal diffusivity (first cycle) of zirconia/AISI 316 composites sintered at 1450°C for 1 hour in argon.

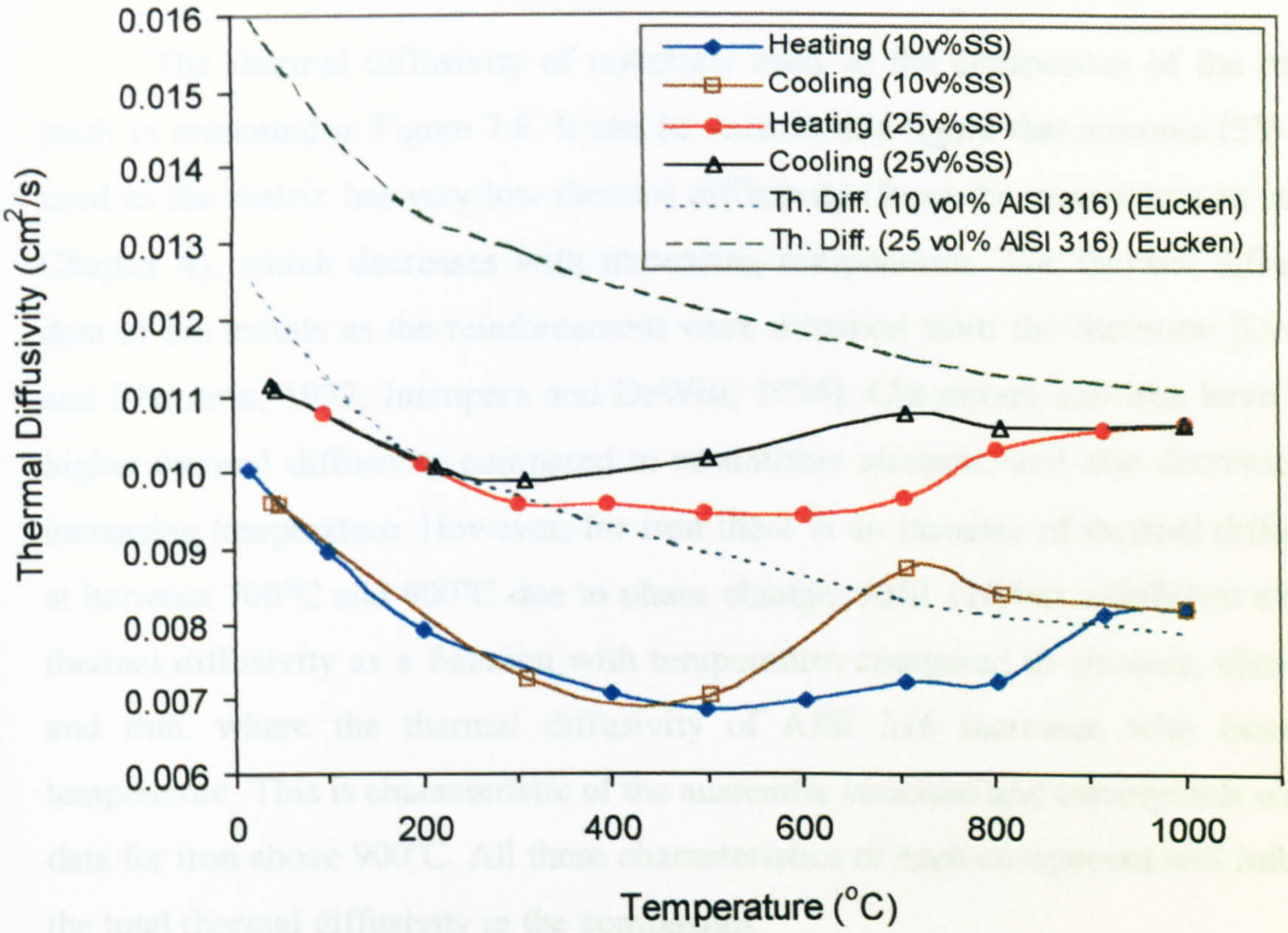

Figure 7.7. The effects of temperature and AISI 316 content on thermal diffusivity (second cycle) of zirconia/AISI 316 composites sintered at 1450°C for 1 hour in argon.

7.1.4. DISCUSSION

The thermal diffusivity of materials used in the composites of the present study is presented in Figure 7.8. It can be seen in this figure that zirconia (3Y-TZP) used as the matrix has very low thermal diffusivity (from the experiment as seen in Chapter 4), which decreases with increasing temperature. The thermal diffusivity data of the metals as the reinforcement were obtained from the literature [Deckner and Bernstein, 1977; Incropera and DeWitt, 1996]. Chromium and iron have much higher thermal diffusivity compared to monolithic zirconia, and also decrease with increasing temperature. However, for iron there is an increase of thermal diffusivity at between 700°C and 900°C due to phase change. AISI 316 has a different trend in thermal diffusivity as a function with temperature compared to zirconia, chromium and iron, where the thermal diffusivity of AISI 316 increases with increasing temperature. This is characteristic of the austenitic structure and corresponds with the data for iron above 900°C. All these characteristics of each component will influence the total thermal diffusivity in the composites.

The above phenomena in thermal diffusivity as well as thermal conductivity can be explained as follow. Two mechanisms that characterise thermal energy transfer are free electrons and lattice vibrations (or phonons). In pure metals, the thermal energy transfer is dominated by free electron mechanisms because the electrons are easy to move. As a result most metals are good conductive materials. At higher temperatures the energy of the electrons and the lattice vibration will increase yielding a tendency of increase of thermal conductivity. The greater lattice vibration however, will scatter the electrons and reduce their mobility leading to a decrease of the thermal conductivity. So these two factors will influence the thermal conductivity at higher temperatures resulting in different behaviour in each metal. In the case of iron, the thermal conductivity decreases up to about 700°C due to lowering the electron mobility then from about 700°C slightly increase due to more lattice vibration. Other factors such as impurity, lattice defects, microstructures and processing will also influence the thermal conductivity. In contrast, the thermal

transfer in ceramics is caused essentially by lattice vibrations (phonons), which are less effective than free electrons [Askeland, 1996 and Callister, 1994].

It has been shown in Section 7.1.1 and 7.1.2 that thermal diffusivity of particulate composites of zirconia/chromium and zirconia/iron is dependent on the diffusivity of its individual components, volume fraction and the degree of connectivity between the particles. Those composites can be considered as having good contact between the matrix and the particles. In contrast, the zirconia/AISI 316 composites (Section 7.2.3) exhibit different character since microcracks are present. These microcracks reduce the thermal diffusivity. It is also shown in Section 7.2.3 that the phenomena of cracks closure and healing occur in zirconia/AISI 316 composites.

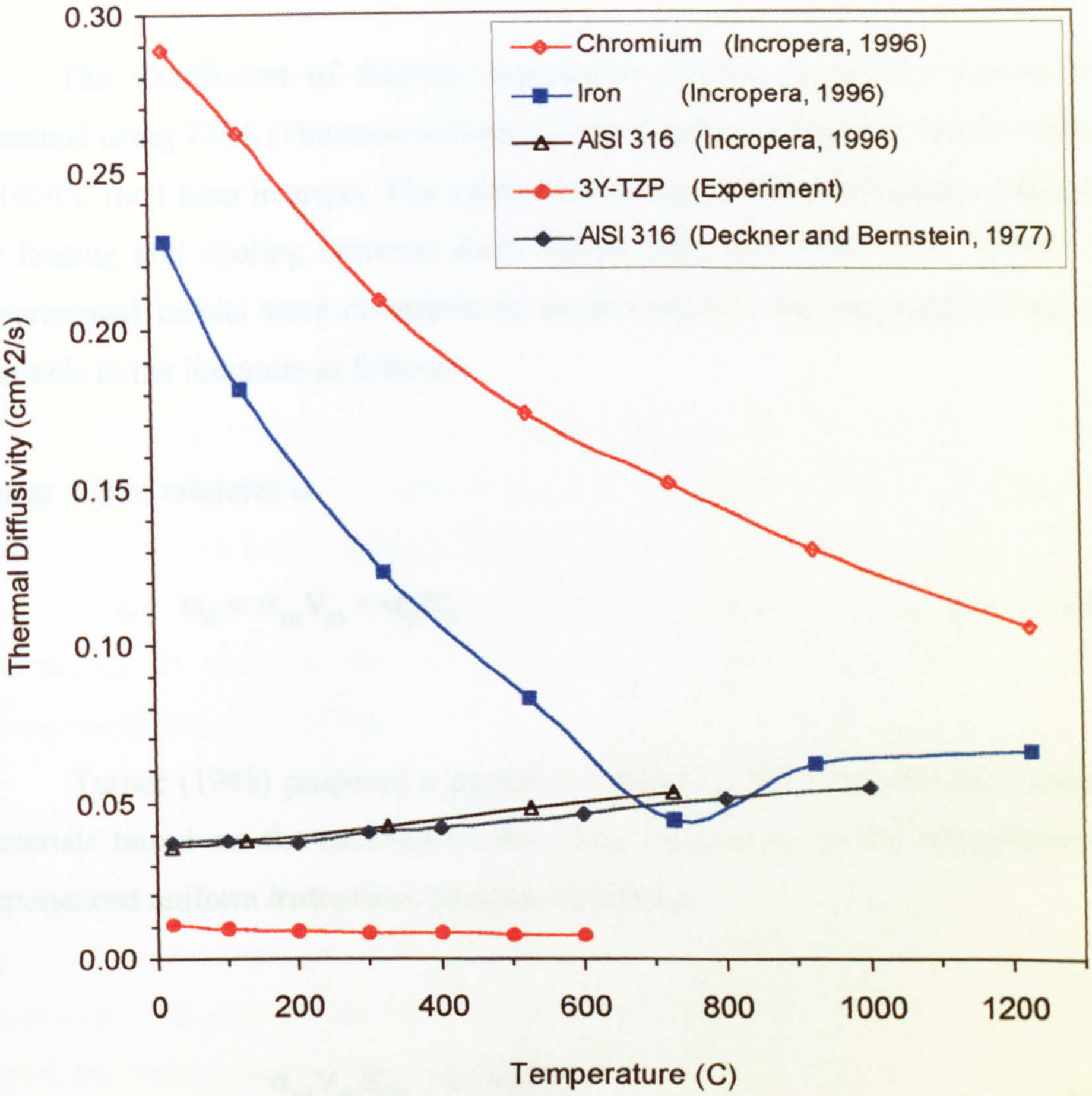

Figure 7.8. Thermal diffusivity of material used in this present study as a function of temperature.

7.2. COEFFICIENT OF THERMAL EXPANSION

The Coefficient of thermal expansions (CTEs) of the composites were measured using TMA (Thermo-mechanical Analysis) equipment on samples sintered at 1450°C for 1 hour in argon. The measurement was performed in argon atmosphere for heating and cooling between room temperature and 1000°C or 1200°C. The experimental results were compared to several models for particulate composites available in the literature as follows:

Linear rule of mixtures is

$$\alpha_c = \alpha_m V_m + \alpha_p V_p \qquad \ldots\ldots\ldots\ldots\ldots\ldots\ldots\ldots\ldots\ldots \quad (7.8)$$

Turner (1946) proposed a model to estimate CTEs of particulate composite materials based on the assumption that each component in the composites only experienced uniform hydrostatic stresses, as follows:

$$\alpha_c = \frac{\alpha_m V_m K_m + \alpha_p V_p K_p}{V_m K_m + V_p K_p} \qquad \ldots\ldots\ldots\ldots\ldots\ldots\ldots\ldots \quad (7.9)$$

Another model given by Kerner (1956) includes the effect of shear and isostatic stresses. The model is in the form of volumetric thermal expansion (β). With the assumption that the materials are isotropic, so the linear thermal expansion (α) can be easily estimated ($\beta = 3\ \alpha$). Kerner's model is as follows [Kerner, 1956; Chawla, 1993]:

$$\beta_c = \beta_m V_m + \beta_p V_p - (\beta_m - \beta_p) V_p \left[\frac{1/K_m - 1/K_p}{V_m/K_p + V_p/K_m + 3G_m/4} \right] \qquad ..(7.10)$$

Where α and β are linear and volumetric coefficient of thermal expansion, respectively; V is volume fraction; K and G denote bulk and shear modulus, respectively; and subscripts c, m and p denote the composite, matrix, and particle reinforcement, respectively.

7.2.1. RESULTS AND DISCUSSION

The representative results of the thermal expansion (expressed as a percent linear change (PLC) versus temperature) of zirconia/chromium, zirconia/iron and zirconia/AISI 316 composites are shown in Figures 7.9, 7.10 and 7.11, respectively. Each figure shows CTE curves on heating and cooling of zirconia composites containing 25 vol% of the reinforcement. The CTE values for the individual components are given in Table 7.1.

A comparison of the experimental and theoretical CTE values obtained by using Turner's equation, rule of mixtures and Kerner's equation is presented in Table 7.2 and the theoretical CTE values shown in Table 7.2 were calculated using the available CTE data of individual components shown in Table 7.1. Although the available values for chromium and iron are not for the same temperature range as that of zirconia and AISI 316, those can be used to give an indication of the theoretical CTE values. The experimental data are fairly close to the theoretical values calculated using those three models. In this case, Kerner's model does not differ significantly from the rule of mixtures (the difference is very small - in the order of 10^{-12}), because the constraint term in the Kerner's model (Equation 7.10) is small.

Table 7.1. CTE values of individual component.

Component	CTE (x 10^{-6}/°C)	Reference
3Y-TZP	10.4 (20 - 1000°C)	This work (Chapter 4)
Chromium	9.4 (20 - 700°C)	Smithells and Brandes (1976)
Iron	14.6 (20 - 800°C)	Smithells and Brandes (1976)
AISI 316	19.0 (20 - 1000°C)	Deckner and Bernstein (177)

Table 7.2. Comparison between the experimental data and the theoretical values (Turner's model, rule of mixtures and Kerner's model)

	CTE Heating/Cooling (x 10^{-6}/°C)	Average CTE (x10^{-6} /°C)	Turner's model (x10^{-6} /°C)	Linear Rule of Mixture (x10^{-6} /°C)	Kerner's model (x10^{-6} /°C)
25 vol% Cr	10.79 / 9.82	10.3	10.1572	10.15	10.15
25 vol% Fe	11.48 / 10.23	10.9	11.4651	11.45	11.45
25 vol% AISI 316	11.00 / 10.27	10.6	12.6296	12.55	12.55

It can be seen in Table 7.2 that the CTEs of the composites do not significantly differ from the CTE of the monolithic zirconia in that up to 25% of reinforcement the CTEs of the composites are predominantly influenced by the matrix (the continuous phase). The CTEs of the composites however, are in between the CTEs of the individual components where the CTE of zirconia/chromium composites is slightly smaller than that of zirconia, while the CTEs of zirconia/iron composites and zirconia/AISI 316 composites are slightly greater.

The thermal expansion curves in Figures 7.9, 7.10 and 7.11 show a change in slope above about 900°C and a hysteresis between heating and cooling which result in swelling of the sample of about 0.2% after cooling. The change in slope may be

caused by oxidation reaction of the metal particles in the matrix which are exposed to the furnace atmosphere in the TMA equipment. The samples for the thermal expansion measurement (about 4 mm x 4 mm x 4 mm) were cut from larger samples and results in some of the metal particles on the sample surface being exposed to the gas atmosphere. During the thermal expansion measurement in argon, the metal particles in the surface react with oxygen (as impurity) in the argon gas (Chapter 5) and forms metal oxide. To confirm this reaction, a piece of sample (with a suitable size for X-ray analysis) was cut from the same material and heated in a horizontal furnace up to 1300°C in argon gas atmosphere. The sample was then examined using the XRD and showed that some metal oxide peaks are present. This metal oxide can cause microcracks on the sample surface and increase the sample volume.

TMA 1500 *(VERSION - V5.12)*

SMP ID: 25 vol% Cr + ZrO_2 RUN ID: ME-4 SIZE: 4.625 mm OPERATOR: MUH GAS: ARGON

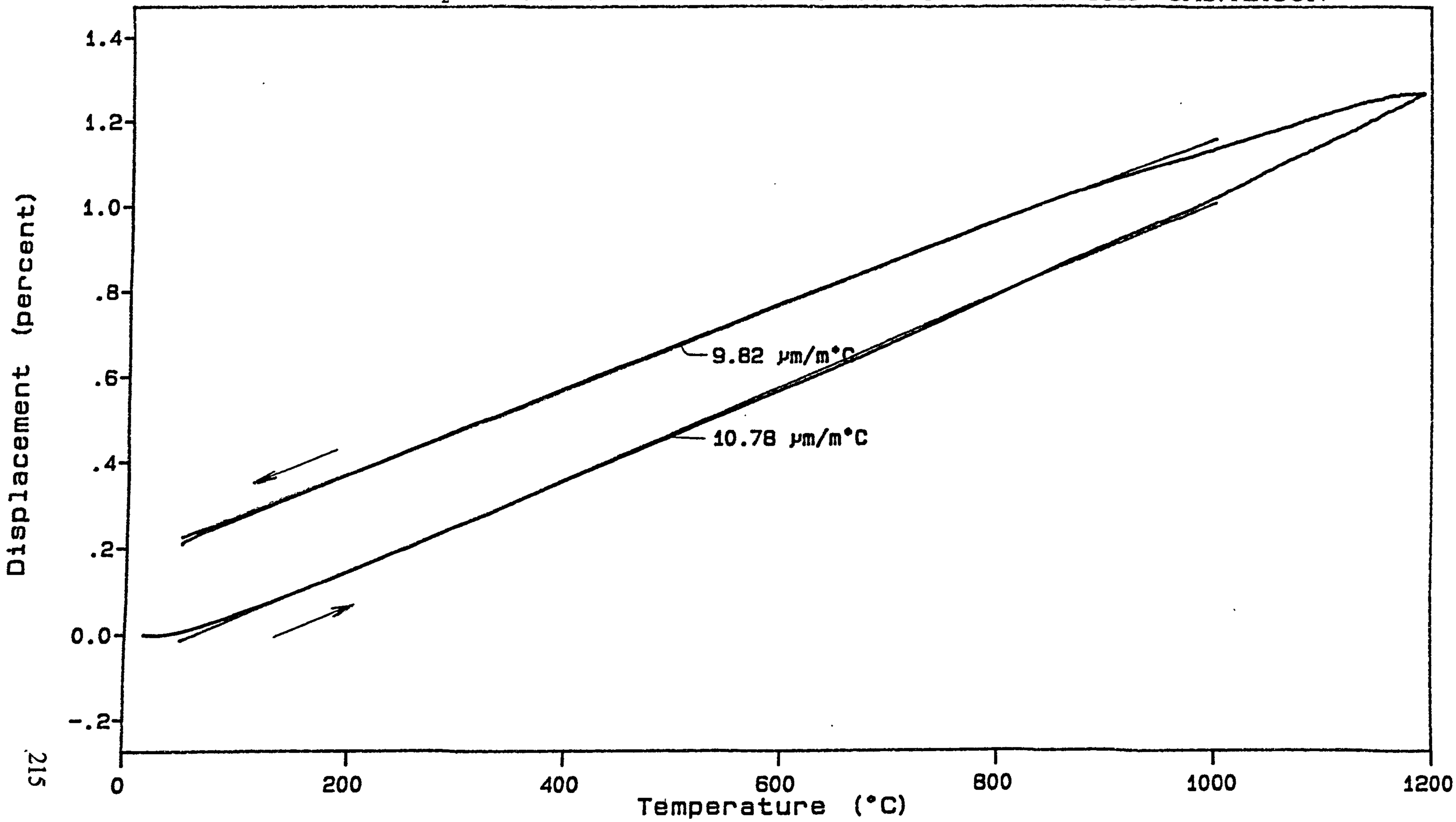

Figure 7.9 Thermal expansion in argon of (25 vol% Cr + ZrO_2 sintered at 1450°C for 1h in argon)

TMA 1500 *(VERSION - V5.12)*

SMP ID: 25 vol% Fe + ZrO_2 RUN ID: MWW-6 SIZE: 4.407 mm OPERATOR: MUH GAS: ARGON

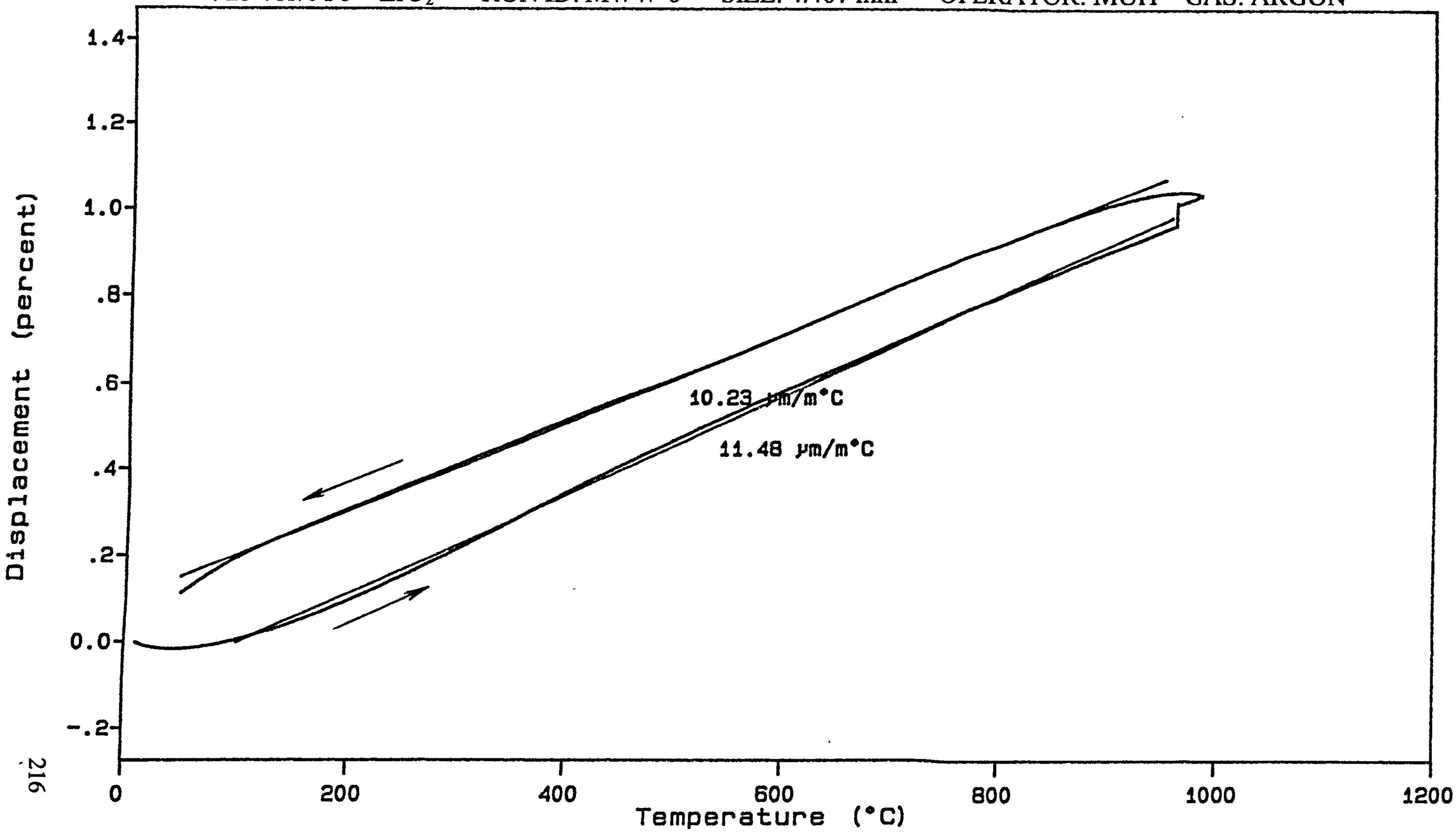

Figure 7.10 Thermal expansion in argon of (25 vol% Fe + ZrO_2 sintered at 1450°C for 1h in argon)

TMA 1500 *(VERSION - V5.12)*

SMP ID: 25 vol% AISI 316 + ZrO_2 RUN ID: ME-3 SIZE: 4.373 mm OPERATOR: MUH GAS: ARGON

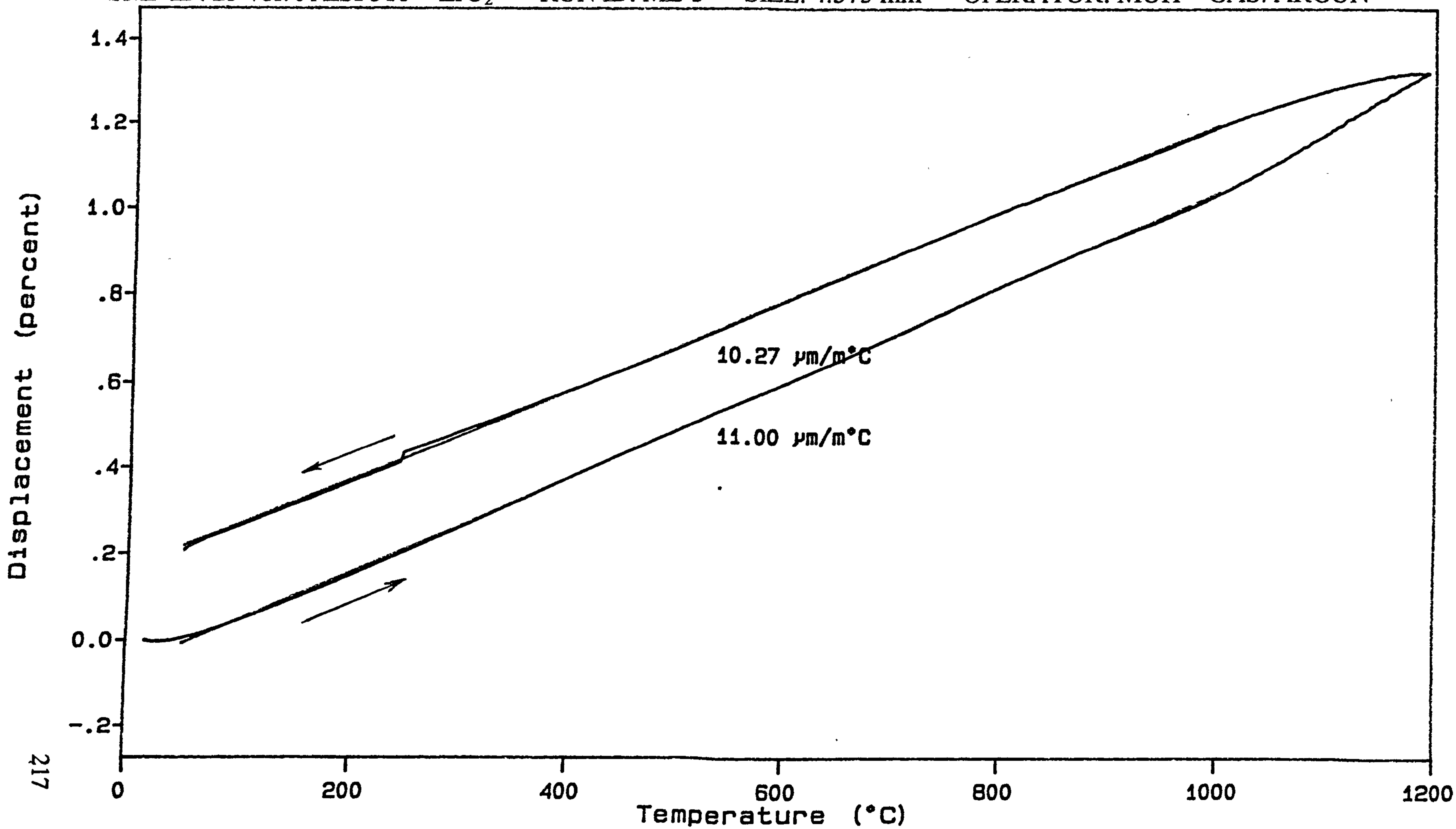

Figure 7.11 Thermal expansion in argon of (25 vol% AISI 316 + ZrO_2 sintered at 1450°C for 1h in argon)

CHAPTER 8

ZIRCONIA/METAL COMPOSITES: ELECTRICAL CONDUCTIVITY

Electrical conductivity is one of the important properties of ceramic materials. The electrical conductivity of ceramics varies over a large range, from the most insulative materials to superconductors. The electrical conductivity of zirconia-based material at room temperature is very low and it can be considered as an insulator, but at high temperature its electrical conductivity becomes quite high mainly due to ionic conduction of mobile oxygen ions [Kingery *et al*, 1959; Badwal and Swain, 1994]. With this property, zirconia can be applied as an oxygen sensor or solid electrolyte in solid oxide fuel cells (SOFC). Yttria-stabilised zirconia (YSZ) is interesting in SOFC applications because it possesses a sufficient level of oxygen ion conductivity and good stability in oxidising or reducing atmospheres. As well as stabilising zirconia, yttria can increase the oxygen vacancy concentration that enhances the ionic conductivity and extends the range of oxygen partial pressure for ionic conduction [Minh, 1993].

To complete the study of zirconia reinforced with metal powder as presented in the previous chapters (the zirconia matrix in Chapter 4, processing and characterisation of zirconia/metal composites in Chapter 5, mechanical properties in Chapter 6 and thermal properties in Chapter 7), the effect of metal reinforcement on the electrical conductivity of zirconia/metal composites at room temperature is presented and discussed in this Chapter.

8.1. RESULTS AND DISCUSSION

Measurement was performed on disc samples of 12 mm diameter and 2 mm

thickness. The sample surfaces in which the terminals for measurement were placed were coated with silver paste. Six measurements were carried out on each sample at different locations.

Table 8.1 presents the electrical resistivity and conductivity of chromium, iron and AISI 316 at room temperature which were obtained from the literature. Among those metals iron is the most conductive material and AISI 316 has the lowest electrical conductivity. At room temperature the monolithic zirconia used in this research can be considered as an insulator because of its very low electrical conductivity which can not be measured with the available instrument.

Table 8.1. Electrical resistivity and conductivity of the reinforcements

Material	Resistivity (ohm.m)	Electrical Conductivity (1/(ohm.m))	Reference
Cr	12.9×10^{-8}	7,751,938	Askeland, 1998
Fe	10.0×10^{-8}	10,000,000	Callister, 1994
AISI 316	71.43×10^{-8}	1,400,000	Callister, 1994

Tables 8.2, 8.3 and 8.4 show the electrical resistivity and conductivity at room temperature of zirconia/chromium, zirconia/iron and zirconia/AISI 316 composites containing up to 25 vol% reinforcement, respectively. It can be seen in the tables that below 20 vol% reinforcement, all the composites are electrically insulative. This is clearly due to the metal particles being isolated in the insulating matrix of monolithic zirconia. Above 20 vol% of the reinforcement the materials become conductive which is due to some interconnection of particles (see the microstructures in Chapter 5 and Figures 8.3 to 8.5). Furthermore, the conductivity increases with increasing reinforcement volume fraction since more particles are clustering at higher contents of reinforcement.

Table 8.2. Electrical resistivity and conductivity of zirconia/chromium composites

Material	Resistivity (ohm.m)	Electrical Conductivity (1/(ohm.m))
ZrO_2	∞	0
5 vol% Cr + ZrO_2	∞	0
10 vol% Cr + ZrO_2	∞	0
15 vol% Cr + ZrO_2	∞	0
20 vol% Cr + ZrO_2	0.3355 ± 0.0398	2.8478 ± 0.3200
25 vol% Cr + ZrO_2	0.09106 ± 0.0085	11.0648 ± 1.0035

Table 8.3. Electrical resistivity and conductivity of zirconia/iron composites

Material	Resistivity (ohm.m)	Electrical Conductivity (1/(ohm.m))
ZrO_2	∞	0
5 vol% Fe + ZrO_2	∞	0
10 vol% Fe + ZrO_2	∞	0
15 vol% Fe + ZrO_2	∞	0
20 vol% Fe + ZrO_2	1.6052 ± 0.1306	0.6271 ± 0.0558
25 vol% Fe + ZrO_2	0.0188 ± 0.0020	53.5632 ± 5.4633

Table 8.4. Electrical resistivity and conductivity of zirconia/AISI 316 composites

Material	Resistivity (ohm.m)	Electrical Conductivity (1/(ohm.m))
ZrO_2	∞	0
5 vol% AISI 316 + ZrO_2	∞	0
10 vol% AISI 316 + ZrO_2	∞	0
15 vol% AISI 316 + ZrO_2	∞	0
20 vol% AISI 316 + ZrO_2	0.0177 ± 0.002	57.152 ± 6.777
25 vol% AISI 316 + ZrO_2	0.0111 ± 0.0013	91.485 ± 14.565

It has been discussed in Chapter 5 that all the three composites (zirconia/chromium, zirconia/iron and zirconia/AISI 316) have almost full density, so the porosity is very small. However, intrinsic microcracks are considered to be present in zirconia/AISI 316 composites. If the particles of each reinforcement are assumed as spherical in shape with the same size and are arranged in an ordered manner, then the distance between particles can be estimated as shown in Table 8.5. On his study of sialon/Ni and sialon/stainless steel, Edrees (1990) mentioned that at the same amount of reinforcement (20 vol%), the smaller particle sizes of nickel than that of stainless steel results in the distance between particles of nickel being smaller than that of stainless steel. This leads to sialon/nickel composites being conductive, while sialon/stainless steel was not. However, the ideal arrangement of particle reinforcement in composites as shown in Figure 8.1 is practically impossible. Additionally, usually the particles do not have the same size and regular shape.

DeBondt *et al* (1992) pointed out that connectivity between conductive particles in composites could play an important role in percolation threshold. As mentioned in Chapter 2 (Section 2.2.6), electrical conductivity of particulate composites is not only depending on the amount of its constituents but also depends on the degree of connectivity of each component [Chiang *et al*, 1997] and the particle morphology [Warren, 1992]. If there is a great difference of electrical conductivity between the matrix and the reinforcement, then at a certain amount of the reinforcement there will be a so called percolation threshold, which is defined as a transition from discontinuous phase to continuous chain. So, if the matrix is insulative and the reinforcement particles are conductive, percolation threshold will occur when the particles start to interconnect each other. DeBondt *et al* (1992) also mentioned that when coarse metal particles are dispersed in a ceramic matrix, microstructures with segregation or skeleton formation in the mixture (as shown Figure 8.2) occurred easily increasing the degree of connectivity, which might lead to reduction in the percolation threshold.

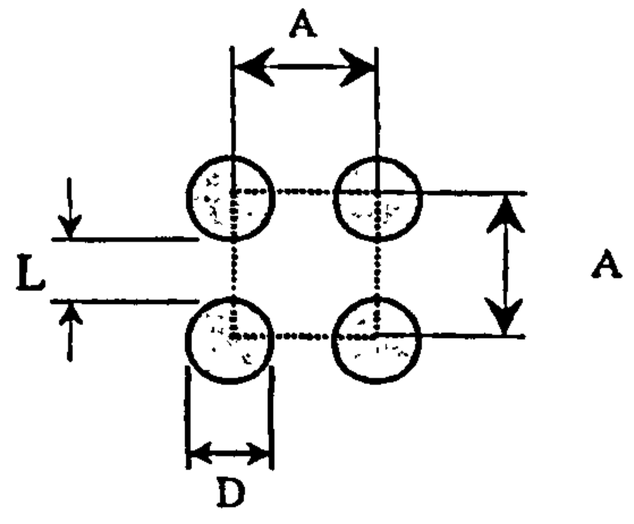

Figure 8.1. An ideal arrangement of particles in zirconia/metal composites

Table 8.5. An ideal arrangement of particles in zirconia/metal composites

Material	D (μm)	A (μm)	L (μm)
20 vol% Cr + ZrO_2	38	52.36	14.36
25 vol% Cr + ZrO_2	38	48.62	10.62
20 vol% Fe + ZrO_2	6	8.27	2.27
25 vol% Fe + ZrO_2	6	7.68	1.68
20 vol% AISI 316 + ZrO_2	45	62.01	17.01
25 vol% AISI 316 + ZrO_2	45	57.57	12.57

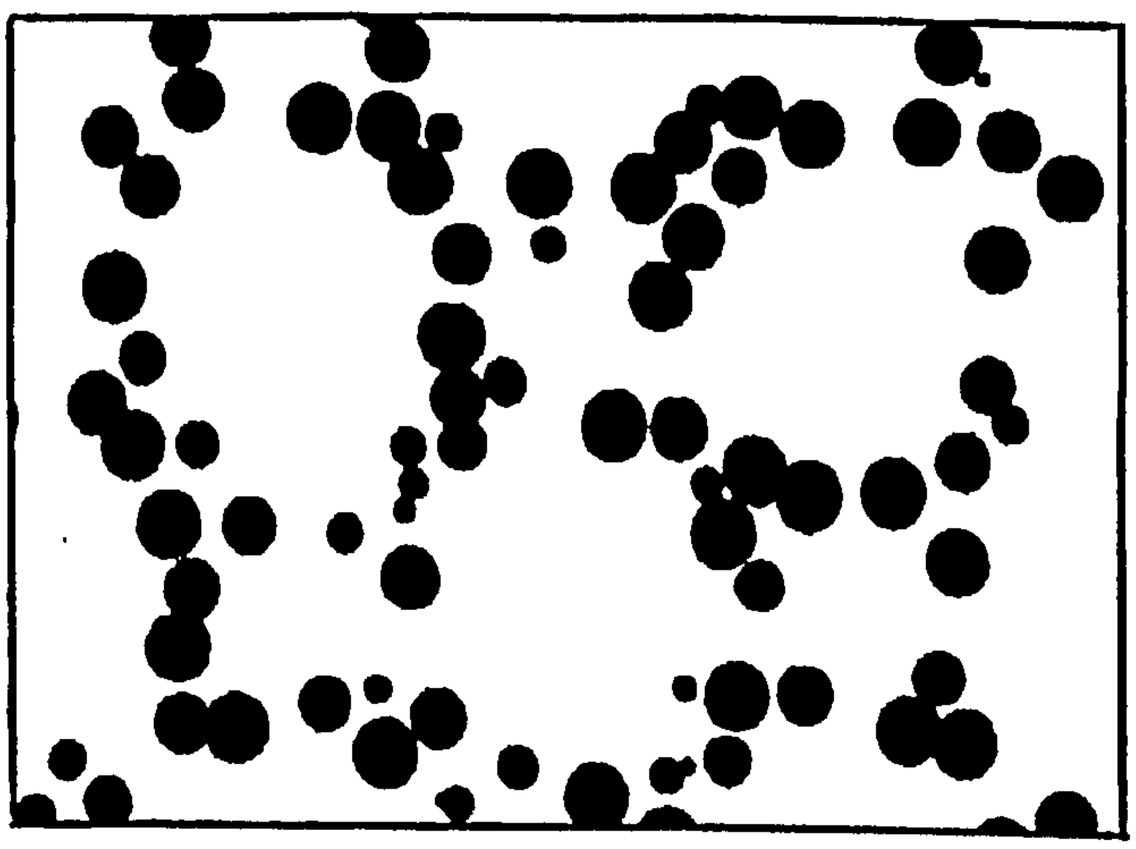

Figure 8.2 Microstructures with skeleton formation [DeBondt *et al*, 1992].

In the case of the present study, the particle sizes of chromium, iron and AISI 316 are 38 μm (max.), 6 -8 μm (mean) and 45 μm (max.), respectively [data from the supplier]. Among those three composites, zirconia/AISI 316 composites have the highest conductivity for composites containing 20 vol% and 25 vol% of reinforcement, although AISI 316 has the lowest electrical conductivity (Table 8.1) of the metals used and intrinsic microcracking seems to occur after fabrication. This may be due to the large particle size of AISI 316, and the rounded and irregular particle shape (Chapter 5) causing skeleton formation of the particles (see Figure 8.5) and increasing the connectivity between the particles as mentioned by DeBondt *et al* (1992). The skeleton formation (un-homogeneous) mixture may also be due to a big difference in density between the matrix and particles.

The conductivity of composites containing 20 vol% of chromium is higher than that of zirconia/iron at the same volume fraction, although the conductivity of iron is higher than that of chromium. This is again thought to be due to the larger particles of chromium causing connectivity between the particles. In contrast, for composites of 25 vol%, zirconia/iron has higher conductivity than that of zirconia/chromium because the iron particles at 25 vol% are dispersed more uniformly in the matrix making the distance between particles closer and more particles join together increasing the connectivity between particles. In fact, in the composites with 25 vol% chromium some particles also join together, but because the conductivity of iron is higher, zirconia/iron has higher conductivity.

Figures 8.3 to 8.5 show the comparison of the microstructures of zirconia/iron, zirconia/chromium and zirconia/AISI 316 composites containing 25 vol% of the reinforcement, respectively. In Figure 8.3, it is clearly seen that small iron particles are distributed uniformly throughout the matrix with some particles are clustered forming into some larger particles. The chromium particles are also distributed well in the matrix, and the large particle size, the angular and irregular in the particle shape causing some interconnection particles as shown in Figure 8.4. A skeleton formation of stainless steel (AISI 316) particles in zirconia matrix can be seen in Figure 8.5 (which is similar to the skeleton formation proposed by DeBondt

et al, 1992 as shown in Figure 8.2). The large particle size of AISI 316, the rounded and irregular in shape and big difference in density between zirconia and AISI 316 may cause this formation. Moreover, this formation has effectively improved the electrical conductivity of zirconia/AISI 316 composites.

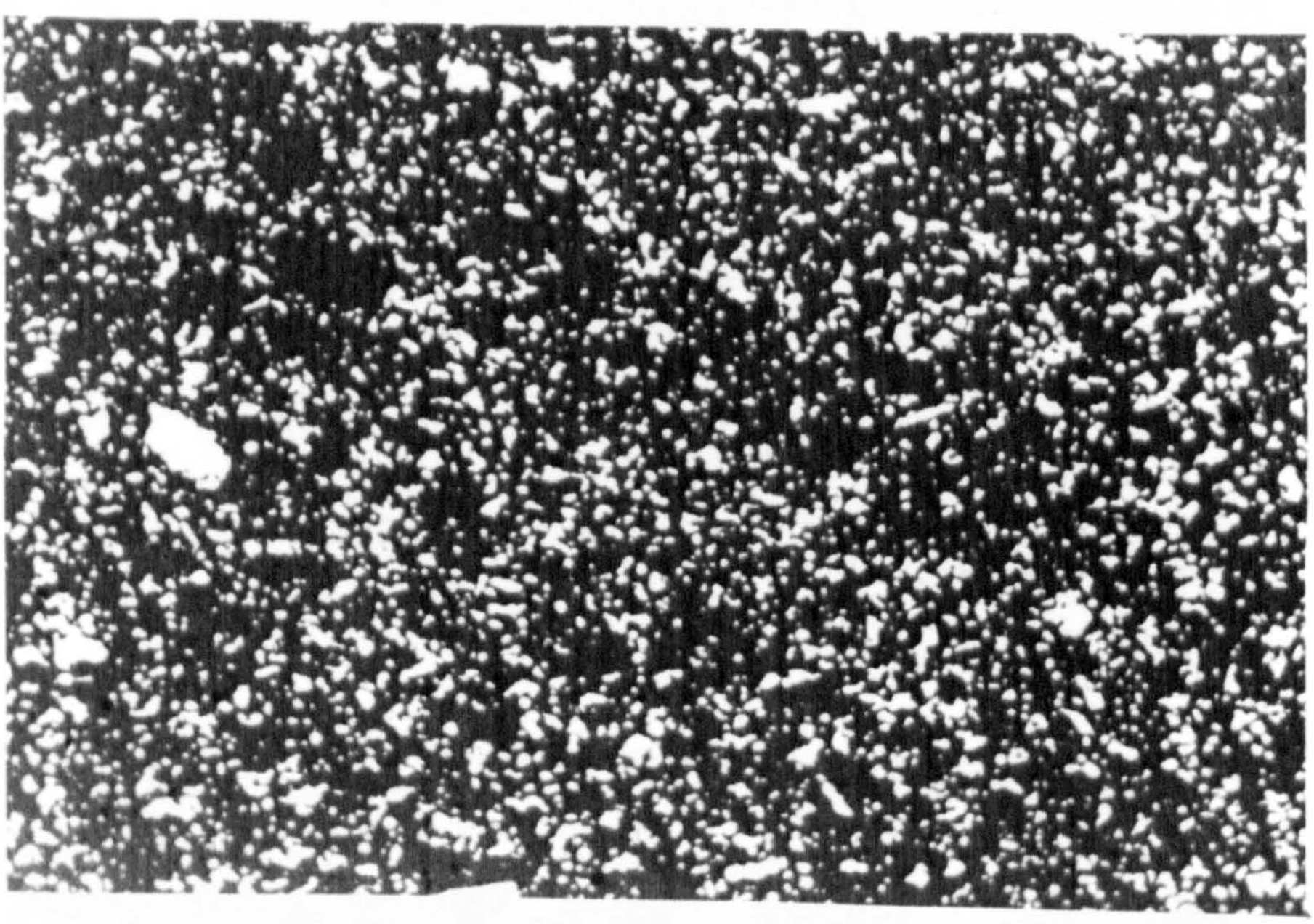

Figure 8.3 Optical micrograph of (25 vol% Fe + ZrO_2) sintered at 1450°C for 1 h in argon.

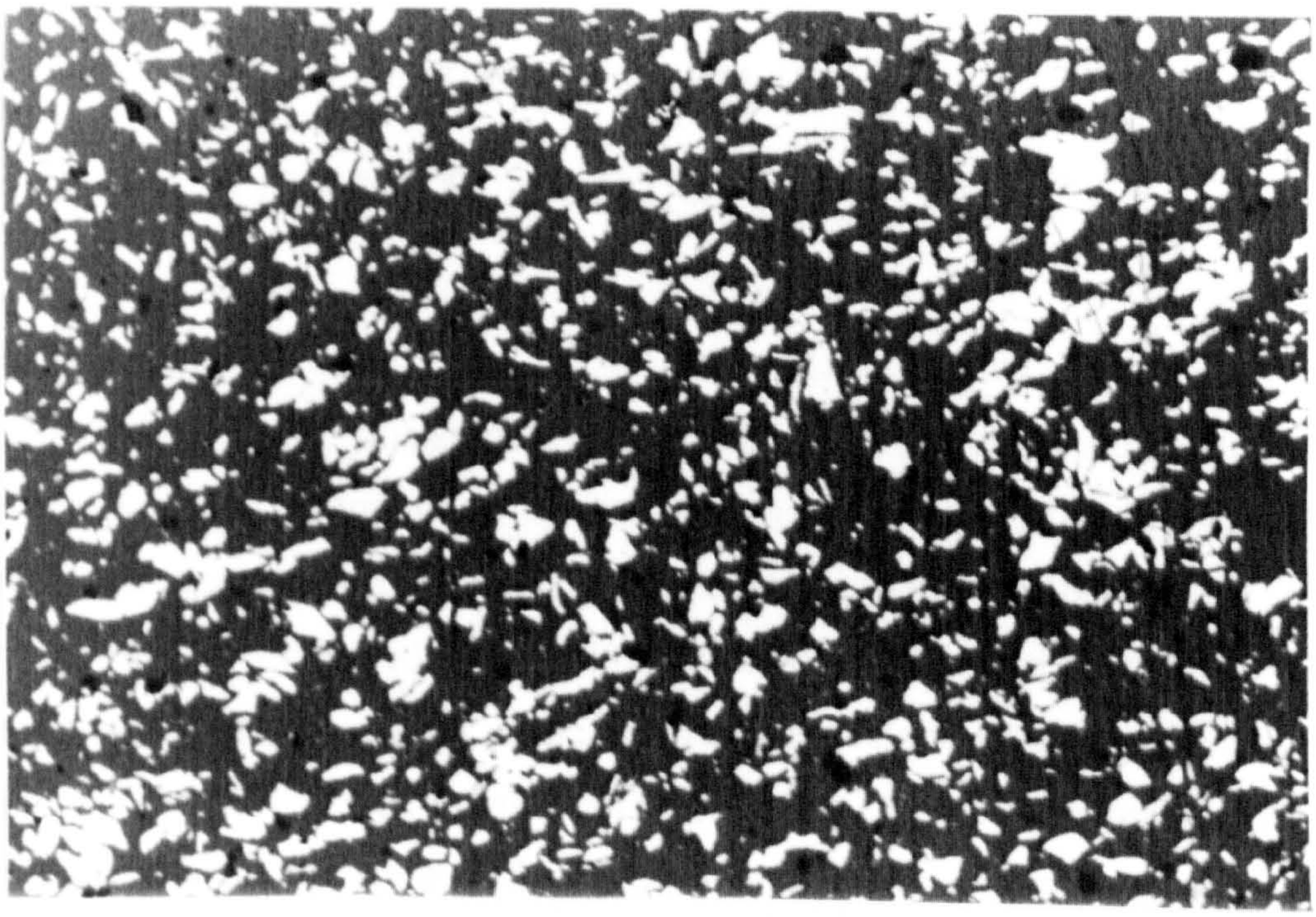

Figure 8.4 Optical micrograph of (25 vol% Cr + ZrO_2) sintered at 1450°C for 1 h in argon.

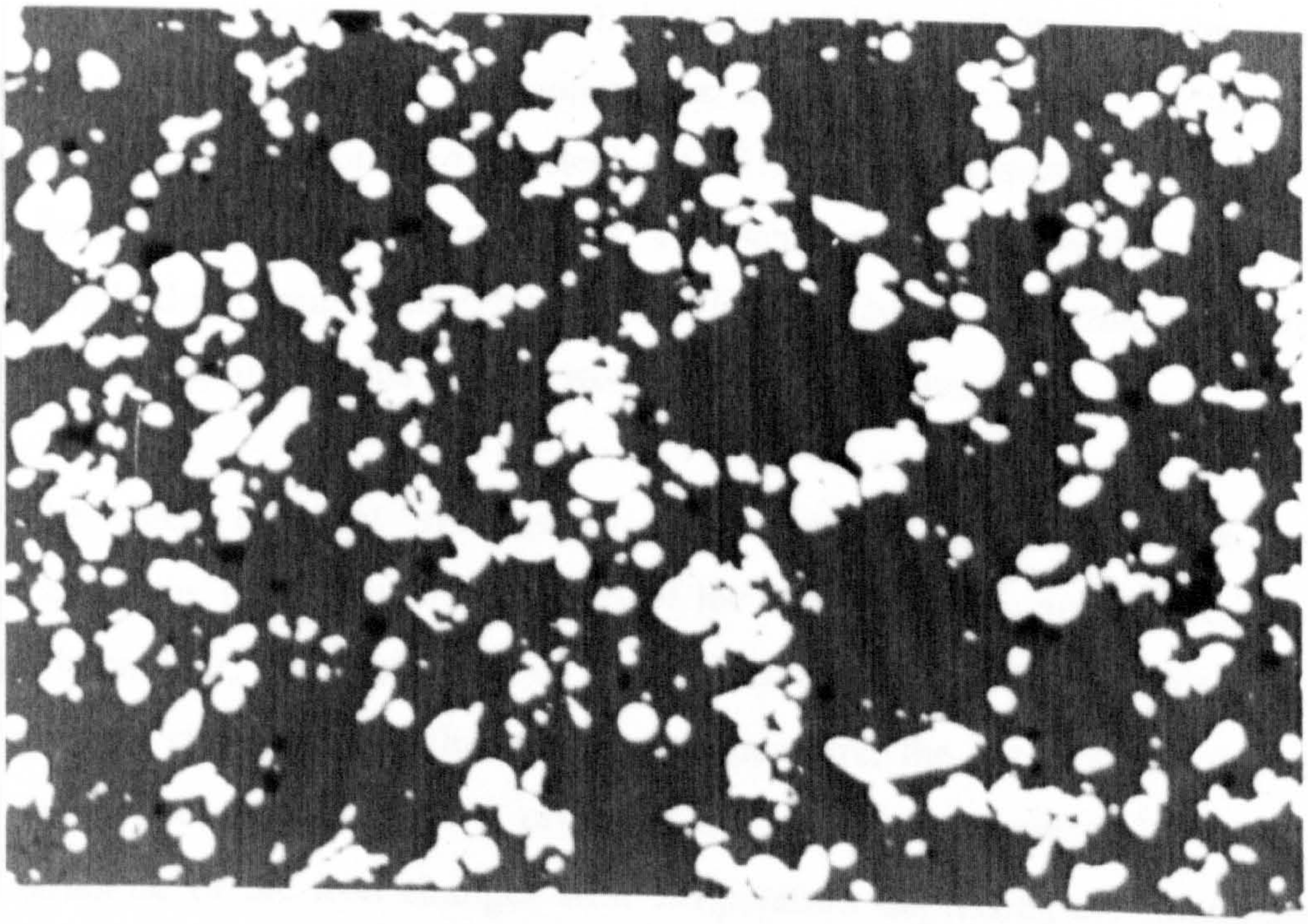

Figure 8.5 Optical micrograph of (25 vol% AISI 316 + ZrO_2) sintered at 1450°C for 1 h in argon.

CHAPTER 9

GENERAL DISCUSSION

The overall aim of this study was to investigate a zirconia-matrix reinforced with metal powder (chromium, iron or stainless steel AISI 316) including the fabrication, the characterisation, and the assessments of their properties. All these works were initially performed on monolithic zirconia as the matrix, and then on the composites to evaluate the effects of the metal reinforcement. Mechanical properties tests (Vickers hardness, fracture toughness and bending strength), thermal diffusivity and electrical conductivity were performed at room temperature. In addition, thermal diffusivity and thermal expansion were also examined on the materials up to 1000°C. The high degree of agreement and interrelation between the different aspects of the investigations have been reported and discussed in the previous Chapters (Chapter 4 to 8). In this Chapter all the previous results will be generally discussed below.

It has been shown in this research that pressureless sintering in argon can be used successfully to produce zirconia-matrix composites reinforced with metal powder (chromium, iron or stainless steel AISI 316) where pressureless sintering at 1450°C for 1 h results in dense materials. This sintering method is the easiest and simplest method in ceramics fabrications. In addition, the low sintering temperature and short sintering time in this present work give other advantages.

The three different systems of zirconia/metal composites have some differences of the reinforcement in terms of the metal stability and reactivity, the sintering behaviour, the coefficient of thermal expansion and the particle size. In terms of metal stability up to the sintering temperature, the chromium is the most stable which does not change the crystal structure and does not melt, while the crystal structure of the iron changes with temperature depending on composition. The iron used in this work has a melting temperature of 1370°C which will melt during fabrication of the zirconia/iron composites. The third reinforcement, stainless

steel (AISI 316) is also stable as austenitic structure, however the melting temperature of 1450°C causes the metal to melt during fabrication of the composites.

In addition, the reactivity of those metals are also different, chromium does not react with the zirconia and/or yttria (the stabiliser of the zirconia). In contrast, the iron reacts with the yttria resulting in de-stabilising of the zirconia. However, the stainless steel (AISI 316) which contains 69% of iron does not have this behaviour, because the structure and properties of AISI as a whole differ from the iron.

Furthermore, the presence of the metal in the zirconia matrix has influenced the sintering behaviour. The zirconia/chromium and zirconia/AISI composites have similar densification temperature to that of monolithic zirconia, although the presence of the metals have reduced the final shrinkage, while the zirconia/iron has densification temperature at about 200°C lower than that of monolithic zirconia. The densification rate of the zirconia/iron and zirconia/AISI 316 composites is slightly higher than that of monolithic zirconia which is caused by melting of the reinforcements.

The coefficient of thermal expansion of the reinforcement has a significant effect on the composites since the thermal expansion mismatch can cause thermal stresses. The reinforcement has coefficients of thermal expansion with the following order (from smallest to largest): chromium, iron, and AISI 316. Therefore the thermal stresses generated in the composites due to thermal expansion mismatch will take place in similar order (from smallest to largest); zirconia/chromium, zirconia/iron and zirconia/AISI 316 composites.

Other differences of the reinforcements are the particle size and shape, where the data given by the supplier shows that the particle size of the chromium is 38 μm (maximum) with angular and irregular shape, the iron particles have spherical shape with size of 6 - 8 μm, and the AISI 316 particle size is 45 μm (maximum) with rounded but irregular shape. The available data of particle size of the iron given by

the supplier is only the mean size, and the maximum size is not known, however from Chapter 5 it can be seen that some particles are clustered forming larger sizes less than 25 micron, which is still smaller than the critical size. The particle size and shape influence the distribution of the particles in the matrix. In addition combination of particle size and the thermal stress analysis can be used to predict microcracking during fabrication. Spontaneous microcracking does not occur in the zirconia/chromium and zirconia/iron composites because the particle sizes are smaller than the critical sizes, however microcracking occurs in the zirconia/AISI 316 composites.

In terms of the properties, the composites show an increase in fracture toughness and a reduction in Vickers hardness and strength with increasing reinforcement content. In addition, the thermal diffusivity of the composites shows an increase with reinforcement content for the zirconia/chromium and zirconia/iron composites, but not for the zirconia/AISI 316 composites due to intrinsic mircocracking. Furthermore, all the composites become electrically conductive with 20 vol% or more of reinforcement

For future investigations of a ceramic-matrix reinforced with metal powder several criteria should be taken into account,

- the structural stability of the matrix and reinforcement from room temperature up to the fabrication temperature and/or the proposed usage temperature of the material
- the reinforcement should not react with the matrix because the reaction may influence the stability of the component
- because thermal expansion mismatch is a significant factor in a composite, so the chosen reinforcement should have coefficient of thermal expansion as close as possible with that of the matrix
- particle size of the reinforcement is also an important aspect, this particle size should be smaller than the critical size to avoid spontaneous microcracking during fabrication. The particle size and shape will also influence the particle distribution and flaw size of the materials

Based on the above discussions, it may be proposed that among those composites, zirconia/chromium can be considered as having the best combination of properties and although further development is needed for such composites in order to be used in real applications in structural engineering, the materials may be developed based on these findings. For example, utilisation of smaller particle size (microns or sub-microns) may be used to optimise the mechanical property improvements. The smaller particle size will also further improve the processing quality and other properties. In addition, the properties of these composites may be used in development of ceramic/metal joining where composite interlayers are often applied.

CHAPTER 10

CONCLUSIONS AND FUTURE WORKS

10.1. CONCLUSIONS

The present work is about an investigation of a zirconia-matrix reinforced with metals. Zirconia stabilised with 5.4 wt% (3 mol%) Y_2O_3 known as 3Y-TZP was used as matrix and chromium (Cr), iron (Fe), and stainless steel (AISI 316) powders were used as reinforcement. Based on the experimental results and discussions in the previous chapters, conclusions are drawn below.

10.1.1. ZIRCONIA

The density of monolithic zirconia (3Y-TZP) pressureless sintered for 1 hour in air or argon at various temperatures (from 1250°C to 1500°C) increases with increasing temperature. Full density was achieved in samples pressureless sintered at between 1400°C and 1500°C for 1 hour in air or argon. The sintering condition at 1450° was then used for fabrication of samples of monolithic zirconia and the composites. It was found that there is no significant effect of air and argon atmosphere on the processing, characterisation and properties (mechanical and thermal) of monolithic zirconia. Pressureless sintering in argon was used for fabrication of the zirconia/metal composites to avoid oxidation. Densification of zirconia monolithic starts at 1100°C and is followed by rapid shrinkage with high densification rate which may indicate liquid phase sintering due to the presence of impurities (Al_2O_3 - SiO_2). The densification was dominated by the heating process up to 1450°C (~85%) and followed by a further small shrinkage during isothermal treatment at 1450°C for 1 hour (~15%).

The crystal structure of the monolithic zirconia after pressureless sintering at 1450°C for 1 hour in air or argon is tetragonal. Microstructures taken by SEM indicate a typical grain size of tetragonal phase of ~ 0.45 μm. Some of this tetragonal phase transforms to monoclinic when a mechanical stress is applied indicating that metastable tetragonal is present in the samples, which is useful for transformation toughening.

Good mechanical properties typical of 3Y-TZP were found in these samples such as high Vickers hardness (~1370 kg/mm^2), indentation fracture toughness (~6 MPa.m$^{0.5}$) and bending strength (~700 MPa).

Two thermal properties were measured, thermal diffusivity and thermal expansion coefficient. The thermal conductivity was calculated. The monolithic zirconia (3Y-TZP) samples exhibit low thermal diffusivity (0.01097 cm^2/s) and thermal conductivity (2.97 W/m.K) at room temperature. These values decrease with increasing temperature up to 500°C and then remain almost constant. In addition, the materials have a coefficient of thermal expansion of (10.45 x 10^{-6}/°C) in the temperature range of (20°C - 1000°C).

9.1.2. ZIRCONIA/METAL COMPOSITES

Almost fully dense samples were achieved in zirconia/chromium and zirconia/AISI 316 composites containing up to 25 vol% reinforcement after pressureless sintering at temperature between (1400°C and 1500°C) for 1 hour in argon. The densification process starts at 1150°C for zirconia/chromium and 1100°C for zirconia/AISI 316, which are close to that of monolithic zirconia. The presence of those metals has reduced the final linear shrinkage. However the trends of the shrinkage are similar to that of monolithic zirconia.

Different trends in density and densification found in zirconia/iron composites. In these composites, almost fully dense samples were achieved at lower

temperature (1200°C). The densification starts at 900°C or 200°C lower than that of monolithic zirconia. Furthermore, densification seems to occur not only in the matrix but also in the reinforcement resulting in the decrease in final shrinkage being less than that of zirconia/chromium and zirconia/AISI 316. It is also found from DTA and TMA analysis that the iron reinforcement melted at about 1370°. All these phenomena combined with the liquid phase sintering of zirconia give a densification rate of zirconia/iron higher than that of monolithic zirconia and the other two composites.

Phase identification using XRD on zirconia/chromium and zirconia/AISI 316 shows that the crystal structure of the zirconia matrix is tetragonal. Moreover chromium and AISI 316 metal are found in zirconia/chromium and zirconia/AISI 316, respectively. In other words, there is no reaction in the samples. Transformation from tetragonal to monoclinic is also found in both composites after a mechanical stress is applied indicating the presence of metastable tetragonal zirconia. This transformation is useful in contributing in toughening mechanisms.

However, different phenomena occur in zirconia/iron composites. In these composites, monoclinic zirconia, tetragonal zirconia and iron phases appear in the sample after fabrication at 1450°C for 1 hour in argon. The presence of monoclinic zirconia is interesting since it does not appear in the other two composites. The explanation of this case is that iron in the composites reacted with yttria as the stabiliser of zirconia, yielding a decrease of soluble yttria and destabilising the zirconia matrix. In their study of Fe-Yttria alloys Kosco and Koss (1993) using TEM and Ogawa (1993) using High Resolution Electron Microscopy (HREM) found unknown phases in the interface of iron and yttria. In the present study, XRD analysis of mixtures of Fe + Y_2O_3 sintered at 1450°C for 1 hour in argon also showed some unknown peaks. Furthermore, DTA analysis of the mixtures heated up to 1500°C in argon showed some unknown endothermic peaks. Therefore it was concluded that iron in zirconia/iron composites reacted with yttria (the stabiliser of zirconia matrix).

The difference in thermal expansion coefficient between the matrix and reinforcement generates thermal stresses. If the thermal stresses are greater than the strength of the matrix and the particle sizes of the reinforcement are greater than the critical particle size, then microcracks may occur spontaneously during cooling from the fabrication temperature [Davidge and Green, 1968]. In the case of zirconia/chromium composites ($\alpha_m > \alpha_p$) the matrix will experience radial compressive and tangential tensile stresses, while the particles are subjected to compressive stress. However these stresses are smaller than the strength of the zirconia matrix and the particle sizes are smaller than the critical size, so cracks should not occur during cooling.

For zirconia/iron and zirconia/AISI 316 composites where ($\alpha_m < \alpha_p$), the particles are subjected to tensile stress, and the matrix to radial tensile and tangential compressive stresses. The stresses in the matrix of these composites are greater than the strength of zirconia matrix. Microcracking will occur spontaneously in zirconia/AISI 316 during cooling from fabrication because the AISI 316 particles are bigger than its critical particle size. In contrast, this intrinsic microcracking should not occur in zirconia/iron composites since the iron particles are smaller than the critical particle size. Microcracking however, may be formed around the particles under applied stress at stresses below the macroscopic fracture stress (stress required for fracture).

The Vickers hardness of all the zirconia/metal composites decreases with increasing amount of metal reinforcement. The Vickers hardness values of the composites are in between the linear rule of mixtures and the inverse rule of mixtures predicted values. The standard deviation values of the Vickers hardness of zirconia/iron composites are smaller than that of zirconia/chromium and zirconia/AISI 316, which may indicate more homogeneous materials in zirconia/iron composites.

The fracture toughness of the composites increases slightly with increasing metal content in the following order from (largest to smallest); zirconia/iron, zirconia/chromium and zirconia/AISI 316. The toughening mechanisms in zirconia/chromium may include toughening transformation and crack deflection. While for zirconia/iron the toughening mechanisms are thought to be microcracking, crack deflection and matrix compression. The toughening transformation in zirconia/iron is difficult to examine since monoclinic zirconia is already in the sample after fabrication. The zirconia/AISI 316 composites have the lowest increase in fracture toughness compared to the other two composites. The toughening mechanisms that are involved in zirconia/AISI 316 composites are crack deflection and matrix compression. However, due to the large thermal expansion mismatch in these composites and large particle size of the AISI 316 powder the microcracking occurs during cooling from fabrication temperature and this microcracking does not contribute to fracture toughness improvement.

All the zirconia/metal composites exhibit reducing strength with increasing metal content. These are due to the increase in critical crack/flaw sizes in the composites as the metal contents increase. The biggest reduction in strength occurs in zirconia/AISI 316, which is due to the presence of microcracking after sintering. If microcracking is widespread in the samples and microcrack-linking occurs, the critical crack/flaw sizes become bigger leading to decrease in strength.

As expected the thermal diffusivity of zirconia/chromium and zirconia/iron composites increase with increasing metal contents. The values of thermal diffusivity of these composites are close to that predicted using the Eucken model. However, above 20 vol% the thermal diffusivity is higher than that predicted using Eucken model, because the particles interconnect forming particle links. Furthermore, the thermal diffusivity of zirconia/chromium and zirconia/iron composites decrease as the temperature increases, because the thermal diffusivity of both the matrix (zirconia) and reinforcement (chromium and iron) decrease with temperature. However, above about 700°C there is a little increase of thermal diffusivity in

zirconia/iron composites, which is due to the effect of iron reinforcement in which the thermal diffusivity of iron also slightly increases above about 700°C.

In contrast, the thermal diffusivity of zirconia/AISI 316 is much lower than that estimated using the Eucken model. In fact the thermal diffusivity of AISI 316 is higher than that of monolithic zirconia. This is caused by the presence of microcracks. Even more, the thermal diffusivity values of the composites containing up to 20 vol% AISI 316 are lower than that of monolithic zirconia. Above 20 vol% AISI 316, the thermal diffusivity of the composites increases because the particles interconnect. In addition, the presence of microcracks also influences the thermal diffusivity as a function of temperatures in which the thermal diffusivity values are much lower than that predicted using the Eucken model and there is irreversibility between heating and cooling. However on the second cycle the thermal diffusivity seems to be higher than that of the first cycle and the irreversibility between heating and cooling is smaller, although at high temperature the data on cooling still exceed those obtained on heating. This may be attributable to further crack closure and healing at higher temperature followed by re-formation of microcracks at lower temperature on cooling.

The coefficient of thermal expansion (CTE) of the zirconia/metal composites containing up to 25 vol% of the reinforcement is not significantly influenced by the presence of the metal. The CTEs of (25 vol%Cr + ZrO_2), (25 vol% Fe + ZrO_2) and (25 vol% AISI 316 + ZrO_2) at the range of temperature of (20 - 1000°C) are (10.31 x 10^{-6}/°C), (10.86 x 10^{-6}/°C) and (10.64 x 10^{-6}/°C) respectively.

At room temperature the electrical conductivity of the zirconia/metal composites containing below 20 vol% shows as insulating materials because the conductive metal particles are isolated by the insulating matrix of zirconia. Above 20 vol% of reinforcement, the composites become conductive since the particles interconnect.

10.2. FUTURE WORK

The present study has opened up many new topics in zirconia-metal composites which will be of considerable importance in the future. Based on experience gained during this research the following may be important for further research:

1. Further investigation of the destabilising of 3Y-TZP by addition of iron reinforcement which is due to reaction between iron and yttria. The methods of electron microscopy (SEM and TEM) and Electron Probe Microanalysis (EPMA) may be used to investigate new phases formed by reaction between iron and yttria in 3Y-TZP/iron composites particularly in the interface between the matrix and iron particles. Thermal analysis (DTA, DSC and TGA) may also be required to study this reaction model systems such as those described in Chapter 5.

2. Fabrication and investigation of the same composite compositions using different metal particle sizes (in microns or sub microns) to determine the effect on both processing and properties (mechanical, thermal and electrical). The same particle size of metal reinforcement should be used in order to make comparison of the three metal reinforcements (chromium, iron and AISI 316) and their effects on the matrix. Of particular interest are particle sizes smaller than the critical particle size which should avoid spontaneous microcracking during cooling from processing temperature as discussed in Chapter 6.

3. The effect of phase transformation of iron reinforcement on thermal stress during fabrication of zirconia/iron composites should be studied. Measurement of the thermal expansion coefficient of each component may be required in predicting the thermal stress generated by thermal expansion mismatch and a clearer picture of these mismatch effects is essential in understanding the effect on properties of these composites.

4. Measurement of electrical resistivity of the composites at high temperature is of interest and in particular where zirconia stabilised with yttria becomes ionic-conductive. This is of particular interest in hydrogen-fuelled solid-oxide fuel cell applications (SOFC).

5. Further investigation of toughening mechanisms in the composites should be studied. Raman spectroscopy may be used to analyse the transformation toughening mechanism where the amount of transformation of metastable tetragonal to monoclinic can be estimated more accurately. Similarly, crack deflection or crack bridging toughening mechanisms can be identified by taking SEM photographs on both matched-surfaces of fracture faces. This observation is then compared to an SEM photograph of crack propagation on a polished surface. Microcracking may also be observed using high magnification scanning electron microscopy.

6. Fracture toughness measurement using conventional methods such as SENB (single edge notch beam) and DCB (double cantilever beam) should be made and the results compared to those of the Indentation Fracture Method.

7. The effects of metal reinforcement in zirconia/metal composites on other mechanical properties such as Young's Modulus, Poisson's ratio and wear resistance can also be measured. (Young's Modulus and Poisson's ratio can be measured using acoustic methods).

REFERENCES

Adams JW, Nakamura HH, Ingel RP and Rice RW, **Thermal Expansion Behavior of Single-Crystal Zirconia,** J. Am. Ceram. Soc., 68[9] (1985) C228-31.

Anstis GR, Chantikul P, Lawn BR and Marshall DB, **A Critical Evaluationof Indentation Techniques for Measuring Fracture Toughness: I, Direct Crack Measurements,** J. Am. Ceram. Soc., 64[9] (1981) 533-38.

Askeland DR, **The Science and Engineering of Materials,** Chapman and Hall, 1996.

Badwal SPS and Swain MV, **Electrical Conductivity of Some Fully and Partially Stabilised Single Grain,** J. Mater.Sci. Lett., 4(1985) 487-89.

Badwal SPS, **Ceramic Superionic Conductors, in Materials Science and Technology,** edited by Cahn RW, Haasen P, and Kramer EJ, Vol. 11, pp. 568-633, VCH Publisher (1994).

Baker H *et al*, **ASM Handbook Volume 3 Alloy Phase Diagrams,** ASM International, 1992.

Bansal GK and Heuer AH, **On A Martensitic Phase Transformation in Zirconia (ZrO_2) - I, Metallographic Evidence,** Acta Metall., 20[11] (1972) 1281-89.

Barsoum M, **Fundamental of Ceramics,** McGraw Hill International, 1997.

Baskin Y, Harada Y and Handwerk JH, **Some Physical Properties of Thoria Reinforced by Metal Fibres,** J. Am. Ceram. Soc., 43[9] (1960) 489-92.

Becher PF, **Overview No. 52: Toughening Behaviour in Ceramics Associated with the transformation of Tetragonal ZrO_2,** Acta Metall., 34[10] (1986) 1885-91.

Becher PF and Rose LRF, **Toughening Mechanisms in Ceramic Systems,** in Materials Science and Technology, edited by Cahn RW, Haasen P, and Kramer EJ, Vol. 11, VCH Publisher (1994).

Bentsen LD, Hasselman DPH and Claussen N, **Effect of Microcracking on the Conduction of Heat in Brittle Composites,** in Proceeding of the Conference on Environmental Degradation of Engineering materials, VPI Press, (1981), 369-82.

Besson VE, **Zirconia Reinforced with Carbon**, PhD Thesis, The University of Strathclyde, Glasgow UK (1996).

Bratton RJ and Lau SK., **Zirconia Thermal Barrier Coating**, Advances in Ceramics Vol. 3: Science and Technology of Zirconia, edited by Heuer AH and Hobbs LW, (1981) 226-40.

Budiansky B, Amazigo JC, and Evans AG, **Small-Scale Crack Bridging and the Fracture Toughness of Particulate-Reinforced Ceramics**, J. of Mechanics and Physics Solids, 36[2] (1988) 167-87.

Butler EP, **Critical Assessment - Transformation - Toughening Zirconia Ceramics**, Mater. Sci. and Tech., 1 (1985) 417.

Callister WD, **Materials Science and Engineering An Introduction**, 3th edition, John Wiley and Son (1994).

Chawla KK, **Ceramic Matrix Composites**, Chapman and Hall (1993).

Chiang Y, Birnie D and Kingery WD, **Physical Ceramics**, John Wiley and Son (1997).

Clarke DR, **Interpenetrating Phase Composites**, J. Am. Ceram. Soc., 75[4] (1992) 739-58.

Claussen N, **Fracture Toughness of Al_2O_3 with an Unstabilised ZrO_2 Dispersed Phase**, J. Am. Ceram. Soc., 59[1] (1976) 49-51.

Claussen N, **Stress Induced Transformation of Tetragonal ZrO2 Particles in Ceramic Matrices**, J. Am. Ceram. Soc., 61[1-2] (1978) 85-86.

Claussen N, Weisskopf KL and Ruhle M, **Tetragonal Zirconia Polycrystals Reinforced with SiC Whiskers**, J. Am. Ceram. Soc., 69[3] (1986) 288-32.

Cornie JA, *et al*, **Processing of Metal and Ceramic Matrix Composites**, Am. Ceram. Soc. Bull., 65[2] (1986) 293-304.

Davidge RW and Green TJ, **The Strength of Two-Phase Ceramic/Glass Materials**, J. Mater. Sci., 3 (1968) 629-34.

De Bondt S, Froyen L and Deruyttere A, **Electrical Conductivity of Composites: A Percolation Approach**, J. Mater. Sci., 27 (1992), 1983-88.

Deckner D and Bernstein IM, **Handbook of Stainless Steel**, McHill Book Co, 1977.

Dees DW, Cloar TD, Easler TE, *et al*, **Conductivity of Porous Ni/ZrO_2-Y_2O_3 Cermets**, J. Electrochem. Soc., 134[9] (1987) 2141-46.

Deve HE and Maloney MJ, **On the Toughening of Intermetallics with Ductile Fibers: Role of Interfaces**, Acta Metall., 39[10] (1991) 2275-84.

Donald, IW and McMillan, PW, **Review Ceramic Matrix Composites**, J. Mater. Sci., 11 (1976) 949-72.

Duwez P, Brown Jr FH and Odell F, **The Zirconia-Yttria System**, J. Electrochem. Soc., 98[9] (1951) 356-62.

Dworak U, Olapinski H and Burger W, **Thermal Stability of PSZ**, in Science and Technology of Zirconia III, Advances in Ceramics 24 (1988) 545 - 548.

Edrees HJ, **Sialon Ceramic Matrix Composites**, PhD Thesis, University of Strathclyde Glasgow, 1990.

Edrees HJ and Hendry A, **Shrinkage and Densification of Particulate Reinforced Ceramic Matrix Composite**, Brit. Ceram. Trans., 98[1] (1999) 6-11.

Evans AG, **The Strength of Brittle Materials Containing Second Phase Dispersions**, Philosophical Magazine, 26 (1972) 1327-44.

Evans AG and Charles EA, **Fracture Toughness Determinations by Indentation**, J. Am. Ceram. Soc., 59[7-8] (1976) 371-2.

Evans AG and Heuer AH, **Review - Transformation Toughening in Ceramics : Martensitic Transformation in Crack - Tip Stress Fields**, J. Am. Ceram. Soc., 63[5-6] (1980) 241-48.

Exter P, Winnubst AJA, and Burggraaf AJ, **The Preparation and Characterization of Y-TZP/20wt% Alumina**, J. Europ. Ceram. Soc., 11 (1993), 497-507.

Faber KT, and Evans AG,[a] **Crack Deflection Processes I: Theory**, Acta Metall., 31[4] (1983) 565-76.

Faber KT, and Evans AG,[b] **Crack Deflection Processes II: Experiment**, Acta Metall., 31[4] (1983) 565-76.

Fantozzi G and Olagnon C, **Ceramic Matrix Composites**, in Materials Science and Technology, edited by Cahn RW, Haasen P and Kramer EJ, VCH Publisher, New York, 1993.

Flinn RA and Trojan PK, **Engineering Materials and Their Applications**, John Wiley and Sons (1995).

Gallagher PK, 1992, **Thermoanalytical Methods**, in Materials Science and Technology Vol. 2A, edited by Cahn, RW, Haasen P and Kramer, EJ, VCH, Germany.

Garvie RC, **Zirconium Dioxide and Some of Its Binary Systems, in High Temperature Oxide Part II**, edited by Alpel, Acad. Press NY (1970) 117-166.

Garvie, RC, **The Thermal Conductivity of Stabilized Zirconia**, J. Mater. Sci. 11 (1976) 1365-67.

Garvie RC, Hannink RH, and Pascoe RT, **Ceramic Steels?**, Nature, 258 [December] (1975) 703-04.

Garvie RC and Nicholson PS, **Phase Analysis in Zirconia Systems**, J. Am. Ceram. Soc., 55[6] (1972) 303-05.

Green DJ, **An Introduction to the Mechanical Properties of Ceramics**, Cambridge University Press (1998).

Guichard JL, Tillement O and Mocellin A, **Preparation and Characterisation of Alumina-Iron Cermets by Hot-Pressing of Nano-Composites Powders**, J. Mater. Sci., 32 (1997) 4513-21

Guichard JL, Tillement O and Mocellin A, **Alumina-Chromium Cermets by Hot-Pressing of Nanocomposite Powders**, J. Europ. Ceram. Soc., 18(1998) 1743-52.

Gupta TK, **A Qualitative Model for the Development of Tough Ceramics**, J. Mater. Sci., 9 (1974) 1585-1589.

Gupta TK., **Sintering of Tetragonal Zirconia and Its Characteristics**, Sci. of Sintering, 10[3] (1978) 205-16.

Gupta TK, Bechtold JH, Kuznicki RC, *et al*, **Stabilisation of Tetragonal Phase in Polycrystalline Zirconia**, J. Mater. Sci., 12(1977) 2421-26.

Gupta TK, Lange FF and Bechtold JH, **Effect of Stress-Induced Phase Transformation on the Properties Polycrystalline Zirconia Containing Metastable Tetragonal Phase**, J. Mater. Sci., 13(1978) 1464-70.

Haberko K and Pampuch R, **Influence of Yttria Content on Phase Composition and Mechanical Properties of Y-PSZ**, Ceramics Int., 9[1] (1983) 8-12.

Hannink RH, Kelly PM, and Muddle BC, **Transformation Toughening in Zirconia-Containing Ceramics**, J. Am. Ceram. Soc., 83[3] (2000) 461-87.

Harris B, **Engineering Composite Materials**, 2nd ed., IOM UK (1999).

Hasselmann DPH, **Effect of Cracks on Thermal Conductivity**, J. Composite Mater., 12[10] (1978) 403-07.

Hasselman, DPH, **Tailoring of the Thermal Transport Properties and Thermal Shock Resistance of Structural Ceramics**, in Tailoring Multiphase and Composite Ceramics, 1986, edited by Tressler *et al*, Plenum New York, pp. 731-54.

Hasselman DPH and Johnson LF, **Effective Thermal Conductivity of Composites with Interfacial Thermal Barrier Resistance**, J. Composite Mater., 21[June] (1987) 508-15.

Hasselman DPH, Johnson LF, Bentsen LD, *et.al.*, **Thermal Diffusivity and Conductivity of Dense Polycrystalline ZrO_2 Ceramic : A Survey**, Am. Ceram. Soc. Bull., 66[5] (1987) 799-806.

Heuer AH, **Transformation Toughening in ZrO_2 - Containing Ceramics**, J. Am. Ceram. Soc. 70[10] (1987) 689-98.

Higgins RA, **Properties of Engineering Materials**, 2nd edition, Edward Arnold (1994).

Hing P and Groves GW, **The Strength and Fracture Toughness of Polycrystalline Magnesium Oxide Containing Metallic Particles and Fibres**, J. Mater. Sci. 7 (1972) 427-34.

Hu W, Guan H, Sun X, *et al*, **Electrical and Thermal Conductivity of Nickel-Zirconia Cermets**, J. Am. Ceram. Soc., 81[8] (1998) 2209-12.

Hutchison JW, **Crack Tip Shielding by Micro-Cracking in Brittle Solids**, Acta Metall., 35[7] (1987) 1605-19.

Incropera FP and Dewitt DP, **Introduction to Heat Transfer**, John Wiley and Son (1996).

Ishizuka T, Ohta Y and Wakashima K, **Fracture Strength Evaluation of Zirconia Particles Reinforced Nickel Matrix Composites by Disk Bending Test**, J. Japan Inst. Metals, 59[8] (1995) 869-77.

Jung YG, Choi S, Oh C and Paik U, **Residual Stress and Thermal Properties of Zirconia / Metal (Nickel, Stainless Steel 304) Functionally Graded Materials Fabricated by Hot Pressing**, J. Mater. Sci. 32 (1997) 3841-50.

Kawashima T and M. Hishinuma, **Thermal Properties of Porous Ni/YSZ Particulate Composites at High Temperature**, Mater. Trans. JIM., 37[9] (1996) 1518-24.

Kerner EH, **The Elastic and Thermo-Elastic Properties of Composite Media**, Proc. Phys. Soc., B69 (1956) 808-813.

Kimizuka N and Katsura T, **Standard Free Energy of Formation of $YFeO_3$, $Y_3Fe_5O_{12}$ and a New Compound YFe_2O_4 in the Fe-Fe_2O_3-Y_2O_3 System at 1200 °C**, J. of Solid State Chemistry, Vol. 13, 1975, pp. 176-81.

Kingery WD, Pappis J, Doty ME, and Hill DC, **Oxygen Ion Mobility in Cubic $Zr_{0.85}Ca_{0.15}O_{1.85}$**, J. Am. Ceram. Soc., 42[8] (1959) 393-98.

Kingery, WD, **Introduction to Ceramics** (1976).

Kondo H, Sekino T, Choa YH and Niihara K, **Mechanical Properties of 3Y-ZrO_2/Ni Composites Prepared by Reductive Sintering**, Key Eng. Mater., Vol. [161-163] (1999) 419-22.

Kosco JB and Koss DA, **Ductile Fracture of Mechanically Alloyed Iron-Yttria Alloys**, Metallurgical Transactions A, 24A [March] (1993) 681-87.

Krstic VV, Nicholson PS, and Hoagland RG, **Toughening of Glasses by Metallic Particles**, J. Am. Ceram. Soc., 64[9] (1981) 499-504.

Lange FF, **The Interaction a Crack Front with a Second Phase Dispersion**, Philosophical Magazine, 22 (1970) 983-92.

Lange FF[a], **Transformation Toughening, Part 3: Experimental Observations in the ZrO_2-Y_2O_3 System**, J. Mater. Sci., 17 (1982) 240-46.

Lange FF[b], **Transformation Toughening, Part 4: Fabrication, Fracture Toughness and Strength**, J. Mater. Sci., 17(1982) 247-54.

Lankford J, **Indentation Microstructure in Palmqvist Crack Regime: Implications for Fracture Toughness Evaluation by the Indentation Method**, J. Mater. Sci. Lett., 1(1982) 493-95.

Lawn BR, Evans AG and Marshall DB, **Elastic/Plastic Indentation Damage in Ceramics: The Median/Radial Crack System**, J. Am. Ceram. Soc., 63[9-10] (1980) 574-80.

Lee W, **Structural Oxide II: Zirconia, in Ceramic Microstructures**, Chapman and Hall, London (1994) 316-87.

Lee HC and Gurland J, **Hardness and Deformation of Cemented Tungsten Carbide,** Mater. Sci. and Eng., 33(1978) 125-133.

Levin EM, Robbins CR and McMurdie, **Phase Diagrams for Ceramists,** American Ceramic Society.

Luo J and Stevens R, **Thermal Diffusivity/Conductivity of Magnesium Oxide/Silicon Carbide Composites,** J. Am. Ceram. Soc., 80[3] (1997) 699-704

Luo J and Stevens R, **Tetragonality of Nanosized 3Y-TZP Powders,** J. Am. Ceram. Soc., 82[7] (1999) 1922-24.

Masaki T, **Mechanical Properties of Toughened ZrO_2-Y_2O_3 Ceramics,** J. Am. Ceram. Soc., 69[8] (1986) 638-40.

Matsui M, Soma T and Oda I, **Effect of Microstructure on the Strength of Y-TZP Components,** Advances in Ceramics Vol. 12 : Science and Technology of Zirconia II, edited by Claussen N *et.al.*, 1984, pp. 371-81.

Matsumoto RKL, **Evaluation of Fracture Toughness Determination Methods as Applied to Ceria-Stabilized Tetragonal Zirconia Polycrystal,** J. Am. Ceram. Soc., 70[12] (1987) C366-68.

McMeeking RM and Evans AG, **Mechanics of Transformation-Toughening in Brittle Materials,** J. Am. Ceram. Soc., 65[5] (1982) 242-46.

Mecartney ML, **Influence of an AmorphousSecond Phase on the Properties of Yttria-Stabilized Zirconia Polycristal (Y-TZP),** J. Am. Ceram. Soc., 70[1] (1987) 54-58.

Mihara T, Asano S, Obata M, *et al*, **Elastic Constant of Zirconia/Stainless Steel Sintered Composite materials Measured by a Line-Focus Beam Acoustic Microscope,** J. Japan Inst. of Metals, 56[3] (1992) 321-26.

Miller DG, Singleton RH and Wallace AV, **Metal Fibre Reinforced Ceramics Composite,** Am. Ceram. Soc. Bull., 45[5] (1966) 513-17.

Minh NQ, **Ceramic Fuel Cells,** J. Am. Ceram. Soc., 76[3] (1993) 563-88.

Mirkovich, VV, **Comparative Method and Choice of Standards for Thermal Conductivity Determination,** J. Am. Ceram. Soc., 48[8] (1965) 387-91.

Moffat WG, **The Handbook of Binary Phase Diagrams,** General Electric, 1978.

Moorhead AJ and Kim H, **Strength and Magnetic Properties of a Laminated Composite of Magnetic Metal Foil and Zirconia,** J. Am. Ceram. Soc., 82[5] (1999) 1349-51.

Nawa M, Yamazaki K, Sekino T and Niihara K, **Microstructure and Mechanical Behaviour of 3Y-TZP/Mo Nanocomposites Processing a Novel interpenetrated Intragranular Microstructure,** J. Mater. Sci., 31(1996) 2849-58.

Nettleship I and Stevens R, **Tetragonal Zirconia Polycrystal - A Review,** Int. J. High Tech. Ceram., 3 (1987) 1-32.

Niihara K, Morena R and Hasselman DPH, **Evaluation of Kic of Brittle Solids by the Indentation Method with Low Crack-to-Indent Ratios,** J. Mater. Sci. Lett., 1 (1982) 13-16.

Ogawa K, **Interface Structure in Sintered Fe-Y_2O_3 Powder Studied by High Resolution Electron Microscopy,** J. Japan Inst. Metals, 57[6] (1993) 706-13.

Palmqvist S, **Metod att Bestämma Segheten hos Spröda material, Särskilt Hård-Metaller,** Jerkont. Ann. 141 [5] (1957) 300-307.

Palmqvist S, **Rißbildungsarbeit bei Vickers-Eindrücken als Maß für die Zähigkeit von Hatmetallen,** Archiv für das Eisenhüttenwesen, 33 [September] (1962) 629-34.

Pascual C and Duran P, **Subsolidus Phase Equilibrium and Ordering in the System ZrO_2-Y_2O_3,** J. Am. Ceram. Soc. 66[1] (1983) 23-27.

Patil RN and Subbarao EC, **Axial Thermal Expansion of ZrO_2 and HfO_2 in the Range temperature to 1400 C,** J. Applied Crystallography, 2(1969)281-88.

Ponton CB and Rwlings RD[a], **Vickers Indentation Fracture Toughness Test Part 1: Review of Literature and Formulation of Standardised Indentation Toughness Equations,** Mater. Sci. and Tech., 5[Sep.] (1989) 865-72.

Ponton CB and Rawlings RD[b], **Vickers Indentation Fracture Toughness Test Part 2: Application and Critical Evaluation of Standardised Indentation Toughness Equations,** Mater. Sci. and Tech., 5[Sep.] (1989) 961-76.

Porter DL and Heuer AH, **Mechanism of Toughening Partially Stabilized Zirconia (PSZ),** J. Am. Ceram. Soc., 60[3-4] (1977) 183-84.

Powell Jr. BR, Youngblood GE, Hasselmann DPH and Bentsen LD, **Effect of Thermal Expansion Mismatch on the Thermal Diffusivity of Glass-Ni Composites,** J. Am. Ceram. Soc., 63[9-10] (1980) 581-86.

Quinn GD and Morrell R, **Design Data for Engineering Ceramics: A Review of Flexural Strength,** J. Am. Ceram. Soc., 74[9] (1991) 2037-66.

Ray KK and Dutta AK, **Comparative Study on Indentation fracture Toughness Evaluation of Soda-Lime-Silica Glass**, Brit. Ceram. Trans., 98[4] (1999) 165-71.

Ruh, R, Mazdiyasni KS, Valentine PG and Bielstein HO, **Phase Relations in the System ZrO_2-Y_2O_3 at Low Y_2O_3 Contents**, J. Am. Ceram. Soc., 67[9] (1984) 190-92C.

Ruhle M, Claussen N, and Heuer AH., **Microstructural Studies of Y_2O_3 Containing Tetragonal ZrO_2 Polycrystals (Y-TZP),** Advances in Ceramics Vol. 12 : Science and Technology of Zirconia II, edited by Claussen N, Ruhle M and Heuer AH, (1984) 352-70.

Ruhle M, **Microscopy of Structural Ceramics**, Advanced Materials, 9[[3] (1997) 195-217.

Schafer U and Schubert H, **Zirconium Dioxide (ZrO_2) Ceramics**, Structure 33 – Struers J. Materialography, (1998) 14-15.

Schmid HK, **Quantitative Analysis of Polymorphic Mixes of Zirconia by X-ray Diffraction,** J. Am. Ceram. Soc., 70[5] (1987) 367-76.

Schubert H, **Anisotropic Thermal Expansion Coefficient of Y_2O_3-Stabilized Tetragonal Zirconia**, J. Am. Ceram. Soc., 69[3] (1986) 270-71.

Scott HG, **Phase Relationship in the Zirconia-Yttria System**, J. Mater. Sci., 10 (1975) 1527-35.

Selsing J, **Internal Stresses in Ceramics**, J. Am. Ceram. Soc., 44[6] (1961) 419.

Sheffield GS, and Schorr JR, **Comparison of Thermal Diffusivity and Thermal Conductivity Methods**, Am. Ceram. Soc. Bull., 70[1] (1991) 102-06.

Shetty DK, Wright IG, Mincer PN and Clauer AH, **Indentation Fracture of WC-Co Cermets,** J. Mater. Sci., 20 (1985) 1873-82.

Siebeneck HJ, Hasselman DPH, Cleveland JJ and Bradt RC, **Effect of Microcracking on the Thermal Diffusivity of Fe_2TiO_5**, J. Am. Ceram. Soc., 59[5-6] (1976) 241-44.

Siebeneck HJ, Hasselman DPH, Cleveland JJ and Bradt RC, **Effects of Grain Size and Microcracking on the Thermal Diffusivity of $MgTi_2O_5$**, J. Am. Ceram. Soc., 60[7-8] (1977) 336-38.

Sigl LS, Mataga PA, Dalgleish, BJ, *et al*, **On the Toughness of Brittle Materials Reinforced with a Ductile Phase**, Acta Metall., 36[4] (1988) 945-53.

Simpson LA and Wasylyshin, **Fracture Energy of Al_2O_3 Containing Mo Fibres**, J. Am. Ceram. Soc., 54[1] (1971) 56-57.

Smith A, **Metal Reinforced Sialon Matrix Composites**, PhD Thesis, University of Strathclyde Glasgow, 1993.

Smithells CJ and Brandes EA, **Metals Reference Book**, 1976, Butterworth and Co.

Srivastava KK, Patil RN, et.al., **Revised Phase Diagram of the System ZrO_2-$YO_{1.5}$**, Trans. J. Brit. Ceram. Soc., 73[3] (1974) 85-91.

Stevens R, **Engineering Properties of Zirconia, in Engineered Materials Handbook Volume 4: Ceramics and Glasses**, edited by Schneider Jr. SJ, ASM International (1994) 775-86.

Stubican VS and Helmann JR, **Phase Equilibria in Some Zirconia Systems**, Advances in Ceramics Vol. 3: Science and Technology of Zirconia, edited by Heuer AH and Hobbs LW, (1981) 25-36.

Stubican VS, Corman GS, Hellmann JR, and Senft G., **Phase Relationships in Some ZrO_2 Systems**, Advances in Ceramics Vol. 12: Science and Technology of Zirconia II, edited by Claussen N *et.al.*, 1984, pp. 96-106.

Subbarao EC, **Zirconia - An Overview**, Advances in Ceramics Vol. 3: Science and Technology of Zirconia, edited by Heuer AH and Hobbs LW, (1981) 1-24.

Swain MV, **Inelastic Deformation of Mg-PSZ and Its Significant for Strength-Toughness Relationship of Zirconia Toughened Ceramics**, Acta Metall., 33[11] (1985) 2083-91.

Takano Y, **Fabrication, Microstructure, and Mechanical Properties of (Cr_2O_3/ZrO_2(2.5Y) Composite Ceramics in the Cr_2O_3-Rich Region**, J. Am. Ceram. Soc., 81[9] (1998) 2497-500.

Takano Y, **Processing and Mechanical Behaviour of CrN/ZrO_2 (2Y) Composites,** J. Am. Ceram. Soc., 83[2] (2000) 448-50.

Tamburini UA, Arimondi M, Maglia F and Spinolo G, **Nickel/Yttria-Stabilized Zirconia Cermets from Combustion Synthesis: Effect of Process Parameters on Product Microstructures,** J. Am. Ceram. Soc., 81[7] (1998) 1765-72.

Taya M, Hayashi S, Albert S, *et al*, **Toughening of A Particulate - Reinforced Ceramic matrix Composite by Thermal Residual Strees,** J. Am. Ceram. Soc., 73[5] (1990) 1382-91.

Tsukuma K, Kubota Y, and Tsukidate T, **Thermal and Mechanical Properties of Y_2O_3-Stabilised Tetragonal Zirconia Polycrystals,** Advance in Ceramics, Vol. 12, Science and Technology of Zirconia II, edited by Claussen N and Ruhle, (1984) 382-90.

Turner PS, **Thermal Expansion Stresses in Reinforced Plastics,** J. Res. Nat. Bureau of Standards, 37[October] (1946) 239-61.

Vaidya RU and Chawla KK, **Thermal Expansion of Metal-Matrix Composites,** Composites Sci. and Tech., 50 (1994) 13-22.

Warren R, **Ceramic-Matrix Composites,** Chapman and Hall, (1992).

Warren R, **The Indentation Hardness of Microstructures Consisting of Hard Particles in a Metallic Matrix,** Proceeding 4th RISO International Symposium on Metallurgy and Materials, 1983, Denmark, pp. 572-82.

Watanabe M, Iio S, and Fukuura I, **Aging Behavior of Y-TZP,** in Advances in Ceramics, Vol. 12, edited by Claussen N *et al*, (1984) 391-98.

Wei GC and Becher PF, **Improvements in Mechanical Properties in SiC by the Addition of TiC Particles,** J. Am. Ceram. Soc., 67[8] (1984) 571-74.

Wenquan Z, Jianxin X and Changjing Z, **Investigation of Sintering Process on Composite of Stainless Steel and Zirconia,** The Fifth IUMRS Int. Conf. on Advanced Materials, IUMRS-ICAM'99, Beijing, China, (1999).

Whittemore Jr, OJ and Ault NN, **Thermal Expansion of Various Ceramic Materials to 1500 °C,** J. Am. Ceram. Soc., 39[12] (1957) 443-44.

Wiemhofer HD, **Surface and Interface Properties of Oxide Exhibiting Fast Oxygen Transport,** Brit. Ceram. Proc., edited by Steele BCH, 56 (1996) 1-23.

Wolten GM, **Diffusionless Phases Transformation,** J. Am. Ceram. Soc., 46[9] (1963) 418-22.

Woods ME and Oda I, **PSZ Ceramics for Adiabatic Engine Components,** in SAE Technical Paper Series, International Congress and Exposition, Michigan, (1982).

Yamada Y, Kawasaki A, Taya M and Watanabe R, **Effect of Debonding at the Phase Interface on Young's Modulus in Sintered PSZ/Stainless Steel Composites,** J. Japan Inst. Metals, 58[2] (1994) 162-68.

Yanagida H, Koumoto K, Miyayama M, **The Chemistry of Ceramics,** Wiley and Maruzen, 1996.

Zhan GD, Lai TR, *et al*, **Microstructures and Mechanical Properties of Yttria-Stabilized Tetragonal Zirconia Polycrystals Containing Dispersed TiC Particles,** J. Mater. Sci., 31 (1996) 2903-07.

Zwissler JG, Fine ME and Groves GW, **Strength and Toughness of a Ceramic Reinforced with Metal Wires,** J. Am. Ceram. Soc., 60 [9-10] (1977) 390-96.